

SEARCH FOR A HEAVY NEUTRAL GAUGE BOSON THROUGH ITS TAU PAIR DECAY MODE USING CMS DETECTOR AT THE LHC

A THESIS

Submitted to the
FACULTY OF SCIENCE
PANJAB UNIVERSITY, CHANDIGARH
for the degree of

DOCTOR OF PHILOSOPHY

2012

Nitish

DEPARTMENT OF PHYSICS
CENTRE OF ADVANCED STUDY IN PHYSICS
PANJAB UNIVERSITY, CHANDIGARH
INDIA



*Dedicated to Almighty GOD, my family,
and friends*

Acknowledgments

This thesis would not have been possible without the guidance and help of several individuals who in one way or another contributed and extended their valuable assistance in the preparation and completion of this study. It is a pleasure to convey my gratitude to all of them in my humble acknowledgment.

First and foremost, my utmost gratitude to my advisor Prof. J.B. Singh for providing me an opportunity to work in an internationally renowned Large Hadron Collider experiment. His accurate, enlightening, still practical advices and suggestions, pointing to the core of the problems, have been a greatly valued guidance. I am also thankful to him for providing me an opportunity to carry out my research work at Tata Institute of Fundamental Research in Mumbai, where I completed a significant fraction of my thesis work. Prof. Singh allowed me to work with some incredible people that have really shaped my thinking about physics.

I express my deep and sincere gratitude to my co-supervisor, Prof. Kajari Mazumdar, who hosted me for several months at TIFR. Her invaluable encouragement, assistance, and support have provided the basis of the present thesis. Her involvement with her originality has triggered and nourished my intellectual maturity that I will benefit from, for a long time to come.

Many thanks goes to Prof. S. Beri, Prof. M. Kaur, and Dr. V. Bhatnagar for their continuous support and efforts to provide us adequate facilities in PUHEP lab. I would like to thank INDIA-CMS Collaboration for providing a good platform to discuss our work by arranging regular collaboration meetings.

Several people played an important role throughout the research work. I was fortunate enough, that I got a chance to work with Prof. Alexei Safonov (Texas A & M, US) and Prof. Simone Gennai (CERN/INFN), the leading tau experts in the world. Their valuable suggestions and fruitful discussions helped me a lot in improving $Z' \rightarrow \tau\tau$ analysis. They always pushed to get maximum out of me. I want to say thank you for all the guidance and support. I am also thankful to all the members of the Exotica Tau group at CMS. It was a great experience working together in a team.

My sincere thanks goes to Prof. Teruki Kamon (Texas A & M, US) for providing me an opportunity to work closely with him for the VBF SUSY analysis. I got many valuable things to learn from him for my professional life as well as for my personal life.

I would like to give a very special recognition to Dr. Alfredo Gurrola (Vanderbilt University, US) for being my mentor throughout my research work. He is a great physicist. I learnt many analysis techniques and physics concepts from him. Thank you Alfredo for all your help and everlasting support.

I am thankful to Prof. Sudhir Malik (University of Nebraska, US) for providing me an opportunity to work with him for my service task. It was very enjoyable working with him. I am also thankful to Prof. Subir Sarkar (SINP, India), Prof. Giuseppe Bagliesi (University of Pisa, IT), and Dr. Letizia Lusito (Northwestern University, US) for helping me in the associated Higgs analysis.

I am thankful to Chairman, Department of Physics, Panjab University for providing adequate facilities to work in the department. The present research has been supported by various organizations including University Grants Commission (UGC) and Department of Science and Technology (DST). I am thankful to them for their confidence in me.

I am indebted to my labmates for providing a stimulating and enjoyable environment in the lab. Thank you Archana mam, Dr. Sunil Bansal, Dr. Supreet Pal Singh, Dr. Monika Bansal, Dr. Vishal Bhardwaj, Dr. Inderpal Singh, Dr. Prabhdeep Kaur, Dr. Jyoti Joshi, Mani mam, Anu mam, Ritu mam, Ruchi, Monika, Manbir, Raman-deep, Amandeep, and Ankita. Dr. Sunil and Dr. Supreet helped me a lot in learning

CMSSW software and with various aspects of the analysis.

I am very thankful to my friends Vijay, Sanjay, Jashandeep, Ripandeep, Simran, Nitin, Gurvir, Rama, Deepika, Mani, Renu, and Mamta for helping me get through the challenging times and for making my life at Panjab University pleasant and enjoyable one.

I am heartily thankful to my friends from TIFR Vipin, Neeraj, Sandeep, Jasmine, Sanjeev, Gouranga, Bibhuti who made my stay at TIFR very comfortable and enjoyable.

I would like to thank all my friends Sudha, Sandhya, Shilpi, Varun, Shivali, and Atanu from Delhi University and Saha Institute with whom I spent a wonderful time during my stay at CERN.

I am grateful to the members of CMS office and purchase section in the department who were always there to help me in my official works.

No words can describe the affection and diligent support that I got from my family. This thesis is simply impossible without them. I am deeply indebted to my father, Om Parkash, for his love and unconditional support. I remember the hardships he had to face for supporting my graduation, post-graduation, and Ph.D. He is the figure whom I always look upto. Love and tenderness of my mother, Kanta Rani, always brought me back home when I got stuck up in difficult times. I feel proud of my elder brother, Sahil Dhingra, who always encouraged me to work hard and supported me to get higher education. I am greatly thankful to my “Bhabi” for her care and affection. I always enjoy playing with my cute nephew when I get back home. I am also thankful to my grandparents for their everlasting love and support. May GOD bless them all with all kind of happiness in their life.

Last but not least, my greatest regards to the infinitely perfect almighty for bestowing upon me the courage to face the complexities of life and complete this project successfully. May your name be exalted, honored, and glorified.

Finally, I would like to thank everybody who was important to the successful realization of this thesis, as well as expressing my sincere apology that I could not mention them personally one by one.

Dated: 19.10.2012

Nitish

Abstract

The Standard Model (SM) of elementary particles has been able to accomodate almost every observed quantum physical process within a single theoretical framework. However, it is widely believed that the SM does not explain a complete picture as it fails to answer many fundamental problems such as the incorporation of fourth fundamental force *i.e.* gravitational force, absence of dark matter candidate, unification of the gauge couplings at high energies, and the origin of mass. In order to incorporate these aspects, *New Physics* models like Supersymmetry (SUSY), Extra-Dimensions, Grand Unified Theory (GUT), *etc.* have evolved over the time. The SM and these new models predict the existence of a particle called, the Higgs boson, which is supposed to be responsible for providing mass to all the fundamental particles. Many extensions of the SM also predict the existence of new heavy gauge bosons. Among these a simplest extension is the one that involves an additional $U(1)$ gauge group with an associated neutral gauge boson, usually labeled as Z' . A common one among such extensions is called Sequential Standard Model (SSM) that includes a neutral gauge boson, Z'_{SSM} , with the same couplings to quarks and leptons as the Standard Model Z boson. Although this model is not gauge invariant but it has been traditionally considered by experiments studying high-mass resonances. Other models, such as the superstring-inspired E_6 model, has more complex gauge group structure, $E_6 \rightarrow SO(10) \times U(1)_\psi$, with a corresponding neutral gauge boson denoted as Z'_ψ . Most of the studies performed in this subject assumed generation-independent gauge couplings for Z' gauge bosons, but models also exist in which Z' couples preferentially to the third generation fermions. In such non-universal scenarios, the sensitivity of the traditional searches for Z' production using e^+e^- and $\mu^+\mu^-$ final decay states may be substantially reduced, motivating the exploration of $\tau^+\tau^-$ decay states. Hence, the search in $Z' \rightarrow \tau^+\tau^-$ final states helps not only in testing the universality of the couplings but it will also help to establish the branching ratio of $Z' \rightarrow \tau^+\tau^-$ relative to $Z' \rightarrow e^+e^-/\mu^+\mu^-$ final states. The Large Hadron Collider (LHC) at CERN has been built to discover the Higgs boson and to probe such *New Physics* scenarios.

In this thesis, we report the results from the search of new heavy neutral gauge bosons, Z' , using proton-proton collision data at center-of-mass energy $\sqrt{s} = 7$ TeV and 8 TeV collected with CMS detector during LHC Runs in Years 2010, 2011, and 2012 respectively. The combined search comprises of four dominant decay channels of $Z' \rightarrow \tau^+\tau^-$ production: $Z' \rightarrow \tau^+\tau^- \rightarrow \tau_h\tau_h$, $Z' \rightarrow \tau^+\tau^- \rightarrow \tau_\mu\tau_h$, $Z' \rightarrow \tau^+\tau^- \rightarrow \tau_e\tau_h$, and $Z' \rightarrow \tau^+\tau^- \rightarrow \tau_e\tau_\mu$, where τ_e and τ_μ refer to leptonically (e and μ) decaying tau-lepton while τ_h refers to hadronically decaying tau-lepton. For LHC data of Run 2010 and Run 2011, the analyses performed in fully hadronic tau final state *i.e.* $Z' \rightarrow \tau^+\tau^- \rightarrow \tau_h\tau_h$, have been presented in details while collision data of Run 2012 is used to perform analysis in $Z' \rightarrow \tau^+\tau^- \rightarrow \tau_\mu\tau_h$ final state. The collision data for Run 2010 and Run 2011 corresponds to an integrated luminosity of 36.1 ± 1.4 pb $^{-1}$ and 4.94 ± 0.11 fb $^{-1}$, respectively. The studies performed with 2012 data corresponds to an integrated luminosity of 5.10 ± 0.22 fb $^{-1}$. The potential backgrounds are estimated mostly using data-driven techniques and excess of events above the Standard Model background predictions is looked for. To quantify the significance of any possible excess of observed events or to set an upper limit on the $Z' \rightarrow \tau\tau$ production rate, we perform a fit of the invariant mass distribution of the two taus and employ Bayesian technique to interpret the results in terms of the upper 95% confidence level limits. The combined limit takes into account the correlation of systematic uncertainties within and across all the four decay channels.

The search performed with 2010 data did not reveal any excess of observed events over the Standard Model background predictions, hence, we excluded a Z'_{SSM} decaying to $\tau^+\tau^-$ below mass 468 GeV/c 2 which exceeded the previous best limit ($M_{Z' \rightarrow \tau^+\tau^-} > 399$ GeV/c 2) set by Tevatron experiments at Fermilab [1]. The search performed with higher statistics of 2011 data again showed no excess of observed events, enabling us to exclude a Z'_{SSM} decaying to $\tau^+\tau^-$ below mass 1.4 TeV and E $_6$ model Z'_ψ decaying to $\tau^+\tau^-$ with mass less than 1.1 TeV. The details of the studies performed with 5.10 ± 0.22 fb $^{-1}$ of 8 TeV data of LHC Run 2012 are also presented in this thesis. A similar search performed by ATLAS experiment with 4.7 fb $^{-1}$ of 7 TeV data of LHC Run 2011, excluded a $Z'_{SSM} \rightarrow \tau^+\tau^-$ below mass 1.3 TeV [2].

Contents

1	Introduction	1
1.1	Standard Model of Particle Physics	2
1.1.1	Fundamental Forces	4
1.1.2	Fundamental Particles	5
1.1.3	Quantum Chromodynamics (QCD)	7
1.1.4	Electroweak Theory and Higgs Mechanism	8
1.2	Need of the Large Hadron Collider (LHC)	10
1.3	Motivation for the search of Z' gauge bosons decaying into a pair of tau-leptons	12
1.4	Organization of Thesis	16
2	Large Hadron Collider and CMS Experiment	19
2.1	Layout of Large Hadron Collider	20
2.1.1	LHC Accelerator System and Injector Complex	22
2.1.2	Luminosity and Center-of-mass energy	23
2.1.3	Experiments at the LHC	25
2.2	Compact Muon Solenoid	28
2.2.1	CMS Co-ordinate system	29
2.2.2	Superconducting Magnet	30
2.2.3	Inner Tracking System	31
2.2.4	Electromagnetic Calorimeter	34
2.2.5	Hadron Calorimeter	38
2.2.6	Outer Hadron Calorimeter	40
2.2.7	Muon System	42
2.2.8	Trigger system	50
2.3	Particle detection through their interaction with CMS detector mate- rial	53

CONTENTS

3	Event Reconstruction Chain and Data Samples	59
3.1	Event Generators	61
3.1.1	PYTHIA	63
3.1.2	MADGRAPH	64
3.1.3	TAUOLA	64
3.2	CMS Detector Simulation	64
3.3	Reconstruction of Physics Objects	66
3.4	Particle Flow Reconstruction	67
3.5	Hadronic Tau Reconstruction	69
3.5.1	Shrinking Cone Algorithm (2010 Data)	69
3.5.2	Hadron-Plus-Strip Algorithm (2011 and 2012 Data)	71
3.6	Missing Transverse Energy	75
3.7	Muon Reconstruction	75
3.8	Monte-Carlo and Collision Data Samples Analyzed	76
3.8.1	Search for $Z' \rightarrow \tau\tau \rightarrow \tau_h\tau_h$ using 2010 collision data	76
3.8.2	Search for $Z' \rightarrow \tau\tau \rightarrow \tau_h\tau_h$ using 2011 collision data	78
3.8.3	Search for $Z' \rightarrow \tau\tau \rightarrow \tau_\mu\tau_h$ using 2012 collision data	80
4	Search for $Z' \rightarrow \tau\tau$ using LHC collision data of Run 2010 collected with CMS detector	83
4.1	Introduction	83
4.2	Signal and Potential Backgrounds	85
4.2.1	Signal Process: $pp \rightarrow Z' + X; Z' \rightarrow \tau\tau \rightarrow \tau_h\tau_h$	85
4.2.2	Background Processes	87
4.3	Event Selection	89
4.3.1	Skimming Criteria	92
4.3.2	Signal Selections	93
4.4	Estimation of Selection Efficiencies using Monte-Carlo Cut-based Method	99
4.5	Hadronic Tau Trigger Algorithm	99
4.5.1	Measurement of Di-Tau Trigger Efficiency Using Fake Taus . .	102

CONTENTS

4.6	Additional Validation Checks	104
4.7	Background Estimation	105
4.7.1	Estimation of QCD multijet background using data driven ap- proach	105
4.7.2	Estimation of other non-QCD SM backgrounds	108
4.8	Data in the Signal Region	109
4.9	Systematic Uncertainties	113
4.10	Statistical Interpretation	115
4.11	Results and Conclusions	120
5	Search for $Z' \rightarrow \tau\tau$ using LHC collision data of Run 2011 collected with CMS detector	125
5.1	Introduction	125
5.2	Pile-Up Reweighting	126
5.3	Event Selection	127
5.3.1	Skimming Criteria	127
5.3.2	Signal Selections	128
5.4	Estimation of Selection Efficiencies using Monte-Carlo Cut-based Method	133
5.5	Di-Tau Trigger Efficiency Measurement Using Fake Taus	133
5.6	Measurement and Validation of Signal Efficiencies	138
5.6.1	Selection of a clean sample of $Z \rightarrow ee$ events and Validation of the offline code	141
5.6.2	Validation of the offline selections and the Trigger	145
5.6.3	Validation of signal selections for the high mass events	146
5.6.4	Trigger efficiency of the Di-Tau trigger	148
5.7	Validation Plots for Signal Selections	149
5.8	Background Estimation	149
5.8.1	Data-driven estimation of QCD multijet background	149
5.8.2	Estimation of $Z \rightarrow \tau\tau$ background	152
5.8.3	Estimation of $Z \rightarrow ee$ background	154

CONTENTS

5.8.4	Estimation of $t\bar{t}$ and $W + jets$ backgrounds	155
5.8.5	Data in Low and High Mass Regions	156
5.9	Systematics Uncertainties	157
5.10	Results and Conclusions	163
6	Search for $Z' \rightarrow \tau\tau$ using LHC collision data of Run 2012 collected with CMS detector	167
6.1	Introduction	167
6.2	Pile-Up Reweighting	168
6.3	Event Selection	168
6.3.1	Skimming Criteria	168
6.3.2	Signal Selections	169
6.4	Background Estimation	173
6.4.1	Estimation of $Z \rightarrow \mu\mu$ background	173
6.4.2	Estimation of $Z \rightarrow \tau\tau$ background	174
6.4.3	Estimation of $W + jets$ background	175
6.4.4	Estimation of $t\bar{t}$ background	178
6.4.5	Estimation of QCD multijet background	180
6.5	Data in the Signal Region and Results	182
7	Summary and Conclusions	185
7.1	Search for Z' gauge bosons decaying to $\tau^+\tau^-$ with the CMS detector	186
	Publications/Conferences	199

List of Figures With Captions

1.1	Building blocks of Standard Model.	3
2.1	Schematic layout of the LHC.	22
2.2	Graph of total integrated luminosity collected by CMS detector during Run 2011 (left) and Run 2012 (right).	23
2.3	The Large Hadron Collider's accelerator complex, in France and Switzerland.	24
2.4	One of the early proton-proton collision event seen in CMS detector at 7 TeV center-of-mass energy during LHC Run 2010.	26
2.5	The Compact Muon Solenoid at the Large Hadron Collider.	29
2.6	Transverse or cross-sectional view (left) and longitudinal view (right) of the CMS detector.	30
2.7	Artistic view of the CMS solenoidal magnet.	31
2.8	Schematic view of the CMS inner tracking system.	33
2.9	Pixel detector of CMS inner tracking system.	34
2.10	Measured resolution of track transverse impact parameter (left) and longitudinal impact parameter as a function of the track transverse momentum (right). Only central tracks with $ \eta < 0.4$ are considered. Black and red points correspond to data and MC simulation, respectively.	35
2.11	Primary vertex resolution in x (a), y (b), and z (c) as function of the number of tracks used in the fitted vertex.	36
2.12	Electromagnetic calorimeter of the CMS detector.	37
2.13	Longitudinal cross-section of the quarter of the CMS detector showing the positions of the hadronic calorimeter barrel (HB), hadronic calorimeter endcap (HE), forward hadronic calorimeter (HF), and outer hadronic calorimeter (HO).	40

LIST OF FIGURES WITH CAPTIONS

2.14	Number of interaction lengths till the last sampling layer of the hadron calorimeter as a function of η . The two shaded regions correspond to the setups with and without the outer hadron calorimeter.	41
2.15	Material thickness in interaction lengths at various depths, as a function of pseudorapidity.	43
2.16	Layout of the one quadrant of the CMS (left) and a display of the collision event with a muon crossing the DT and CSC chambers in the overlap region between barrel and endcap (right).	43
2.17	Layout of the CMS barrel muon DT chambers in one of the 5 wheels. The chambers in each wheel are identical with the exception of wheels -1 and +1 where the presence of cryogenic chimneys for the magnet shortens the chamber in 2 sectors. Note that in sectors 4 (top) and 10 (bottom) the MB4 chambers are cut in half to simplify the mechanism assembly and the global chamber layout.	45
2.18	The layout of muon cathode strip chambers (CSCs) in one quarter of the CMS. Most of the cathode strip chambers are highlighted in dark-red, the ME4/2 chamber is not highlighted, because it was assumed that it would not be installed at the start-up of the LHC, but delays in the LHC start-up schedule allowed for its installation for the first collision data.	46
2.19	Transverse view of the muon system layout in the barrel region, showing the positions of the DT and RPC stations.	48
2.20	Resolution on transverse momentum as measured with $\sim 40 \text{ nb}^{-1}$ of integrated luminosity (blue) compared to the Monte Carlo resolution computed from Monte Carlo truth (red points) and from the fit (black squares). The gray band in data represents the error on the fitted function for data computed from the errors on the parameters.	49
2.21	Architecture of Level-1 trigger	51
2.22	Architecture of Data Acquisition system	52
2.23	Schematic view of an electromagnetic shower.	54

LIST OF FIGURES WITH CAPTIONS

2.24	Fractional energy loss of electron per radiation length in lead as function of electron energy.	55
2.25	Slice of CMS detector showing interactions of various particles in sub-detectors of CMS.	57
3.1	Basic steps in event generation, simulation and data analysis.	61
3.2	Feynman diagram for tree level Drell-Yan process.	63
3.3	The signal and isolation cones in shrinking cone algorithm.	71
3.4	Illustration of elliptical isolation. The electron-positron pairs coming from photons originated from the decay of neutral pions can be swept out of the circular signal cone region, hence, they can fall into the isolation cone. By using an elliptical signal cone, a good fraction of tau-leptons can be recovered which would have been lost otherwise.	72
4.1	Production of a SSM Z' gauge boson and its subsequent decay to a pair of tau-leptons.	86
4.2	Product of theoretical cross-section for a SSM Z' times the branching ratio to a pair of tau-leptons as a function of Z' mass.	86
4.3	Illustration of jet hadronization process.	90
4.4	Feynman diagram for the $pp \rightarrow Z + X; Z \rightarrow \tau^+\tau^-$ production.	90
4.5	Feynman diagram for the $pp \rightarrow Z + X; Z \rightarrow e^+e^-$ production.	90
4.6	Feynman diagram for Standard Model $W + jets$ production.	91
4.7	Feynman diagram for Standard Model $t\bar{t}$ production.	91
4.8	Illustration of P_ζ^{vis} and P_ζ	97
4.9	Distribution of P_ζ vs. P_ζ^{vis} for MC based $Z' \rightarrow \tau\tau$ events.	98
4.10	Distribution of P_ζ vs. P_ζ^{vis} for $W + jets$ events.	98
4.11	Tau trigger efficiencies for Level-1 (left), HLT (right), plotted against offline PFTau E_T for $Z \rightarrow ee$ MC, $Z \rightarrow \tau\tau$ MC, and data.	103

LIST OF FIGURES WITH CAPTIONS

4.12	Overall hadronic tau trigger efficiency (Level-1 + HLT) for $Z \rightarrow ee$, $Z \rightarrow \tau\tau$, and 2010 electron dataset (left), Overall hadronic tau trigger efficiency for $Z \rightarrow \tau\tau$ MC and data (left). The $Z \rightarrow \tau\tau \rightarrow \tau_\mu\tau_h$ data candidates were selected from events passing the SingleMuon trigger.	104
4.13	Dielectron distributions from double tau trigger data with reversed anti-electron cuts and $Z \rightarrow ee$ MC for validation of the double tau analysis: (a) Invariant mass of the two electrons, (b) \cancel{E}_T distribution, (c) transverse momentum of electrons reconstructed as PFTau candidates.	106
4.14	QCD mass distribution after all selections except the track multiplicity requirement, <i>i.e.</i> , considering all; 1, 2 and 3 prong taus.	109
4.15	Comparison of mass and \cancel{E}_T distributions for 1 prong taus and 1 or 2 or 3 prong taus, normalized to their area, without \cancel{E}_T requirement.	110
4.16	Comparison of mass and \cancel{E}_T distributions for 1 prong taus and 1 or 2 or 3 prong taus, normalized to their area, requiring $\cancel{E}_T \geq 15$ GeV.	111
4.17	Ratio of the number of selected data events with an opposite-sign pair to those with a like-sign pair after subtracting all of the MC-based backgrounds independently: (a) full invariant mass for $\cancel{E}_T \geq 0$ GeV, (b) invariant mass of the leading p_T tau and \cancel{E}_T for $\cancel{E}_T \geq 15$ GeV. The significant value is extracted with a one-dimensional fit in regions with small background contamination: (a) 1.20 ± 0.09 (b) 1.1 ± 0.2 . Plots (c) and (d) show the relative contribution of each background, requiring opposite-sign pairs except in the case of QCD, which is estimated from like-sign pairs from data.	112
4.18	Data, backgrounds and signal invariant mass distributions after all cuts for a Z' with mass of $500 \text{ GeV}/c^2$.	114
4.19	(a) Poisson likelihood, (b) 95% C.L. limits for a sample of pseudo-experiments.	119

LIST OF FIGURES WITH CAPTIONS

4.20	(a) Example of pseudo-experiment (with $Z'(400)$) resulting in $\sigma_{95} = 4.4 \text{ pb}$ (b) Example of pseudo-experiment (with $Z'(350)$) resulting in $\sigma_{95} = 12.8 \text{ pb}$	119
4.21	$\tau\tau$ invariant mass distributions for data, backgrounds, and signal, after all cuts for a Z' with mass of $350 \text{ GeV}/c^2$ (top) and $700 \text{ GeV}/c^2$ (bottom).	121
4.22	95% C.L. upper limits on the cross-section for (a) $\tau_\mu\tau_h$, (b) $\tau_e\tau_h$, (c) $\tau_e\tau_\mu$, and (d) $\tau_h\tau_h$ channels.	122
4.23	$\tau\tau$ invariant mass distributions for (a) $\tau_\mu\tau_h$, (b) $\tau_e\tau_h$, (c) $\tau_e\tau_\mu$, after all cuts for a Z' with mass of $350 \text{ GeV}/c^2$	123
4.24	Combined $= \tau_\mu\tau_h + \tau_e\tau_h + \tau_e\tau_\mu + \tau_h\tau_h$ limit on the $Z' \rightarrow \tau\tau$ production cross-section as a function of Z' mass.	124
5.1	Distribution of number of pile-up interactions in a Summer 11 MC sample ($Z \rightarrow \tau\tau$) before and after reweighting. The pile-up distribution in collision data is also overlayed. The pile-up distribution in MC matches with the distribution in the collision data after pile-up reweighting is applied.	127
5.2	Level-1, Level-2, and Level-3 relative trigger efficiencies and overall trigger efficiency for HLT_DoubleIsoPFTau20_Trk5.	140
5.3	Level-1, Level-2, and Level-3 relative trigger efficiencies and overall trigger efficiency for HLT_DoubleIsoPFTau35_Trk5_eta2p1.	141
5.4	Level-1, Level-2, and Level-3 relative trigger efficiencies and overall trigger efficiency for HLT_DoubleIsoPFTau45_Trk5_eta2p1_v{1-7}.	142
5.5	Level-1, Level-2, and Level-3 relative trigger efficiencies and overall trigger efficiency for HLT_DoubleIsoPFTau45_Trk5_eta2p1_v8 for Run2011B. In addition to the factorized efficiencies (red line), we fit the overall efficiency using only one error function shown in green.	143
5.6	$Z \rightarrow ee$ visible mass and electrons (fake taus) η distribution of both legs in the $Z \rightarrow ee$ control region of the double hadronic tau analysis using $\tau_e\tau_h$ dataset.	145

LIST OF FIGURES WITH CAPTIONS

5.7	$Z \rightarrow ee$ visible mass, transverse mass of the leading leg and the \cancel{E}_T , \cancel{E}_T , and both taus p_T distribution for the $Z \rightarrow ee$ control region. Note that $ \eta < 1.0$	146
5.8	$Z \rightarrow ee$ visible mass, transverse mass of the leading leg and the \cancel{E}_T , \cancel{E}_T , and both taus p_T distribution for the $Z \rightarrow ee$ control region of the double hadronic tau analysis. Note that $ \eta < 1.0$	148
5.9	(N-1) distributions for both taus p_T , \cancel{E}_T , ζ , $\Delta R(\tau_1, \tau_2)$, and $\cos\Delta\phi(\tau_1, \tau_2)$	150
5.10	Ratio of opposite-sign to like-sign events passing all the signal selections, for different p_T and \cancel{E}_T requirements.	153
5.11	Ratio of opposite-sign to like-sign events passing all the signal selections, for $p_T > 35$ GeV/ c and $\cancel{E}_T > 15$ GeV/ c requirements.	153
5.12	Transverse mass of the leading p_T tau and the \cancel{E}_T , (a) and (b); and the cosine of the angle between the leading p_T tau and the \cancel{E}_T , (c) (d); obtained by loosening the minimum \cancel{E}_T requirement to 15 GeV and requiring opposite-sign charges, (a) and (c); or same-sign charges, (b) and (d).	155
5.13	Ditau full invariant mass, and visible mass for the $Z \rightarrow \tau\tau$ control region for the first run period explored: runs 163269 to 165970.	156
5.14	Di-tau invariant mass $M(\tau_1, \tau_2, \cancel{E}_T)$ fitted shapes after applying all selection cuts.	159
5.15	Di-tau invariant mass, visible mass, and \cancel{E}_T for the $Z' \rightarrow \tau_h \tau_h$ signal region. The right-most bin indicates the overflow.	160
5.16	Probability, in $Z' \rightarrow \tau\tau$, to obtain n additional jets (non-tau and non-lepton) in the event.	161
5.17	Depiction of the recalculation of MET due to JES, TES, and LES considerations.	162
5.18	$M(\tau_1, \tau_2, \cancel{E}_T)$ distributions for all four final states: (a) $\tau_e \tau_\mu$, (b) $\tau_e \tau_h$, (c) $\tau_\mu \tau_h$, and (d) $\tau_h \tau_h$. The dashed line represents the mass distribution for a $Z'_{SSM} \rightarrow \tau\tau$ with a mass of 750 GeV/ c^2	164

LIST OF FIGURES WITH CAPTIONS

5.19	95% C.L. upper limits on the $Z' \rightarrow \tau\tau$ production cross-section as a function of Z' mass for (a) $\tau_\mu\tau_h$, (b) $\tau_e\tau_h$, (c) $\tau_e\tau_\mu$, and (d) $\tau_h\tau_h$ final states.	165
5.20	Combined 95% C.L. upper limits on the $Z' \rightarrow \tau\tau$ production cross-section as a function of Z' mass for all the four final states: $\tau_\mu\tau_h$, $\tau_e\tau_h$, $\tau_e\tau_\mu$, and $\tau_h\tau_h$	166
6.1	Figure shows the distribution for (a) Transverse momentum of τ -lepton, (b) Transverse momentum of μ , (c) Invariant mass of $\mu - \tau$ pair; $M(\mu, \tau)$, and (d) p_T asymmetry between μ and τ -lepton in $Z \rightarrow \mu\mu$ control region.	174
6.2	Figure shows the distribution for (a) Transverse momentum of τ -lepton, (b) $\cos\Delta\phi(\mu, \tau)$, (c) Missing Transverse Energy, and (d) One-dimensional ζ in $Z \rightarrow \tau\tau$ control region.	176
6.3	Figure shows the distribution for (a) $\cos\Delta\phi(\mu, \tau)$, (b) Transverse mass of μ - \cancel{E}_T pair, (c) Invariant mass of μ - τ pair, and (d) One-dimensional ζ in $W + jets$ Control Region 1.	178
6.4	Figure shows the distribution for transverse mass of μ - \cancel{E}_T pair in $W + jets$ Control Region 2.	179
6.5	Figure shows the distribution for (a) $\cos\Delta\phi(\mu, \tau)$, (b) Transverse mass of μ - \cancel{E}_T pair, (c) Invariant mass of μ - τ pair, and (d) One-dimensional ζ in $t\bar{t}$ Control Region 1.	181
6.6	Figure shows the distribution for number of jets tagged as b-tags in $t\bar{t}$ Control Region 2.	182
7.1	Combined $= \tau_\mu\tau_h + \tau_e\tau_h + \tau_e\tau_\mu + \tau_h\tau_h$ limit on the $Z' \rightarrow \tau\tau$ production cross-section as a function of Z' mass.	188
7.2	Combined 95% CL upper limit on the $Z' \rightarrow \tau\tau$ production cross-section as a function of Z' mass for all the four channels: $\tau_\mu\tau_h$, $\tau_e\tau_h$, $\tau_e\tau_\mu$, and $\tau_h\tau_h$	188

List of Tables with Details

1.1	Details of the four fundamental forces known in nature.	5
1.2	Three generations of elementary particles.	7
3.1	Branching fractions of the dominant hadronic decays of the τ -lepton, the symbols and masses of the intermediate resonances. The h stands for both ρ and K , but in this analysis the ρ mass is assigned to all charged particles. The table is symmetric under charge conjugation. .	74
3.2	Definition of different working points of HPS tau isolation.	75
3.3	Collision Data Samples for LHC Run 2010.	77
3.4	List of MC samples used. All these samples correspond to <i>GEN-SIM-RECO</i> chain.	78
3.5	Collision Data Samples for LHC Run 2011.	79
3.6	List of MC samples used. Note that the QCD multijet background is extracted directly from the collision data.	79
3.7	Collision Data Samples for LHC Run 2012.	80
3.8	List of MC samples used. Note that the QCD background is extracted directly from the collision data.	80
4.1	Branching Ratios of $\tau^+\tau^-$ decay modes.	84
4.2	SSM Z' cross-section times the branching ratios to $\tau\tau$ for various mass points.	87
4.3	Table shows the skimming efficiencies for various MC samples.	92
4.4	Summary of the trigger paths according to the run range applied on data.	94

LIST OF TABLES WITH DETAILS

4.5	Relative efficiencies for double hadronic tau selection in case of signal (with Z' mass of $500 \text{ GeV}/c^2$) and low energy QCD-jets with ranges of final state parton transverse momenta in $2 \rightarrow 2$ subprocesses given in GeV/c . Note that MC-based estimation of QCD multijet background is not used for this channel. The error reported here is statistical error only.	100
4.6	Relative efficiencies for double hadronic tau selection for QCD-jets, with ranges of final state parton transverse momenta in $2 \rightarrow 2$ subprocesses given in GeV/c , $W + jets$ and $t\bar{t}$ backgrounds. Note that MC-based estimation of QCD multijet background is not used for this channel. The error reported here is statistical error only.	101
4.7	Estimated signal and background contributions along with the observed events.	113
4.8	List of Systematics for MC and Data	116
5.1	Table showing the skim efficiencies.	128
5.2	Summary of the trigger paths according to the run-range applied on the collision data.	130
5.3	Cut flow relative efficiency table, calculated from raw generator events in case of MC, i.e., before pile-up reweighing or normalization to luminosity. These efficiencies are rounded off to the last decimal shown. “LL” refers to the leading leg, and “SL” to the subleading leg. The skimming selects events with at least one pair of HPS taus, each of which must have a leading track p_T of at least $5 \text{ GeV}/c$, and pass the HPS discriminant by decay mode finding. The preselection is applied to both legs and involves a p_T cut of $20 \text{ GeV}/c$, $ \eta < 2.2$, and HPS discriminant by decay mode finding set to true (selects 1 or 3 prong taus).	134

LIST OF TABLES WITH DETAILS

5.4	Cut flow relative efficiency table, calculated from raw generator events in case of MC, i.e., before pile-up reweighing or normalization to luminosity. These efficiencies are rounded off to the last decimal shown. “LL” refers to the leading leg, and “SL” to the subleading leg. The skimming selects events with at least one pair of HPS taus, each of which must have a leading track p_T of at least 5 GeV/ c , and pass the HPS discriminant by decay mode finding. The preselection is applied to both legs and involves a p_T cut of 20 GeV/ c , $ \eta < 2.2$, and HPS discriminant by decay mode finding set to true (selects 1 or 3 prong taus).	135
5.5	Cut flow relative efficiency table for the signal samples, calculated from raw generator events, i.e., before pile-up reweighing or normalization to luminosity. These efficiencies are rounded to the last decimal shown. “LL” refers to the leading leg, and “SL” to the subleading leg. The preselection is applied to both legs and involves a p_T cut of 20 GeV/ c , $ \eta < 2.2$, and HPS discriminant by decay mode finding set to true (selects 1 or 3 prong taus).	136
5.6	Cut flow relative efficiency table for the signal samples, calculated from raw generator events, i.e., before pile-up reweighing or normalization to luminosity. These efficiencies are rounded to the last decimal shown. “LL” refers to the leading leg, and “SL” to the subleading leg. The preselection is applied to both legs and involves a p_T cut of 20 GeV/ c , $ \eta < 2.2$, and HPS discriminant by decay mode finding set to true (selects 1 or 3 prong taus).	137
5.7	Datasets used for the measurement of the trigger efficiency.	139
5.8	Triggers used during 2011 data taking period. The “D” in the HLT and Level-1 seed refers to “Double”.	139
5.9	Event rate in the $Z \rightarrow ee$ control region for the dataset considered (2.1 fb $^{-1}$). Note that the contributions of non-QCD backgrounds are estimated using the MC predictions.	147
5.10	Estimation of the event rate of like-sign events and opposite-sign QCD contributions after nominal cuts for the $\tau_h\tau_h$ analysis.	154

LIST OF TABLES WITH DETAILS

5.11	Comparison of the expected SM background contributions (rates) and events observed in data for $\int Ldt = 4.9 \text{ fb}^{-1}$, for the entire region as well as for high mass regions, where the sensitivity of this analysis dominates. The uncertainties are presented as statistical \pm systematics.	157
5.12	Comparison of the expected signal rates and the sensitivity for $\int Ldt = 4.9 \text{ fb}^{-1}$ for four different SSM Z' masses, for the entire region as well as for higher mass regions.	158
6.1	Table shows the skim efficiencies for various MC samples.	169
6.2	Events in the $Z \rightarrow \mu\mu$ control region for data and MC.	175
6.3	Events in the $Z \rightarrow \tau\tau$ control region for data and MC.	177
6.4	Events in the $W + jets$ Control Region 1 for data and MC.	177
6.5	Events in the $W + jets$ Control Region 2 for data and MC.	180
6.6	Cut efficiencies and expected number of $W + jets$ events in the signal region.	180
6.7	Number of events in the $t\bar{t}$ Control Region 1 for data and MC.	182
6.8	$t\bar{t}$ extraction efficiencies and expected number of $t\bar{t}$ events in the signal region.	183
6.9	Number of events in the signal region for data and MC backgrounds.	183

1

Introduction

The word “Science” has originated from the Latin word “Scientia” which in English means “Knowledge”. Science is a way to answer all the fundamental questions regarding natural phenomena occurring around us in the daily life. Science covers many different fields of study. Particle physics is a branch of science which aims to understand the matter to its deepest level and to study the fundamental laws that govern the building of matter and the physical universe. In the past century, different theories, experimental results, and discoveries have resulted into a remarkable picture of the fundamental structure of the matter, which is known as the Standard Model (SM) [3]. It is a very successful model which explains the structure of the matter and forces acting between the fundamental particles. The postulates of the SM are well tested by different experiments at the Large Electron-Positron (LEP) collider, Tevatron, B-factories, *etc.* However, there are strong indications that SM gives incomplete description of the nature and there are possibilities of the major discoveries in the current and future high energy particle colliders. In order to observe *New Physics* and discover new particles at these colliders, it is very essential to have a very good understanding of the SM physics. In the light of the *New Physics* predicted at TeV energy scale, several extensions of the SM have been developed. Out of such extensions of the SM, some include models which predict the existence of new heavy gauge bosons Z' and W' .

CHAPTER 1. INTRODUCTION

In this Chapter, an overview of the Standard Model and the properties of the fundamental particles and forces acting among them, is presented. The physics and motivation for the search of a theoretically predicted gauge boson, Z' , decaying into a τ -lepton pair, which is the ultimate aim of the present work, is also presented.

1.1 Standard Model of Particle Physics

The Standard Model (SM) is a beautiful theoretical framework that describes how matter is composed of the fundamental constituents and various types of interactions acting among these constituents. The underpinning of the SM is a quantum field theory, a powerful theory that describes the fundamental principles of quantum mechanics and special relativity. Developed in the early 1970s, the SM has successfully explained most of the experimental results and precisely predicted a wide variety of phenomena. The SM is a gauge invariant theory which is described by the gauge groups: $SU(3)_C \otimes SU(2)_L \otimes U(1)_Y$, where C means color charge, L stands for weak isospin, and Y represents the hypercharge. According to SM, all visible matter in the universe is made up of twelve basic building blocks called “fundamental particles”, categorized in three generations of leptons and three generations of quarks. The first generation of leptons consists of the electron (e) and the corresponding electron-neutrino (ν_e). The second generation of leptons consists of the muon (μ) and the corresponding muon-neutrino (ν_μ). Similarly, the tau (τ) and the tau-neutrino (ν_τ), form the third generation of leptons. The most significant difference between generations of leptons are the masses of the particles. For example, the mass of the electron is $0.511 \text{ MeV}/c^2$ while the mass of the tau lepton is $1777 \text{ MeV}/c^2$, a difference of almost 10^4 . Like the leptons, quarks are also divided into three generations. The up (u) and down (d) quarks are the first generation quarks and combine themselves to form the protons and neutrons within the atoms. The charm (c) and strange (s) quarks form the second generation of quarks, while the top (t) and bottom (b) quarks form the third generation. The fundamental forces acting between these elementary particles and the matter are: electromagnetic force, weak force, and the

1.1. STANDARD MODEL OF PARTICLE PHYSICS

strong force. The gauge groups of the SM govern the symmetries and the underlying physics behind the bosons that mediate the forces. For example, the gauge group $SU(3)_C$ contains the underlying symmetries and governs the way, the strong force is felt by particles with color charge, such as quarks. The theory of strong interaction is known as “*Quantum Chromodynamics*” (QCD). The $SU(3)_C$ symmetry group has eight generators (gauge bosons), called “*gluons*” which are massless and carry color charge. The electromagnetic interactions are described by unitary group $U(1)$. This interaction is mediated by a massless particle “*photon*” and the corresponding theory is called “*Quantum Electrodynamics*” (QED). Weak interaction is described in the form of continuous $SU(2)$ group with 3 gauge bosons (W^\pm , Z^0). The gravity is not included in the SM because of the lack of the theoretical description and experimental clues of “Graviton”, the boson which is supposed to mediate the gravitational interaction. The characteristics of the four fundamental forces and the fundamental particles are briefly discussed in the next Subsections.

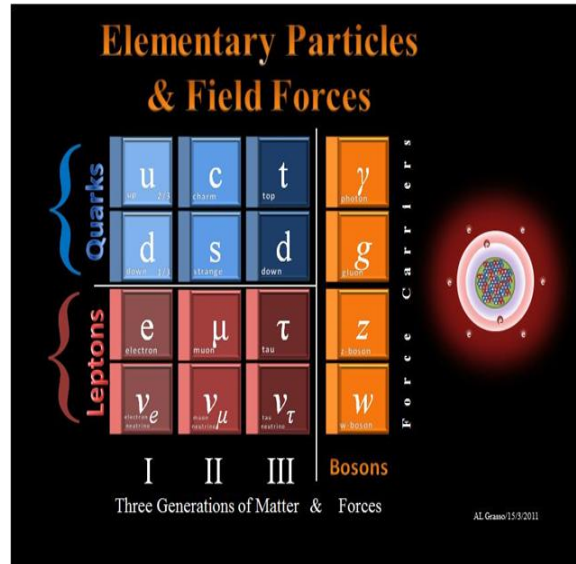


Figure 1.1: Building blocks of Standard Model.

1.1.1 Fundamental Forces

All matter in the universe interacts via four distinct forces - gravitational, electromagnetic, strong, and weak. These forces are characterized on the basis of following criteria: the types of particles that experience the force, the relative strength of the force, the range over which the force is effective, and the nature of particles that mediate the force. A brief description of the basic properties of these fundamental forces is given below:

1. **Strong Interaction:** It is responsible for holding the nucleus together against the repulsive electromagnetic force due to the presence of protons inside the nucleus. Yukawa modeled the strong force as an exchange force in which the exchange particles are pions. It is the strongest of all the four fundamental forces but with a very short range of the order of 1 femtometer (10^{-15} m). The strong force arises from the exchange of quanta of the strong color field known as “gluon”. The strong force acts between the particles carrying color charge (quantum number).
2. **Electromagnetic Interaction:** The electromagnetic interaction exists between all the particles which have an electromagnetic charge. For example, electrons (negatively charged) bind with the nucleus of an atom, due to the presence of protons (positive charge). The force is long range, in principle extending over infinite distance. The electromagnetic force is carried by the exchange of a massless and chargeless particle, called photon.
3. **Weak Interaction:** The weak force is responsible for the radioactive decay of unstable nuclei and the interactions of neutrinos and other leptons with matter. It arises from an exchange of intermediate vector bosons W^\pm and Z^0 , which are very massive.
4. **Gravitational Interaction:** It is the weakest of all the four interactions and has an infinite range. This force is supposed to be mediated by a gauge boson called “graviton” which has not been observed experimentally till now. This

1.1. STANDARD MODEL OF PARTICLE PHYSICS

Force	Mediating boson	Charge	Spin	Mass (GeV/c ²)	Range (m)	Relative strength at atomic scale
Strong	8 gluons(g)	0	1	0	10 ⁻¹⁵	1
EM	Photon(γ)	0	1	0	∞	10 ⁻²
Weak	W [±]	±1	1	80.403±0.029	10 ⁻¹⁸	10 ⁻⁹
	Z ⁰	0	1	91.187±0.002		
Gravity	graviton	0	2	0	∞	10 ⁻³⁸

Table 1.1: Details of the four fundamental forces known in nature.

force is extremely weak, having a relative strength of 10⁻³⁸ with respect to the strong force at the atomic scale. It is a purely attractive force which can travel even through the empty space to attract the two masses towards each other. This force is responsible for the attraction of objects towards the earth and elliptical motion of the planets around the sun.

A comparison of the relative strengths of the four forces at the atomic scale is given in Table 1.1.

1.1.2 Fundamental Particles

As discussed in the Section 1.1, six “*quarks*” and six “*leptons*” are considered as the fundamental particles according to the SM. These fundamental particles appear to be pointlike when probed at the shortest distance scales accessible to the current particle accelerators. The quarks carry fractional charges and half-integral spin quantum numbers ($\frac{1}{2}$). The colorless combination of quarks gives rise to particles called “hadrons” as described below:

- quark and anti-quark ($q\bar{q}$) combination gives rise to particles known as “mesons”. Mesons have an integral spin and follow Bose-Einstein statistics.
- combination of three quarks (qqq) gives rise to particles known as “baryons”. Baryons are half-integral spin particles that follow Fermi-Dirac statistics.

CHAPTER 1. INTRODUCTION

The antiparticle of a quark *i.e.* antiquark has opposite sign of electric charge, baryon number, strangeness, charm, bottomness, and topness. Since quarks are fermions with spin $\frac{1}{2}$, they should obey Pauli's exclusion principle, *i.e.* no two identical fermions can exist in same quantum state. However, for the particular case of three baryons: $\Delta^{++} = uuu$, $\Delta^{-} = ddd$, and $\Omega^{-} = sss$, all three quarks have the same quantum numbers with at least two quarks having their spin in the same direction because there are only two choices: spin up (\uparrow) and spin down (\downarrow). This would seem to violate the Pauli's exclusion principle. To resolve this anomaly, it was suggested that the quarks possess another quantum number "color" which enables them to interact strongly with one another.

The color quantum number has three-fold degrees of freedom. There are three primary color charges for quarks: red (R), green (G), and blue (B). Antiquarks have complementary colors: cyan (\bar{R}), magenta (\bar{G}), and yellow (\bar{B}). All particle states observed in the nature are "colorless"; baryons have a color state "RGB" and mesons have color states of $R\bar{R}$, $G\bar{G}$, and $B\bar{B}$. Gluons, the quanta of the color field that bind the quark states, are bicolored and come in eight states: $R\bar{B}$, $R\bar{G}$, $B\bar{G}$, $B\bar{R}$, $G\bar{R}$, $G\bar{B}$, $\frac{1}{\sqrt{2}}(R\bar{R} - B\bar{B})$, $(\frac{1}{\sqrt{6}}(R\bar{R} + B\bar{B} - 2G\bar{G}))$. Ideally, one would expect $3^2 = 9$ combinations from three colors and three anticolors, but one state $(\frac{1}{\sqrt{3}}(R\bar{R} + B\bar{B} + G\bar{G}))$ carries no net color charge and is excluded.

Leptons are the particles with fractional spin ($\frac{1}{2}$) and they do not interact strongly. Leptons can either carry one unit of electric charge or they can be neutral. As discussed in Section 1.1, the charged leptons are the electron (e), muon (μ), and tau (τ). Each of them possesses an electric charge and a distinct mass. Each charged lepton has an associated neutral partner called neutrino: ν_e , ν_μ , and ν_τ , that has no electric charge and possesses a non-zero mass. The mass of the antileptons is identical to that of the leptons, but all of the other properties are reversed. Table 1.2 shows the three families of "fermions", the constituents of matter. Particles in higher generations are heavier and unstable. Therefore, particles in higher generations decay into the particles in lower generations, conserving quantum numbers (Charge, Lepton number, Baryon number, and Spin).

1.1. STANDARD MODEL OF PARTICLE PHYSICS

Gen	Leptons (spin = $\frac{1}{2}$)			Quarks (spin = $\frac{1}{2}$)		
	Flavor	Charge	Mass (MeV/c ²)	Flavor	Charge	Mass (MeV/c ²)
1	e	-1	0.511	d	$-\frac{1}{3}$	3.0-7.0
	ν_e	0	$< 2 \times 10^{-6}$	u	$+\frac{2}{3}$	1.5 - 3.0
2	μ	-1	105.66	s	$-\frac{1}{3}$	95 ± 25
	ν_μ	0	< 0.19	c	$+\frac{2}{3}$	$(1.25 \pm 0.09) \times 10^3$
3	τ	-1	1776	b	$-\frac{1}{3}$	$(4.70 \pm 0.07) \times 10^3$
	ν_τ	0	< 18.2	t	$+\frac{2}{3}$	$(172.5 \pm 2.7) \times 10^3$

Table 1.2: Three generations of elementary particles.

1.1.3 Quantum Chromodynamics (QCD)

Quantum Chromodynamics (QCD) [4], the gauge field theory that describes the strong interactions of colored quarks and gluons, is the $SU(3)$ component of the $SU(3)_C \otimes SU(2)_L \otimes U(1)_Y$ gauge group describing Standard Model (SM) of particle physics.

QCD has specific features known as *asymptotic freedom* and *confinement*, which determine the behaviour of quarks and gluons in particle interactions at high and low energy scales:

- **Confinement:** Confinement means the color-charged particles *i.e.* quarks and gluons, cannot be found individually and they remain confined in groups with other quarks. All particles observed in nature like baryons (three quarks with three different colors) and mesons (quark-antiquark with opposite color) are colorless. Particles such as ud or $uddd$ that cannot be combined into color-neutral states, are never observed.

The quarks in a given hadron, exchange gluons among them. If one of the quarks in a given hadron is pulled away from its neighbors, the color-force field between that quark and its neighbours gets stretched. More and more energy is added to the color-force field as the quarks are pulled apart. At some point, it becomes

CHAPTER 1. INTRODUCTION

energetically favorable for the color-force field to break into a new $q\bar{q}$ pair and the energy in this process is conserved because the energy of the color-force field is converted into the mass of the new $q\bar{q}$ pair. Thus, the quarks cannot exist individually because the color-force increases as they are pulled apart. This property is called “*quark confinement*”, which aids in understanding the absence of isolated quarks so far.

- **Asymptotic Freedom:** The term “Asymptotic Freedom” [5] is used to describe the behaviour of quarks at high energy or momentum transfers, or equivalently at small distances. This feature is based on the experimental observations. In high energy scattering processes between leptons (*e.g.* electrons or neutrinos) and protons (or neutrons), the dynamics reveals that the scattering occurs at pointlike and massless constituents, the “quarks”, rather than at a homogeneous object. Apparently, at sufficiently high momentum transfers, quarks behave like free or weakly bound particles. Mathematically, in QCD the effective coupling constant is given by:

$$\alpha_s(Q^2) = \frac{12\pi}{33 - 2n_f \ln(\frac{Q^2}{\Lambda^2})} \quad (1.1)$$

where n_f is the number of quarks flavors, Λ is the QCD scaling parameter and Q is the momentum transfer during the interaction. As $Q^2 \rightarrow \infty$, $\alpha_s \rightarrow 0$, which means that at large Q^2 , the interaction is quite weak. Thus the fact that the strong interaction becomes “weak” at high energy scales and vanishes to zero at asymptotically high energies, justifies the term “Asymptotic Freedom”.

1.1.4 Electroweak Theory and Higgs Mechanism

The unification of the weak interaction and the electromagnetic interaction into a single mathematical formalism by Sheldon Lee Glashow, Abdus Salam, and Steven Weinberg in 1968, was the most remarkable success of the theoretical physics in the second half of the 20th century. The unified interaction is known as “Electroweak” (EWK) interaction and the corresponding theory is called “Electroweak theory” [6] [7] [8].

1.1. STANDARD MODEL OF PARTICLE PHYSICS

The simplest unification of parity violating weak force and parity conserving electromagnetic force was done using $SU(2)_L \otimes U(1)_Y$ gauge theory. The electroweak theory describes both the electromagnetic force and the weak force in one unified framework. Superficially, these forces appear quite different. The weak force acts only across distances smaller than the atomic nucleus, while the electromagnetic force can extend over great distances, weakening only with the square of the distance. Moreover, comparison of the strength of these two fundamental interactions between two protons, for instance, reveals that the weak force is some 10^{-4} times weaker than the electromagnetic force at the atomic scale. The electroweak theory is basically an outcome of the attempt to produce a self-consistent gauge theory for the weak force, in analogy with quantum electrodynamics, the successful modern theory of the electromagnetic force developed during the 1940s.

During the 1960s, Glashow, Salam, and Weinberg independently discovered that they could construct a gauge-invariant theory of the weak force, provided they also include the electromagnetic force. But the unified theory of electromagnetic and weak interactions, as described above, was unsatisfactory due to the fact that it contained four massless gauge bosons, while only one was observed experimentally at that time, namely the photon. This implies that the underlying symmetry of the theory is hidden or broken by some mechanism that gives mass to the particles exchanged in weak interactions but not to the photons exchanged in the electromagnetic interactions. The assumed mechanism involves an additional interaction with an otherwise unseen field, called the “Higgs field”, that pervades all over the space. The quanta of this Higgs field is known as Higgs boson. This led to the idea of spontaneous symmetry breaking and the Higgs Mechanism. It is widely believed that the Higgs Mechanism is the key to explain this mass generation of W^\pm and Z gauge bosons.

In the early 1970s, Gerardus’t Hooft and Martinus Veltman provided the mathematical foundation to renormalize the unified electroweak theory proposed earlier by Glashow, Salam, and Weinberg. Renormalization removed the inherent physical inconsistencies present in the earlier calculations of properties of the carrier particles, permitted precise calculations of their masses and led to a more general acceptance

of the electroweak theory. The experimental proof of the existence of force carriers, the neutral Z particles and the charged W particles, came in 1983 with the discovery of the W and Z bosons by the UA1 and UA2 collaborations in proton-antiproton collisions [9] [10] [11] [12]. The masses of these particles were found to be consistent with their predicted values.

1.2 Need of the Large Hadron Collider (LHC)

As discussed earlier, the Standard Model is able to explain most of the particle physics phenomena. The predictions of the SM have been verified experimentally at the level of 0.1% by various colliders like Large Electron Positron (LEP), SLAC (Stanford Linear Accelerator Center), KEK b-factories and TEVATRON. In spite of being the most successful theory, surviving the experimental testing, SM is not the complete theory in the context of the origin of mass. There are several reasons to believe that the SM is not the ultimate theory of nature. A few facts or motivations which force us to think beyond the SM are:

- **Gravity:** The SM includes the strong and electroweak forces but it is not able to accommodate the fourth fundamental force in nature *i.e.* the gravitational force [13].
- **Fermion generations:** The SM does not explain why there are exactly three generations of leptons and quarks, nor why the fermion masses span over many orders of magnitude.
- **Higgs boson mass:** In the SM, the mass of the Higgs boson is quadratically divergent when radiative corrections are applied. Some fine tunings are required to suppress this divergence.
- **Unification problem:** It has been verified experimentally that the coupling constants of the EM, weak, and strong interactions vary with energy. As per the predictions of the Grand Unified Theory (GUT) [14], these couplings should unify at a single value α_G , at very high energy scale ($\sim 10^{19}$ eV). In SM, this type

1.2. NEED OF THE LARGE HADRON COLLIDER (LHC)

of unification is not possible as observed from extrapolation of experimentally measured couplings to a very high energy regime. On the other hand, unification is accessible in more general theories like Supersymmetry (SUSY).

- **Neutrino masses:** In SM, neutrinos are assumed to be massless but recent experimental observations with solar and atmospheric neutrinos have shown, however, that the three generations of neutrinos mix with each other (neutrino oscillations). This is only possible if the neutrinos have some definite mass values [15].
- **Dark energy and matter:** According to the cosmological observations, approximately 5% of the universe is made of baryonic matter. The rest is dark energy (72%) and dark matter (23%). The SM can explain only the ordinary matter (5%).
- **Matter-Antimatter asymmetry:** At the beginning of the universe, matter and antimatter were created in equal amounts. The SM offers no satisfactory explanation for the matter-dominated universe we observe.

To summarize, despite of SM's success in describing most of the phenomena in particle physics, it is nevertheless incomplete. Perhaps it is able to explain only a part of the bigger picture that may include *New Physics* which has been hidden till now, either deep inside the subatomic world or in the darkness of this universe.

The Large Hadron Collider (LHC) has been built at CERN, Geneva with the aim of answering all these mysteries of the universe, including missing blocks of the Standard Model. The LHC is the highest energy proton-proton collider with 14 TeV designed center-of-mass energy. The details of the LHC machine are given in the Chapter 2.

As discussed earlier, the present work deals with the search for a particle, Z' that has been predicted theoretically by many extensions of the SM. The details on the physics of Z' gauge bosons and motivation for the search of Z' gauge bosons in tau-pair final states have been presented in the next Section.

1.3 Motivation for the search of Z' gauge bosons decaying into a pair of tau-leptons

The existence of additional gauge bosons beyond the ones associated with the Standard Model gauge group structure, remains an open question in particle physics. After the introduction of the unified electroweak theory described by the symmetry groups $SU(2)_L \otimes U(1)_Y$, theories containing additional symmetry groups, were also proposed. Just like the Higgs mechanism, that was introduced to account for the $SU(2)_L \otimes U(1)_Y$ symmetry breaking, it is possible to construct theoretical models by incorporating additional gauge fields that can lead to new heavy gauge bosons. Although there are several ways in which new heavy gauge bosons can appear, the simplest one is the extension of the SM gauge structure, in which the new heavy gauge bosons are simply the gauge field of a new local broken symmetry. Examples of such models are:

1. **Grand Unified Theory based models:** In Grand Unified Theories (GUTs), the strong and electroweak interactions are merged into a single interaction, described by a higher symmetry group. The choice of the symmetry group, however, varies. The two most popular scenarios are the Left-Right Symmetric Model (LRM) and E_6 models [16] [17]. These models involve $SO(10)$ symmetry group. The E_6 scenario gives rise to four neutral gauge bosons: Z'_ψ , Z'_χ , Z'_η , and Z'_ν , while LRM model gives rise to two new gauge bosons, one charged and one neutral, both couple to right handed quarks and leptons.
2. **Stueckelberg extension:** The Stueckelberg extension [18] of the Standard Model also predicts the existence of new gauge bosons. In the Stueckelberg extension, particle masses are generated without the Higgs Mechanism. The Stueckelberg gauge field has no direct couplings to the Standard Model fields and connects only through mixing with the SM gauge bosons. LEP results [19] gave an upper limit of 10^{-3} on the mixing between SM gauge bosons and Z' .

1.3. MOTIVATION FOR THE SEARCH OF Z' GAUGE BOSONS DECAYING INTO A PAIR OF TAU-LEPTONS

3. **Sequential Sequential Model:** Additional neutral gauge bosons are also predicted by Sequential Standard Model (SSM) [20] which serves as a “standard candle” for the experimentalists. The SSM is a simplest extension of the SM which assumes that the Z' gauge boson has same couplings as that of the SM Z gauge boson. The new neutral gauge boson is assumed to be a heavy version of the Standard Model Z gauge boson. This model is not a gauge invariant and therefore, not a very realistic model, but it is a useful reference model. If a Z' gauge boson is created in the pp collisions at the LHC it can decay into any of the known fermion-antifermion pair.

In the Little Higgs models [21] there is typically an enlarged gauge sector which is broken down to the SM gauge symmetry around the TeV scale that results in one or more Z' bosons. The existence of Z' bosons is also predicted by models inspired by Extra Dimensions [22]. The simplest case involves a single extra dimension of radius R which implies the existence of Kaluza-Klein excitations [23] of the states that can propagate in the bulk. The Randall Sundrum (RS) model [24] also predicts the existence of new gauge bosons. The RS model assumes a single highly curved (wrapped) extra dimension. In this scenario, the gravity is localized on one brane (membrane) in the extra dimension and the SM particles are located on the other.

In most of the extended gauge theories, the symmetry breaking scale is at sufficiently high energies that the associated extra bosons are beyond the reach of current or planned experiments. However, there exists several models that allow a relatively light Z' . If the new gauge couplings are not much smaller than unity, then the $U(1)$ group must be spontaneously broken at a scale larger than the electroweak scale to account for the non-observation of the Z' boson at LEP and the Tevatron. Such models can have a Z' that is of the order of TeV scale and is in the reach of current experiments like the Large Hadron Collider experiment at CERN.

The theoretically predicted Z' gauge boson is supposed to be an electrically

CHAPTER 1. INTRODUCTION

neutral, spin-1 particle. The physics processes governing the neutral current interactions of fermions, J , in the SM are described with the following Lagrangian:

$$L = gJ_3^\mu W_{3\mu} + g'J_Y^\mu B_\mu \quad (1.2)$$

Here g and g' represent the $SU(2)_L$ and $U(1)_Y$ gauge couplings, respectively, while $W_{3\mu}$ is the $SU(2)_L$ gauge boson and B_μ is the $U(1)_Y$ gauge boson. The J_3^μ and J_Y^μ represent the electromagnetic and weak currents among the fermions. If one considers the symmetry breaking of $SU(2)_L \otimes U(1)_Y$, the mass eigen states corresponding to neutral gauge bosons, the massless field A_μ , and the massive Z_μ are given by:

$$A_\mu = \sin\theta_W W_{3\mu} + \cos\theta_W B_\mu \quad (1.3)$$

$$Z_\mu = \cos\theta_W W_{3\mu} - \sin\theta_W B_\mu \quad (1.4)$$

where the weak angle $\theta_W = \tan^{-1}(g'/g)$. When an extra $U(1)'$ field is introduced with new gauge couplings $e = g\sin\theta_W$ and $g_1^2 = g^2 + g'^2 = g^2/\cos^2\theta_W$, the Lagrangian describing the neutral currents of fermions becomes:

$$L = eJ_{EM}^\mu A_\mu + \Sigma g_\alpha J_\alpha^\mu Z_{\alpha\mu}^0 \quad (1.5)$$

where $\alpha = 1 \rightarrow n+1$ and g_1 , $Z_{1\mu}^0$, and J_1^μ are the gauge couplings, gauge boson and current of the SM. Additionally, g_α and $Z_{\alpha\mu}^0$ are the gauge couplings and bosons of the additional $U(1)'$ extension. If one assumes the electrically neutral scalar fields attain vacuum expectations values such that A_μ remains massless, then the $Z_{\alpha\mu}^0$ fields acquire mass terms $\frac{1}{2}M_{\alpha\beta}^2 Z_{\alpha\mu}^0 Z_{\beta\mu}^{0\mu}$ such that:

$$M_{\alpha\beta}^2 = 2g_\alpha g_\beta \Sigma Q_{\alpha i} Q_{\beta i} |\phi^2| \quad (1.6)$$

where $M_{11} = M_{Z^0}^2$ is the mass of SM Z boson. Upon diagonalization the mass matrix, one can obtain $n+1$ massive eigenstates $Z_{\alpha\mu}$ with mass M_α . Although this is the simplest scenario in which new massive eigenstates can be generated; however the underlying mathematics and physical motivation behind the other extensions of the SM work in a similar manner.

1.3. MOTIVATION FOR THE SEARCH OF Z' GAUGE BOSONS DECAYING INTO A PAIR OF TAU-LEPTONS

The searches for Z' gauge bosons are of two kinds: indirect and direct. The indirect searches look for deviations from the SM that might be associated with the existence of a Z' gauge boson. Due to the presence of extra gauge groups, a mixing between the SM Z and Z' can happen. Changes in some of the measured values of SM parameters and observables can result from this $Z - Z'$ mixing. This, usually involves precision electroweak measurements at, below, and above the Z -pole. Additionally, precise measurements of W mass can set limits in the amount of the allowed $Z - Z'$ mixing. The constraints on the $Z - Z'$ mixing allows one to set limits on the Z' mass.

In contrast, the direct searches rely on the explicit production of the Z' . The direct searches are categorized in terms of the initial state how a Z' is produced and the final state into which it decays. In e^+e^- colliders, the process for Z' production is: $e^+e^- \rightarrow Z' \rightarrow l^+l^-$ ($l = e, \mu$) and for hadron colliders the Z' production process is: $pp \rightarrow Z' \rightarrow l^+l^-$ ($l = e, \mu, \tau$). The common final states for Z' searches involve: two oppositely charged light leptons (e^+e^- , $\mu^+\mu^-$), two oppositely charged tau-leptons ($\tau^+\tau^-$), and decay into $t\bar{t}$ pair.

Although most of the studies performed on the search of Z' gauge bosons have assumed generation-independent gauge couplings for Z' , there exists models [25] [26] in which the Z' couples preferentially to third generation fermions. Although the sensitivity for discovering a Z' gauge boson is more for leptonic final states (e^+e^- , $\mu^+\mu^-$), but in the context of such non-universal scenarios, the sensitivity for the search of Z' production using e^+e^- and $\mu^+\mu^-$ final states may be substantially reduced, motivating the exploration of its decay to $\tau^+\tau^-$ final states. The previous search on a $Z'_{SSM} \rightarrow \tau^+\tau^-$ performed by the CDF experiment at Fermilab in Year 2005, excluded a Z'_{SSM} decaying to $\tau^+\tau^-$ below mass 399 GeV/c². For comparison, the most stringent limits on a Z'_{SSM} gauge boson in the di-electron and di-muon decay channels combined are 2.21 TeV from ATLAS experiment [27] and 2.32 TeV [28] from CMS experiment.

1.4 Organization of Thesis

In the present study, the search for a new theoretically predicted gauge boson, Z' , has been performed using the pp collision data collected with the CMS detector at $\sqrt{s}=7$ TeV energy accumulated in the LHC Runs in the Years 2010, 2011 and at 8 TeV energy in Year 2012. The layout of the thesis is as follows:

Chapter 1 covers a brief overview of the Standard Model (SM), Electroweak theory, shortcomings of the SM, and the need of Large Hadron Collider. The physics motivation behind the search of a Z' gauge boson decaying to tau-pair final states is also presented.

Chapter 2 gives a brief overview of the Large Hadron Collider machine (LHC) and the various experiments being conducted at LHC. The main emphasis is given on the Compact Muon Solenoid (CMS) detector, as present work utilizes the data collected with the CMS detector. Also, a brief overview of various sub-detectors of CMS detector, their construction and interaction of particles with the detector material of different sub-detectors has been presented.

Chapter 3 gives a brief description of the event generation methodology with different Monte Carlo event generators, simulation of the detector geometry and reconstruction of the particles in the detector. Also, a brief overview of the reconstruction of the physics object used in various analyses of the present work: tau-leptons, missing transverse energy, and the muons has been presented. This Chapter also lists the Monte Carlo and data samples which are used in the search for a Z' gauge boson decaying into a pair of tau-leptons.

Chapter 4 covers the details of the analysis workflow for the search of $Z' \rightarrow \tau^+\tau^-$ using LHC data of Run 2010 at $\sqrt{s}=7$ TeV, collected using the CMS detector. The focus has been placed on the studies performed in the $Z' \rightarrow \tau\tau \rightarrow \tau_h\tau_h$ final state. In this Chapter, the signal and potential background processes have been discussed in details. The estimation of each contributing

1.4. ORGANIZATION OF THESIS

background process in the high mass *i.e.* signal region is also discussed. The details of the tau-identification, isolation, and signal event selection are also discussed.

Chapter 5 covers the details of the analysis workflow for the search of $Z' \rightarrow \tau^+\tau^-$ using LHC data of Run 2011 at $\sqrt{s}=7$ TeV, collected using the CMS detector. Since the methodology remains almost the same as that of 2010 analysis, only differences with respect to 2010 analysis have been discussed in details. The focus has been placed on the studies performed in the $Z' \rightarrow \tau^+\tau^- \rightarrow \tau_h\tau_h$ final state.

Chapter 6 covers the details of the analysis workflow for the search of $Z' \rightarrow \tau^+\tau^-$ using LHC data of Run 2012 at $\sqrt{s}=8$ TeV, collected using the CMS detector. The studies performed in the $Z' \rightarrow \tau^+\tau^- \rightarrow \tau_\mu\tau_h$ final state using $5.10 \pm 0.22 \text{ fb}^{-1}$ of collision data are presented, in details.

Chapter 7 summarizes the observations and experimental results of the analyses presented in this thesis.

2

Large Hadron Collider and CMS

Experiment

The Large Hadron Collider (LHC) [29] is a superconducting-magnet based particle accelerator built at the European Center for Nuclear Research (CERN), located on the French-Swiss border near Geneva, Switzerland. The LHC is the world's biggest and the most energetic particle accelerator till date. It was two decades of planning, developing, and building that came to an end in Year 2009, when the LHC finally started the collision operation. There are roughly 10,000 physicists from more than thirty Nations world-wide, that work jointly to achieve this project, unified by the wish to understand the universe we live in. The LHC is a circular machine, about 100 meters underground, spanning 27 kms in circumference, built to recreate the conditions that existed just after the Big-Bang and to probe *New Physics*. It has been designed to collide two counter-rotating proton beams at 14 TeV center-of-mass energy with a designed luminosity of $\mathcal{L} = 10^{34} \text{ cm}^{-2}\text{s}^{-1}$, aiming for the discovery of the Higgs boson and physics beyond the Standard Model.

The decision to build the LHC machine in the tunnel of Large Electron Positron (LEP) collider, was strongly influenced by the cost saving. Hence, it was con-

CHAPTER 2. LARGE HADRON COLLIDER AND CMS EXPERIMENT

structed during the period 2000-2008 into the already existing tunnel complex of the LEP collider. After eight years of construction, the LHC had the first beams injected in the Summer-2008. After an unfortunate technical accident in September 2008, it became operational again and provided first proton-proton collisions at 900 GeV center-of-mass energy on 23rd November 2009. A few months later, on 30th March 2010, the energy of the proton beams was increased to 3.5 TeV, resulting into a center-of-mass energy $\sqrt{s} = 7$ TeV. The core of the whole project is the LHC and its four independent particle detectors: ATLAS, CMS, ALICE, and LHCb. Present work deals with the search for $Z' \rightarrow \tau\tau$ using CMS detector at the LHC, so the details of the LHC machine and the CMS detector are presented in the subsequent Sections.

2.1 Layout of Large Hadron Collider

The basic layout of LHC machine follows the LEP tunnel geometry as shown in Figure 2.1. The LHC tunnel has eight arcs and eight straight sections. Each straight section is approximately 528 m long and serves as an experimental or utility insertion. The two high luminosity experimental detector caverns (insertions) are located at diametrically opposite straight sections: the ATLAS experiment is located at Point 1 and the CMS experiment at Point 5. Two more detectors are located at Point 2 and Point 8, which also include the injection systems for Beam 1 and Beam 2, respectively. The injection kick occurs with the two beams arriving at the LHC from the Super Proton Synchrotron. Two counter-rotating proton beams intersect at four different locations of the LHC ring. The remaining four straight sections do not have beam crossings. Each of the insertions at Points 3 and 7 contain two collimation systems. The insertion at Point 4 contains two RF systems: one independent system for each LHC beam. The straight section at Point 6 contains the beam-dump insertion, where the two beams are extracted from the machine using a combination of horizontally deflecting fast-pulsed (“kicker”) magnets and vertically-deflecting

2.1. LAYOUT OF LARGE HADRON COLLIDER

double steel septum magnets. Each beam features an independent abort system. The LHC accelerator lattice has evolved over several versions.

The LHC machine uses a large number of magnets for circulating the proton beams around the entire LHC ring. It comprises of 1232 dipole magnets, which provide a magnetic dipole field of 8.33 T at an energy of 7 TeV per proton beam. The superconducting dipole magnets are cooled with super-fluid helium down to temperatures of 1.9 K. Each proton beam is separated into bunches of $N_p = 1.15 \times 10^{11}$ protons per bunch, with a bunch-spacing of 25 ns. This corresponds to a collision frequency of 40 MHz. The design value for the number of bunches per beam is $n_b = 2808$.

The LHC achieved a peak luminosity of $\mathcal{L} = 2 \times 10^{32} \text{ cm}^{-2}\text{s}^{-1}$ in the Year 2010. The LHC machine continued to perform marvellously, and on 22nd April 2011, it set a new world record for the beam intensity at a hadron collider by colliding proton beams with a luminosity of $4.67 \times 10^{32} \text{ cm}^{-2}\text{s}^{-1}$. This exceeds the previous world record of $4.024 \times 10^{32} \text{ cm}^{-2}\text{s}^{-1}$, set by Fermi National Accelerator Laboratory's Tevatron collider (US) in the Year 2010, and it marks an important milestone in the LHC commissioning. The LHC provided $\sim 36.1 \pm 1.4 \text{ pb}^{-1}$ of proton-proton collision data at 7 TeV for physics analyses during Run 2010. During Run 2011, LHC provided $5.1 \pm 0.11 \text{ fb}^{-1}$ of pp collision data at 7 TeV for physics analyses, and till date its operation at 8 TeV for Run 2012 has delivered more than 16 fb^{-1} of data. Figure 2.2 shows the total integrated luminosity of the data delivered by the LHC and the data collected by the CMS detector during LHC Run 2011 and current Run 2012.

Recently, on 4th July, 2012, CERN announced the observation of a new particle [30] which is most likely to be the elusive Higgs boson predicted theoretically by Prof. Peter Higgs in 1964 and this observation marks the success of the LHC project. The observation of this Higgs-like boson has been reported by two independent experiments: ATLAS (A Toroidal LHC ApparatuS) and CMS (Compact Muon Solenoid) at the LHC. The current LHC run is scheduled till

CHAPTER 2. LARGE HADRON COLLIDER AND CMS EXPERIMENT

the end of February 2013. This time period will be enough for LHC experiments to collect enough data to study the properties of this new Higgs-like boson and also to explore the “potential” *New Physics* (like the search for Z' , SUSY *etc.*) before preparing for higher energy and higher luminosity run.

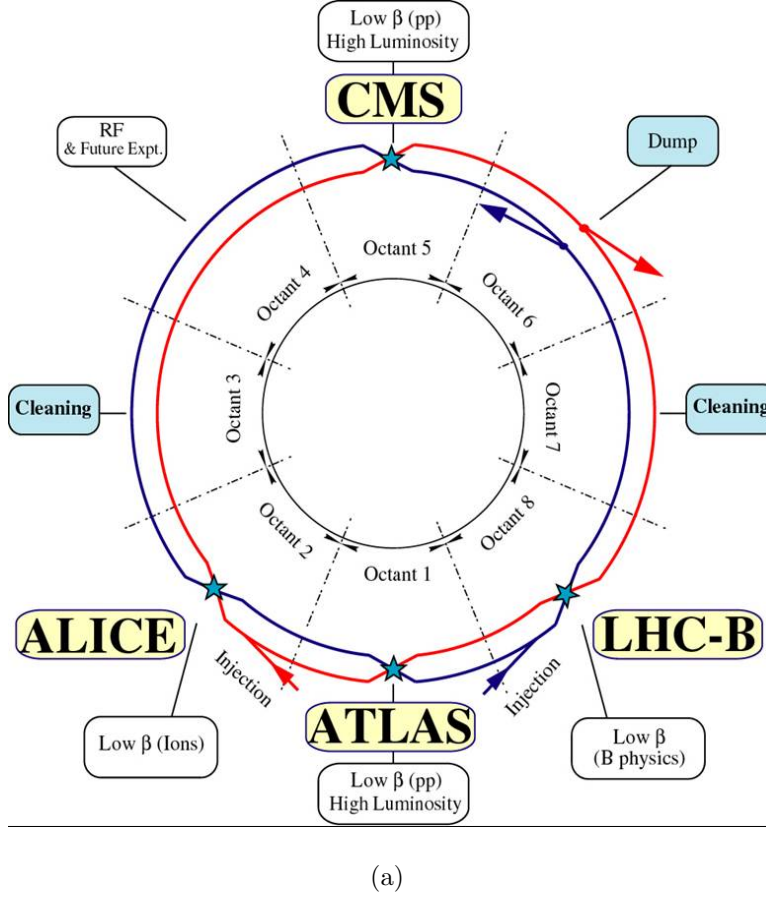


Figure 2.1: Schematic layout of the LHC.

2.1.1 LHC Accelerator System and Injector Complex

Figure 2.3 gives an overview of the LHC accelerator complex. The proton beams are supplied to the LHC via the following injector chain:

Linac2 \rightarrow Proton Synchrotron Booster (PSB) \rightarrow Proton Synchrotron (PS) \rightarrow Super Proton Synchrotron (SPS) \rightarrow LHC. Prior to injection into the main LHC accelerator ring, the proton beams are accelerated by a series of accelerator systems

2.1. LAYOUT OF LARGE HADRON COLLIDER

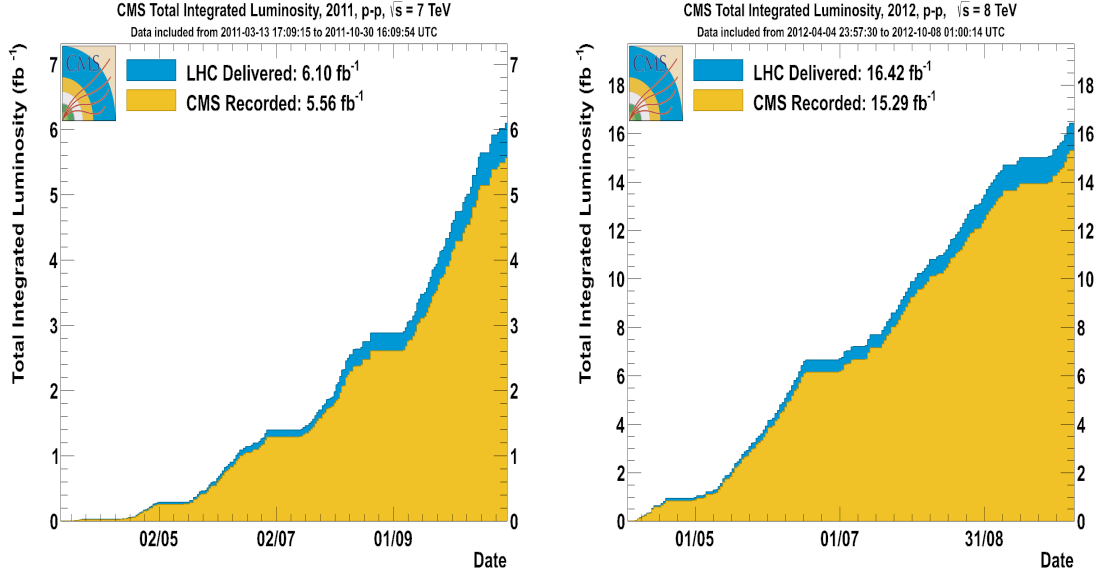


Figure 2.2: Graph of total integrated luminosity collected by CMS detector during Run 2011 (left) and Run 2012 (right).

that increase their energy successively. The first system is the linear particle accelerator *LINAC-2* accelerating protons upto 50 MeV, which feeds the *Proton Synchrotron Booster* (PSB). By PSB the protons are accelerated upto 1.4 GeV and injected into the *Proton Synchrotron* (PS), where they are accelerated further to 26 GeV. Finally the *Super Proton Synchrotron* (SPS) is used to further increase their energy upto 450 GeV before they are injected (over a period of 20 minutes) at last into the main LHC ring. Here the proton bunches are accumulated, accelerated to their peak energy of 7 TeV, and kept circulating for 10 to 24 hours, having collisions at the four intersection points.

2.1.2 Luminosity and Center-of-mass energy

The luminosity is a measurement of the number of the collisions that can occur in a detector per square centimeter and per second. The luminosity \mathcal{L} of a collider experiment is defined as:

$$\mathcal{L} = \frac{N^2 k_{rev} \gamma}{4\pi \epsilon_n \beta^*} F, \quad (2.1)$$

CHAPTER 2. LARGE HADRON COLLIDER AND CMS EXPERIMENT

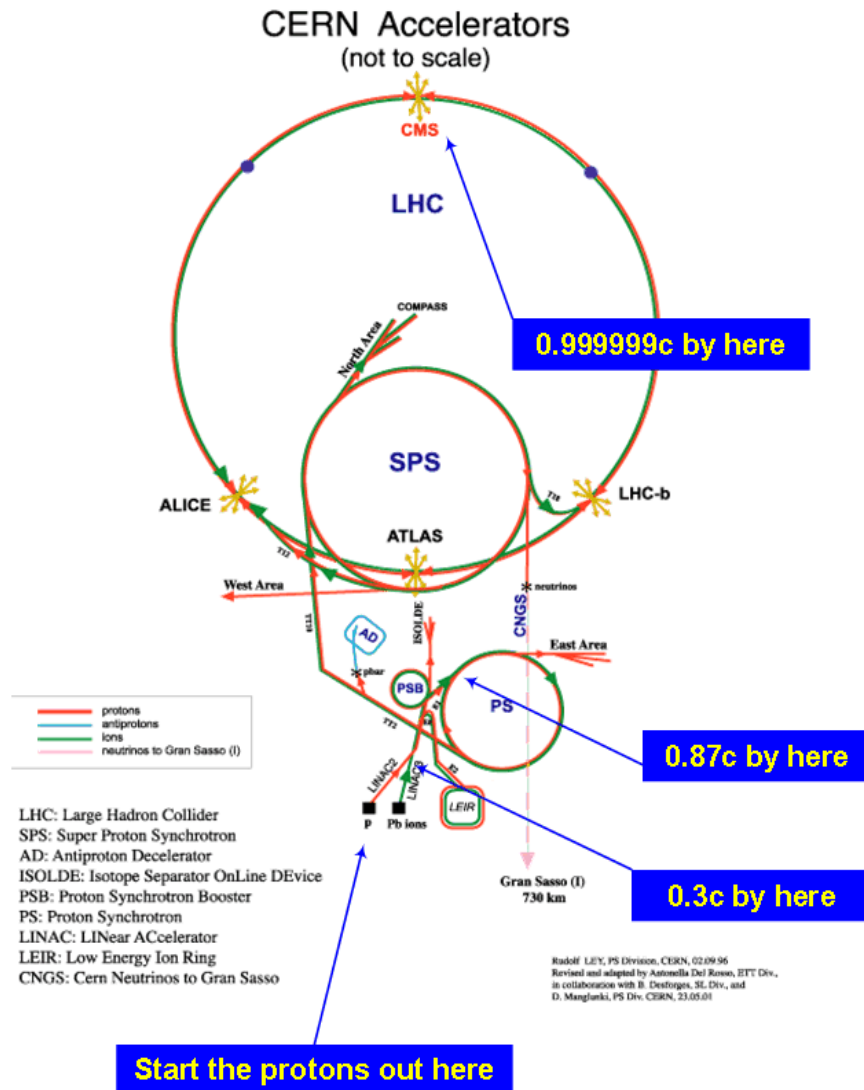


Figure 2.3: The Large Hadron Collider's accelerator complex, in France and Switzerland.

2.1. LAYOUT OF LARGE HADRON COLLIDER

where,

- N is the number of particles in each of the k circulating bunches.
- f_{rev} is the revolution frequency.
- β^* is the value of betatron function at the crossing point.
- ϵ_n is the emittance corresponding to one σ contour of the beam (nominal value $3.75 \mu\text{m}$).
- γ is the Lorentz factor.
- F is the reduction factor due to the bunch-crossing angle.

The center-of-mass energy (generally used in any collider experiment) for a given value of beam energy, E_{beam} , is calculated as:

$$E_{CM}^{collider} = 2E_{beam}. \quad (2.2)$$

As mentioned previously, there are four main points where the two counter-rotating proton beams cross and are made to intersect each other. At each of the four intersection points, a detector is placed in order to record the collision events for the study of interactions among the particles.

2.1.3 Experiments at the LHC

At four different interaction points of the LHC, there are four main experiments: ATLAS, CMS, ALICE, and LHCb. The CMS [31] and ATLAS [32] are two multipurpose detectors and they are designed to cover a wide range of physics measurements at the energy frontier as well as for the precision measurements of Standard Model processes. Important areas of *New Physics* include the potential discovery of the Higgs boson, signatures of supersymmetric particles, heavy gauge bosons, and other exotic particles. ATLAS and CMS are complemented by two special purpose detectors: LHCb [33] and ALICE [34]. The LHCb experiment is particularly designed for the study of b-physics at a peak luminosity of $10^{34} \text{ cm}^{-2}\text{s}^{-1}$. The LHCb will aid the precise measurements of CP-violation, which allows for indirect searches of

CHAPTER 2. LARGE HADRON COLLIDER AND CMS EXPERIMENT

New Physics in the rare decays. In addition to the proton physics, LHC physics programme includes the physics of heavy ions using ALICE detector. The ALICE experiment is a dedicated heavy-ion experiment for the studies of lead-lead collisions and subsequently for the search of Quark-Gluon Plasma (QGP) [35]. The design energy per nucleon in Pb-Pb collisions is 2.76 TeV, which results in a total energy of 1148 TeV of the two colliding lead nuclei. The LHC was operated with heavy-ion collisions at the end of Year 2010 and Year 2011. Figure 2.4 shows one of the early proton-proton collision event seen in the CMS detector during LHC Run 2010 at 7 TeV center-of-mass energy.

The total proton-proton interaction cross-section is expected to be roughly 100 mb

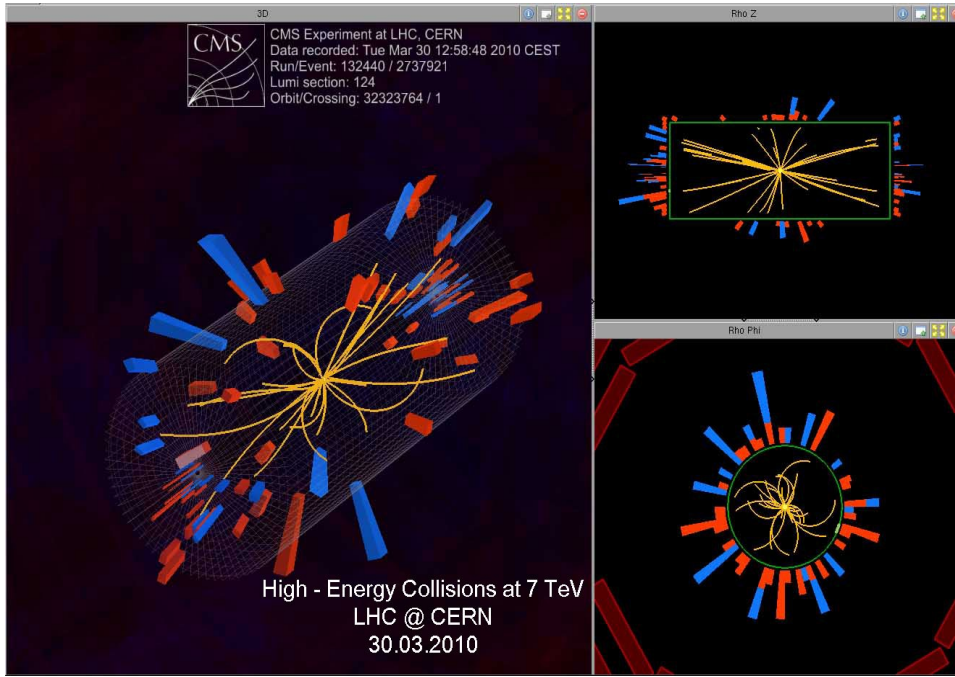


Figure 2.4: One of the early proton-proton collision event seen in CMS detector at 7 TeV center-of-mass energy during LHC Run 2010.

at 14 TeV center-of-mass energy. At design luminosity the general-purpose detectors will, therefore, observe an event rate of approximately 10^9 inelastic events/sec. This leads to a number of formidable experimental challenges *e.g.* storage space required for such large number of events. The online event selection process (trigger) must

2.1. LAYOUT OF LARGE HADRON COLLIDER

therefore, reduce the huge rate to about 100 events for storage and subsequent data analysis. The short time between bunch crossings, 25 ns, has major implications for the design of the read-out and trigger systems.

At the design luminosity, a mean of about 20 inelastic collisions will be superimposed on the single event of interest. This implies that around 1000 charged particles will emerge from the interaction region every 25 ns. Therefore, the products of an interaction under study may be confused with those coming from other interactions in the same bunch crossing. This problem clearly becomes more and more severe when the response time of the detector element and its electronic signal is longer than 25 ns. This is called pile-up and effect of this pile-up can be reduced by using high-granularity detectors with good time resolution. However this requires a large number of detector channels, resulting in millions of detector electronic channels having very good synchronization. The large flux of particles coming from the interaction region leads to high radiation levels, requiring radiation-hard detectors and front-end electronics. The detector requirements to meet the goal of the physics programme at the LHC are mentioned as follows:

- Good muon identification and momentum measurement over a wide range of momenta and angles, good di-muon mass resolution (1% at 100 GeV), and the ability to determine unambiguously the charge of muons with $p_T < 1$ TeV.
- Good charged-particle momentum resolution and reconstruction efficiency in the inner tracker. Efficient triggering and offline tagging of top quarks and b-jets, requiring the pixel detectors close to the interaction region.
- Good electromagnetic energy resolution, good di-photon and di-electron mass resolution (1% at 100 GeV), wide geometric coverage, π^0 rejection, and efficient photon and lepton isolation at high luminosities.
- Good missing transverse energy and di-jet mass resolution, requiring hadron calorimeters with a large hermetic geometric coverage and with fine lateral segmentation.

The Compact Muon Solenoid (CMS), one of the two general purpose detectors at

CHAPTER 2. LARGE HADRON COLLIDER AND CMS EXPERIMENT

the LHC, has been designed to meet the above goals of the LHC physics programme. The details of the CMS detector are discussed in next Section.

2.2 Compact Muon Solenoid

The CMS detector is a hermetic, 4π coverage multipurpose detector, shown in Figure 2.5. A comprehensive description of the CMS detector can be found in Ref. [31]. All sub-detectors are arranged concentrically around the cylindrical beam pipe and the interaction point (IP). The CMS detector is divided into two regions: a central region, called barrel and two endcap regions. The main feature of the CMS detector is the 3.8 T magnetic field, created by a superconducting solenoid, which allows for an excellent momentum resolution of reconstructed charged particles. The weight of the solenoid including the iron return yoke is 10,000 tons and the total weight of the whole detector is 12,500 tons. The CMS detector is 22 m in length and 15 m in diameter. Since these dimensions are relatively smaller than the complementary experiment ATLAS, hence, CMS detector is named as “Compact” Muon Solenoid.

The fully silicon-based inner tracking system comprises of 3 layers of silicon-pixel and 10 layers of silicon-strip detector, which allow for an excellent spatial resolution close to the interaction point, as well as a high momentum resolution. The electromagnetic calorimeter (ECAL) is composed of lead-tungstate (PbWO_4) crystals, which provide an excellent electromagnetic energy measurement of electrons and photons. It is optimized for a potential discovery of a light, neutral Higgs boson, decaying in to a pair of photons ($\text{H} \rightarrow \gamma\gamma$). A sampling hadronic calorimeter (HCAL) composed of brass absorbers and plastic scintillators completes the calorimetric system, which is hosted inside the solenoid. A typical feature of the CMS detector is the presence of the inner tracking system, as well as the complete calorimetry (ECAL and HCAL) “inside” the solenoid magnet coil. The calorimetric system is supplemented by an additional outer hadron (abbreviated as HO) calorimeter, which detects possible tails of hadronic showers. HO is generally referred to as a “tail-catcher”. Furthermore, CMS detector has three different subdetectors for the detection of muons, located

2.2. COMPACT MUON SOLENOID

outside the solenoid. In the barrel region, aluminium drift tubes (DTs) are used while cathode strip chambers (CSCs) are used in the endcaps. Both muon systems are complemented by Resistive Plate Chambers (RPCs) for improved trigger timing. The sandwich-like arrangement of the muon detectors and the iron return yoke gives rise to the characteristic appearance of the CMS detector.

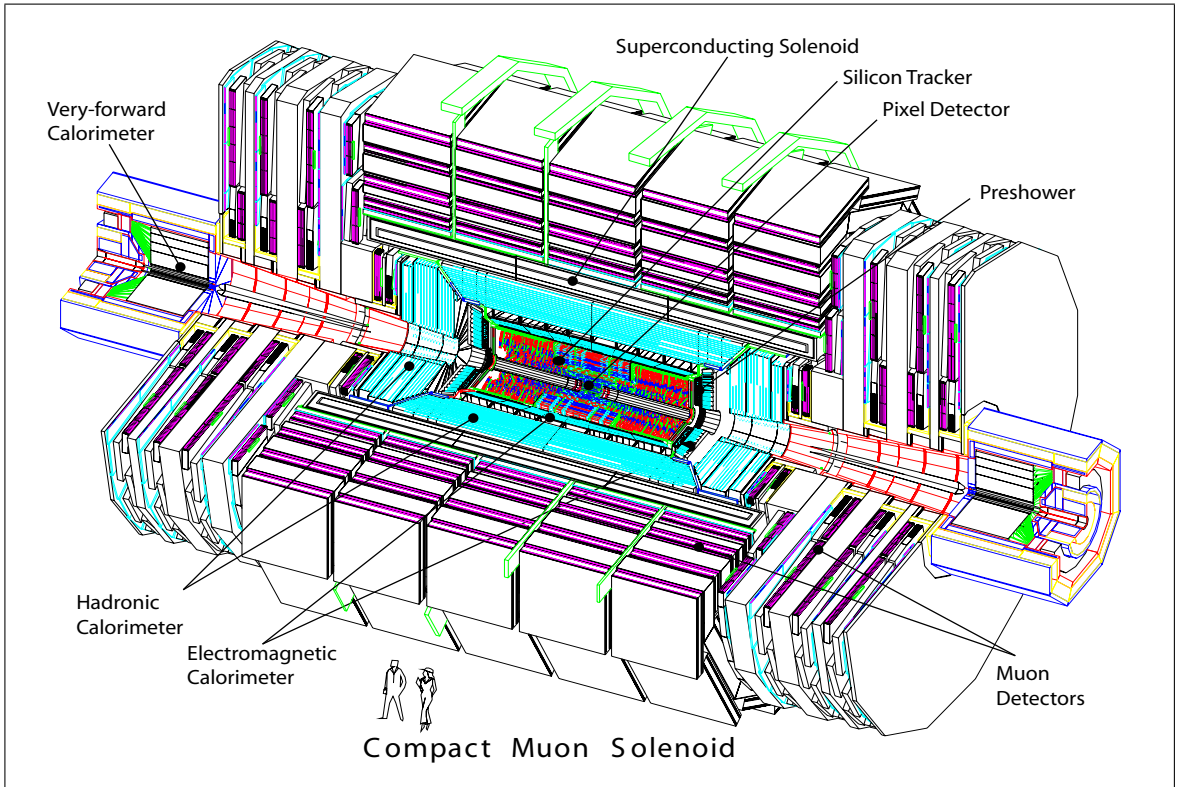


Figure 2.5: The Compact Muon Solenoid at the Large Hadron Collider.

2.2.1 CMS Co-ordinate system

Figure 2.6 represents the cross-sectional (left) and the longitudinal view (right) of CMS detector. The co-ordinate system adopted by CMS detector has the origin centered at the nominal collision point inside the detector:

- the y-axis points vertically upward (perpendicular to the LHC plane).
- the x-axis points radially inward towards the center of the LHC ring.

CHAPTER 2. LARGE HADRON COLLIDER AND CMS EXPERIMENT

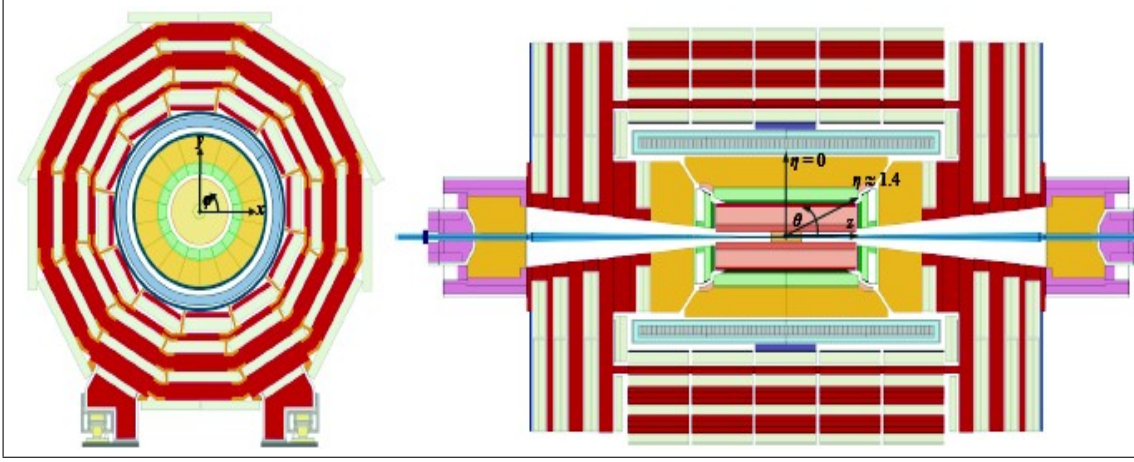


Figure 2.6: Transverse or cross-sectional view (left) and longitudinal view (right) of the CMS detector.

- the z-axis points along the beam direction.
- the azimuthal angle ϕ is measured from the x-axis in the x-y plane.
- the radial co-ordinate in this plane is denoted by r.
- the polar angle θ is measured with respect to the z-axis.

The pseudorapidity is given by $\eta = -\ln(\tan(\theta/2))$ and is used more often than the polar angle θ . The particle occupancy is measured in a portion of the detector ($d\eta$), which can be quantified in terms of θ as:

$$d\eta = -\frac{d\theta}{\sin\theta} \quad (2.3)$$

2.2.2 Superconducting Magnet

In order to measure the momentum of the charged particles from their bending in the magnetic field, CMS detector uses a superconducting solenoidal magnetic field. Due to the solenoidal configuration of the CMS magnet, bending of charged particles starts at the beam axis which minimizes the detector size for a given bending power. The superconducting magnet for CMS detector has been designed to reach a 4 T field in a free bore of 6m diameter and 12.5m length with a stored energy of 2.7 GJ at full current. The magnetic flux is returned through a 10,000 ton return iron-yoke

2.2. COMPACT MUON SOLENOID

comprising of 5 wheels and 2 endcaps (composed of three disks). An artistic view of the CMS magnet is shown in Figure 2.7.

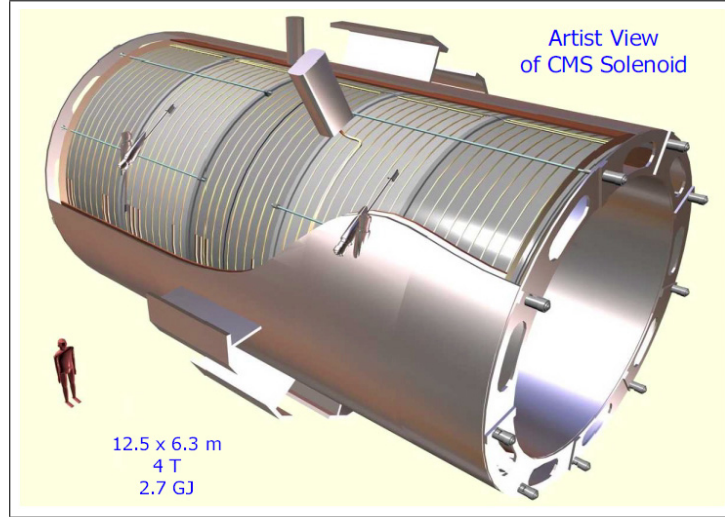


Figure 2.7: Artistic view of the CMS solenoidal magnet.

2.2.3 Inner Tracking System

One of the most important aspects of the LHC physics programme requires a robust, efficient, and precise reconstruction of the trajectories of charged particles with transverse momentum above $1 \text{ GeV}/c$ in the pseudorapidity range $|\eta| < 2.5$. A precise measurement of the secondary vertices and the impact parameters is necessary for the efficient identification of jets originating from heavy quarks like bottom or charm, which are produced in many of the interesting physics channels. Together with the electromagnetic calorimeter and the muon system, the tracker has to identify the electrons and muons, respectively. In order to reduce the event rate from the LHC bunch crossing rate of 40 MHz to about 100 Hz, which can be stored permanently, tracking information is heavily used in the high level trigger of CMS.

The inner tracking system of CMS detector is designed to provide a precise and efficient measurement of the trajectories of the charged particles emerging from the LHC collisions, as well as a precise reconstruction of secondary vertices. It surrounds the interaction point and has a length of 5.8 m, with a diameter of 2.5 m. The CMS

CHAPTER 2. LARGE HADRON COLLIDER AND CMS EXPERIMENT

solenoid magnet provides a homogeneous magnetic field of 3.8 T over the full volume of the tracker. At the LHC design luminosity of $10^{34} \text{ cm}^{-2}\text{s}^{-1}$, there will be, on an average, about 1000 particles from more than 20 overlapping proton-proton interactions, traversing the tracker for each bunch crossing, *i.e.* every 25 ns. Therefore, a detector technology featuring high granularity and fast response is required, such that the trajectories can be identified reliably and attributed to the correct bunch crossing. However, these features imply a high power density of the detector electronics which in turn require efficient cooling. However, this is in direct conflict with the aim of keeping the minimum amount of material in order to limit multiple scattering, bremsstrahlung, photon conversion, and nuclear interactions. A compromise had to be found in this respect. The intense particle flux will also cause severe radiation damage to the tracking system. The main challenge in the design of the tracking system was to develop detector components which are capable of operating in this harsh environment for an expected lifetime of 10 years. These requirements on granularity, speed, and radiation hardness lead to a tracker design entirely based on silicon detector technology.

The inner tracking system is divided into two sub-detectors: pixel tracker, which is also referred to as vertex detector and the strip tracker. Both subsystems are fully based on silicon sensors. The inner tracking system consists of 66 million silicon pixel channels and 9.6 million silicon strip channels. Figure 2.8 shows a schematic view of the CMS inner tracking system.

- **Silicon Pixel detector**

In the barrel region, close to the interaction point, three layers of pixel detectors are placed in parallel to the beam pipe at radii of $r = 4.4, 7.3,$ and 10.2 cm with a pixel-size of $100 \times 150 \text{ } \mu\text{m}^2$. Additionally, there are two pixel endcap disks in the forward direction transverse to the beam line, both having two pixel layers at distances of $|z| = 34.5$ and 46.5 cm . The pixel tracker is also referred to as vertex detector, because the main task of the inner tracking system is to provide information about the primary interaction point (primary vertex) and displaced interaction points (secondary vertices) from the decay of long-lived

2.2. COMPACT MUON SOLENOID

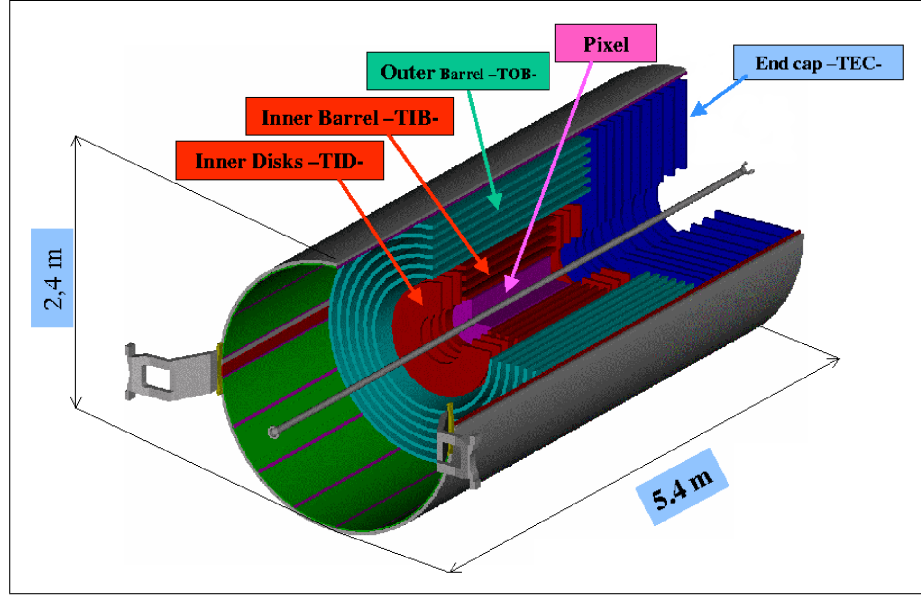


Figure 2.8: Schematic view of the CMS inner tracking system.

unstable particles, like bottom or charm quarks. Due to the strength of high magnetic field, charged particles traversing the silicon sensors are detected by the Lorentz force. In the endcap disks, the blades carrying the pixel modules are rotated by 20° to compensate for the detection, which leads to a turbine-like geometry of the endcaps, which is shown in Figure 2.9.

- Silicon Strip detector** The silicon strip tracker system provides a coverage of $|\eta| < 2.4$ and consists of almost 15400 modules, which are mounted on a carbon-fiber structure and operated at a temperature of around -20°C . The micro-strip tracker covers a region between $20 < r < 110$ cm, where the particle flux decreases with respect to the innermost region of the pixel tracker. The tracker inner barrel (TIB) consists of four layers of strip detectors. In the first two layers of the TIB, the modules are mounted as stereo modules with an angle of 100 mrad in order to provide a measurement in $(r-\phi)$ and $(r-z)$ direction. The outermost region of the inner tracking system is referred to as the tracker outer barrel (TOB), which covers a radius between $55 < r < 110$ cm. The significantly lower particle flux allows for the use of larger-pitch silicon microstrip detectors with a good signal-to-noise ratio. The TOB comprises of six layers of silicon

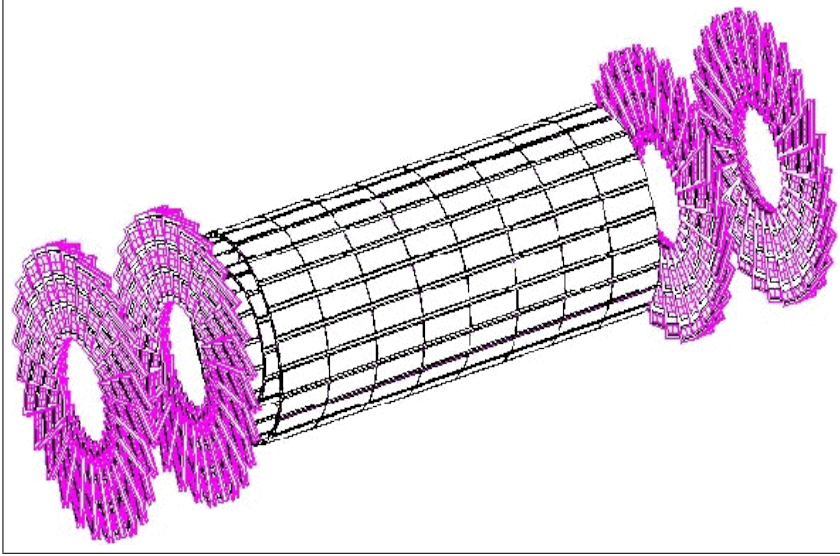


Figure 2.9: Pixel detector of CMS inner tracking system.

strip detectors, where the first two layers are also mounted as stereo modules. In the forward region, there are nine layers of micro-strips in each of the two tracker endcaps (TEC). Additionally, there are three layers of tracker inner disks (TID) on each side, in order to fill the gap in the transition region between TIB and TEC. Figure 2.10 shows the transverse and longitudinal impact parameter resolution as a function of track transverse momentum. The transverse resolution is better than the longitudinal, since the transverse beam size is measured more precisely than the longitudinal one. The study of the resolution of the primary vertex reconstruction as a function of the number of tracks used in fitting the vertex is reported in Ref. [36] and the performance is shown in Figure 2.11. The results shown in Figure 2.10 and Figure 2.11 are using pp collision data collected at 7 TeV CM energy corresponding to an integrated luminosity of 10.9 nb^{-1} .

2.2.4 Electromagnetic Calorimeter

The calorimetry provides an inclusive energy measurement of the particles. Energy of electromagnetically interacting particles, like the electron and the photon, are measured in the electromagnetic calorimeter (ECAL) [37]. The electromagnetic calorime-

2.2. COMPACT MUON SOLENOID

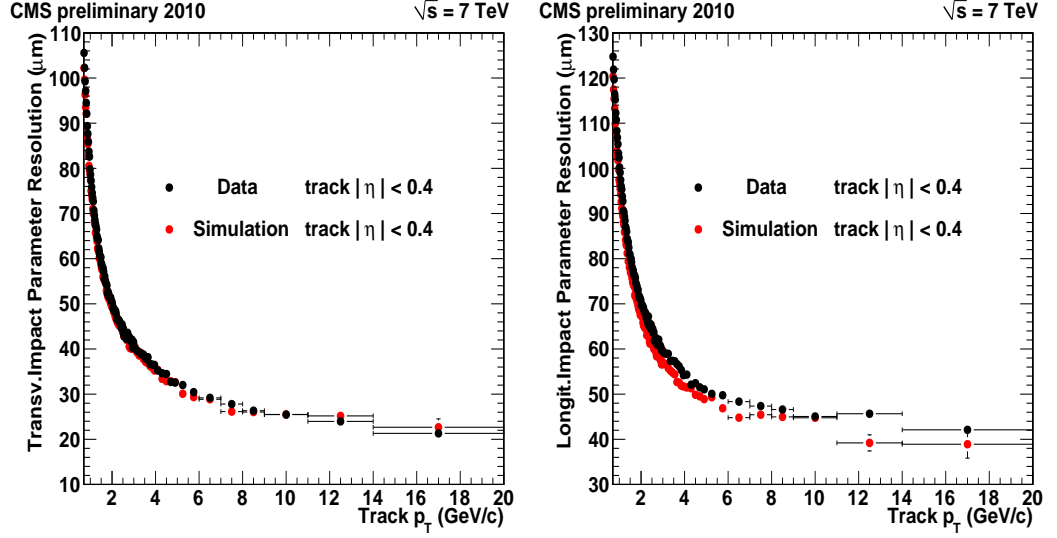


Figure 2.10: Measured resolution of track transverse impact parameter (left) and longitudinal impact parameter as a function of the track transverse momentum (right). Only central tracks with $|\eta| < 0.4$ are considered. Black and red points correspond to data and MC simulation, respectively.

ter of CMS detector is a hermetic, homogeneous calorimeter made up of 61,200 lead tungstate (PbWO_4) crystals [38] mounted in the barrel part, closed by 7324 crystals in each of the two endcaps. To have better showering, a preshower detector is placed in front of the endcap crystals. Avalanche photo-diodes (APDs) are used as photodetectors in the barrel and vacuum photo triodes (VPTs) in the endcaps. With the use of high density crystals, the calorimeter has fine granularity and is radiation resistant, which all are important characteristics in the LHC environment. One of the driving criteria in the design was the capability to detect the decay of postulated Higgs boson to a pair of photons. This capability is enhanced by the good energy resolution provided by a homogeneous crystal calorimeter. The characteristics of the PbWO_4 crystals make them an appropriate choice for operation at LHC. The crystals are characterized by high density (8.28 g/cm^3) and a short radiation length ($X_0=0.89 \text{ cm}$), so the calorimeter is very compact and can be placed inside the magnetic coil. Furthermore, it has a small Molière radius ($R_M=2.2 \text{ cm}$), which results in a fine gran-

CHAPTER 2. LARGE HADRON COLLIDER AND CMS EXPERIMENT

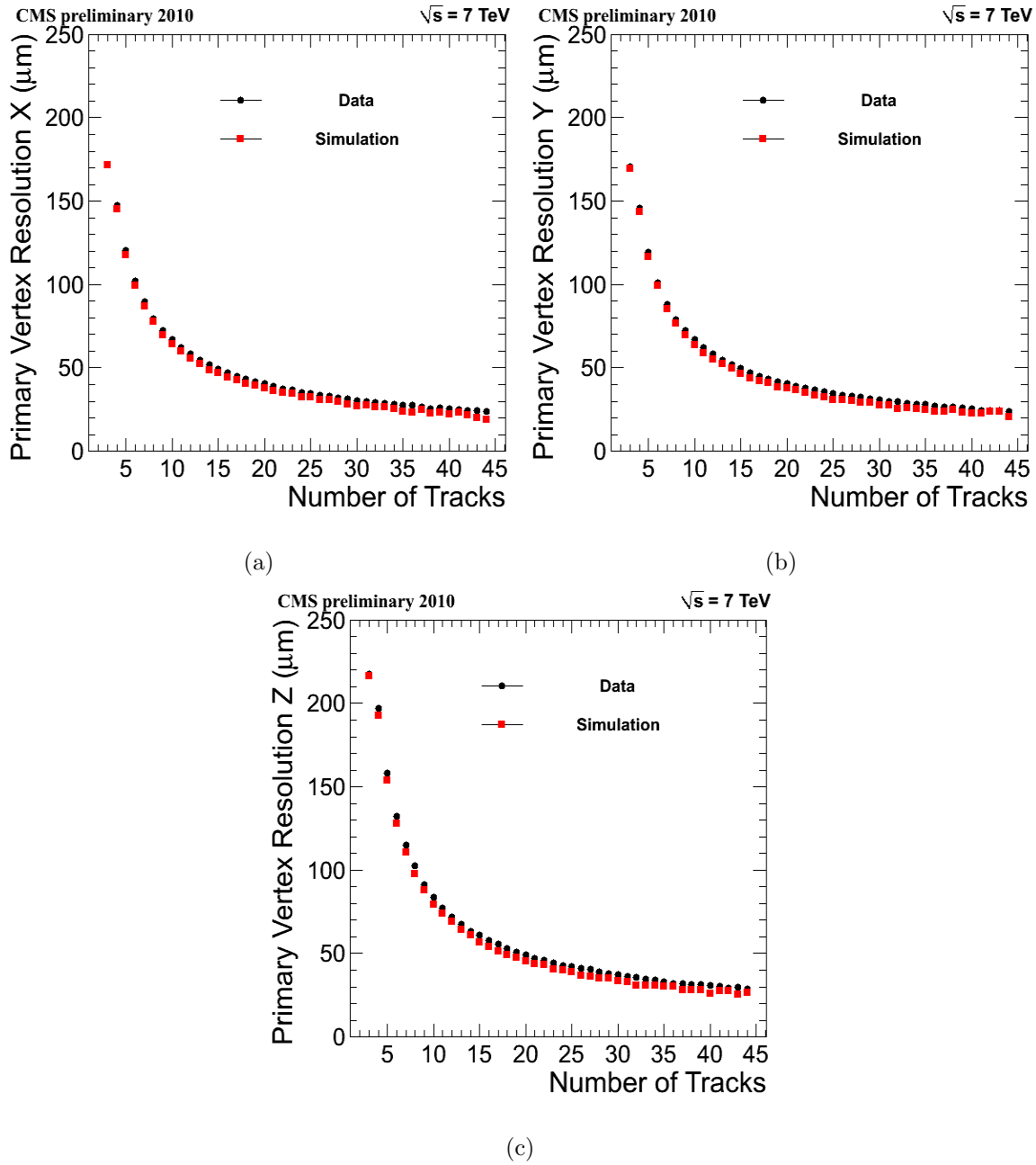


Figure 2.11: Primary vertex resolution in x (a), y (b), and z (c) as function of the number of tracks used in the fitted vertex.

2.2. COMPACT MUON SOLENOID

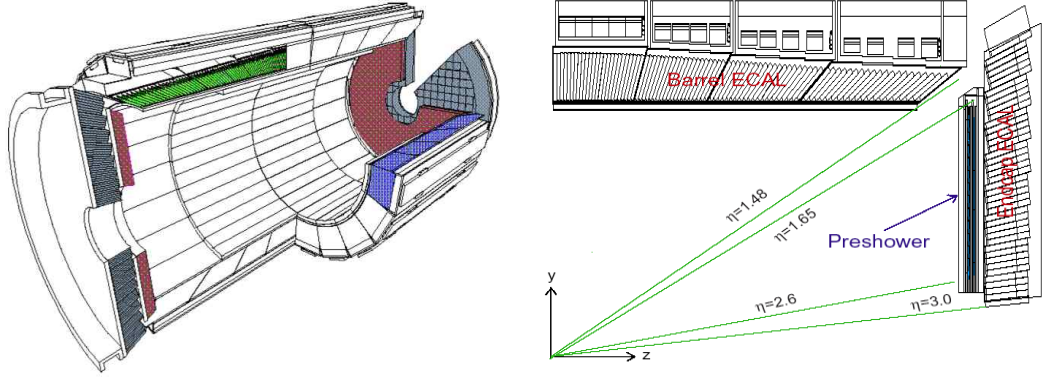


Figure 2.12: Electromagnetic calorimeter of the CMS detector.

ularity, needed because of high particle density produced at LHC. Molière radius is the radius of a cylinder containing 90% of the electromagnetic shower energy deposition. In recent years, PbWO_4 scintillation properties and other qualities have been progressively improved, leading to the mass production of optically clear, fast, and radiation-hard crystals. The scintillation decay time of these production crystals is of the same order of magnitude as the LHC bunch crossing time: about 80% of the light is emitted in 25 ns. The ECAL barrel (EB) covers a region in pseudorapidity of $0 < |\eta| < 1.479$ as shown in Figure 2.12. The inner radius of the EB is 129 cm. The crystals of the ECAL have a front face cross-section of $22 \times 22 \text{ mm}^2$ and a length of 230 mm, which corresponds to nearly 26 radiation lengths (X_0). The crystals in the EB are grouped into 36 identical supermodules. The ECAL barrel has a granularity $\Delta\eta \times \Delta\phi = 0.0175 \times 0.0175$. The ECAL endcaps (EE) cover a region in pseudorapidity of $1.479 < |\eta| < 3.0$. Each of the two endcaps consists of two semi-circular aluminium plates (dees), where 25 crystals are arranged into an array of 5×5 supercrystals. They have a front face cross-section of $28.6 \times 28.6 \text{ mm}^2$ and a length of 220 mm, which corresponds to nearly $25X_0$.

In front of each EE, a silicon based preshower (ES) device is mounted between $1.653 < |\eta| < 2.6$, which is shown in Figure 2.12. The aim of the preshower detector is to identify the signal of photons coming from the neutral pions (π^0 s), by making use of its high granularity. The preshower is a sampling calorimeter made of 2 layers of

CHAPTER 2. LARGE HADRON COLLIDER AND CMS EXPERIMENT

lead radiators and silicon strip sensors situated immediately after the lead radiators. The total thickness of the preshower silicon detector is 20 cm ($= 3X_0$ long).

The energy resolution of the ECAL can be parametrized as:

$$\left(\frac{\sigma}{E}\right)^2 = \left(\frac{S}{\sqrt{E(\text{GeV})}}\right)^2 + \left(\frac{N}{E(\text{GeV})}\right)^2 + C^2 \quad (2.4)$$

where S is the stochastic term which includes the effects of fluctuations in the number of the photo-electrons as well as in the shower containment, N is the noise term which includes contribution from the electronics and pile-up, and C is the constant term related to the calibration of the calorimeter. The ECAL energy resolution measured using test beams of electrons with energy ranging from 20 to 250 GeV [39] is given as:

$$\left(\frac{\sigma}{E}\right)^2 = \left(\frac{2.8\%}{\sqrt{E(\text{GeV})}}\right)^2 + \left(\frac{12\%}{E(\text{GeV})}\right)^2 + (0.3\%)^2 \quad (2.5)$$

The result is in good agreement with the design-goal performance expected for a perfectly calibrated calorimeter.

2.2.5 Hadron Calorimeter

The hadronic calorimeter (HCAL) [40] allows for the measurement of energy and position of the hadrons. This calorimeter plays an essential role in the identification of the quarks and gluons, by measuring the energy and direction of the jets. Moreover, it can indirectly detect particles that do not interact with the detector material such as the neutrino (by conservation of the momentum in transverse plane *i.e.* missing transverse energy). The measurement of the missing transverse energy is really important in the search of supersymmetric particles. For good missing energy resolution, a calorimeter coverage over a large range of pseudorapidity is required. In addition, the HCAL will also aid in the identification of muons in conjunction with the tracker, electromagnetic calorimeter, and muon systems.

The design of the HCAL is strongly influenced by the choice of magnet parameters since most of the CMS calorimeter is located inside the CMS superconducting magnet coil and surrounds the ECAL system. An important requirement of the HCAL is to

2.2. COMPACT MUON SOLENOID

minimize the non-Gaussian tails in the energy resolution and to provide good containment of hadronic shower and hermeticity for missing energy measurements. The HCAL design maximizes the material inside the magnet coil in terms of interaction lengths. The brass has been chosen as absorber material as it has a reasonably short interaction length and it is a non-magnetic material. The requirement of maximizing the amount of absorber before the magnet, results into minimum space for the active medium. The scintillator tile technology makes an ideal choice. It consists of plastic scintillator tiles having wavelength-shifting (WLS) fibres to transport the light to the photodetectors. The WLS fibres are spliced to high attenuation-length clear fibres outside the scintillator that carry the light to the readout system-photodetectors. The photodetection readout is based on multi-channel hybrid photodiodes (HPDs). The gap between the barrel and the endcap HCAL, through which the cable services of the ECAL and inner tracker pass, is inclined at 53° and points away from the center of the detector.

The HCAL of CMS detector is thus subdivided into four regions, 2 barrels-HB (HCAL Barrel), the HO (HCAL Outer), 2 endcaps- HE (HCAL Endcap), and the HF (HCAL Forward), which provide a good segmentation, a moderate energy resolution, and full angular coverage upto $|\eta| = 5$.

The barrel (HB) part of HCAL consists of 32 towers covering the pseudorapidity region $-1.4 < |\eta| < 1.4$, resulting in 2304 towers with a segmentation $\Delta\eta \times \Delta\phi = 0.087 \times 0.087$. There are 15 brass plates, each with a thickness of about 5 cm, plus 2 external stainless steel plates for the mechanical strength. The particles leaving the ECAL volume, first sees a scintillator plate with a thickness of 9 mm rather than 3.7 mm for other scintillator plates. There are two endcaps (HE), each one consists of 14 η towers with 5° segmentation, covering the pseudorapidity region $1.3 < |\eta| < 3.0$. For the outermost towers (at smaller η), the ϕ segmentation is 5° and the η segmentation is 0.087. For the 8 innermost towers, the ϕ segmentation is 10° , while η segmentation varies from 0.09 to 0.35 at the highest η . The total number of HE towers is 2304. The region with $3.0 < |\eta| < 5.0$ is covered by hadron forward (HF) detectors. These are made up of steel and quartz fibres. The signal originates from the Cerenkov light

CHAPTER 2. LARGE HADRON COLLIDER AND CMS EXPERIMENT

emitted in the quartz fibres, which is then channeled by the fibres to photomultipliers. There are 13 towers in η , all with a size given by $\Delta\eta = 0.175$, except for the lowest η towers with $\Delta\eta = 0.1$ and the highest η towers with $\Delta\eta = 0.3$. The ϕ segmentation of all the towers is 10° , except for the highest η one, which has $\Delta\phi = 20^\circ$. This leads to 900 towers and 1800 channels in two HF modulus. The HCAL acceptance region and layout is shown in Figure 2.13.

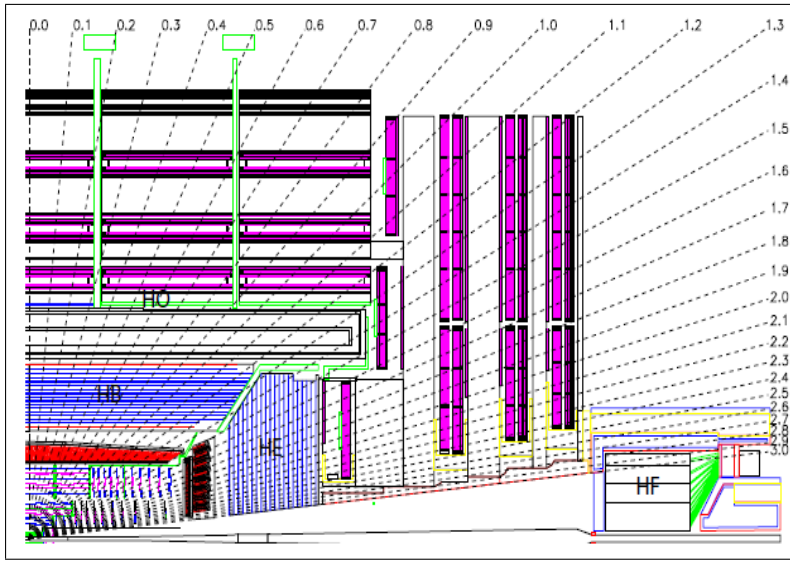


Figure 2.13: Longitudinal cross-section of the quarter of the CMS detector showing the positions of the hadronic calorimeter barrel (HB), hadronic calorimeter endcap (HE), forward hadronic calorimeter (HF), and outer hadronic calorimeter (HO).

2.2.6 Outer Hadron Calorimeter

The HCAL plays an important role in CMS experiment for the measurement of jets and missing transverse energy. The HCAL is placed inside the solenoid and it is not thick enough to contain complete hadronic shower. Therefore, HCAL is extended outside the solenoid coil. This extended part of HCAL is called Outer Hadronic Calorimeter (HO) [41]. The HO utilizes the coil as an additional absorber material equal to $1.4/\sin\theta$ interaction lengths (λ). It is used to measure energy for late shower development and to measure the shower energy beyond the geometrical reach of HB.

2.2. COMPACT MUON SOLENOID

Close to the interaction point at $\eta = 0$, HB provides minimum interaction length to the hadrons. Therefore, the central ring (Ring 0) has two layers of HO plastic scintillators. All other rings ($\pm 1, \pm 2$) have single HO layer. The total depth of the hadron calorimeter is thus extended to a minimum of 11.8λ as shown in Figure 2.14, except the barrel-endcap boundary region. The HO layers are physically located inside the barrel muon system.

The design of HO is constrained by the geometry of the muon system. The sizes and positions of the tiles in HO are supposed to roughly map with the layers of HB to make towers of granularity 0.087×0.087 in η and ϕ . The HO is physically divided in to five rings in η direction. The rings are numbered as -2, -1, 0, 1, 2 with increasing η . Each ring of the HO is divided into 12 identical ϕ sectors and each sector has 6 slices or trays in ϕ direction. The ϕ slices of a layer are identical in all the sectors. The scintillation light from the tiles is collected using wave length shifting (WLS) fibers of diameter 0.94 mm and transported to the photo detectors located on the structure of the return yoke by splicing a clear fiber (high attenuation length).

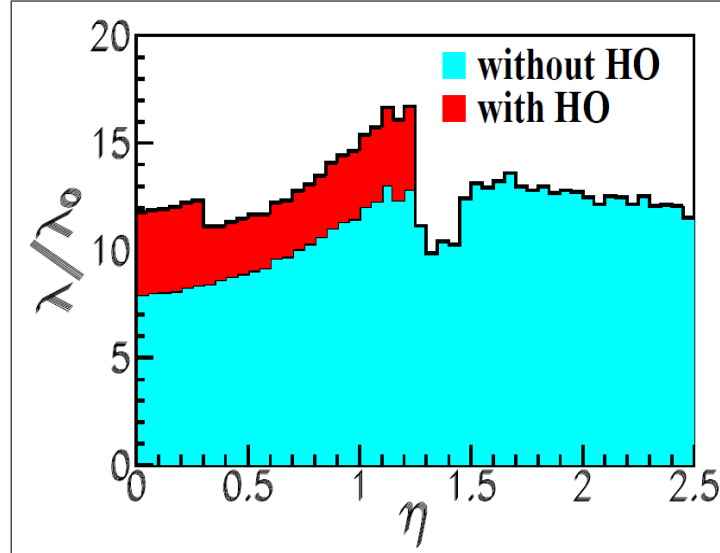


Figure 2.14: Number of interaction lengths till the last sampling layer of the hadron calorimeter as a function of η . The two shaded regions correspond to the setups with and without the outer hadron calorimeter.

2.2.7 Muon System

Muon detection is a powerful tool for recognizing signatures of interesting processes over the very high background rate expected at LHC with full luminosity. For example, the predicted decay of the Standard Model Higgs boson into ZZ or ZZ^* , which in turn decay into 4 leptons, has been called “gold plated” decay mode for the case in which all the leptons are muons. Besides the relative ease in detecting muons, the best 4-particle mass resolution can be achieved if all the leptons are muons because they are less affected than electrons by radiative losses in the tracker material. This example and other particles from SUSY models, emphasize the discovery potential of muon final states and the necessity of wide angular coverage for muon detection.

Therefore, as is implied by the experiment’s middle name, the detection of muons is of central importance to CMS: precise and robust muon measurement was a central theme from its earliest design stages. The muon system has 3 functions: muon identification, momentum measurement and triggering. Good muon momentum resolution and trigger capability are enabled by the high field solenoidal magnet and its flux-return yoke. The latter also serves as a hadron absorber for the identification of muons. The material thickness crossed by muons, as a function of pseudorapidity, is shown in Figure 2.15

The CMS muon system is designed to have the capability of reconstructing the momentum and the charge of the muons over the the entire kinematic range of the LHC. The CMS detector uses 3 types of gaseous particle detectors for muon identification, namely: Resistive Plate Chambers, Cathode Strip Chambers and Drift Tubes. The details of all these detectors can be found in Ref. [42]. Due to the shape of the solenoid magnet, the muon system was naturally driven to have a cylindrical barrel section and two planar endcap regions. Because the muon system consists of about 25,000 m² of detection planes, the muon chambers had to be inexpensive, reliable, and robust. A schematic view of the one quadrant of the CMS muon system is shown in Figure 2.16.

2.2. COMPACT MUON SOLENOID

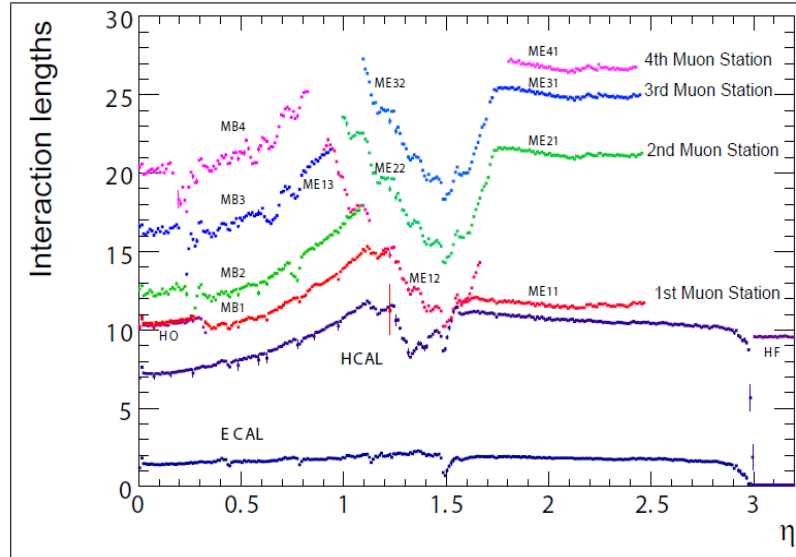


Figure 2.15: Material thickness in interaction lengths at various depths, as a function of pseudorapidity.

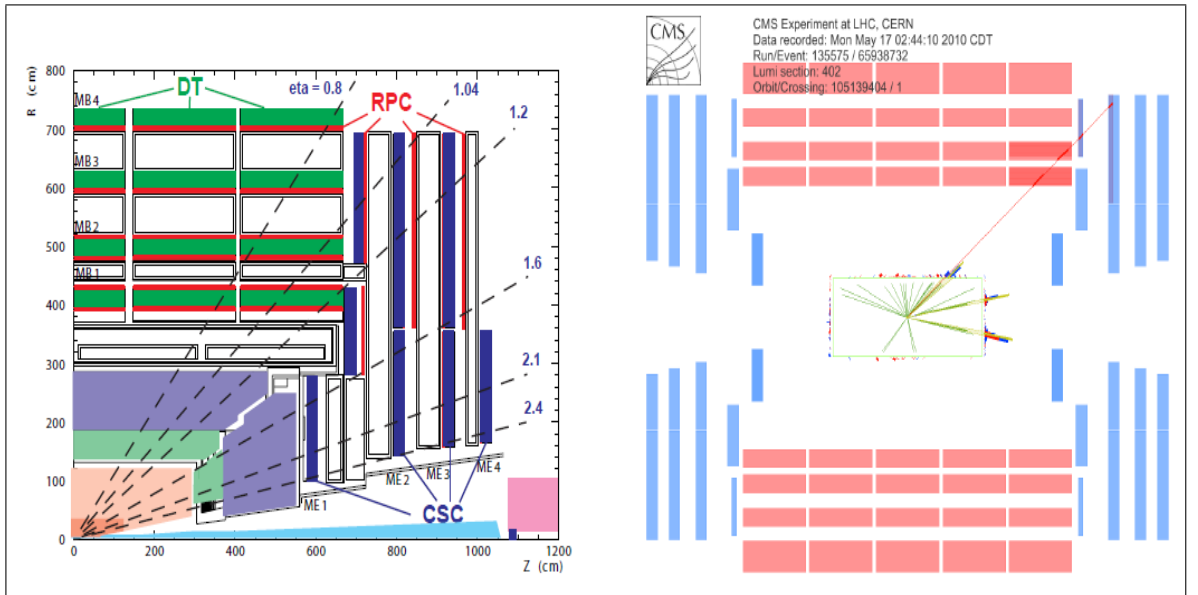


Figure 2.16: Layout of the one quadrant of the CMS (left) and a display of the collision event with a muon crossing the DT and CSC chambers in the overlap region between barrel and endcap (right).

CHAPTER 2. LARGE HADRON COLLIDER AND CMS EXPERIMENT

Drift Tube Chambers

The Drift Tube (DT) chambers [43] based muon detection subsystem, covers a pseudorapidity range, $|\eta| < 1.2$. It consists of five wheels, each wheel divided into 12 sectors, each covering an azimuthal region of 30° . Sectors are numbered anticlockwise, starting from the right-most vertical sector shown in Figure 2.17, in the direction of increasing azimuthal angle ϕ . Each sector consists of four chambers, one on the inside of magnet return yoke, one on the outside, and two sandwiched in between the magnet return yoke. The support for the magnet return yoke is placed in between the chambers, so they do not overlap in azimuthal angle ϕ , thus insuring complete ϕ coverage by the DT chambers.

Each drift-tube chamber is made of either two or three superlayers (SL), each superlayer, in turn, is made up of four layers of long rectangular drift cells staggered by half a cell. The drift cell is 2.4 m long with the cross-section $13 \times 42 \text{ mm}^2$. A thin anode wire is stretched in the middle of the tube along the long side of it. The characteristic transverse dimension of the drift cell is 21 mm, thus the maximum drift time is 380 ns in the gas mixture of 85% Ar and 15% CO₂. The two superlayers on the outside of chamber have wires inside the cell parallel to the beam line, thus providing accurate measurement of the azimuthal angle. The superlayer inside the chamber has wires perpendicular to the beam line, thus measuring the z-position. The superlayer measuring z-position is not present in the last muon station. The superlayer is a basic measuring unit of the DT station. One superlayer, that is, a group of 4 consecutive layers of thin tubes staggered by half a tube, gives an excellent time-tagging capability, with a time resolution of a few nanoseconds. This capability provides efficient bunch crossing identification. The time tagging is delayed by a constant amount of time equal to the maximum possible drift-time, which is determined by the size of the tube, the electrical field, and the gas mixture. The design and the precise mechanical construction of the DT chamber allows the CMS detector to achieve $100 \mu\text{m}$ precision in global $r - \phi$ position measurement.

CHAPTER 2. LARGE HADRON COLLIDER AND CMS EXPERIMENT

Cathode Strip Chambers

The Cathode Strip Chambers (CSCs) [44] constitute an essential component of the CMS muon detector, providing precise tracking and triggering of muons in the end-caps. Their performance is critical to many physics analyses based on muons. The region between $0.9 < |\eta| < 1.2$ is covered by both the DT chambers and CSCs. There are 468 CSCs in the two muon endcaps. Each endcap consists of 4 “stations” of chambers, labelled ME1 to ME4 in order of increasing distance from the collision point, which are mounted on the disks enclosing the CMS magnet, perpendicular to the beam direction. In each disk the chambers are divided into 2 concentric rings around the beam axis (3 for ME1 chambers). Each CSC 2.18 (right) is trapezoidal in

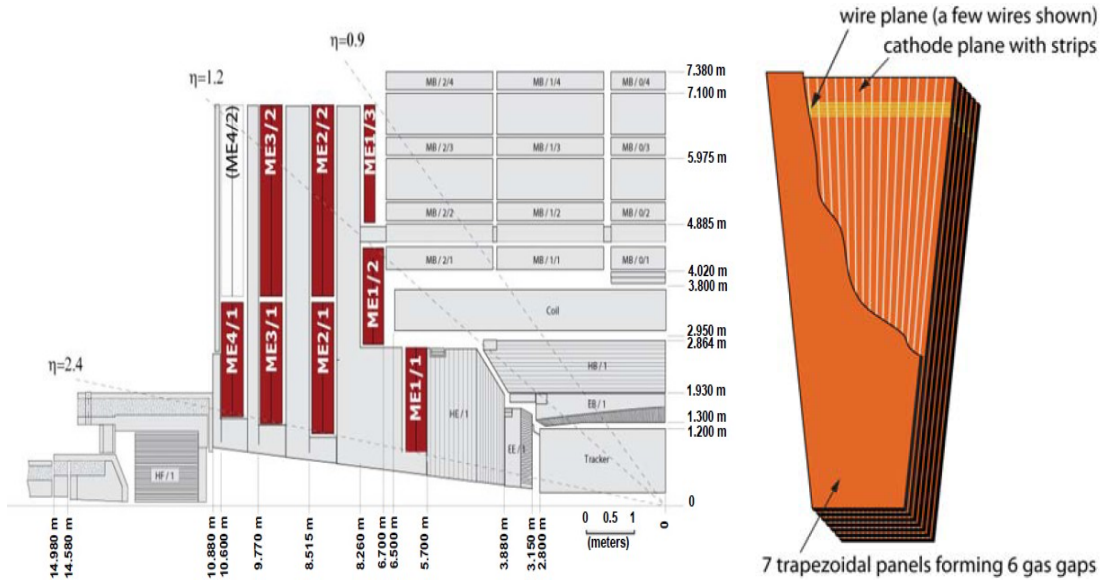


Figure 2.18: The layout of muon cathode strip chambers (CSCs) in one quarter of the CMS. Most of the cathode strip chambers are highlighted in dark-red, the ME4/2 chamber is not highlighted, because it was assumed that it would not be installed at the start-up of the LHC, but delays in the LHC start-up schedule allowed for its installation for the first collision data.

shape and consists of 6 gas gaps, each gap having a plane of radial cathode strips and a plane of anode wires running almost perpendicularly to the strips. All CSCs, except

2.2. COMPACT MUON SOLENOID

those in ME1/3, are overlapped in ϕ to avoid gaps in the muon acceptance. There are 36 chambers in each ring of a muon station, except for the innermost (highest η) rings of ME2-ME4 which have 18 chambers. The gas ionization and subsequent electron avalanche caused by a charged particle traversing each plane of a chamber produces a charge on the anode wire and an image charge on a group of cathode strips. Thus, each CSC measures the space coordinates (r , ϕ , z) in each of the 6 layers. Figure 2.18 (left) shows the drawing of a quadrant of CMS detector highlighting the CSC sub-detector.

Resistive Plate Chamber System

Resistive Plate Chambers (RPCs) [45] are gaseous parallel-plate detectors that combine adequate spatial resolution with a time resolution comparable to that of scintillators [46] [47]. The RPC is capable of tagging the time of an ionizing particle in a much shorter time compared to the 25 ns between LHC bunch crossings (BXs). Therefore, a fast dedicated muon trigger device based on RPCs can identify unambiguously the relevant BX to which a muon track is associated with, even in the presence of the high particle rate and background expected at the LHC. Signals from such a device directly provide the time and position of a muon hit with the required accuracy. A trigger based on RPCs has to provide the BX assignment to candidate tracks and estimate the transverse momenta with high efficiency in an environment where rates may reach 10^3 Hz/cm².

The RPC detectors are employed in CMS as a dedicated trigger system in both the barrel as well as in the endcap regions. They complement the muon tracking system: drift tubes (DTs) in the barrel and cathode strip chambers (CSCs) in the endcaps. From the geometrical point of view, the muon system is divided into five wheels in the barrel and three disks in each endcap. Each barrel wheel is divided into 12 sectors, covering the full azimuthal dimension as shown in Figure 2.19. Each sector consists of four layers of DTs and six layers of RPCs, with a total of 480 RPC stations covering average area of 12 m². The two innermost DT layers are sandwiched between RPC layers (RB1_{in} and RB1_{out} for the innermost DT layer, RB2_{in} and RB2_{out} for the

CHAPTER 2. LARGE HADRON COLLIDER AND CMS EXPERIMENT

second one). The third and fourth DT layers are complemented with a single RPC layer, placed on their inner side (RB3 and RB4). For the initial data-taking period, until the next long shutdown (early 2013) of the LHC machine, the RPC coverage extends only to the pseudorapidity region $|\eta| < 1.6$, which would be increased later on.

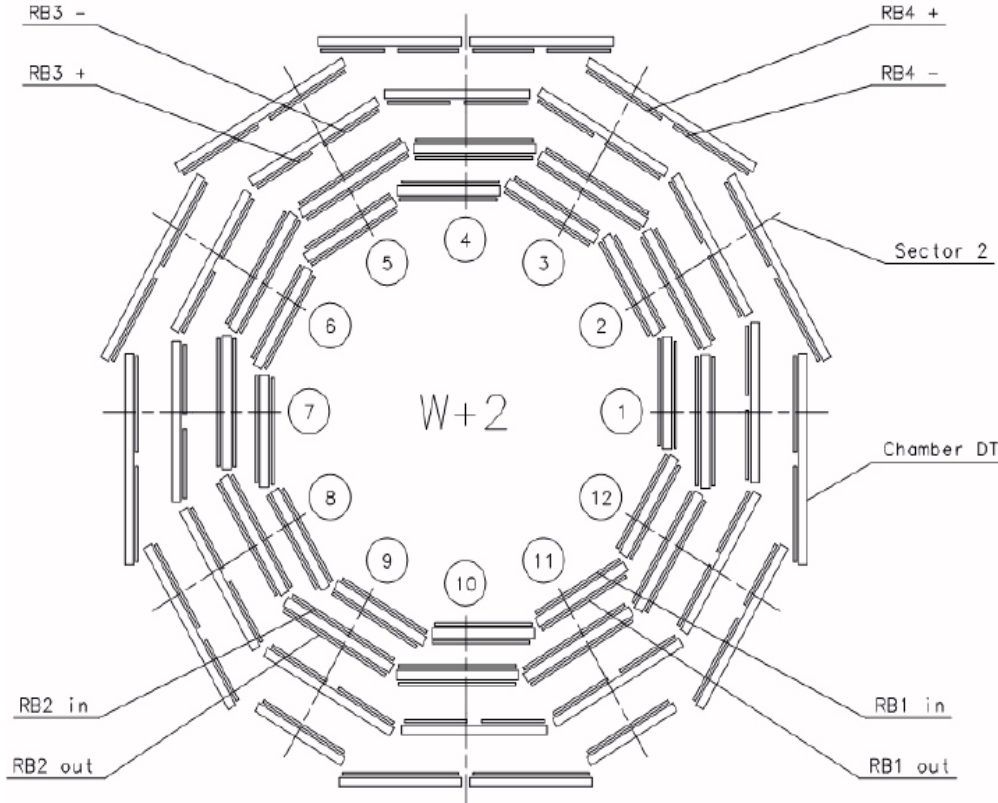


Figure 2.19: Transverse view of the muon system layout in the barrel region, showing the positions of the DT and RPC stations.

The measurement of the momentum of the charged particles is affected by systematic uncertainties due to the limited knowledge and modeling of the detector material, the magnetic field, the alignment, and the reconstruction algorithms used to fit the track trajectory. By studying the mass of resonances like Z , improvements in the modeling of the detector material and eventually the final calibration of the tracks and muons can be achieved. The study of the resolution of the transverse momentum as a function of muon pseudorapidity [48], measured with 40 nb^{-1} of integrated

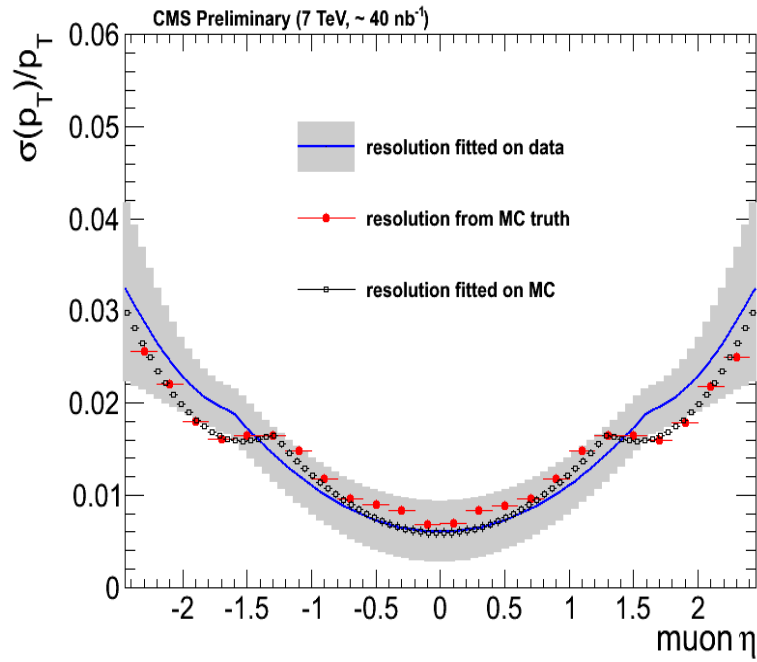


Figure 2.20: Resolution on transverse momentum as measured with $\sim 40 \text{ nb}^{-1}$ of integrated luminosity (blue) compared to the Monte Carlo resolution computed from Monte Carlo truth (red points) and from the fit (black squares). The gray band in data represents the error on the fitted function for data computed from the errors on the parameters.

CHAPTER 2. LARGE HADRON COLLIDER AND CMS EXPERIMENT

luminosity with CMS is shown in Figure 2.20.

2.2.8 Trigger system

Level-1 Trigger

The LHC provides proton-proton collisions with a very high interaction rate. The designed bunch crossing interval for proton beams is 25 ns, which corresponds to a bunch crossing frequency of 40 MHz. Depending on luminosity, several collisions occur at each crossing of the proton bunches (approximately 20 simultaneous proton-proton collisions at the nominal design luminosity of $10^{34} \text{ cm}^{-2}\text{s}^{-1}$). Since it is impossible to store and process the large amount of data associated with such a high number of events, a drastic reduction in the event-rate has to be achieved. This task is performed by the Trigger System, which is the start of the physics event selection process. The rate is reduced in two steps called Level-1 (L1) Trigger [49] and High-Level Trigger (HLT) [50], respectively.

The Level-1 Trigger consists of custom-designed, largely hardware based programmable electronics, whereas the HLT is a software based system implemented in a filter farm of about one thousand commercial computer processors. The event-rate reduction capability is designed to be at least a factor of 10^6 for the combined Level-1 Trigger and HLT. The design output rate limit of the Level-1 Trigger is 100 kHz. The Level-1 Trigger uses coarsely segmented data from the calorimeters and the muon system, while holding the high-resolution data in pipelined memories in the front-end electronics. The High-Level Triggers, implemented as a computer processing farm that is designed to achieve a rejection factor of 10^3 , write up to 100 events/second to mass computer storage. The last stage of High-Level Trigger processing does reconstruction and event filtering with the primary goal of making datasets of different signatures on easily accessible media.

The Level-1 Trigger System is organized into three major subsystems: the Level-1 Global Calorimeter trigger (GCT), the Level-1 Global Muon trigger (GMT), and the Level-1 Global trigger (GT). The muon trigger is further organized into subsystems

2.2. COMPACT MUON SOLENOID

representing the 3 different muon detector systems, the Drift Tube Trigger in the barrel, the Cathode Strip Chamber (CSC) trigger in the endcap, and the Resistive Plate Chamber (RPC) trigger covering both barrel and endcap. The Level-1 muon trigger also has a global muon trigger that combines the trigger information from the DT, CSC, and RPC trigger systems and sends this information to the Level-1 Global trigger. The Global trigger takes the decision to reject an event or to accept it for further evaluation by the HLT. The decision is based on algorithm calculations and on the readiness of the sub-detectors and the Data Acquisition System (DAQ), which is determined by the Trigger Control System (TCS). The Level-1 Accept (L1A) decision is communicated to the sub-detectors through the Timing, Trigger and Control (TTC) system. The architecture of the Level-1 Trigger is depicted in Figure 2.21. The Level-1 Trigger has to analyze event information for every bunch crossing. The allowed Level-1 Trigger latency, between a given bunch crossing and the distribution of the trigger decision to the detector front-end electronics, is $3.2 \mu s$. The processing must therefore be pipelined in order to enable a quasi-deadtime-free operation. The Level-1 Trigger electronics is housed partly on the detectors, partly in the underground control room located at a distance of approximately 90 m from the experimental cavern.

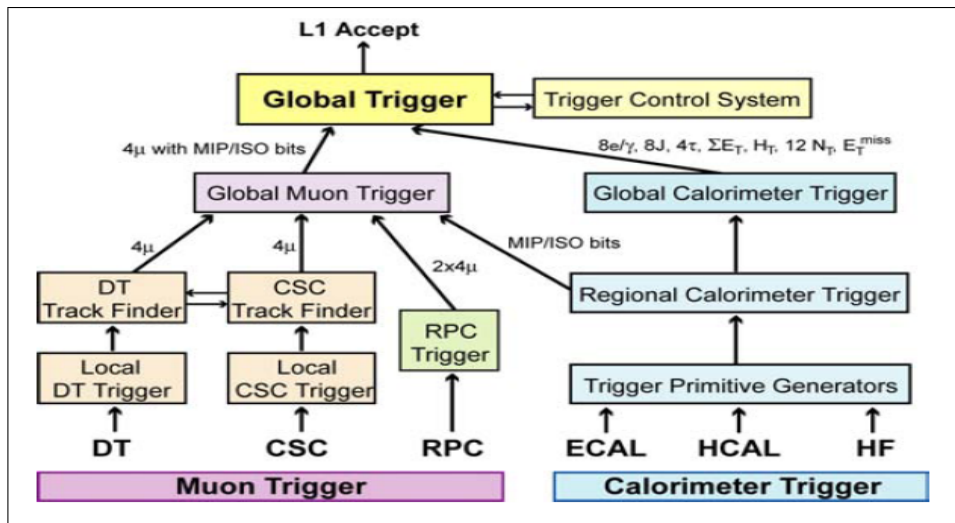


Figure 2.21: Architecture of Level-1 trigger

CHAPTER 2. LARGE HADRON COLLIDER AND CMS EXPERIMENT

Data Acquisition and High-Level Trigger

The architecture of the Data Acquisition system (DAQ) of CMS detector is shown schematically in Figure 2.22. The CMS Trigger and DAQ System is designed to collect and analyze the detector information at the LHC bunch crossing frequency of 40 MHz. The DAQ system must sustain a maximum input rate of 100 kHz and must provide enough computing power for a software filter system, the High-Level Trigger (HLT), to reduce the rate of stored events by a factor of 1000. Thus the main purpose of the Data Acquisition (DAQ) and High-Level Trigger (HLT) system is to read the CMS detector event information for those events that are selected by the Level-1 Trigger and to select, among those events, the most interesting ones for output to mass storage. The proper functioning of the DAQ at the desired performance will be a key element in reaching the physics potential of the CMS experiment. In addition,

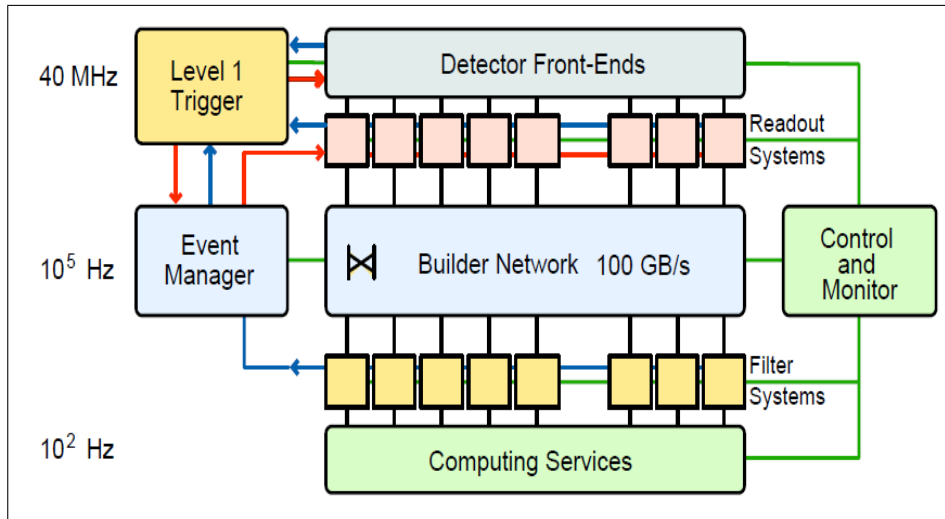


Figure 2.22: Architecture of Data Acquisition system

to maximize this physics potential, the selection of events by the HLT must be kept as broad and as inclusive as possible, not to lose signal too. In summary, the online event filtering process in the CMS experiment is carried out in two steps:

- The Level-1 Trigger, with a total processing time of $3 \mu s$, including the latencies for the transport of the data and control signals. During this time interval,

2.3. PARTICLE DETECTION THROUGH THEIR INTERACTION WITH CMS DETECTOR MATERIAL

the data are stored in the pipeline memories in the front-end electronics. The Level-1 Trigger is designed to accept a maximum rate of 100 kHz.

- The High-Level Trigger, with a total processing time of up to ~ 1 s. During this time interval, the data are stored in random-access memories. The High-Level Trigger is designed to output a maximum event rate of ~ 100 Hz.

2.3 Particle detection through their interaction with CMS detector material

Collider detectors which are designed, subsequently to discover new particles, must detect all the possible decay products, identify them and should be capable of measuring their position and energy very accurately. Particle identification is the most important aspect while designing a detector. The basic layout of the modern collider detector is remarkably uniform.

- During crossing of proton bunches in the two circulating beams, interactions take place and a large number of particles are produced in these interactions. These produced particles should be detected by various components of the CMS detector. The particle produced at the interaction point (IP) has to pass first through the tracking system made up of silicon detector. Tracking device is the innermost part of the CMS detector close to the IP. When charged particle passes through the silicon detector, it creates electron-hole pairs which are collected by electrodes to give signal. To remove the thermally generated electron-hole pairs, the silicon detector is operated in reverse bias mode. Signals from different silicon-pixels and silicon-strips are combined to form track of charged particles.
- After the detector tracking layers, the particles enters into the Electromagnetic Calorimeter (ECAL). In ECAL, the particles having high electromagnetic interaction cross-section like electrons and photons deposit most of their energy by EM interactions (*i.e.* ionization, bremsstrahlung, pair production, Compton scattering, *etc.*). An energetic electron passing into the ECAL, will radiate

CHAPTER 2. LARGE HADRON COLLIDER AND CMS EXPERIMENT

photons, through Bremsstrahlung. If the energy of the Bremsstrahlung photon is sufficiently high ($> 2M_e \sim 1.02$ MeV) it will, in turn, produce an electron-positron pair, through pair-production. Each of the pair-production partner will then radiate photons. The processes of Bremsstrahlung and pair-production will then result into an “electromagnetic shower”, shown in Figure 2.23. The growth of this shower will continue until the secondary particles are no longer capable of multiplying. At that point, the maximum number of shower particles, N_{max} , exists. Beyond the depth of the maximum shower development, the number of electrons dies away due to ionization and photons by Compton scattering. The energy loss by an electron is characterized in terms of radiation length (X_0), defined by the relation:

$$-\frac{dE}{dx} = \frac{E}{X_0} \quad (2.6)$$

Thus radiation length, is defined as the distance over which the electron losses $(1/e)$ fraction of its energy by radiation loss only. The other quantity, which is

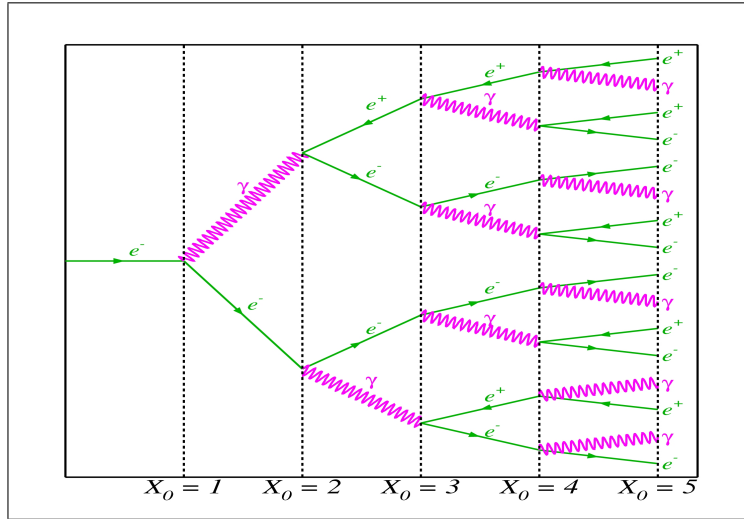


Figure 2.23: Schematic view of an electromagnetic shower.

vitally important for describing the energy loss mechanism, is the critical energy, E_c . The critical energy is that energy above which radiative processes dominates. For an electron with energy less than 8 MeV (E_c of electron in lead), the energy loss of electron mainly occurs through ionization, whereas for high

2.3. PARTICLE DETECTION THROUGH THEIR INTERACTION WITH CMS DETECTOR MATERIAL

energies radiative process dominates. Figure 2.24 shows the various mechanisms by which electron losses energy while passing through lead. For photons with energy less than 500 KeV, photoelectric effect dominates. In case energy is higher than 500 KeV and less than few MeV, energy loss by Compton scattering dominates. When the energy of photons increases above 100 MeV, pair-production cross-section dominates. Muons do not usually show EM showering because their critical energy is ~ 300 GeV, so they deposit energy because of ionization only. The charged hadrons also deposit energy by ionization process only. The material of EM calorimeter is chosen in such a way that full EM shower for electron and photon remains confined within the ECAL. For example, in CMS we use PbWO_4 crystals which have radiation length (X_0) of 0.9 cm and total thickness of the calorimeter is $25X_0$ to contain full EM shower. So all electrons and photons produced in the interaction are absorbed in the ECAL and energy, direction of these particles is measured.

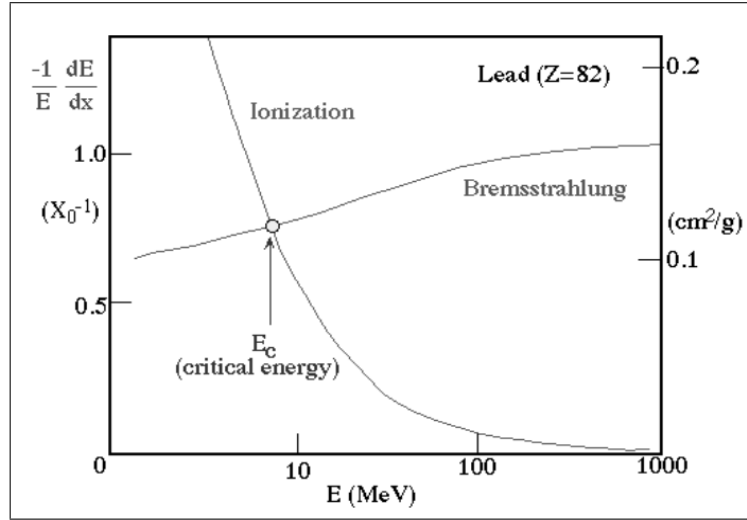


Figure 2.24: Fractional energy loss of electron per radiation length in lead as function of electron energy.

- The next detector layer which the particle has to travel through is the hadronic calorimeter (HCAL), where the charged and neutral hadrons deposit their energy. The detection of hadronic energies is more complex than electromagnetic

CHAPTER 2. LARGE HADRON COLLIDER AND CMS EXPERIMENT

processes. In passing through matter, a hadron can therefore build up a shower through multiple strong interactions, resulting in the production of a large number of particles in each secondary interaction. This process results into hadron shower development. The hadron shower can be parametrized by a “nuclear interaction length (λ_0)”, similar to the radiation length for electromagnetic showers. For heavy materials, the interaction length is much larger than the radiation length, so the hadronic showers start later than the electromagnetic shower and lasts long too. This forms the basis of setting ECAL before the HCAL while designing a detector. However, unlike the case of electromagnetic shower, it should be noted that there are many different processes possible in the development of high energy hadronic showers, due to which in general, not all the hadron energy will be “visible”:

- Electromagnetic component: Some of the hadronic particles like η and π^0 decay in two energetic photons which initiate the EM shower. On an average one third of the mesons produced in the first interaction are π^0 . If kinematically allowed, charged hadrons produce more π^0 in next interaction. Thus good fraction of hadronic shower consists of EM shower also. Depending on the numbers of π^0 -mesons produced in the early stages of the hadronic cascade, the shower may develop in either a predominantly electromagnetic or a hadronic mode contributing substantially to the variation in energy deposit, which will limit the energy resolution in a hadronic calorimeter.
- Up to 30% of hadron energy may be lost due to nuclear excitation and nuclear break-up, spallation or “evaporation” of slow neutrons and protons, by the escape of neutrinos, and also by muons which are produced by the decay of heavy mesons. In case of hadrons, the medium itself is excited unlike the electromagnetic calorimeter in which the medium does not participate in cascade processes such as Bremsstrahlung and pair-production. In hadronic cascade, due to the interaction with the nucleons of the nucleus, a substantial amount of hadronic energy will go into “binding energy losses” where the nucleus is excited. However, the binding energy ultimately appears in

2.3. PARTICLE DETECTION THROUGH THEIR INTERACTION WITH CMS DETECTOR MATERIAL

the calorimeter when the nucleus de-excites emitting a slow neutron, photon or other fragment, but the calorimeter response time is short as compared to this de-excitation process, thus this energy deposit is not detected.

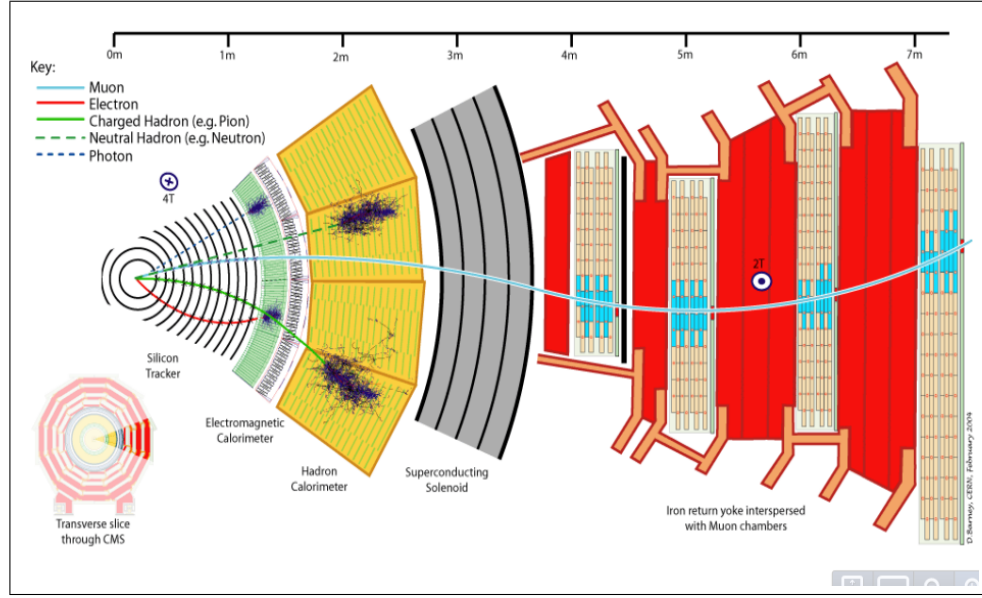


Figure 2.25: Slice of CMS detector showing interactions of various particles in sub-detectors of CMS.

The next layer and the final sub-detector which the particles have to enter are the muon chambers. At the end of HCAL, only muons and neutrinos survive. Neutrinos pass through the detector without any interaction. Therefore, the only particles being in the muon chambers are the muons, which are weakly interacting particles. The muon deposits energy equal to minimum ionizing particle in ECAL and HCAL. Thus muon will be the only particle passing through chamber and being detected by this system. The various types of interactions of particles in different parts of CMS detector are shown in Figure 2.25.

In this Chapter, a brief description of the LHC machine and the CMS detector is presented. Also, the purpose and working of each sub-detector of the CMS detector has been discussed in details. In the end, a short description of the mechanisms by which various particles produced in the pp interactions interact and deposit their energy in various sub-detectors of CMS detector, is presented.

3

Event Reconstruction Chain and Data Samples

The simulation of events is as much fundamental for a high energy experiment as the particle detectors themselves. It is an art of mimicking nature and man-made particle detectors. It is an essential component of any experiment from the very early design stage up to the final commissioning stage. The simulation study of the detector and the physics processes is quite important before the start of the experiment as well as after the start of real data taking in the experiment. Performance and calibration of various components of the detector can be monitored using simulation techniques. With the help of simulation studies, it is also possible to decide the nature of backgrounds for a particular physics process and then decide the analysis strategy accordingly. The designing of a robust and highly sensitive analysis is quite difficult if one merely considers a set of theoretical equations that drive the underlying physics of interest. An outcome with 100% certainty is difficult to predict in high energy physics, the only possibility is to define the probability with which a certain outcome can occur. For example, consider the case of hadron colliders, if a given number of events N are produced, it cannot be determined with 100% certainty that n events out of the total events, correspond to *e.g.* $pp \rightarrow Z' \rightarrow \tau\tau$ production. If p is the probability associated with the production of such event, then on the average, we

CHAPTER 3. EVENT RECONSTRUCTION CHAIN AND DATA SAMPLES

expect $n=Np$ events due to $pp \rightarrow Z' \rightarrow \tau\tau$ production. Therefore, construction of an analysis requires the generation of an ensemble of simulated events that can be used to determine the characteristics of the signal process of interest on a statistical basis. The comparison of results from simulation with the real data helps in fine-tuning of the event generators and also checks for the modeling of detector in simulation. No data analysis or physical interpretation can be done without the help of simulated data acting as a reference to the experimental outcome. All the results from real data rely on the efficiency and the acceptance correction factor estimated using the simulated events. Even the associated systematic errors include the simulation uncertainties, thus the nature of physics results is strongly dependent on the quality of the simulation predictions.

The term *Monte Carlo* (MC) is widely used to describe any technique which makes use of the random numbers to solve a numerical problem. These techniques are often used to simulate or solve complex physical or mathematical systems when it is difficult to obtain the exact result using deterministic equations or algorithms. In statistical analysis, MC methods are employed when the model of interest contains significant uncertainty for the inputs. In mathematics, MC methods can be utilized to solve complex integration problems. In fact, MC integration methods have been used to extract the statistical significance of the results as can be seen in the next Chapters.

At CMS, the event simulation takes place in two main steps. The first step is the generation of events with the help of an event generator, based on the Standard Model or a beyond Standard Model theory. The event generator produces all the particles that are expected to be produced in the pp collisions. The second step is to simulate the interactions of these particles with the CMS detector and translate them into electrical signals for reconstruction of the event. The reconstruction step is same for both the simulation and the real data. The general structure of the physics process modeling and event generation is shown in Figure 3.1.

3.1. EVENT GENERATORS

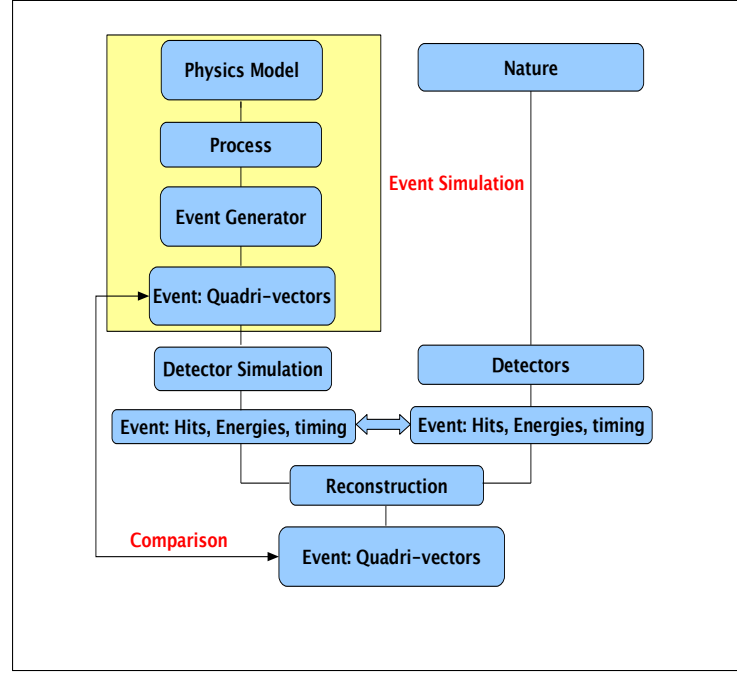


Figure 3.1: Basic steps in event generation, simulation and data analysis.

3.1 Event Generators

The main motive of the event generators is to generate events as realistic as could be from a real experiment. Event generators are intended to generate complete events by subdividing the task into simpler steps. For generation of a given hard process, the basic steps are as follows: generation of the Feynman diagrams involved in the physics process of interest, construction of the matrix elements which after being integrated over whole phase space provides the total and differential cross-section. Finally, the events are randomly generated according to the full differential cross-section and provide a set of four momentum vectors each associated with one of the final state particles. At the theoretical level, it is straight forward to calculate the matrix elements with “reasonable” accuracy (leading order calculations, LO). The level of accuracy is analysis dependent. Depending upon the scope of the experiment and a particular analysis, it may become difficult to achieve accuracy beyond LO calculations due to increase in the number of Feynman diagrams and complex

CHAPTER 3. EVENT RECONSTRUCTION CHAIN AND DATA SAMPLES

mathematical calculations involved. For example, it has been shown that the LO diagram for the production of a Standard Model Z boson occurs via $q\bar{q}$ annihilation as depicted in Figure 3.2. However, in the next to leading order (NLO) matrix elements, additional effects such as the exchange of gluons between initial state quarks also exist. Therefore, the NLO diagrams can take place via $qg \rightarrow Zq$ or $q\bar{q} \rightarrow Zg$. The number of Feynman diagrams and required mathematical calculations increase significantly when one considers higher order processes.

Parton showering is built upon well motivated belief that the radiation from partons can be built up from a series of similar processes where a parton loses energy as it radiates a gluon ($q \rightarrow qg$). The shower begins at the energy scale of the hard process or initial interacting partons and continues to evolve until the radiated partons do not have sufficient energy to continue to shower. Because the strong force does not allow for asymptotic freedom, the partons (quarks and gluons) cannot exist in the bare state. Hence, these partons get hadronized to produce hadrons as they move apart. Thus a general scheme of the event generation assumes the evaluation of the hard process, then evolve the event through a parton showering and hadronization step, and the decay of the unstable particles such as τ -leptons. The event information contains the four momenta of all the final state particles (hadrons, leptons, and photons) and the position of their decay vertices.

There are specific generator packages such as PYTHIA [51] and MADGRAPH [52] which simulate the transformation of partons into hadrons through the parton showering and hadronization algorithms. At hadron colliders like LHC, the hadronic processes are even more complex due to non-elementary structure of proton. There will be large number of possible initial hard scattering states. Moreover, the Multiple Parton Interactions (MPI) between the partons, not involved in the hard scattering, must be taken into account. During the collision of two proton bunches in LHC, more than 25 inelastic events may be superimposed on the single possible interesting event. These events must also be simulated in order to come as close as possible to the real situation in the CMS detector. The details of the implementation of various physics aspects are different in each of these generators, however the underlying principle is

same for all the generators.

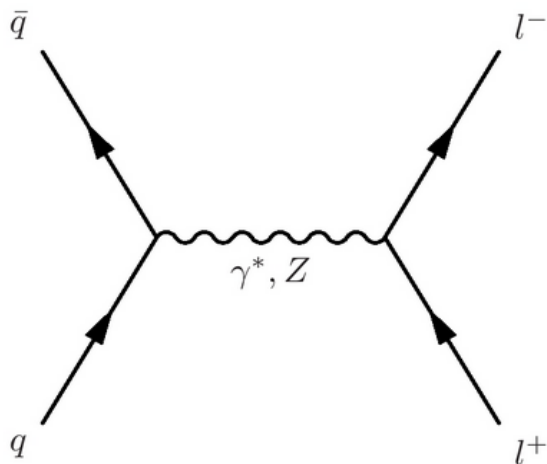


Figure 3.2: Feynman diagram for tree level Drell-Yan process.

3.1.1 PYTHIA

The PYTHIA package is a general-purpose generator which is used quite frequently for generation of events in pp, ee, ep collisions. It is designed to generate events, in as much details as experimentally observable ones, within the bounds of our current understanding of underlying physics. PYTHIA contains the subprocess library and generation machinery, initial and final state showers, underlying events, hadronization, and decay of the unstable particles. It contains a much richer selection, with around 300 different hard processes: $2 \rightarrow 1$ processes, $2 \rightarrow 2$ ones, $2 \rightarrow 3$ ones, *etc.* all at the LO. This aspect is quite important from programming point of view since more particles in the final state means more complicated phase space, hence, the whole generation procedure. PYTHIA is optimized for $2 \rightarrow 1$ and $2 \rightarrow 2$ processes only. The subsequent decay of unstable particles (W^\pm , Z , Higgs, and others) brings up the partonic multiplicity. The spin correlations for many processes is taken into account during the decay. The external processes can be evolved through the parton showering and hadronization. The initial state shower is based on the backward evolution, *i.e.* starting at the hard scattering and moving backward in time to the

CHAPTER 3. EVENT RECONSTRUCTION CHAIN AND DATA SAMPLES

shower initiator whereas, the final state shower is based on the forward evolution.

3.1.2 MADGRAPH

The MADGRAPH package is one of the most widely used automatized matrix element generators. It allows for the generation of additional hard parton radiation. It can be interfaced with general purpose generators such as PYTHIA to perform the showering and hadronization steps. MADGRAPH automatically generates the amplitudes for all the relevant sub-processes and produces the mappings for the integration over the phase space. It is usable both for Standard Model and Beyond Standard Model (BSM) processes.

3.1.3 TAUOLA

The TAUOLA package is an universal interface to various Event Generators (PYTHIA, MADGRAPH, HERWIG) for the processing of decay of τ -leptons, as described in Ref. [53]. The package incorporates a substantial amount of results from high precision τ -lepton measurements. The universal interface of TAUOLA requires a general purpose MC generator, such as PYTHIA-6, to produce stable τ -leptons. The event content, which is provided by the MC generator, is searched through for all stable τ -leptons and neutrinos. It is required, that a flavored pair of particles ($\tau^+\tau^-$ or $\tau\nu_\tau$) originates from the same mother particles. Finally, the decay of the tau-pair is performed by TAUOLA. The TAUOLA package provides not only the correct branching ratios for tau-lepton decays, but also accounts for the polarization of tau-leptons that affect the momentum distribution of corresponding decay products.

3.2 CMS Detector Simulation

Simulated events are of great importance in checking and/or correcting for non-trivial or unforeseen detector or physics effects, as well as comparing detector performance with expectations. With the possible exception of the effects being studied, simulated

3.2. CMS DETECTOR SIMULATION

events should be as close as possible to real data events. Hence, the primary goal of the simulation programme is to model closely the physical interactions involved, the detector performance and the event reconstruction. The CMS full simulation is based on the GEANT4 simulation toolkit [54] which includes a rich set of physics processes describing electromagnetic and hadronic interactions in details.

GEANT4 also provides tools for modeling the full geometry and the interfaces required for retrieving information from particle tracking through the sub-detectors. It also allows the description of the magnetic field. The GEANT4 functionality is interfaced to the core of CMS software through one single module coming with a set of parameters which are configurable at run time. Among them, one of the most relevant is the physics list for the processes to be simulated. Many physics processes have been tested with GEANT4 together with different particle production cuts. An interface for the possible tuning of the GEANT4 objects at simulation time is also implemented. The detailed CMS detector simulation workflow is described as follows:

- A physics group configures an appropriate Monte Carlo event generator to produce the data samples of interest.
- The production team/system runs the generator software to produce generator event data files in High-Energy Physics Monte-Carlo (HepMC) [55] format.
- The physics group validates the generated data samples and selects a configuration for the GEANT4 simulation (detector configuration, physics cuts, *etc.*).
- The production team/system runs the GEANT4-based simulation of CMS, with generator events as input, to produce (using the standard CMS framework) persistent hits in the sensitive detectors.
- The physics group validates this hit data which are then used as input to the subsequent digitization step, allowing for pile-up. This step converts hits into digitizations (also known as “digis”) which correspond to the output of CMS electronics.

The output of the simulation program is used as input for reconstructing the Physics objects (*e.g.* electrons, muons, taus, jets, and photons).

3.3 Reconstruction of Physics Objects

Particle reconstruction is the operation of constructing physics quantities (four-momenta) from the raw data collected in the experiment. In order to perform an analysis, the raw data have to be converted into particle classes, which are referred to as physical objects. The process of reconstruction of these objects uses the information of one or more sub-detectors of the CMS detector to build different classes of particle candidates.

The reconstruction process can be divided into 3 steps, corresponding to local reconstruction within an individual detector module, global reconstruction within a whole detector and combination of these reconstructed objects to produce higher-level objects. The reconstruction units providing local reconstruction in a detector module use as input real data from the DAQ system or simulated data representing the real data. These data in either case are called “digis”. The output from the reconstruction units are “RecHits”, reconstructed hits which are typically position measurements (from times or clusters of strips or pixels) in tracking-type detectors (Muon and Tracker systems) and calorimetric clusters in Calorimeter systems. The RecHits are used as the input to the global reconstruction.

In the global reconstruction step, information from the different modules of a sub-detector are combined. For example, Tracker RecHits are used to produce reconstructed charged particle tracks and Muon RecHits are used to produce candidate muon tracks. The final reconstruction step combines reconstructed objects from individual sub-detectors to produce higher-level reconstructed objects suitable for high-level triggering or for physics analyses. For example, tracks in the Tracker system and tracks in the Muon system are combined to provide final muon candidates while the electron candidates from the Calorimeter system are matched to tracks in the Tracker system. The process of reconstruction and identification of all the objects used in this search: taus, muons, and missing transverse energy, is described in the next Subsections.

3.4 Particle Flow Reconstruction

Taus are the heaviest leptons among the family of leptons, with a mass of $1.77 \text{ GeV}/c^2$ and a lifetime of 2.9×10^{-13} seconds. It is the only lepton with enough mass to decay both leptonically and hadronically. Because of very short lifetime, τ 's decay immediately after being produced, hence, the existence of hadronically decaying taus (τ_h 's) must be inferred from the corresponding signatures of the decay products in the CMS detector. One way of hadronic tau reconstruction uses only calorimeter based energy deposits and tracking information to reconstruct other decay products. More recently, Particle Flow (PF) reconstruction [56] techniques have been used to construct a mutually exclusive collection of reconstructed particles – namely muons, electrons, photons, charged hadrons, and neutral hadrons – which are then used as input for the tau reconstruction algorithms.

The PF reconstruction and identification is performed by combining the information from each sub-detector of the CMS, in the form of charged particle tracks, calorimeter clusters and muon tracks. Because of the much better resolution of the tracking system, momentum and position of charged particles are measured in the tracker rather than the calorimeters. This is true even for particles with $p_T > 100 \text{ GeV}/c$, hence, the tracker sub-detector plays a key role in the particle flow algorithm.

An iterative tracking technique is used to ensure high efficiency of track finding and negligible fake rates at the desired p_T (\sim a few hundred MeV/c). This is accomplished by seeding and reconstructing tracks using stringent criteria so as to achieve a negligible fake rate. The first iteration, however, does not achieve significantly high enough track finding efficiency. Therefore, during subsequent iterations, hits that are unambiguously assigned to the tracks are removed, and less stringent seeding criteria is used. This increases the probability to find a real track, while hardly increasing the probability to reconstruct a track that is a fake track. Only a few iterations are required to achieve a track finding efficiency of $\sim 99.5\%$ for muons and $> 90\%$ for charged hadrons from jets. Finally, in the last few iterations, tracks found in the initial stages of the iterative tracking algorithm are required to satisfy relaxed con-

CHAPTER 3. EVENT RECONSTRUCTION CHAIN AND DATA SAMPLES

straints on the origin of the vertex to allow the reconstruction of secondary charged particles from photon conversions, nuclear interactions in the tracker material, and the decay of long lived particles such as K_S^0 's or Λ 's [56].

After the track reconstruction, the PF algorithm uses a calorimeter clustering algorithm [56] to: (1) detect and measure the energy, direction of stable neutral particles such as photons and neutral hadrons; (2) separate energy deposits due to neutral particles from charged hadrons; (3) reconstruct and identify electrons and all accompanying Bremsstrahlung photons; (4) improve the energy measurement of charged hadrons for which the track parameters were not determined accurately, which more often occurs in cases where the tracks have low quality fit parameters, or high p_T tracks. The calorimeter clustering algorithm is performed separately for ECAL Barrel (EB), ECAL Endcap (EE), HCAL Barrel (HB), and HCAL Endcap (HE). The clustering algorithm is not applied to the forward calorimeter (HF). First, any calorimeter cell with energy above some given energy threshold is identified as a “cluster seed.” Next, neighboring cells with energy values that sit two standard deviations above the noise level, 100 MeV in the barrel and 300 MeV in the endcaps, are combined with the “cluster seeds” to form “topological clusters.” Because charged particles such as electrons will produce both tracks and calorimeter clusters, a linking algorithm must be employed to resolve any ambiguities and remove the double counting from different sub-detectors. To establish their link, a track is extrapolated from its hits in the outer layers of the tracker to (1) the ECAL depth expected from a typical electron shower profile; (2) the HCAL depth expected from a hadron shower profile. A link is established if the extrapolated position is within the cluster boundary. In order to collect Bremsstrahlung energy from electrons, tangents to the tracks at each tracker layer are extrapolated to the ECAL with the requirement that the extrapolated tangents lie within the cluster boundary. Establishing a link between the ECAL and HCAL clusters is achieved by requiring ECAL clusters to be within the HCAL cluster boundaries. Finally, in order to create a link between a track in the inner tracker layers and a track in the muon chambers, a global fit between the two segments of a track is performed and a link is determined if the χ^2 value is within

3.5. HADRONIC TAU RECONSTRUCTION

the acceptable range.

The final stage of the particle flow reconstruction is to construct the mutually exclusive collection of particles from the links between clusters, tracker tracks, and muon tracks. First, a “PF muon” is constructed if the global fit of the tracker and muon tracks results in a combined momentum that is within three standard deviations from the momentum of the track from the inner tracker. If a track passes the criteria for a particle flow muon, the link is removed from consideration. Remaining tracks considered for the reconstruction of charged hadrons are required to have relative p_T uncertainty that is within the calorimetric energy resolution expected for charged hadrons. Neutral hadrons are reconstructed by comparing the momentum of tracks with the energy detected in the clusters linked to tracks. If there is more energy in the linked cluster than accounted for from the linked tracks (considering the resolution of the tracks and calorimeters), neutral hadron candidates and photon candidates are formed.

3.5 Hadronic Tau Reconstruction

3.5.1 Shrinking Cone Algorithm (2010 Data)

The main challenge in the identification of hadronically decaying tau-leptons is their discrimination against generic QCD jets (quarks or gluons) which are produced with a cross-section, several orders of magnitude larger. CMS has developed several algorithms to reconstruct and identify hadronically decaying taus based on particle flow objects. For the analysis with 2010 data, a simple cone based algorithm called “Shrinking Cone” PF tau algorithm (SCPFTau) has been used to reconstruct hadronically decaying taus. The simplicity and robustness of the SCPFTau algorithm makes it ideal for early data analysis.

Hadronically decaying high p_T tau-leptons produce a very collimated jet of one or three charged particles along with neutral pions. This characteristic allows us to differentiate a real tau from the more common QCD jet by defining a narrow region

CHAPTER 3. EVENT RECONSTRUCTION CHAIN AND DATA SAMPLES

around the highest p_T object in the jet (leading pion). This narrow cone around the leading pion is called the signal cone. PF candidates found within the signal cone are associated to the parent tau. In the shrinking cone algorithm, the size of the signal cone depends on the E_T of the tau jet, *i.e.*, $0.07 < \Delta R_\tau^{Signal} = 5.0/E_T < 0.15$, where $\Delta R = \sqrt{(\Delta\eta^2 + \Delta\phi^2)}$ with $\Delta\eta$ and $\Delta\phi$ being the distances in pseudorapidity and azimuthal angle co-ordinates.

In order to enforce the isolation requirement on the reconstructed tau, a second region around the signal cone is defined (isolation cone) with $\Delta R = 0.5$. Any PF candidate with p_T above threshold (usually 1 GeV/c) within the isolation region but outside of the signal region is counted towards the determination of tau isolation. The signal and isolation cones are illustrated in Figure 3.3.

Neutral pions, produced in the decay of the parent tau, decay immediately into a pair of photons. As these photons pass through the tracking material they can interact producing e^+e^- pairs. If these electrons are swept by the magnetic field into the isolation region, the isolation requirement will no longer be satisfied. Some of the efficiency loss due to the γ -conversion can be recovered by expanding the signal region in the ϕ -direction resulting in an elliptical signal cone used to search for PF gamma candidates. Any PF gamma candidate falling within this elliptical cone is not counted towards the calculation of tau ECAL isolation.

The introduction of the elliptical signal cone results in the definition of separate signal region for PF charged hadrons and PF gammas:

- $\Delta R_\tau^{Tracker\ Signal} = 5.0/E_T$
- $R_\phi^{ECAL\ Signal} = 0.15$
- $R_\eta^{ECAL\ Signal} = 0.07$
- $\left(\frac{\Delta\eta^\gamma}{R_\eta^{ECAL\ Signal}}\right)^2 + \left(\frac{\Delta\phi^\gamma}{R_\phi^{ECAL\ Signal}}\right)^2 < 1$
- $\Delta R_\tau^{Isolation} = 0.5$

Candidates that reside in the signal region are used to recalculate the four-momenta of the PF tau. Any associated PF candidates that fall outside the sig-

3.5. HADRONIC TAU RECONSTRUCTION

nal region and within some outer isolation region are labeled as PF tau isolation candidates. Figure 3.4 shows the effect of elliptical isolation on tau-identification.

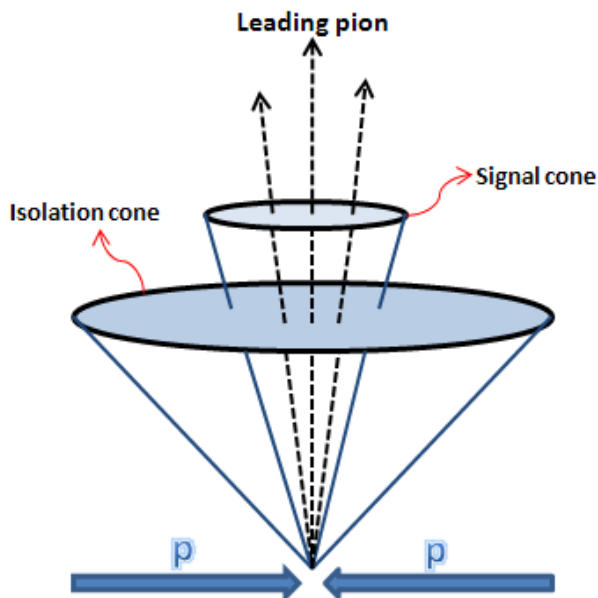


Figure 3.3: The signal and isolation cones in shrinking cone algorithm.

3.5.2 Hadron-Plus-Strip Algorithm (2011 and 2012 Data)

For the analyses with 2011 and 2012 data, we have used the hadronic taus reconstructed using the hadron-plus-strips (HPS) algorithm described in Ref. [57]. The HPS algorithm is the main algorithm which is being used currently in CMS physics analyses with τ 's in the final state. In HPS algorithm, the reconstruction of a τ_h candidate starts from a PF jet, whose four-momentum is reconstructed using the anti- k_T algorithm with a distance parameter $R = 0.5$. Using a PF jet as an initial seed, the algorithm first reconstructs the π^0 components of the τ_h , then combine them with charged hadrons to reconstruct the hadronic tau decay modes and calculate the tau four-momentum and isolation quantities.

In HPS algorithm, a special attention is paid to photon conversions in the CMS tracker material. The bending of electron/positron tracks under the influence of

CHAPTER 3. EVENT RECONSTRUCTION CHAIN AND DATA SAMPLES

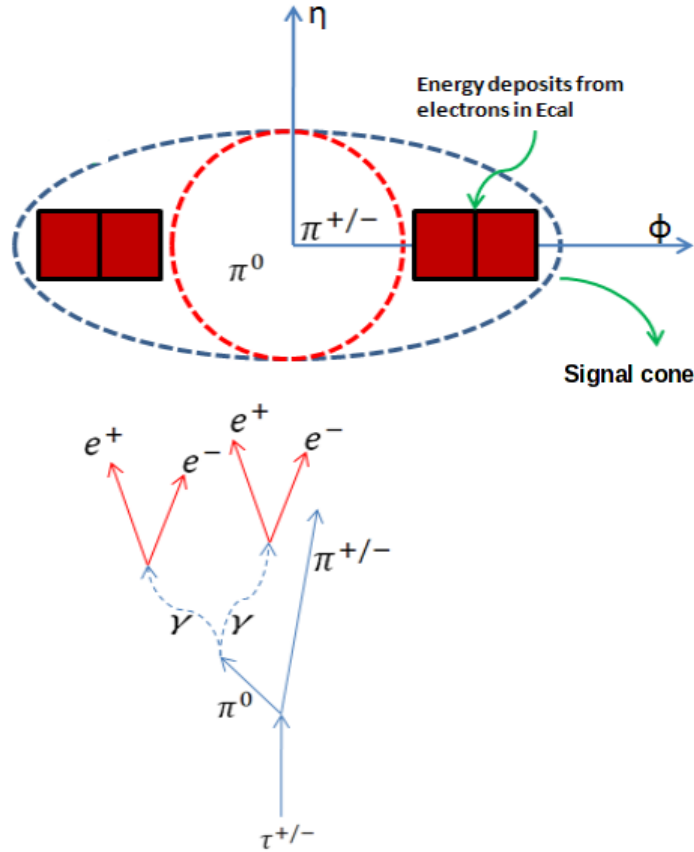


Figure 3.4: Illustration of elliptical isolation. The electron-positron pairs coming from photons originated from the decay of neutral pions can be swept out of the circular signal cone region, hence, they can fall into the isolation cone. By using an elliptical signal cone, a good fraction of tau-leptons can be recovered which would have been lost otherwise.

3.5. HADRONIC TAU RECONSTRUCTION

solenoidal magnetic field of CMS detector broadens the calorimeter signatures of neutral pions in the azimuthal direction. This effect is taken into account in the HPS algorithm by reconstructing photons in “strips”, objects that are built out of electromagnetic particles (PF photons and electrons). The most energetic electromagnetic particle within the PF jet acts as the center of the strip. The algorithm then searches for other electromagnetic particles within a window of size $\Delta\eta = 0.05$ and $\Delta\phi = 0.20$ centered on the strip center. If other electromagnetic particles are found within this window, the most energetic one gets associated with the strip and four-momentum of the strip is recalculated. This procedure is repeated until no further particles are found that can be associated with the strip. The strips satisfying a minimum transverse momentum requirement of $p_T^{strip} > 1 \text{ GeV}/c$ are finally combined with the charged hadrons to reconstruct individual τ_h decay modes.

The decay topologies that are considered by the HPS tau-identification algorithm are:

1. *Single hadron* corresponding to $h^-\nu_\tau$ and $h^-\pi^0\nu_\tau$ decays in which the neutral pions have too little energy to be reconstructed as strips.
2. *One hadron + one strip* reconstructs the decay mode $h^-\pi^0\nu_\tau$ in events in which the photons from π^0 decay are close together on the calorimeter surface.
3. *One hadron + two strips* corresponds to the decay mode $h^-\pi^0\nu_\tau$ in events in which photons from π^0 decays are well separated.
4. *Three hadrons* corresponds to the decay mode $h^-h^+h^-\nu_\tau$. The three charged hadrons are required to come from the same secondary vertex.

There are no separate tau decay topologies for the $h^-\pi^0\pi^0\nu_\tau$ and $h^-h^+h^-\pi^0\nu_\tau$ decay modes. They are reconstructed via the existing topologies. All charged hadrons and strips are required to be contained within a cone of size $\Delta R = (2.8 \text{ GeV}/c)/p_T^{\tau_h}$, where $p_T^{\tau_h}$ is the transverse momentum of the τ_h as reconstructed by HPS algorithm. The four-momentum vector of the reconstructed tau is required to match the (η, ϕ) direction of the original PF jet within a maximum distance of $\Delta R = 0.1$, where $\Delta R = \sqrt{(\Delta\eta)^2 + (\Delta\phi)^2}$.

CHAPTER 3. EVENT RECONSTRUCTION CHAIN AND DATA SAMPLES

The four-momenta of charged hadrons and strips are reconstructed according to the respective τ_h decay topology hypothesis, assuming all charged hadrons to be pions, and are required to be consistent with the masses of the intermediate meson resonances listed in Table 3.1. The invariant mass windows allowed for candidates are: $50 - 200 \text{ MeV}/c^2$ for π^0 , $0.3 - 1.3 \text{ GeV}/c^2$ for ρ , and $0.8 - 1.5 \text{ GeV}/c^2$ for a_1 . In cases where a τ_h decay is consistent with more than one hypothesis, the hypothesis giving the highest $p_T^{\tau_h}$ is chosen.

Finally, isolation is imposed on the reconstructed candidates. The isolation criterion requires that, apart from the τ_h decay products, there should be no charged hadrons or photons present within an isolation cone of size $\Delta R = 0.5$ around the direction of the τ_h . By adjusting the p_T threshold for particles that are considered in the isolation cone, three working points, “loose”, “medium”, and “tight” are defined as shown in Table 3.2. The working points are determined using a simulated sample of QCD dijet events. The “loose” working point corresponds to a probability of approximately 1% of the jets to be misidentified as τ_h . Successive working points reduce the misidentification rate by a factor of two with respect to the previous one.

Decay Mode	Resonance	Mass (MeV/c^2)	Branching fraction (%)
$\tau^- \rightarrow h^- \nu_\tau$			11.6
$\tau^- \rightarrow h^- \pi^0 \nu_\tau$	ρ^-	770	26.0
$\tau^- \rightarrow h^- \pi^0 \pi^0 \nu_\tau$	a_1^-	1200	9.5
$\tau^- \rightarrow h^- h^+ h^- \nu_\tau$	a_1^-	1200	9.8
$\tau^- \rightarrow h^- h^+ h^- \pi^0 \nu_\tau$			4.8

Table 3.1: Branching fractions of the dominant hadronic decays of the τ -lepton, the symbols and masses of the intermediate resonances. The h stands for both ρ and K , but in this analysis the ρ mass is assigned to all charged particles. The table is symmetric under charge conjugation.

3.6. MISSING TRANSVERSE ENERGY

Working point	p_T^{PFchad} threshold (GeV/c)	$p_T^{PF\gamma}$ threshold (GeV/c)
Loose Isolation	1.0	1.5
Medium Isolation	0.8	0.8
Tight Isolation	0.5	0.5

Table 3.2: Definition of different working points of HPS tau isolation.

3.6 Missing Transverse Energy

The CMS detector is able to detect all known particle species (except for neutrinos) produced in pp collisions up to $|\eta| \sim 5$. This feature allows for a fairly precise measurement of the momentum imbalance in the transverse direction relative to the beam direction (missing transverse energy, \vec{E}_T [58]). At CMS, the MET vector, \vec{E}_T , is calculated by using energy depositions in the calorimeters (CaloMET) or by using reconstructed particle momenta obtained by combining information from all the sub-detectors (PFMET). For the search presented in this thesis we have used the PFMET which makes use of the more complex particle flow algorithm to reconstruct the momenta of individual particles as follows:

$$\vec{E}_T = - \sum_i \vec{p}_i \quad (3.1)$$

where the index i runs over all PF candidates.

3.7 Muon Reconstruction

Muon reconstruction is a multistep process that begins with the information gathered from the muon sub-detector. As a first step, standalone muons are reconstructed from hits in the individual drift tube (DT) and cathode strip (CSC) chambers. Hits from the innermost muon stations are combined with hits in the other muon segments using the Kalman filter algorithm. The standalone muon trajectory is reconstructed by extrapolating from the innermost muon station to the outer tracker surface. This standalone trajectory is then used to find a matching track reconstructed in the silicon

CHAPTER 3. EVENT RECONSTRUCTION CHAIN AND DATA SAMPLES

tracker. Finally, standalone muons and matching tracker tracks are used to perform a global fit resulting in a “global” muon. Muon reconstruction is described in more detail in Ref. [59] [60].

Once a muon is required to have matching tracks in the inner and outer detectors, the main source of background consists of charged hadrons that leave a signature in the inner silicon tracker while also penetrating through the hadronic calorimeter and creating hits in the muon chambers. However, unlike muons, charged hadrons, that penetrate the hadronic calorimeter and leave hits in the muon system, will deposit significant energy in the calorimeters. Therefore, muon identification is based on an inside out algorithm that quantifies how well a muon track or global fit is compatible with that of expected for a real muon.

3.8 Monte-Carlo and Collision Data Samples Analyzed

3.8.1 Search for $Z' \rightarrow \tau\tau \rightarrow \tau_h\tau_h$ using 2010 collision data

Collision Data samples used

For the search of $Z' \rightarrow \tau\tau$, the proton-proton collision data at 7 TeV center-of-mass energy, collected using CMS detector during LHC Run 2010 are used. The datasets correspond to an integrated luminosity of $36.1 \pm 1.4 \text{ pb}^{-1}$. The collision data is stored into different blocks with the help of online trigger selection, *e.g.* double-tau triggered data is stored separately from double-electron triggered data. In this analysis, the Double-Tau triggered data has been used which requires atleast two taus in an event above a given p_T threshold at the online selection level. In particular, the primary datasets listed in Table 3.3 have been used in this analysis. These primary datasets correspond to distinct run-periods of the LHC machine.

Monte-Carlo samples used

For comparing the experimental results with the predictions of theory, the signal and the background samples generated by various Monte-Carlo (MC) generators have

3.8. MONTE-CARLO AND COLLISION DATA SAMPLES ANALYZED

Physics Sample	CMS Official Datasets
Run 2010A BTau	<i>/BTau/Run2010A – Nov4ReReco_v1/RECO</i>
Run 2010B BTau	<i>/BTau/Run2010B – Nov4ReReco_v1/RECO</i>
Run 2010A JetMETTau	<i>/JetMETTau/Run2010A – Nov4ReReco_v1/RECO</i>
Run 2010A MinimumBias	<i>/MinimumBias/Run2010A – Nov4ReReco_v1/RECO</i>

Table 3.3: Collision Data Samples for LHC Run 2010.

been used. All the MC samples used in this study are listed in Table 3.4.

- **Signal Monte-Carlo:** Due to the unavailability of CMS official Z' samples, private signal samples for various Z' mass points ranging from 350 GeV/c² to 1000 GeV/c² were generated using PYTHIA.
- **Monte-Carlo samples for background processes:**
 - **DY $\rightarrow \tau^+\tau^-$:** has been generated using TAUOLA package interfaced with parton shower generator PYTHIA-6 having Tune-Z2 for underlying event modeling. A lower cut on the di-lepton invariant mass of the final state particles has been set to 20 GeV/c², *i.e.* CKIN(1) parameter in PYTHIA-6.
 - **DY $\rightarrow e^+e^-$:** has been generated using parton shower generator PYTHIA-6 having Tune-Z2. A lower cut on the di-lepton invariant mass of the final state particles has been set to 20 GeV/c².
 - **W + jets:** samples with W decaying into any lepton flavor and the corresponding neutrino, generated with Tune-Z2 of PYTHIA-6 have been used.
 - **$t\bar{t}$ pair:** samples generated using TAUOLA and parton showered with PYTHIA-6 Tune-Z2 have been used.
 - **QCD multijet:** MC samples for QCD multijet process were generated using PYTHIA-6 having Tune-Z2 for the underlying event modeling. A lower and an upper cut off on the \hat{p}_T of hard interaction *i.e.* (CKIN(3) and CKIN(4) parameter in PYTHIA), has been applied at the generation level to produce the QCD multijet sample in different \hat{p}_T bins. QCD multijet samples gener-

CHAPTER 3. EVENT RECONSTRUCTION CHAIN AND DATA SAMPLES

Physics Sample	CMS Official Datasets
$Z'(500) \rightarrow \tau^+\tau^-$	private production
$Z \rightarrow \tau^+\tau^-$	<code>/DYToTauTau_M-20_TuneZ2_7TeV-pythia6-tauola/Fall10-START38_V12-v1/</code>
$Z \rightarrow e^+e^-$	<code>/DYToEE_M-20_TuneZ2_7TeV-pythia6/Fall10-START38_V12-v1/</code>
$W + jets$	<code>/WJetsToLNu_TuneZ2_7TeV-madgraph-tauola/Fall10-START38_V12-v1/</code>
$t\bar{t}$	<code>/TT_TuneZ2_7TeV-pythia6-tauola/Fall10-START38_V12-v1/</code>
qcd 15 \rightarrow 30	<code>/QCD_Pt_15to30_TuneZ2_7TeV-pythia6/Fall10-START38_V12-v1/</code>
qcd 30 \rightarrow 50	<code>/QCD_Pt_30to50_TuneZ2_7TeV-pythia6/Fall10-START38_V12-v1/</code>
qcd 50 \rightarrow 80	<code>/QCD_Pt_50to80_TuneZ2_7TeV-pythia6/Fall10-START38_V12-v1/</code>
qcd 80 \rightarrow 120	<code>/QCD_Pt_80to120_TuneZ2_7TeV-pythia6/Fall10-START38_V12-v1/</code>
qcd 120 \rightarrow 170	<code>/QCD_Pt_120to170_TuneZ2_7TeV-pythia6/Fall10-START38_V12-v1/</code>
qcd 170 \rightarrow 300	<code>/QCD_Pt_170to300_TuneZ2_7TeV-pythia6/Fall10-START38_V12-v1/</code>
qcd 300 \rightarrow 470	<code>/QCD_Pt_300to470_TuneZ2_7TeV-pythia6/Fall10-START38_V12-v1/</code>

Table 3.4: List of MC samples used. All these samples correspond to *GEN-SIM-RECO* chain.

ated with the generator level transverse momentum \hat{p}_T in the range: 15-30, 30-50, 50-80, 80-120, 120-170, 170-300, and 300-470 GeV/c, were used in this analysis. Note that the MC based QCD multijet background estimation was performed for sensitivity studies only. The final QCD multijet estimation is done in a data-driven way taking rates and shapes directly from the collision data.

3.8.2 Search for $Z' \rightarrow \tau\tau \rightarrow \tau_h\tau_h$ using 2011 collision data

Collision Data samples used

The search for $Z' \rightarrow \tau\tau$ is performed using proton-proton collision data at 7 TeV center-of-mass energy, collected using CMS detector during LHC Run 2011. The datasets correspond to an integrated luminosity of $4.94 \pm 0.11 \text{ fb}^{-1}$. The primary

3.8. MONTE-CARLO AND COLLISION DATA SAMPLES ANALYZED

datasets listed in Table 3.5 are used in this analysis.

Physics Sample	CMS Official Datasets
Run 2011A May10ReReco	/Tau/Run2011A-May10ReReco-v1
Run 2011A PromptReco-v4	/Tau/Run2011A-PromptReco-v4
Run 2011A PromptReco-v5	/Tau/Run2011A-PromptReco-v5
Run 2011A PromptReco-v6	/Tau/Run2011A-PromptReco-v6
Run 2011B PromptReco-v1	/Tau/Run2011B-PromptReco-v1

Table 3.5: Collision Data Samples for LHC Run 2011.

Monte-Carlo samples used

All the background MC samples used in this study are listed in Table 3.6. The signal MC samples used for this study involve Z'_{SSM} and Z'_ψ samples with various mass points ranging from 350–1750 GeV/c² corresponding to cross-sections 7.51–0.0009 pb. All the MC samples correspond to CMS official “Summer11” production.

Physics Sample	CMS Official Datasets	$\sigma(pb)$
$Z \rightarrow \tau^+\tau^-$	/DYToTauTau_M-20_TuneZ2_7TeV-pythia6-tauola/Summer11	1666
$Z \rightarrow e^+e^-$	/DYToEE_M-20_TuneZ2_7TeV-pythia6/Summer11	1666
$W + jets$	/WJetsToLNu_TuneZ2_7TeV-madgraph-tauola/Summer11	31314
$t\bar{t}$	/TT_TuneZ2_7TeV-pythia6-tauola/Summer11	165
QCD	Data-driven	—

Table 3.6: List of MC samples used. Note that the QCD multijet background is extracted directly from the collision data.

CHAPTER 3. EVENT RECONSTRUCTION CHAIN AND DATA SAMPLES

3.8.3 Search for $Z' \rightarrow \tau\tau \rightarrow \tau_\mu\tau_h$ using 2012 collision data

Collision Data samples used

The search for $Z' \rightarrow \tau\tau$ is performed in $Z' \rightarrow \tau\tau \rightarrow \tau_\mu\tau_h$ final state using proton-proton collision data at 8 TeV center-of-mass energy, collected using CMS detector during LHC Run 2012. The datasets correspond to an integrated luminosity of $5.10 \pm 0.22 \text{ fb}^{-1}$. The primary datasets used for this study are listed in Table 3.7.

Physics Sample	CMS Official Datasets
Run 2012A PromptReco-v1	/SingleMu/Run2012A-PromptReco-v1/RECO
Run 2012B PromptReco-v1	/SingleMu/Run2012B-PromptReco-v1/RECO

Table 3.7: Collision Data Samples for LHC Run 2012.

Monte-Carlo samples used

All the background MC samples used in this study are listed in Table 3.8. The signal MC samples used for this study involve Z'_{SSM} and Z'_ψ samples with various mass points ranging from 500–2000 GeV/ c^2 corresponding to cross-sections 2.505–0.0027 pb. All the MC samples are taken from CMS official “Summer12” production.

Physics Sample	CMS Official Datasets	$\sigma(pb)$
$Z \rightarrow \tau\tau$	/DYToTauTau_M-20_TuneZ2star_8TeV-pythia6-tauola/Summer12	1915.083
$Z \rightarrow \mu\mu$	/DYToMuMu_M-20_TuneZ2star_8TeV-pythia6/Summer12	1915.083
$W + jets$	/WJetsToLNu_TuneZ2star_8TeV-madgraph-tarball/Summer12	36257.2
$t\bar{t}$	/TTJets_TuneZ2star_8TeV-madgraph-tauola/Summer12	225.197
QCD	Data-driven	—

Table 3.8: List of MC samples used. Note that the QCD background is extracted directly from the collision data.

In this Chapter, a brief description of the general steps involved in the physics

3.8. MONTE-CARLO AND COLLISION DATA SAMPLES ANALYZED

analysis are discussed. Starting with the MC event generators, a short description of the detector simulation is given. The reconstruction of the Physics objects: muons, hadronically decaying tau-leptons, and missing transverse energy *i.e.* all the Physics objects used in the present work, have been discussed in details. A brief description of various MC event generators *i.e.* PYTHIA, MADGRAPH, and TAUOLA, used in this search is also given.

Search for $Z' \rightarrow \tau\tau$ using LHC collision data of Run 2010 collected with CMS detector

4.1 Introduction

The Standard Model of Particle Physics is able to explain most of the physics processes which have been verified experimentally. Still there are some assumptions that need experimental verifications. In view of that, various extensions of the Standard Model (SM) have been formulated. There exists some extensions of the SM which predict the existence of additional heavy gauge bosons, Z' [16] [17] [61]. Although most models with extra gauge bosons obey the universality of the couplings, some models include generational dependent couplings resulting in a Z' gauge boson that decays preferentially to a pair of tau-leptons [62]. One can conceive, at the simplest level, a $U(1)$ extension of the SM in which the Z' gauge boson has same interactions as the Standard Model Z boson. Such an extension is commonly known as Sequential Standard Model (SSM) where the mass of this new heavy gauge boson is the only unknown parameter. Although it is more probable to discover a Z' gauge boson in its leptonic decay modes ($Z' \rightarrow \mu^+\mu^-$, $Z' \rightarrow e^+e^-$) due to reduced backgrounds, still,

CHAPTER 4. SEARCH FOR $Z' \rightarrow \tau\tau$ USING LHC COLLISION DATA OF RUN 2010 COLLECTED WITH CMS DETECTOR

Final State	Branching Ratio (%)
$\tau^+\tau^- \rightarrow \mu^+\mu^-\nu_\tau\bar{\nu}_\tau\nu_\mu\bar{\nu}_\mu$	3.1
$\tau^+\tau^- \rightarrow e^+e^-\nu_\tau\bar{\nu}_\tau\nu_e\bar{\nu}_e$	3.1
$\tau^+\tau^- \rightarrow e^\pm\mu^\mp\nu_\tau\bar{\nu}_\tau\nu_e(\bar{\nu}_e)\bar{\nu}_\mu(\nu_\mu)$	6.2
$\tau^+\tau^- \rightarrow he^\pm\nu_\tau\bar{\nu}_\tau\nu_e(\bar{\nu}_e)$	23.1
$\tau^+\tau^- \rightarrow h\mu^\pm\nu_\tau\bar{\nu}_\tau\nu_\mu(\bar{\nu}_\mu)$	22.5
$\tau^+\tau^- \rightarrow hh\nu_\tau\bar{\nu}_\tau$	42.0

Table 4.1: Branching Ratios of $\tau^+\tau^-$ decay modes.

it is critical to probe the $Z' \rightarrow \tau^+\tau^-$ final states in order to measure the couplings relative to $Z' \rightarrow l^+l^-$ ($l = \mu, e$) final states and also to test the universality of the coupling constants.

In this Chapter, the search for a $Z' \rightarrow \tau\tau$ in the proton-proton collisions at 7 TeV center-of-mass energy is reported using $36.1 \pm 1.4 \text{ pb}^{-1}$ of the LHC data, collected with the CMS detector in Year 2010. Since a tau-lepton can decay into $e\bar{\nu}_e\nu_\tau$ (17.8%), $\mu\bar{\nu}_\mu\nu_\tau$ (17.4%), and hadrons+ ν_τ (64.8%), there are six possible final states for a pair of tau-leptons: (1) $\tau_\mu\tau_\mu$, (2) $\tau_e\tau_e$, (3) $\tau_e\tau_\mu$, (4) $\tau_e\tau_h$, (5) $\tau_\mu\tau_h$, and (6) $\tau_h\tau_h$, where τ_e , τ_μ , and τ_h refer to $e\bar{\nu}_e\nu_\tau$, $\mu\bar{\nu}_\mu\nu_\tau$, and hadronically decaying tau-lepton, respectively. The six possible decay modes of $Z' \rightarrow \tau\tau$ along with their branching ratios are listed in Table 4.1. The combined search for a $Z' \rightarrow \tau\tau$ involves four decay modes, *viz.*, $Z' \rightarrow \tau\tau \rightarrow \tau_\mu\tau_h$, $Z' \rightarrow \tau\tau \rightarrow \tau_e\tau_h$, $Z' \rightarrow \tau\tau \rightarrow \tau_e\tau_\mu$, and $Z' \rightarrow \tau\tau \rightarrow \tau_h\tau_h$. Because of their small branching ratios and copious Drell-Yan $Z/\gamma^* \rightarrow e^+e^-$, $\mu^+\mu^-$ production, the $\tau_e\tau_e$ and $\tau_\mu\tau_\mu$ modes are not considered in this search. Furthermore, it will be difficult to distinguish the $\tau_e\tau_e$ and $\tau_\mu\tau_\mu$ final states from the direct production of $e^+e^-/\mu^+\mu^-$ from new resonances of similar mass. The $Z' \rightarrow \tau\tau \rightarrow \tau_e\tau_\mu$ final state has the smallest branching fraction but it provides the lowest possible background contamination due to the lower jet \rightarrow lepton fake rate (jet \rightarrow electron fake rate is $\sim 10^{-2}$ and jet $\rightarrow \mu$ fake rate is $\sim 10^{-4}$ – 10^{-3}).

In this Chapter, the studies on the search for $Z' \rightarrow \tau\tau$ in the fully hadronic

4.2. SIGNAL AND POTENTIAL BACKGROUNDS

mode is presented. In order to ensure the robustness of the selection cuts, analysis relies on the collision data itself, whenever possible, to understand and validate the reconstruction efficiency and estimation of various backgrounds. By making minimal changes to the signal selection criteria, some control regions are defined where each background has high purity. Once a background enriched control region is created, selection efficiencies are measured in those regions which are then used to extrapolate to the region where signals of new massive resonances are expected. When a complete data-driven estimation is not possible the analysis makes use of the scale-factors *i.e.* the ratio between data events and expected Monte Carlo (MC) events in these control regions to estimate the background contribution in the signal region. The quantification of the significance of any possible excess or setting of upper limits on the $Z' \rightarrow \tau\tau$ production rate is done by fitting the invariant mass distribution of the reconstructed τ -pair. A Bayesian technique is then applied to interpret the results in terms of the upper 95% confidence level limits.

4.2 Signal and Potential Backgrounds

4.2.1 Signal Process: $pp \rightarrow Z' + X; Z' \rightarrow \tau\tau \rightarrow \tau_h\tau_h$

As discussed above, various extensions of the SM provide the possibility of new heavy gauge bosons, Z' . Out of these extensions, a simplest extension involving an additional $U(1)$ gauge field is called Sequential Standard Model (SSM), where the Z' has same interactions as that of a Standard Model Z boson. The tree level Feynman diagram for the production of a Sequential Standard Model Z' gauge boson, decaying into a tau-pair as shown in the Figure 4.1. In order to calculate the cross-section one can use same couplings to τ 's as that of a Standard Model Z boson. The theoretically predicted values of cross-section as a function of the SSM Z' mass are given in the Table 4.2 and also depicted in Figure 4.2. All the signal samples and MC samples for possible backgrounds are listed in Section 3.8.1.

CHAPTER 4. SEARCH FOR $Z' \rightarrow \tau\tau$ USING LHC COLLISION DATA OF RUN 2010 COLLECTED WITH CMS DETECTOR

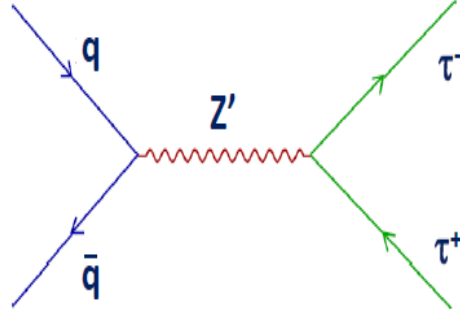


Figure 4.1: Production of a SSM Z' gauge boson and its subsequent decay to a pair of tau-leptons.

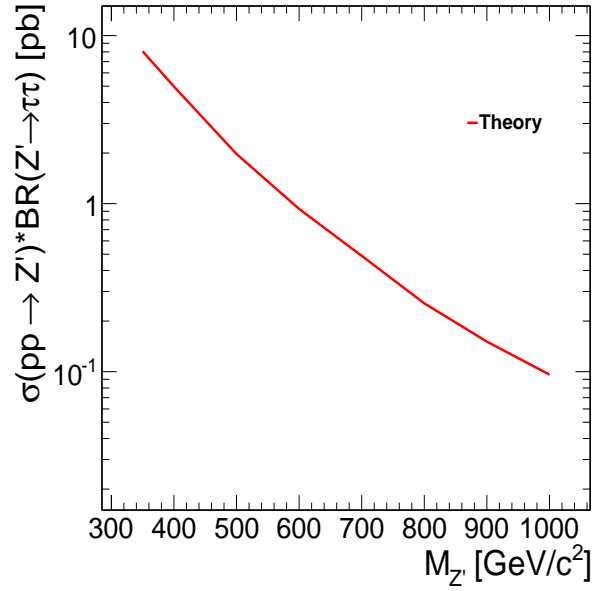


Figure 4.2: Product of theoretical cross-section for a SSM Z' times the branching ratio to a pair of tau-leptons as a function of Z' mass.

4.2. SIGNAL AND POTENTIAL BACKGROUNDS

$M_{Z'} \text{ (GeV/c}^2\text{)}$	$\sigma(pp \rightarrow Z') \times \text{BR}(Z' \rightarrow \tau\tau) \text{ (pb)}$
350	8.061
400	4.980
500	1.974
600	0.930
700	0.489
800	0.255
900	0.151
1000	0.096

Table 4.2: SSM Z' cross-section times the branching ratios to $\tau\tau$ for various mass points.

4.2.2 Background Processes

Various processes which can mimic the signal process are considered as background processes and are described below:

- QCD multijet background:** One of the main experimental challenges at the hadron colliders is the identification and discrimination of hadronically decaying tau-leptons from the detector signatures of quarks or gluons that produce hadrons. The two seemingly different particles can produce similar physics signatures in the CMS detector. The probability of a quark/gluon jet to be misidentified as a tau-jet is known as jet-to-tau fake rate. The production rate of this type of events is several orders of magnitude larger than the signatures of *New Physics* processes beyond the standard model (BSM) such as sequential Z' production. When two partons from incoming protons interact, they often produce pairs of quarks and gluons traversing in the opposite direction (seen in the center-of-mass frame of reference). However, because of the confinement property (quarks and gluons cannot stay in free state) of the strong force, a process known as *hadronization* causes the color field of these seemingly free partons to

CHAPTER 4. SEARCH FOR $Z' \rightarrow \tau\tau$ USING LHC COLLISION DATA OF RUN 2010 COLLECTED WITH CMS DETECTOR

break into two through the creation of quark-antiquark pairs. Since the strength of the strong force is directly proportional to the distance between these partons, as the partons move away from each other this color field becomes strong enough to produce additional quark-antiquark pairs. This process of hadronization can be understood in analogy to an elastic rubber band that is being pulled apart from the two ends until it breaks into two bands. The ends represent quarks, while the band itself represents the gluon field.

This process of hadronization will continue till the energy of gluon field is sufficient to produce new quark-antiquark pairs. Once the energy of the gluon field is insufficient to produce further new particles, the remaining quarks and antiquarks will combine to form bound states of quarks known as Hadrons. This process of hadronization is shown in Figure 4.3. Hence, the end step of this process is the collimated sprays of hadrons, generally referred to as *hadronic jets*, or QCD jets. Since these hadronic jets are produced from the bounded states produced by quark-antiquark pairs, they usually contain most common hadrons, *pions*. Since a τ -lepton can decay into final states containing mostly one or three charged pions and a few neutral pions, hence, they resemble QCD jets quite well. Hadronic jets are produced at high rates at the LHC. For example, the typical QCD dijet production has a cross-section approximately 10^6 larger than the rates of sequential Z' production. The QCD multijet serves as the most dominant background for this final state.

- **$Z \rightarrow \tau\tau$ background:** The Drell-Yan (DY) processes $pp \rightarrow Z/\gamma^* \rightarrow \tau^+\tau^-$ are one of the promising dominant τ -pair production mechanisms at the LHC. Since the τ 's in the pair can undergo hadronic decay, the DY processes can very well mimic the final state of new massive resonances decaying into τ -lepton pairs. Since it is difficult to obtain a clean sample of high energy τ -leptons, one of the basic concerns of this analysis is to verify whether the τ_h identification criteria still remains valid for the particular energy regime. The above concern is equally valid for any analysis dealing with high p_T jets or leptons. In this analysis, this concern is addressed by verifying following: (1) whether the τ_h identification

criteria works well at low- p_T ($p_T < 100$ GeV/ c) and is consistent with the MC expectations by using data-driven techniques to obtain a clean sample of $Z \rightarrow \tau\tau$ events, (2) τ_h identification criteria is well understood in MC simulated samples, and (3) using τ_h identification criteria it is highly unlikely to cause any difference between MC and data. In this way, being a background, this process plays a key role in the validation of final selection criteria and the identification of τ -leptons. A typical Feynman diagram for $Z \rightarrow \tau\tau$ process is given in the Figure 4.4.

- **$Z \rightarrow ee$ background:** This process can mimic the signal process when both electrons are misidentified as tau-leptons. A typical Feynman diagram of $pp \rightarrow Z + X; Z \rightarrow ee$ is given in the Figure 4.5.
- **$W + jets$ background:** W boson produced in association with jets ($W + jets$) can mimic the signal process when there is a lepton (e/μ) from W decay which is misidentified as a hadronic tau or a real hadronic tau from W decay and the jet fakes the other hadronic tau. The contamination from $W + n jets$ events in the signal region is highly dependent on the $jet \rightarrow \tau_h$ fake rate. Feynman diagram for $W + jets$ production is shown in the Figure 4.6.
- **$t\bar{t}$ background:** The top (t) quark decays primarily into a bottom quark (b) plus a W^+ boson and similarly, anti-top (\bar{t}) decays into an anti-bottom quark (\bar{b}) plus a W^- boson. This process can mimic the signal process when there is a lepton (e/μ) from W decay which is misidentified as a hadronic tau or a real hadronic tau from W decay. The presence of additional b-jets in the events makes it easier to suppress this background by applying veto on the b-jets and some topology specific selections. Feynman diagram for $t\bar{t}$ production is shown in the Figure 4.7.

4.3 Event Selection

Before applying the actual signal event selection criteria, the events are pre-selected based on some loose selection criteria (skimming) as described in the next Subsection.

CHAPTER 4. SEARCH FOR $Z' \rightarrow \tau\tau$ USING LHC COLLISION DATA OF RUN 2010 COLLECTED WITH CMS DETECTOR

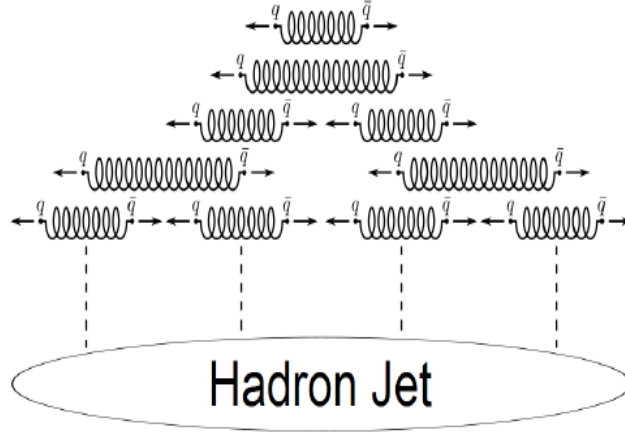


Figure 4.3: Illustration of jet hadronization process.

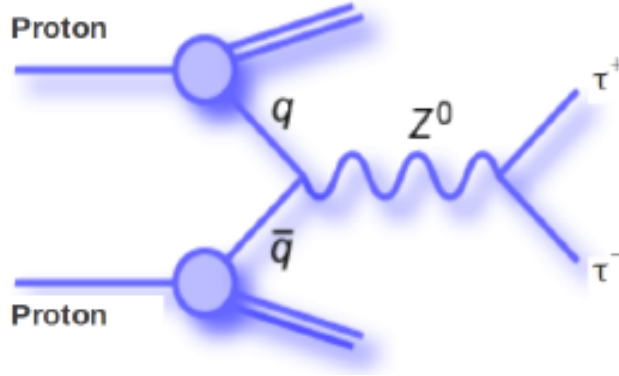


Figure 4.4: Feynman diagram for the $pp \rightarrow Z + X; Z \rightarrow \tau^+\tau^-$ production.

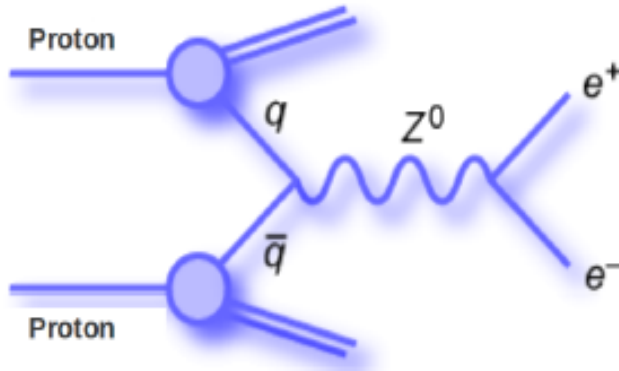


Figure 4.5: Feynman diagram for the $pp \rightarrow Z + X; Z \rightarrow e^+e^-$ production.

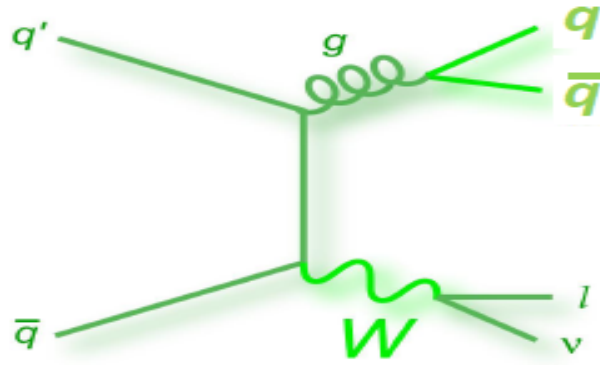


Figure 4.6: Feynman diagram for Standard Model $W + jets$ production.

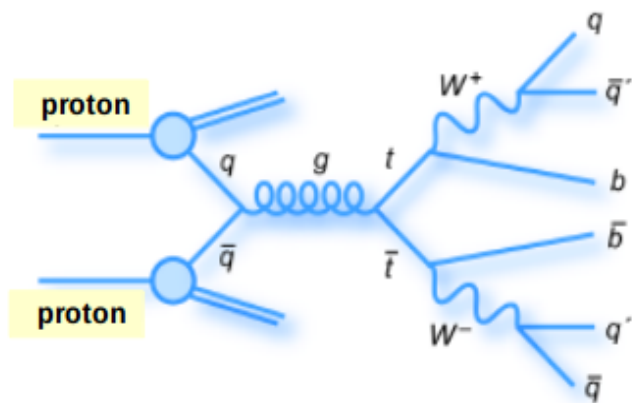


Figure 4.7: Feynman diagram for Standard Model $t\bar{t}$ production.

CHAPTER 4. SEARCH FOR $Z' \rightarrow \tau\tau$ USING LHC COLLISION DATA OF RUN 2010 COLLECTED WITH CMS DETECTOR

4.3.1 Skimming Criteria

- Event should have ≥ 1 τ -lepton per leg containing a leading pion with $p_T > 5$ GeV/c.
- Event should have ≥ 1 τ -pair with $\Delta R > 0.7$, where $\Delta R = \sqrt{\Delta\eta^2 + \Delta\phi^2}$ with $\Delta\eta$ and $\Delta\phi$ being distances in pseudorapidity and azimuthal angle between the two taus. The choice of this ΔR requirement is based on the jet reconstruction algorithm from which hadronic taus are reconstructed.

The triggers are not applied at the skim level for MC samples since it may cause differences between MC and the collision data. Table 4.3 shows the MC skim efficiencies for signal and various background processes.

Sample	$\sigma \times$ Filter Efficiency (pb)	Events processed	Final N events	ϵ^{Skim}
$Z'(500) \rightarrow \tau\tau$	1.94	19000	19000	1.0
$Z \rightarrow \tau\tau$	1653	2057446	523610	0.254
$W + jets$	29349	15123740	1905577	0.126
qcd $0 \rightarrow 5$	4.844e+10	549809	191	0.000347
qcd $5 \rightarrow 15$	3.675e+10	1648096	1114	0.000676
qcd $15 \rightarrow 30$	8.159e+08	5454640	189292	0.0347
qcd $30 \rightarrow 50$	5.312e+07	3264660	767803	0.235
qcd $50 \rightarrow 80$	6.359e+06	3191546	1731944	0.543
qcd $80 \rightarrow 120$	7.843e+05	3208299	2482437	0.774
qcd $120 \rightarrow 170$	1.151e+05	3045200	2706267	0.889
qcd $170 \rightarrow 300$	2.426e+0	3220080	3056213	0.949
$t\bar{t}$	149.6	1099550	1072196	0.975

Table 4.3: Table shows the skimming efficiencies for various MC samples.

4.3.2 Signal Selections

As discussed in the previous Sections, the main background for fully hadronic tau final state is the QCD multijet production. Therefore, the selections are chosen to hammer down the QCD multijet background maximally. The analysis selections are based on the detector signatures of the final state tau-leptons and topology of the signal events. The hadronically decaying taus/tau-jets have typical collimated signatures inside the calorimeter while QCD jets are spread up, hence, tight isolation requirement on tau-leptons ensures significant reduction of QCD multijet background. The QCD jets have high multiplicity of particles while the tau-jets mostly consist of one or three charged particles along with some neutral particles. Hence, the requirement on the multiplicity of jets provides another good tool to suppress the QCD multijet background further. The signal selection criteria is divided into three categories: kinematic and geometric acceptance, tau-lepton identification, and topological selections. It should be noted that the surviving pairs of tau candidates are preserved at each intermediate stage in the selections. If an event has more than one pair of unique tau candidates passing all the selections, the one with highest invariant mass is selected. This requirement is imposed just to ensure that a single tau pair candidate (passing all the selections) per event gets selected. An explicit check on this requirement was made and this requirement was found to be 100% efficient. The full list of online and offline selection cuts is given below:

- **Online Event Selection**

Since $Z \rightarrow \tau\tau$ events serve both as a background and an important tool to validate the tau-identification selections, hence, un-prescaled double tau triggers having lowest p_T thresholds have been used to select the interesting events from the collision data. During data taking, various triggers have to be prescaled with increasing instantaneous luminosity in order to cope with the total bandwidth for recording of the events. For collision data, events are required to pass the un-prescaled double tau triggers with the minimum threshold on the transverse momentum of the tau candidates. The combination of various double-tau trig-

CHAPTER 4. SEARCH FOR $Z' \rightarrow \tau\tau$ USING LHC COLLISION DATA OF RUN 2010 COLLECTED WITH CMS DETECTOR

Details of HLT Trigger Paths			
Trigger path	HLT Thresholds	Run range	Data ($\int \mathcal{L} dt \text{ pb}^{-1}$)
HLT_DoubleLooseIsoTau15	$p_T > 15 \text{ GeV}/c, \eta < 5.0$	136035-144114	3.16
HLT_DoubleLooseIsoTau15_Trk5	$p_T > 15 \text{ GeV}/c, \eta < 5.0$	146428-149294	32.64

Table 4.4: Summary of the trigger paths according to the run range applied on data.

gers *i.e.* HLT_DoubleLooseIsoTau15 and HLT_DoubleLooseIsoTau15_Trk5 have been used depending on run range as summarized in Table 4.4.

• Offline Event Selection

For the identification and reconstruction of the hadronically decaying tau-leptons, a simple Shrinking Cone algorithm has been used. The details on this algorithm are given in the Subsection 3.5.1 of Chapter 3. The various categories of the offline selection criteria are:

– Acceptance:

- * Event should have at least one Particle Flow (PF) τ per leg with $|\eta| < 2.1$, $p_T > 20 \text{ GeV}/c$ and leading track with $p_T > 5 \text{ GeV}/c$.

- τ_h Identification: The hadronically decaying τ -leptons can be reconstructed from fake electrons as well as from fake muons, hence, typical vetos have to be applied to reject electrons and muons faking hadronically decaying tau-leptons.

- * **Rejection of muons faking τ_h 's:** Since the muons can fake hadronically decaying tau-leptons, so muon rejection helps in removing the muons which are misidentified as hadronically decaying tau-leptons. To reject the muons faking hadronic tau-leptons, the tau seed track is required to have compatible hits or energy deposits expected for a pion:

- $\mu \text{ veto} = a \cdot \text{Calo-Compatibility} + b \cdot \text{Segment-Compatibility} < 1$

Here the Calo-Compatibility is quantified by taking the muon trajectory and searching for energy deposits compatible with a minimum ionizing particle in the calorimeter and Segment-Compatibility is quantified by

4.3. EVENT SELECTION

extrapolating the tracker track outward and searching for compatible muon hits and segments in the muon sub-detector. The following values of coefficients (recommended by the muon POG) have been used: $a = 0.8$, $b = 1.2$.

- * **Rejection of electrons faking τ_h 's:** The electrons can also fake hadronically decaying tau-leptons, so electron rejection is imposed to remove the electrons which are misidentified as hadronically decaying tau-leptons. The following condition is required for electron rejection:

The number of tracker hits of the leading track ≥ 12 and $H_{3 \times 3}/p_{Lead} > 0.03$, where $H_{3 \times 3}/p_{Lead}$ is the ratio of energy deposited in the HCAL 3×3 clusters in $\Delta R < 0.184$ around ECAL impact point of the leading track and the leading track momentum.

- * **Fake tau rejection:** The hadronic taus produce narrow pencil like calorimetric signatures, so the rejection of fake taus is performed by requiring the tau-leptons to be isolated by demanding that there should be no track with $p_T > 1.0 \text{ GeV}/c$ and no gamma with $p_T > 1.5 \text{ GeV}/c$ inside the isolation annulus between the signal cone and isolation cone. Technically, this requirement translates as (elliptical isolation): $\sum p_T^{chad} < 1.0 \text{ GeV}/c$ and $\sum p_T^{gammas} < 1.0 \text{ GeV}/c$ with $p_T^{chad} > 1 \text{ GeV}/c$, $p_T^{gammas} > 1.5 \text{ GeV}/c$.

Here the $\Delta R_{iso} = 0.5$, $\Delta R_{signal} = 5/E_T$, $R_\eta = 0.07$, $R_\phi = 0.15$.

- * **Single prong requirement:** About 70% of τ_h 's decay into one charged pion (π^\pm) accompanied by some neutral pions (π^0 's), about 25% of the rest decay into three charged pions along with some neutral pions. As explained earlier the multiplicity of jets provide a good way of suppressing the QCD multijet background. Hence, both tau-jets are required to have exactly one charged hadron with $p_T^{chad} > 1 \text{ GeV}/c$ and $\Delta R_{sig} = 5/E_T$, where E_T is the transverse energy of the jet. The last two requirements are very effective against QCD multijet background as explained in the previous Section.

CHAPTER 4. SEARCH FOR $Z' \rightarrow \tau\tau$ USING LHC COLLISION DATA OF RUN 2010 COLLECTED WITH CMS DETECTOR

– Topological requirements:

τ -pairs passing the acceptance and τ_h identification criteria described above are also required to pass these topology-specific selections to reduce the contamination from QCD multijet, $t\bar{t}$, $Z \rightarrow ee$, and $W + jets$ backgrounds:

- * **Opposite sign charge requirement:** The tau-leptons forming the pair should have opposite sign charges (determined from the sign of leading charged hadrons) *i.e.* $Q(\tau_1) = -Q(\tau_2)$. Due to the electric charge neutrality of Z' gauge boson, the pair of tau-leptons coming from Z' decay should have opposite charge. This requirement also provides a good handle over QCD multijet background.
- * **Strong antiparallelism:** Since a Z' gauge boson is supposed to be quite heavy, hence, the tau-leptons coming from its decay are expected to be almost back-to-back. So, the tau-leptons in the pair are required to be nearly back-to-back by imposing the condition:
 - $-1.0 \leq \cos(\Delta\phi(\tau_1, \tau_2)) \leq -0.95$.
- * **Missing transverse energy requirement (\cancel{E}_T):** Due to the presence of two neutrinos in the fully hadronic tau final state ($Z' \rightarrow \tau\tau \rightarrow hh'\nu_\tau\bar{\nu}_\tau$, where $h, h' = \text{hadrons}$), a fair amount of missing transverse energy is expected in the signal events. The signal-like events are required to have missing transverse energy (\cancel{E}_T) > 30 GeV. This threshold is chosen in such a way to provide the best background suppression while preserving the best fraction of $Z \rightarrow \tau\tau$ events in order to validate the tau-identification criteria.
- * **ζ cut:** For final states involving a pair of tau-leptons, the \cancel{E}_T in the event is expected to be in the direction collinear to the visible tau decay products. Moreover, the measurement of \cancel{E}_T is entirely correlated to the visible tau decay products. In $W + jets$ events, the direction and magnitude of this momentum imbalance is completely correlated to the lepton from W boson decay, but uncorrelated to the jet. The events are required to be consistent with the signature of a particle decaying into a

4.3. EVENT SELECTION

pair of tau-leptons by defining a unit vector along the bisector of visible tau decay products ($\hat{\zeta}$) and two projection variables P_ζ and P_ζ^{vis} :

$$P_\zeta^{vis} = (\vec{P}_\zeta^{vis})_{\tau_1} \cdot \hat{\zeta} + (\vec{P}_\zeta^{vis})_{\tau_2} \cdot \hat{\zeta}, \quad (4.1)$$

$$P_\zeta = P_\zeta^{vis} + \vec{E}_T \cdot \hat{\zeta} \quad (4.2)$$

The P_ζ cut is illustrated in Figure 4.8. The separation between $Z' \rightarrow \tau\tau$ and $W + jets$ events in $P_\zeta^{vis}-P_\zeta$ plane is shown by Figures 4.9 and 4.10. There is a strong correlation between P_ζ^{vis} and P_ζ for $Z' \rightarrow \tau\tau$ events while there is no such strong correlation between P_ζ^{vis} and P_ζ for $W + jets$ events due to the presence of a jet which is uncorrelated to the τ and ν_τ from the W boson decay. Therefore, one can use this fact to suppress backgrounds by defining a “ ζ ” cut as the linear combination of P_ζ and P_ζ^{vis} :

- $P_\zeta - 0.875 \times P_\zeta^{vis} > -7$.

This requirement is vital to suppress the contribution of $W + jets$ and $t\bar{t}$ backgrounds.

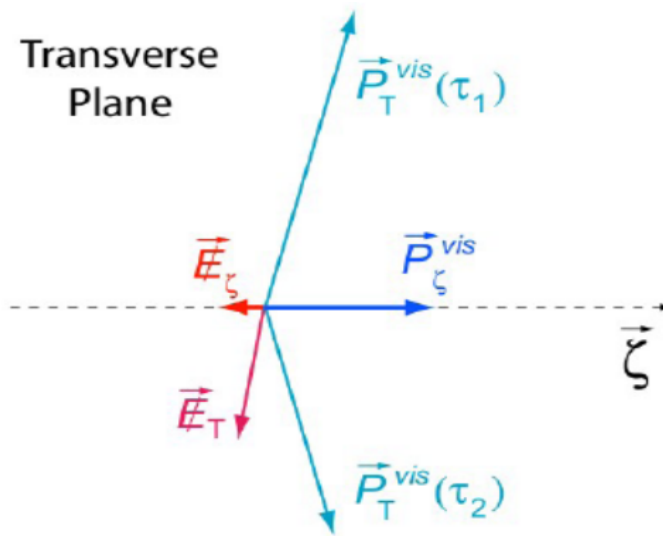


Figure 4.8: Illustration of P_ζ^{vis} and P_ζ .

CHAPTER 4. SEARCH FOR $Z' \rightarrow \tau\tau$ USING LHC COLLISION DATA OF RUN 2010 COLLECTED WITH CMS DETECTOR

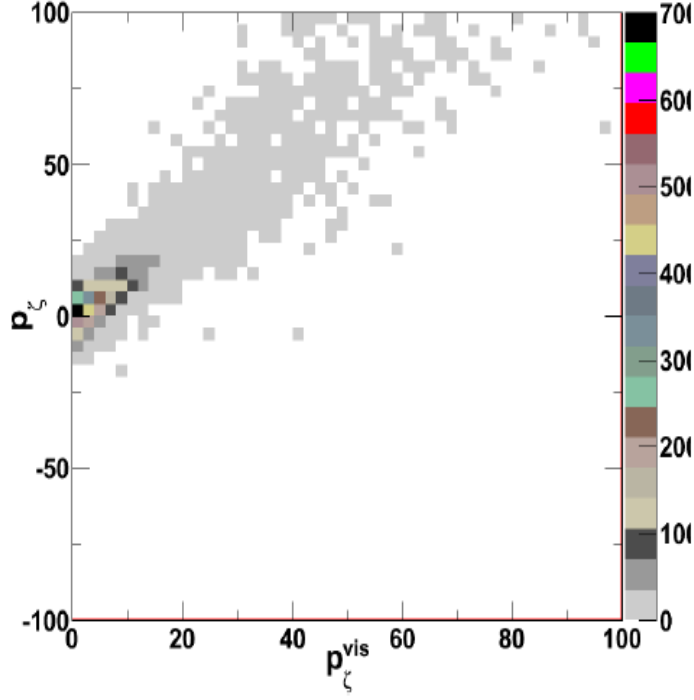


Figure 4.9: Distribution of P_ζ vs. P_ζ^{vis} for MC based $Z' \rightarrow \tau\tau$ events.

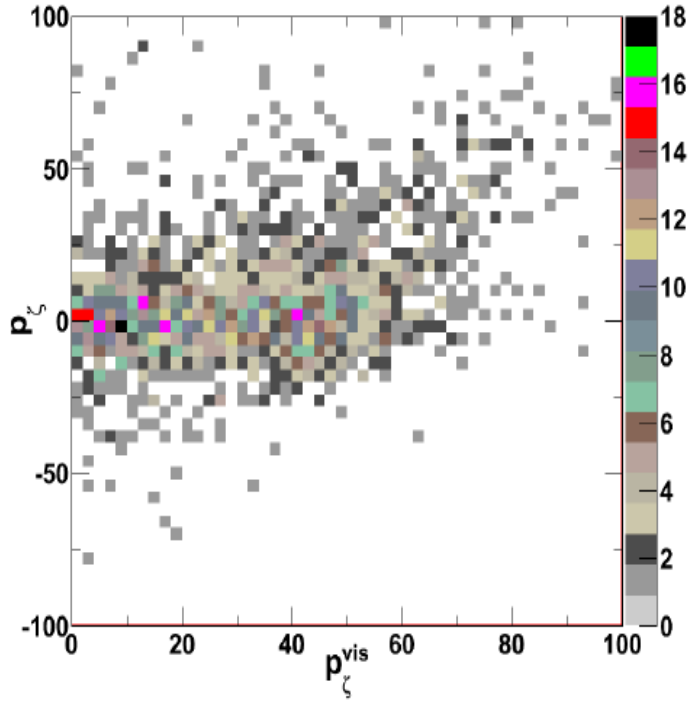


Figure 4.10: Distribution of P_ζ vs. P_ζ^{vis} for $W + jets$ events.

4.4. ESTIMATION OF SELECTION EFFICIENCIES USING MONTE-CARLO CUT-BASED METHOD

4.4 Estimation of Selection Efficiencies using Monte-Carlo Cut-based Method

Tables 4.5 and 4.6 show the relative efficiencies of various selections for signal and the relevant SM background processes. The relative efficiencies are defined with respect to the number of events passing previous selections as described below:

$$\epsilon_{rel} = \frac{\text{Number of events passing (i+1)}^{th} \text{ cut}}{\text{Number of events passing i}^{th} \text{ cut}} \quad (4.3)$$

4.5 Hadronic Tau Trigger Algorithm

The selections used to trigger on hadronic tau candidates are distributed among the levels of the trigger matching capabilities of the global CMS trigger infrastructure. The Level-1 (L1) of hadronic tau trigger algorithm is largely based on the generic jet trigger and is an integral part of the full Level-1 jet collection. The Level-1 trigger, on the basis of calorimetry data alone (ECAL and HCAL), selects the tau candidate events from jets with $|\eta| \leq 3$. Isolation criteria is imposed by requiring the jet's energy to be contained within two square regions of the calorimeters, each region spanning 4x4 trigger towers (TT), i.e. 20° in ϕ and 0.348 in η . Furthermore, the *L1 tau veto* ensures that the individual energy deposits are contained within squares of 2x2 TT, each square being 5° in ϕ and 0.087 in η . Jets with $E_T > 20$ GeV (14 for the ditau case) passing the isolation and *L1 tau veto* requirements are fed further to the High Level Trigger (HLT). Due to a decrease in the isolation and *L1 tau veto* efficiencies at high E_T , candidate jets failing one or both requirements may still be passed on to the HLT provided that their $E_T \geq 30$ GeV. The HLT produces particle flow (PF) candidates from the L1 seeds. Jet matching is performed with a shrinking cone whose acceptance radius starts at 5 and scales up quadratically with the jet's E_T . Furthermore, tracks are reconstructed and a minimum leading track p_T of 5 GeV/ c is required. Lastly, tracker-based isolation selects candidate events containing

CHAPTER 4. SEARCH FOR $Z' \rightarrow \tau\tau$ USING LHC COLLISION DATA OF RUN 2010 COLLECTED WITH CMS DETECTOR

Cut-Wise Event Selection Efficiency estimated from Monte-Carlo						
Cut/Selection	Signal	Backgrounds				
$Z'(500) \rightarrow \tau\tau$	$Z \rightarrow \tau\tau$	QCD 15-30	QCD 30-50	QCD 50-80	QCD 80-120	
$\tau_1 \eta , \tau_2 \eta < 2.1$	86.64 ± 0.45	79.97 ± 0.12	91.92 ± 0.06	92.81 ± 0.03	94.09 ± 0.02	94.93 ± 0.01
$\tau_1, \tau_2 p_T > 20 \text{ GeV}/c$	95.47 ± 0.30	38.51 ± 0.17	0.59 ± 0.02	9.31 ± 0.03	29.68 ± 0.04	43.67 ± 0.03
τ_1, τ_2 seed track $p_T > 5 \text{ GeV}/c$	97.79 ± 0.21	86.23 ± 0.19	86.61 ± 1.07	83.36 ± 0.15	84.76 ± 0.05	88.1 ± 0.03
τ e veto (both τ 's)	84.88 ± 0.53	71.93 ± 0.26	62.08 ± 1.64	69.04 ± 0.20	74.47 ± 0.07	79.34 ± 0.04
τ μ veto (both τ 's)	96.51 ± 0.29	98.95 ± 0.07	99.26 ± 0.37	98.37 ± 0.07	98.07 ± 0.02	97.91 ± 0.02
τ track Iso < 1 (both τ 's)	67.3 ± 0.77	73.91 ± 0.31	17.29 ± 2.48	4.15 ± 0.16	0.91 ± 0.03	0.43 ± 0.02
τ Ecal Iso < 1 (both τ 's)	76.24 ± 0.85	73.55 ± 0.36	39.52 ± 3.37	27.63 ± 0.49	20.39 ± 0.29	19.69 ± 0.32
τ NProngs = 1 (both τ 's)	58.14 ± 1.13	40.14 ± 0.46	5.26 ± 1.81	3.17 ± 0.23	3.61 ± 0.17	3.41 ± 0.19
$Q(\tau_1) * Q(\tau_2) < 0$	97.31 ± 0.49	99.44 ± 0.11	52.63 ± 4.05	51.66 ± 0.66	51.42 ± 0.47	51.53 ± 0.54
$\cos \Delta\phi(\tau_1, \tau_2) < -0.95$	91.88 ± 0.83	71.27 ± 0.68	51.7 ± 2.91	58.82 ± 0.50	47.99 ± 0.32	32.75 ± 0.29
$\cancel{E}_T > 30 \text{ GeV}$	68.17 ± 1.48	3.36 ± 0.32	0 ± 0	0.71 ± 0.11	2.21 ± 0.14	6.96 ± 0.27
$P_\zeta - 0.875 P_\zeta^{vis} > -7$	90.57 ± 1.12	83.96 ± 3.56	0 ± 0	60.00 ± 7.75	69.96 ± 2.88	76.00 ± 1.74

Table 4.5: Relative efficiencies for double hadronic tau selection in case of signal (with Z' mass of 500 GeV/ c^2) and low energy QCD-jets with ranges of final state parton transverse momenta in $2 \rightarrow 2$ subprocesses given in GeV/ c . Note that MC-based estimation of QCD multijet background is not used for this channel. The error reported here is statistical error only.

4.5. HADRONIC TAU TRIGGER ALGORITHM

Cut-Wise Event Selection Efficiency estimated from Monte-Carlo						
Cut/Selection	QCD 120-170	QCD 170-300	QCD 300-470	$Z \rightarrow ee$	W+Jets	$t\bar{t}$
$\tau_1 \eta , \tau_2 \eta < 2.1$	95 ± 0.01	95.04 ± 0.01	95.42 ± 0.01	92.43 ± 0.03	92.7 ± 0.02	99.43 ± 0.01
$\tau_1, \tau_2 p_T > 20 \text{ GeV}/c$	41.82 ± 0.03	35.81 ± 0.03	29.3 ± 0.03	54.6 ± 0.06	25.04 ± 0.03	74.51 ± 0.04
τ_1, τ_2 seed track $p_T > 5 \text{ GeV}/c$	89.73 ± 0.03	89.68 ± 0.03	88.98 ± 0.04	98.98 ± 0.01	92.19 ± 0.04	92.96 ± 0.03
τ e veto (both τ 's)	81.97 ± 0.04	83.10 ± 0.04	83.49 ± 0.05	1.70 ± 0.02	45.26 ± 0.08	77.19 ± 0.05
τ μ veto (both τ 's)	97.63 ± 0.02	97.26 ± 0.02	96.61 ± 0.03	98.86 ± 0.12	47.14 ± 0.12	86.89 ± 0.04
τ track Iso < 1 (both τ 's)	0.38 ± 0.02	0.49 ± 0.02	0.08 ± 0.002	18.81 ± 0.46	8.46 ± 0.10	2.37 ± 0.02
τ Ecal Iso < 1 (both τ 's)	19.11 ± 0.37	17.61 ± 0.38	8.81 ± 0.08	73.58 ± 1.21	46.99 ± 0.59	29.67 ± 0.42
τ NProngs = 1 (both τ 's)	3.81 ± 0.24	2.55 ± 0.21	0.37 ± 0.02	69.18 ± 1.47	12.07 ± 0.56	13.17 ± 0.57
$Q(\tau_1) * Q(\tau_2) < 0$	51.32 ± 0.62	49.89 ± 0.67	50.87 ± 0.16	93.38 ± 0.95	84.65 ± 1.79	77.68 ± 1.95
$\cos \Delta\phi(\tau_1, \tau_2) < -0.95$	26.61 ± 0.28	22.85 ± 0.27	19.02 ± 0.32	66.46 ± 1.87	26.32 ± 2.38	18.31 ± 2.05
$\cancel{E}_T > 30 \text{ GeV}$	13.25 ± 0.42	23.21 ± 0.56	40.76 ± 0.92	1.18 ± 0.53	36.67 ± 5.08	86.15 ± 4.28
$P_\zeta - 0.875P_\zeta^{vis} > -7$	79.63 ± 1.37	74.01 ± 1.22	72.42 ± 1.31	40 ± 21.91	48.48 ± 8.7	58.93 ± 6.57

Table 4.6: Relative efficiencies for double hadronic tau selection for QCD-jets, with ranges of final state parton transverse momenta in $2 \rightarrow 2$ subprocesses given in GeV/c , $W + jets$ and $t\bar{t}$ backgrounds. Note that MC-based estimation of QCD multijet background is not used for this channel. The error reported here is statistical error only.

CHAPTER 4. SEARCH FOR $Z' \rightarrow \tau\tau$ USING LHC COLLISION DATA OF RUN 2010 COLLECTED WITH CMS DETECTOR

no tracks with p_T greater than 1 GeV/ c inside the isolation annulus.

4.5.1 Measurement of Di-Tau Trigger Efficiency Using Fake Taus

The standard procedure to measure lepton trigger efficiency is to select leptons from $Z \rightarrow \ell\ell$ using Tag and Probe techniques. For light leptons this technique can be applied with relative ease since the identification of the tag can be done with high efficiency with very little background contamination. But measuring the hadronic tau trigger is more complicated due to the much difficult task of obtaining a tau sample pure enough to be used as Tags. At the same time, the sample of clean taus should be large enough, not to be dominated by the statistical uncertainty. This difficulty can be removed if we select objects that pass every offline tau identification requirement (including isolation) and use them as proxies for real taus. The trigger efficiency is then measured as the ratio of “tau-like” object reconstructed offline, matched to online taus passing the different trigger requirements vs “tau-like” object reconstructed offline and matched to online taus.

For this purpose we use electrons as proxies for real taus in the measurement of the tau trigger efficiency. Electrons should pass every offline tau identification requirement except for the electron-discriminator cut designed to discriminate electrons from taus. The efficiency of the different trigger requirements is measured vs isolated “tau-like” objects identified as PFTau with $E_T > 20$ GeV, $|\eta| < 2.5$, and leading track $p_T > 5$ GeV/ c . In addition the offline object is required to pass the muon-discriminator cut. When dealing with electrons it has been ensured that the “tau-like” object is electron-like by requiring that it fails the electron-discriminator.

The efficiencies for Level-1 and HLT are shown in Figure 4.11. In the figure the efficiency for data measured from the electron dataset (/Electron/Run2010B) compared to the efficiency measured from $Z \rightarrow ee$ and $Z \rightarrow \tau\tau$ MC samples is shown. The efficiency curves plateau at 94.72, 94.39, and 94.54% efficiency for $Z \rightarrow ee$ MC, $Z \rightarrow \tau\tau$ MC, and electron dataset, respectively. The main difference in the measured

4.5. HADRONIC TAU TRIGGER ALGORITHM

efficiencies are located in the turn-on curve. Most of the difference comes from the different calorimetric response between hadronic and electromagnetic showers at Level-1. However, for this analysis most of the taus have p_T well above the efficiency plateau value. For a Z' with mass of $350 \text{ GeV}/c^2$ only about 10% of the τ -pairs have one reconstructed τ_h with $p_T < 35 \text{ GeV}/c$. The overall Level-1 plus HLT trigger efficiency is shown in Figure 4.12.

A conservative estimate of the trigger efficiency systematic uncertainty has been made by calculating $\frac{\epsilon_{\text{MC}_i}^\tau - \epsilon_{\text{Data}_i}^e}{\epsilon_{\text{MC}_i}^\tau}$, where $\epsilon_{\text{MC}_i}^\tau$ is the efficiency measured from $Z \rightarrow \tau\tau$ MC in bin i and $\epsilon_{\text{Data}_i}^e$ is the trigger efficiency measured from data using the electron dataset in the same bin. The final systematic uncertainty is the average of the bin by bin systematic. This procedure yields an uncertainty of 4%.

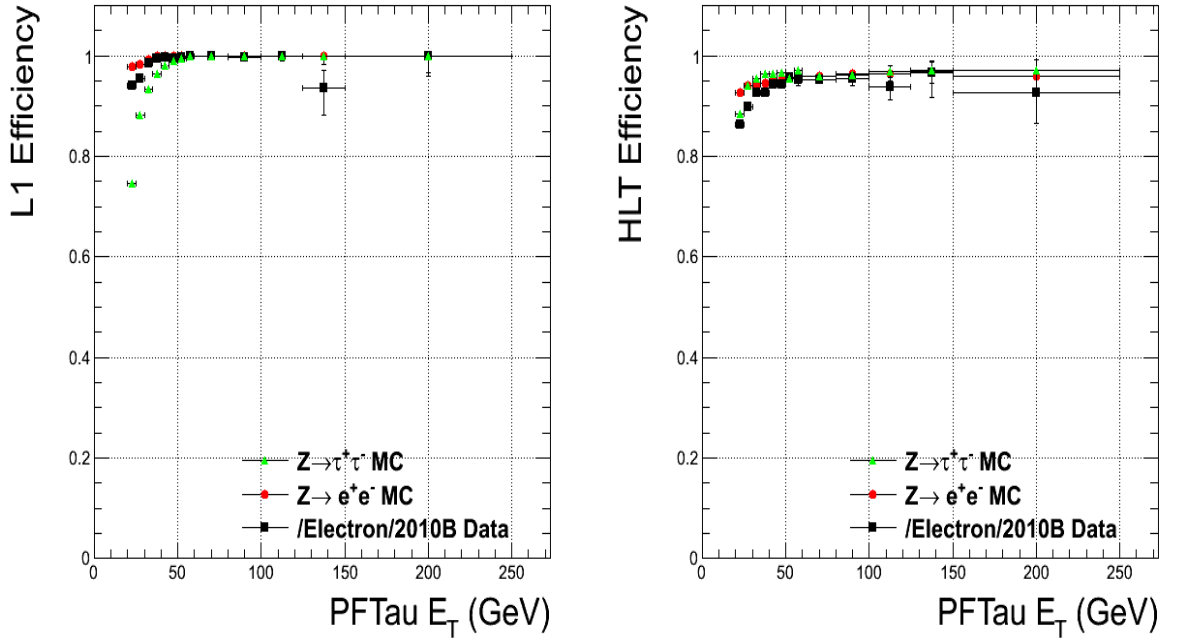


Figure 4.11: Tau trigger efficiencies for Level-1 (left), HLT (right), plotted against offline PFTau E_T for $Z \rightarrow ee$ MC, $Z \rightarrow \tau\tau$ MC, and data.

CHAPTER 4. SEARCH FOR $Z' \rightarrow \tau\tau$ USING LHC COLLISION DATA OF RUN 2010 COLLECTED WITH CMS DETECTOR

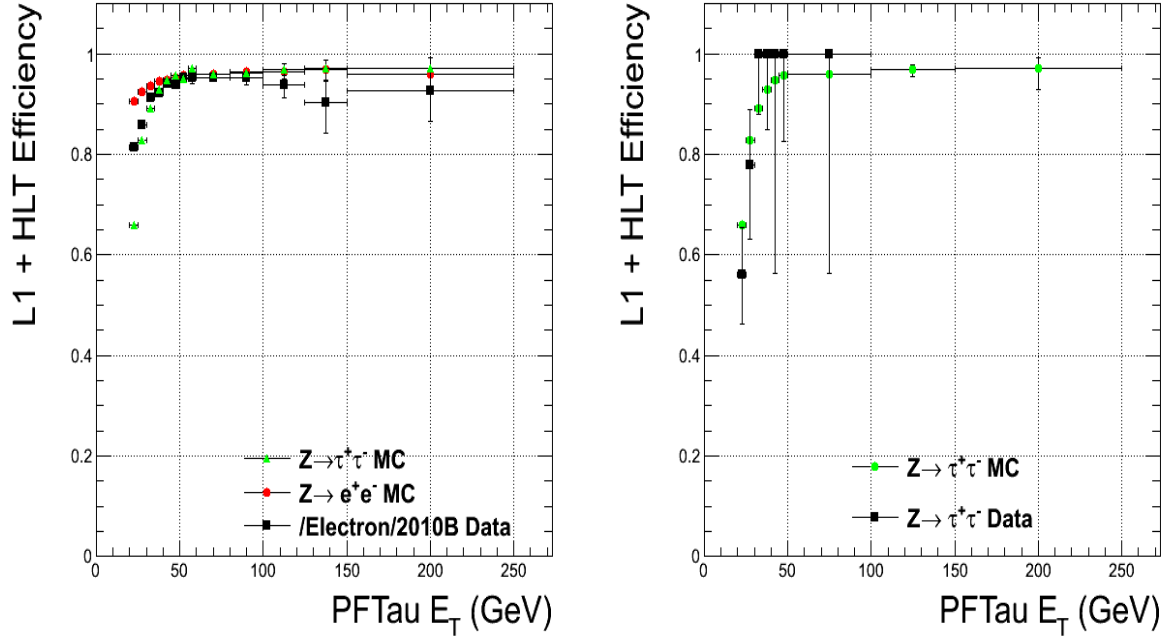


Figure 4.12: Overall hadronic tau trigger efficiency (Level-1 + HLT) for $Z \rightarrow ee$, $Z \rightarrow \tau\tau$, and 2010 electron dataset (left), Overall hadronic tau trigger efficiency for $Z \rightarrow \tau\tau$ MC and data (left). The $Z \rightarrow \tau\tau \rightarrow \tau_\mu \tau_h$ data candidates were selected from events passing the SingleMuon trigger.

4.6 Additional Validation Checks

The fact that electrons can be reconstructed as perfect taus (provided electron rejection cuts are reversed or removed) proves useful in validating the reliable reconstruction of tau-pairs. Ideally, no \cancel{E}_T is expected in $Z \rightarrow ee$ events, hence, to obtain a clean sample of $Z \rightarrow ee$ events, the electron rejection has to be reversed in addition to the removal of \cancel{E}_T requirement. The following modifications are made to the signal selections outlined in the Subsection 4.2.2:

- $H_{3 \times 3}/p_T^{\tau^{seed}} < 0.1$.
- No \cancel{E}_T requirement.

Proper scale factors have been applied to account for the double-tau trigger efficiencies shown in (left) Figure 4.12 (note the similarity of the two efficiency curves for taus and electrons even at the trigger level, the small differences are because taus

4.7. BACKGROUND ESTIMATION

have softer track momentum spectrum due to decays involving neutral pions and the difference in energy response for hadronic and electromagnetic showers in Level-1). The description of the measurement of the tau trigger efficiency is given in the Subsection 4.5.1. Figure 4.13 shows the invariant mass, \cancel{E}_T , and tau-jet p_T distributions obtained using the same data sample as for the actual analysis but with the electron rejection cuts reversed. There is a good agreement between data and MC, showing that the tau-identification and trigger efficiencies are well understood. $Z \rightarrow ee$ MC is used to estimate the expected shape and scale of the electron-positron content in double-hadronic tau triggered data.

4.7 Background Estimation

To estimate the number of surviving events from various backgrounds, control regions in which each background dominates are generally defined. The efficiency of the cuts used to create the control regions are determined in the control regions themselves, and then these used to determine the relative proportions of background events in the control and signal regions. By counting the number and analyzing kinematical distributions of background events in the control region of the data samples, the number of background events in the signal region can be inferred either directly or using simulation predictions adjusted for appropriate scale factors measured in data.

4.7.1 Estimation of QCD multijet background using data driven approach

A data-driven approach has been followed to estimate the QCD multijet background contamination. It should be noted that the definition of QCD multijet includes events where both tau candidates are infact misidentified hadronic jets, so it can have additional contributions with respect to the QCD dijet production, e.g. $W(\rightarrow q\bar{q}) + jets$, $Z(\rightarrow q\bar{q}) + jets$ etc. The QCD multijet background estimation relies on the classical method of counting events selected in the exact same way as the signal events but selecting tau pairs with the like-sign charge, which should lead to events heavily dom-

CHAPTER 4. SEARCH FOR $Z' \rightarrow \tau\tau$ USING LHC COLLISION DATA OF RUN 2010 COLLECTED WITH CMS DETECTOR

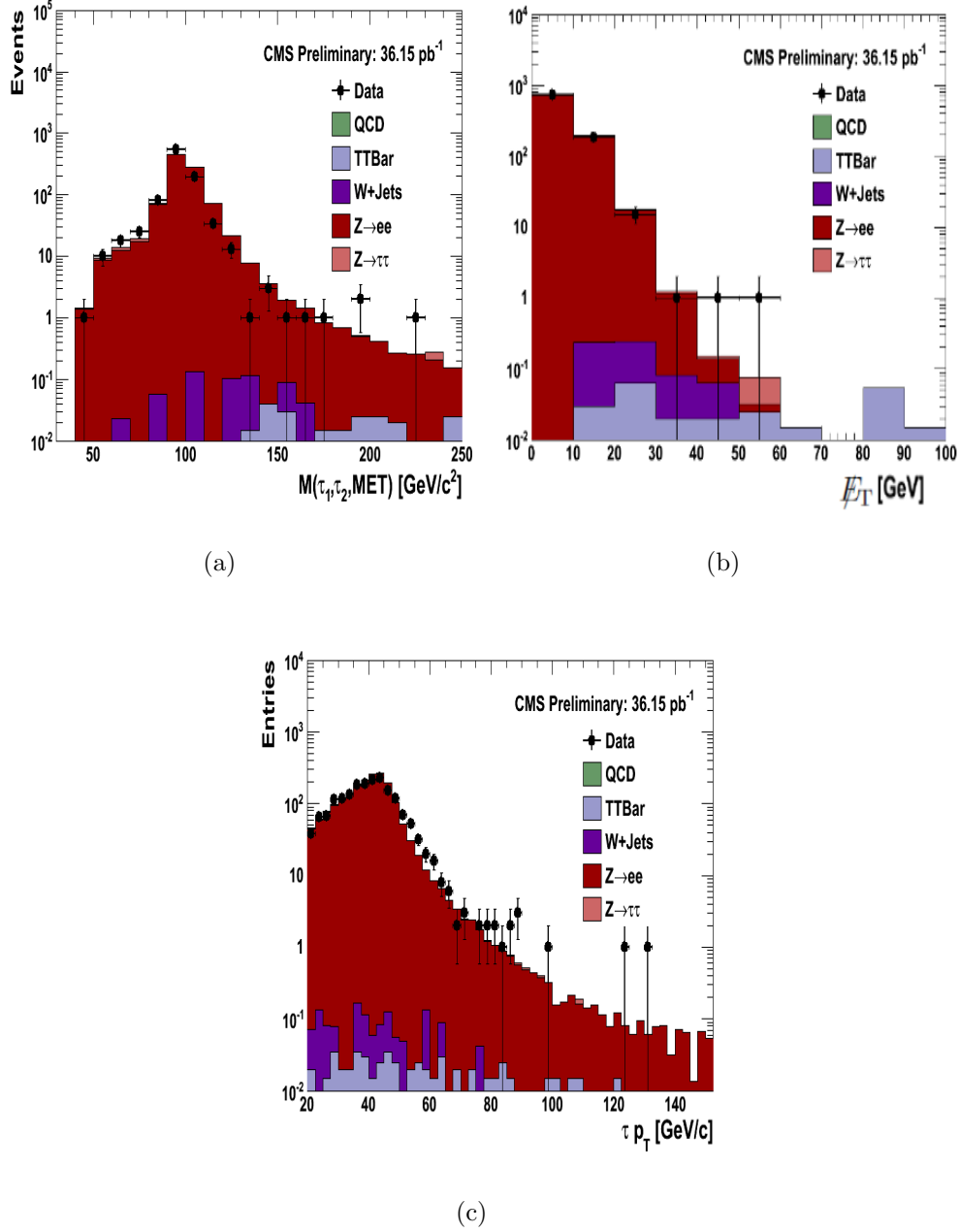


Figure 4.13: Dielectron distributions from double tau trigger data with reversed anti-electron cuts and $Z \rightarrow ee$ MC for validation of the double tau analysis: (a) Invariant mass of the two electrons, (b) E_T distribution, (c) transverse momentum of electrons reconstructed as PFTau candidates.

4.7. BACKGROUND ESTIMATION

inated by the QCD multijet background. Assuming that QCD dijets are charge-blind, the number of like-sign events (N_{LS}) should be equal to the number of opposite-sign (N_{OS}) QCD multijet events after correcting N_{LS} measured in data for known electroweak backgrounds using simulation. Unfortunately, there are two shortcomings of this procedure. First, the number of remaining events is too small to obtain the shape of the QCD multijet background to use in the final fit, and second, the assumption of charge symmetry in events with two jets is not necessarily true. The first concern is addressed by measuring the shape of the invariant mass $M(\tau_1, \tau_2, \cancel{E}_T)$ distribution associated with multijet background using events with like-sign tau pairs where tau candidates are allowed to have either 1, 2, or 3 charged particles. Note that here the charge of a tau candidate is determined by the charge of the leading track, so that even-prong tau candidates still have a well defined charge. The validity of such approximation is verified by using events with no missing transverse energy, where the invariant mass distribution for pairs of 1-prong tau candidates is compared to that with the loosened requirement. Figure 4.14 shows the distribution of the invariant mass of the two visible tau candidate momenta and missing transverse energy in events with $N^{prong} = 1, 2$ or 3 along with the fit to a functional form given in Eq. 4.4, which is used later to extract the statistical significance of the results of this analysis. Figures 4.15 and 4.16 show the mass and \cancel{E}_T distributions of the QCD background using 1 prong taus and 1 or 2 or 3 prong taus in two minimum \cancel{E}_T scenarios: 0 GeV and 15 GeV (the statistics become compromised for higher thresholds). These are obtained by selecting like-sign events from collision data and subtracting off the leading backgrounds estimated from MC with like-sign candidate pairs. While the agreement is not perfect, the similarity in the shapes suggests that they are not correlated with the track multiplicity.

$$f(x) = \frac{1}{a + \exp[b \cdot (x - c)] + d \cdot (x - c)^2} \quad (4.4)$$

As for the second concern, an asymmetry in the charges of jets in multijet events can arise from the remaining correlation between the quark charge and the leading track charge of the jet in events where quark charges are correlated, e.g. $gg \rightarrow q\bar{q}$,

CHAPTER 4. SEARCH FOR $Z' \rightarrow \tau\tau$ USING LHC COLLISION DATA OF RUN 2010 COLLECTED WITH CMS DETECTOR

$W \rightarrow q\bar{q}'$. Note that the correlation between the charge of the quark and the charge of the track becomes stronger in jets, in which the entire jet fluctuated into just a single high momentum track. Therefore, the ratio $R_{OS/LS}$ of opposite-sign to like-sign events can be a function of tau candidate multiplicity (stronger correlation for tau candidates with just a single track) and tau isolation (stronger correlation for highly isolated tau candidates). In order to determine $R_{OS/LS}$, we use two alternative methods. First, we calculate this ratio in events with pairs of 1-prong tau candidates with no requirement on the missing transverse energy applied, which greatly enhances the QCD multijet background. After correcting for non-QCD backgrounds ($W + jets$, $Z + jets$ including $Z \rightarrow \tau\tau$) using simulation, the ratio is calculated as a function of the invariant mass and yields the ratio $R_{OS/LS} = 1.2 \pm 0.09$. Figures 4.17 (a) and (c) show this ratio and the comparison of data to the background corrected using this factor, respectively. In the fitting of $R_{OS/LS}$, we use the low mass region to be less susceptible to uncertainties due to electroweak backgrounds. We then measure the same ratio in events with $\cancel{E}_T > 15$ GeV, where we measure $R_{OS/LS}$ as a function of the transverse mass of the leading tau candidate and the missing transverse energy. The fit (see Figs. 4.17 (b) and (d)) is again performed in the low transverse mass region to avoid the regions with enhanced content of the $W + jets$ events with the W decaying to either an electron misidentified as a tau or to a true tau. We finally, conservatively, use the ratio $R_{OS/LS} = 1.1 \pm 0.2$ to accommodate for statistical uncertainties in the measurement, difference between the two measurements, and the difference of the measured ratio with 1. Finally, the prediction for the normalization of the invariant mass distribution for QCD multijet events is calculated as $(N_{LS} - N_{cor}) \times R_{OS/LS}$, where $N_{LS} = 9$ is the number of events with all final selections except the inverted charge product, and N_{cor} is the (small) correction for electroweak backgrounds in the like-sign sample (dominated by $W + jets$ events) obtained from the simulation.

4.7.2 Estimation of other non-QCD SM backgrounds

The QCD multijet is really the dominant of all the backgrounds and the other backgrounds are relatively negligible. Moreover, the other background processes are well

4.8. DATA IN THE SIGNAL REGION

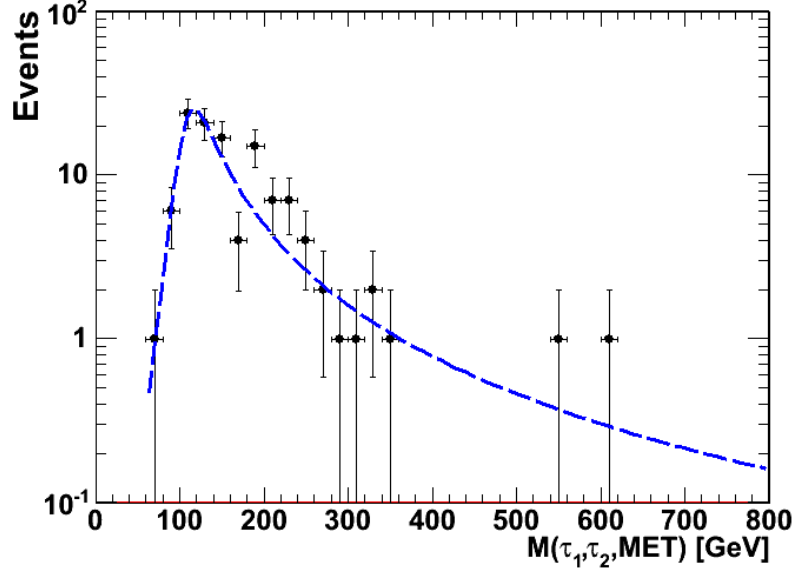


Figure 4.14: QCD mass distribution after all selections except the track multiplicity requirement, *i.e.*, considering all; 1, 2 and 3 prong taus.

simulated by Monte Carlo as seen in the other analysis channels for $Z' \rightarrow \tau\tau$ search, so the estimation of other backgrounds is taken directly from the Monte Carlo expectations after correcting for differences between data and MC expectations, if any.

4.8 Data in the Signal Region

The signal region consists of events satisfying the criteria outlined in Subsection 4.3.2. The contributions of various SM backgrounds and data events surviving all the selections can be seen in Table 4.7. The QCD multijet comes out to be the largest background, as expected. The $Z \rightarrow \tau\tau$ is the second dominant background. The contribution of rest of the backgrounds is quite small. The contamination from these backgrounds is further small in the high mass region ($M(\tau_1, \tau_2, \cancel{E}_T) > 150 \text{ GeV}/c^2$) where the presence of a new resonance is expected. The number of events expected for a Z' of mass $500 \text{ GeV}/c^2$ amounts to 1.5 ± 0.02 . The suitable cross-checks made in the control regions suggest that the non-QCD background shapes can be taken

CHAPTER 4. SEARCH FOR $Z' \rightarrow \tau\tau$ USING LHC COLLISION DATA OF RUN 2010 COLLECTED WITH CMS DETECTOR

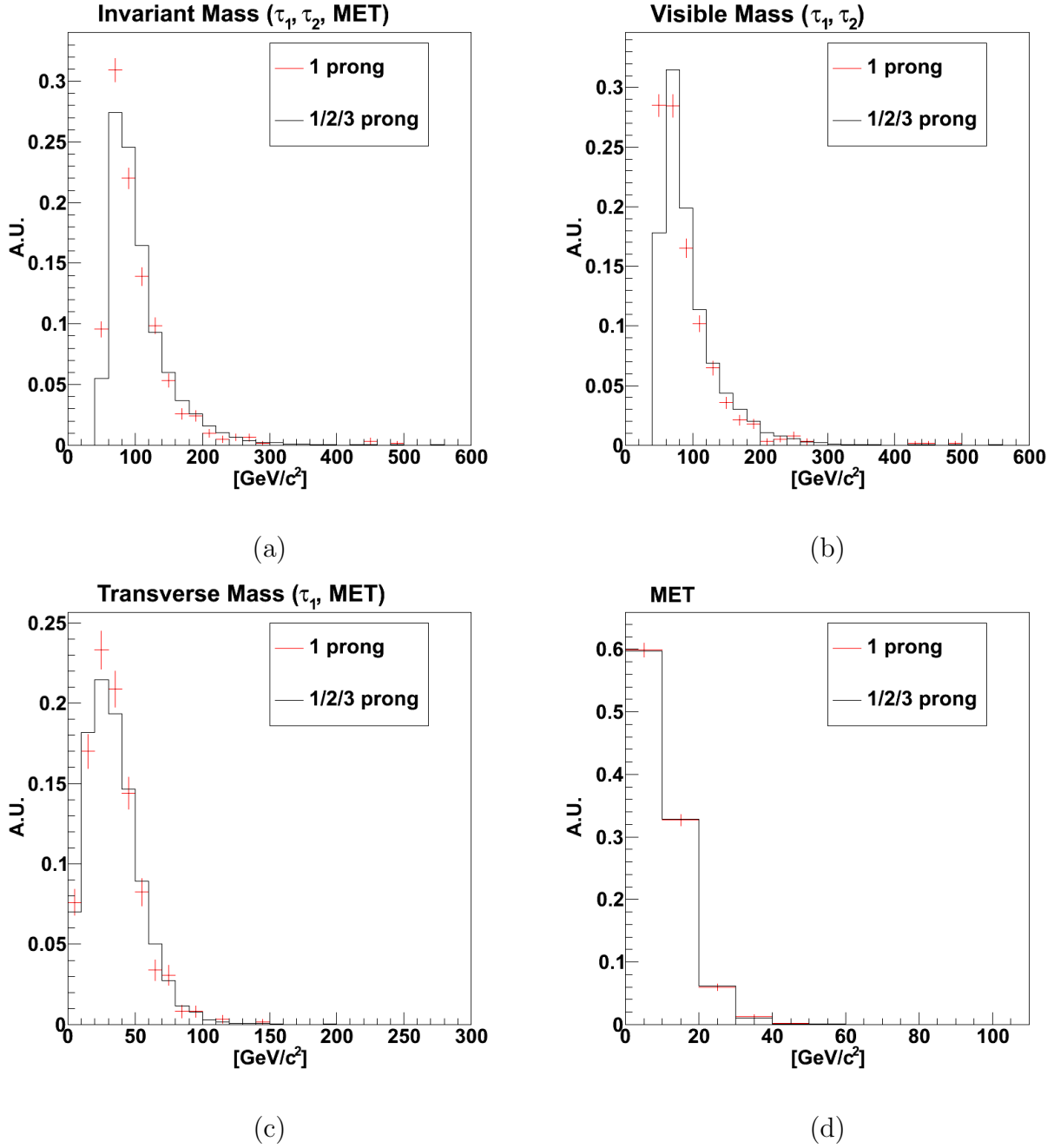


Figure 4.15: Comparison of mass and \cancel{E}_T distributions for 1 prong taus and 1 or 2 or 3 prong taus, normalized to their area, without \cancel{E}_T requirement.

from the simulated MC samples and fit to obtain smooth shapes in the high mass regions. Hence, the mass shapes are taken from the simulated MC samples and fit to obtain smooth trends in the high mass regions. For determination of the final 95% Confidence Level (C.L.) upper limit on the cross-section times the branching

4.8. DATA IN THE SIGNAL REGION

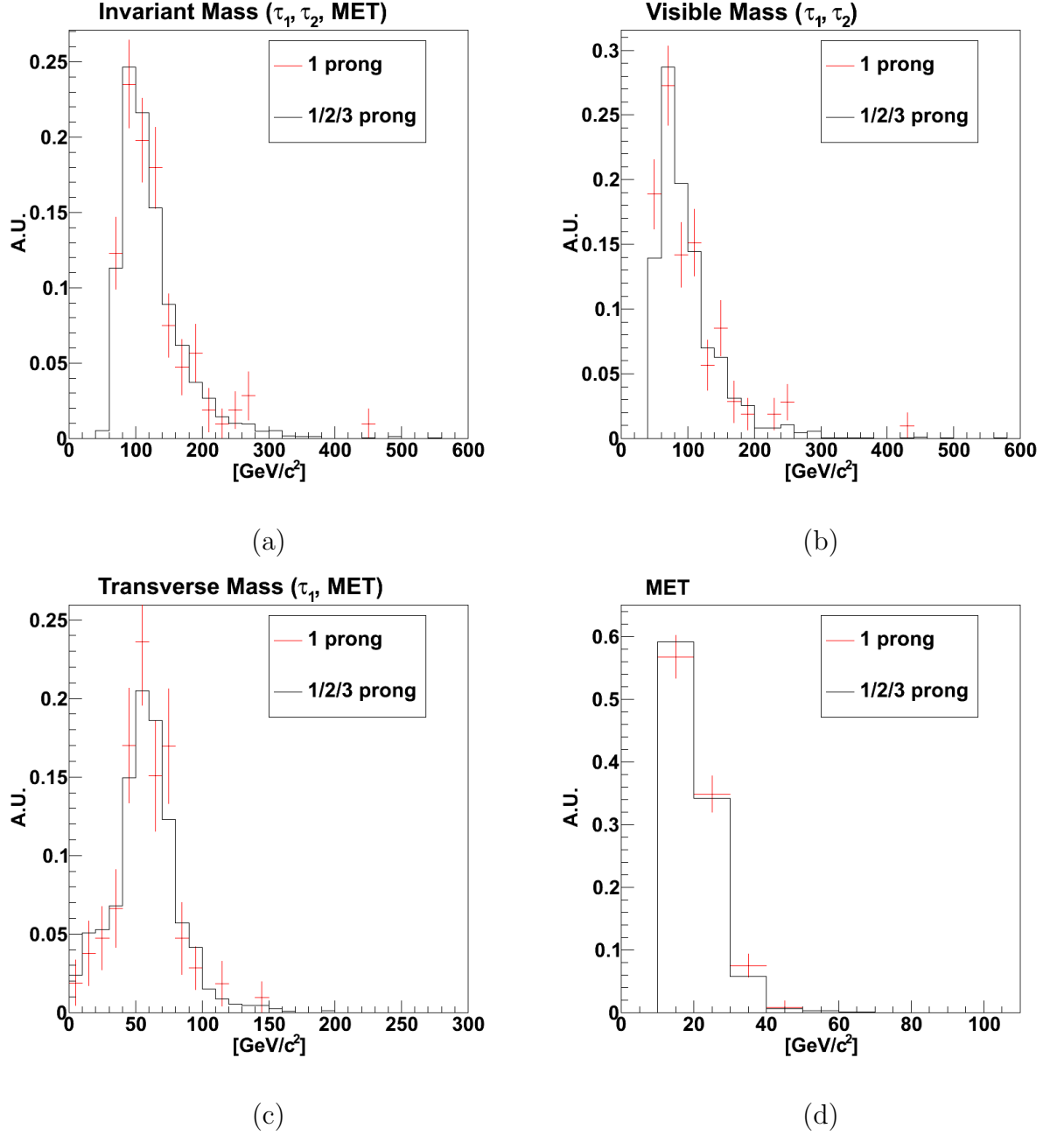


Figure 4.16: Comparison of mass and \cancel{E}_T distributions for 1 prong taus and 1 or 2 or 3 prong taus, normalized to their area, requiring $\cancel{E}_T \geq 15$ GeV.

ratio to tau-lepton pair, systematic effects arising from the incomplete knowledge of the shapes have been taken into account. Figure 4.18 shows the invariant mass distribution of tau-pair and \cancel{E}_T prior to fit. The signal distribution expected for a new resonance (Z') of mass 500 GeV/ c^2 is also overlayed.

CHAPTER 4. SEARCH FOR $Z' \rightarrow \tau\tau$ USING LHC COLLISION DATA OF RUN 2010 COLLECTED WITH CMS DETECTOR

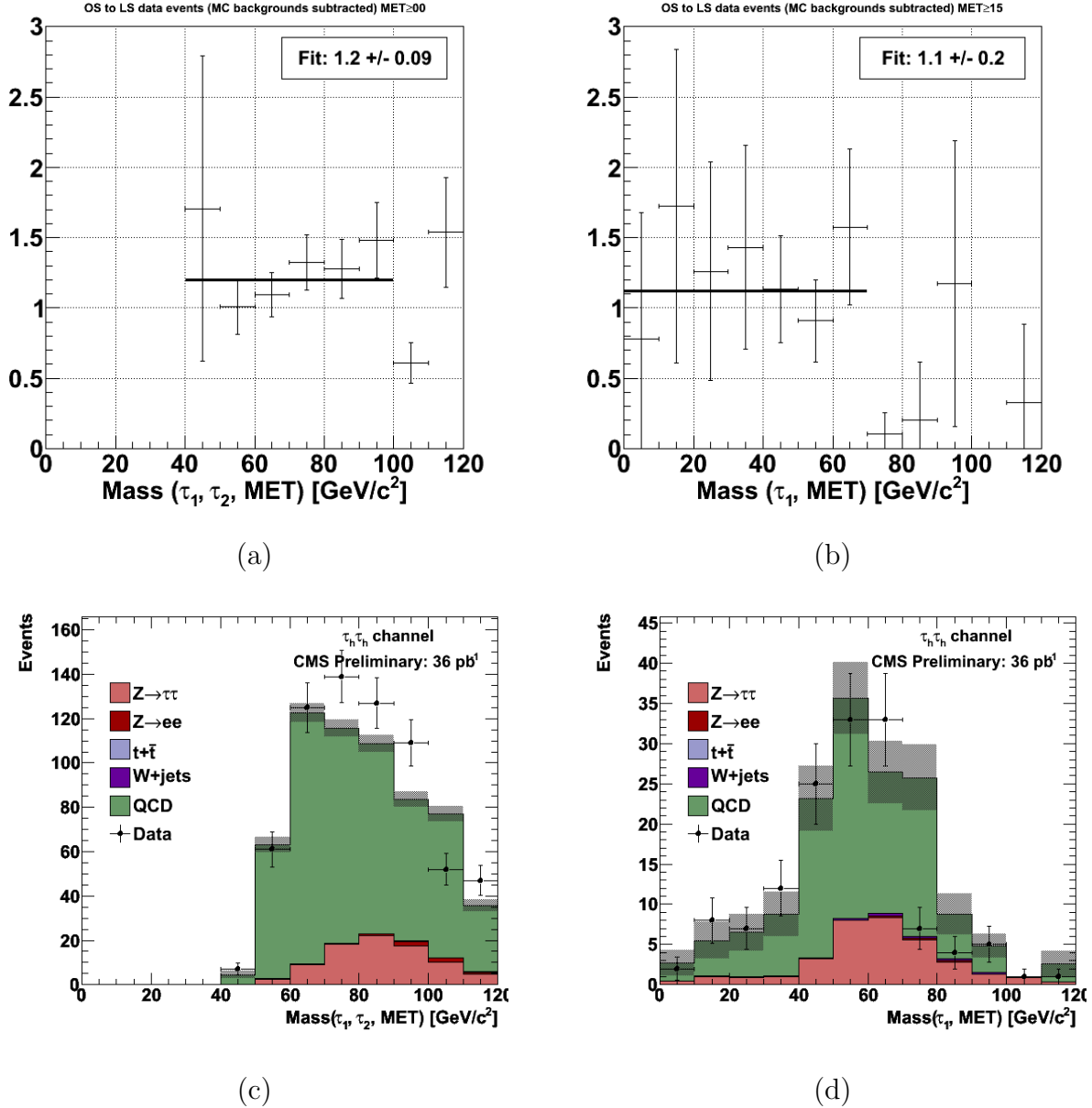


Figure 4.17: Ratio of the number of selected data events with an opposite-sign pair to those with a like-sign pair after subtracting all of the MC-based backgrounds independently: (a) full invariant mass for $\cancel{E}_T \geq 0$ GeV, (b) invariant mass of the leading p_T tau and \cancel{E}_T for $\cancel{E}_T \geq 15$ GeV. The significant value is extracted with a one-dimensional fit in regions with small background contamination: (a) 1.20 ± 0.09 (b) 1.1 ± 0.2 . Plots (c) and (d) show the relative contribution of each background, requiring opposite-sign pairs except in the case of QCD, which is estimated from like-sign pairs from data.

4.9. SYSTEMATIC UNCERTAINTIES

Sample	Events	Events for $M(\tau_1, \tau_2, \cancel{E}_T) > 150 \text{ GeV}/c^2$
QCD	10 ± 4	2 ± 2
$W + jets$	0.62 ± 0.06	0.37 ± 0.05
$t\bar{t}$	0.108 ± 0.005	0.0682 ± 0.004
$Z \rightarrow \tau\tau$	3.04 ± 0.08	0.60 ± 0.02
$Z \rightarrow ee$	0.02 ± 0.02	0 ± 0
Total expected events	14 ± 4	3 ± 2
Observed events	7	4

Table 4.7: Estimated signal and background contributions along with the observed events.

4.9 Systematic Uncertainties

The main source of systematic uncertainty in this analysis comes from the background estimation due to the lack of statistics in the signal region (*e.g.* 28% for $\tau_h\tau_h$). There may be small effect due to contamination of other backgrounds in the control regions since it is difficult to obtain a 100% pure control region. In cases, where a data-driven estimation is not possible, the systematic uncertainty is driven by the uncertainty in the expected number of events in the signal region for the particular background. Nevertheless, this effect is negligible with respect to the uncertainty introduced by the lack of statistics.

The second most dominant source of systematic uncertainty is due to the tau-identification uncertainty. For this analysis, the shrinking cone algorithm along with elliptical isolation have been used for tau-identification and reconstruction. This algorithm is subject to the following systematic effects:

- The efficiency of track finding associated with each charged hadron.
- Efficiency of track finding convoluted with the probability of having a three prong tau with all the tracks collinear such that it appears as one-prong tau. This can occur with the high p_T taus.

CHAPTER 4. SEARCH FOR $Z' \rightarrow \tau\tau$ USING LHC COLLISION DATA OF RUN 2010 COLLECTED WITH CMS DETECTOR

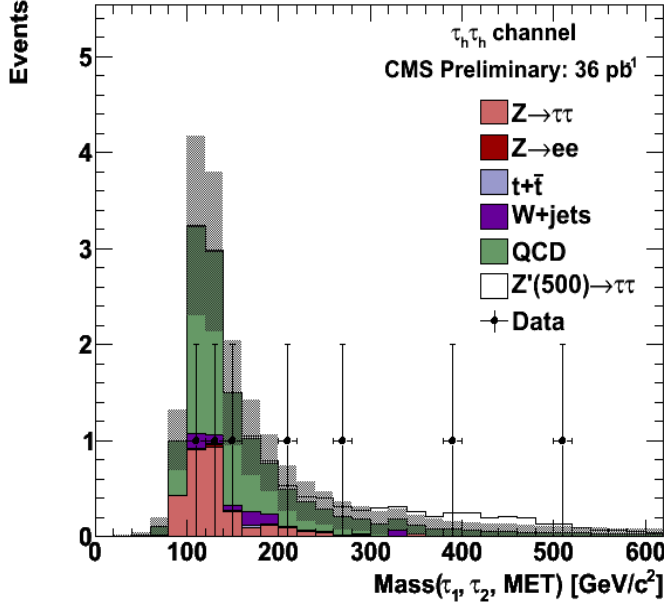


Figure 4.18: Data, backgrounds and signal invariant mass distributions after all cuts for a Z' with mass of $500 \text{ GeV}/c^2$.

- Probability associated with the charged or neutral pions to fall outside the tau-signal cone.
- Probability for tracks/photons coming from underlying events/pile-up to fall into the isolation cone.
- Probability for tracks coming from underlying events to fall into the isolation cone, hence, affecting the one or three prong requirement.

The systematic effect arising from the three-prong taus falling outside the isolation cone is not explicitly applicable to this analysis since one prong hadronic taus are used in the analysis. However, if three-prong tau has badly reconstructed tracks, then it can still be reconstructed as a one-prong tau. This effect is measured by using $Z \rightarrow \tau\tau$ MC samples and counting how many reconstructed three-prong taus, matched to generator level taus ($\Delta R < 0.25$), were identified as one-prong taus. The result shows that about 0.74% of the three prong taus are identified as one-prong taus. This result is well applicable to high p_T taus although the effect becomes small.

4.10. STATISTICAL INTERPRETATION

The probability for tracks and/or photons coming from underlying or pile-up events to fall into the isolation region is same for muons, electrons, and taus provided the isolation cone sizes are the same. Hence, the standard $Z \rightarrow \mu\mu$ tag and probe technique [63] can be applied to measure this effect.

The uncertainty on track finding (4%) for charged pions is determined by measuring the ratio of neutral charm meson (D^0) decay to two or four charged particles [64]. This value is included as a part of total systematic uncertainty on the tau-identification. The above described effect gives an overall systematic uncertainty value less than 5%, but we use a conservative value of 7% as recommended by the Tau Physics Object Group (Tau POG) [57].

The uncertainty introduced by imprecise knowledge of parton distribution function (PDF) is determined by comparing CTEQ6.6L PDF with the default PDF (CTEQ6L) and variations within the CTEQ6.6 family of parameterizations. The systematic effects arising from tau, lepton, and jet energy scale can also affect the mass shapes. These systematic effects are measured by “smearing” the default values by the corresponding uncertainty and determine the effect of these newly calculated variables on the event rates and mass shapes. As an example, the systematic effect on p_T of τ_h is measured using the Equation:

$$p_T^{smeared} = k_{scale} \cdot p_T^{generator} + k_{resolution} \cdot (p_T^{reconstructed} - p_T^{generator}) \quad (4.5)$$

where $p_T^{generator}$ is the true generator level transverse momentum of τ , $p_T^{reconstructed}$ is the default transverse momentum of τ at the reconstruction level, k_{scale} is the momentum scale smearing factor, and $k_{resolution}$ is the momentum resolution smearing factor.

The complete list of systematic uncertainties discussed above, is given in the Table 4.8.

4.10 Statistical Interpretation

Several experiments in High Energy Physics involve binary outcome *i.e.* result is either a true (discovery) or false (exclusion) *e.g.* the search for a Higgs boson at the

CHAPTER 4. SEARCH FOR $Z' \rightarrow \tau\tau$ USING LHC COLLISION DATA OF RUN 2010 COLLECTED WITH CMS DETECTOR

Source of Systematics	$\tau_h\tau_h$
Luminosity	4%
Tau Trigger	4%
Tau ID	7.0%
Parton Distribution Functions	3.96%
Initial State Radiation	2.14%
Final State Radiation	1.7%
Tau Energy Scale (3%)	2.1%
Tau Energy Resolution	Negligible
Background Estimation	28%

Table 4.8: List of Systematics for MC and Data

LHC. Such experiments that are performed with “ n ” independent trials which yield a true or false outcome with a probability of success “ p ”, follow a binomial distribution $B(n, p)$. The binomial probability to obtain “ k ” successes out of “ n ” independent trials, in a particular experiment is given by:

$$f(k, n, p) = \frac{n!}{k!(n-k)!} p^k (1-p)^{n-k} \quad (4.6)$$

When the number of independent trials are very large and the probability of success is small, the binomial probability distribution reduces to a Poisson distribution.

$$\lim_{n \rightarrow \infty} f(k, n, p) = \lim_{n \rightarrow \infty} \frac{n!}{k!(n-k)!} p^k (1-p)^{n-k} = \frac{\mu^k e^{-\mu}}{k!} \quad (4.7)$$

where $\mu = np$. In Eqn. 4.7, “ k ” represents the number of observed events and μ is the number of expected events defined as:

$$\mu_i = L_i \sigma_{signal} \epsilon_i + b_i \quad (4.8)$$

where L_i is the integrated luminosity, σ_{signal} is the signal cross section, ϵ_i is the cumulative efficiency after applying all selection cuts, and b_i is the number of background events surviving all selection cuts applied.

The set of above equations is sufficient to quantify the signal significance for a simple counting experiment, but to achieve greater sensitivity, this analysis uses a

4.10. STATISTICAL INTERPRETATION

binned likelihood. The invariant mass of tau pair provides best separation between the signal and background and hence, it has been chosen for this purpose. Therefore, the Eqn. 4.7 can be written as:

$$\mathcal{L}(\epsilon_1, \epsilon_2, \dots, \epsilon_n) = \prod_{i=1}^{Nbins} \mathcal{L}_i(\mu_i, \nu_i) = \frac{\mu_i^{k_i} e^{-\mu_i}}{k_i!} \quad (4.9)$$

where $\mathcal{L}_i(\mu_i, k_i)$ is the Poisson probability of observing k_i events in collision data for a bin i , given an expectation of $\mu_i(\sigma) = [\text{Background} + \text{Signal}(\sigma)]_i$.

The likelihood distribution is used to extract the 95% C.L. upper limit on the cross section. To study the sensitivity of the analysis, pseudo-data samples are generated from background only distributions, using Poisson based random event generator. The concept of pseudo-experiments and pseudo-data is used to understand the probability for a given outcome to occur. This can be understood as follows: let us consider that the estimation of total background contribution gives 14 events. This number represents only the *mean expected* number which means if several experiments are performed, most of them will result in 14 events, while other may show upward (18 events) or downward (10 events) fluctuations. For the case of counting experiments, probability or the spread is determined by the Poisson probability density function.

A search which has been presented in this Chapter represents only one experiment. Since its a single experiment, an analysis has to be designed to minimize the probability for results to fluctuate. Pseudo-experiments or pseudo-data are generated by creating an ensemble of experiments, with each experiment representing a new possible result. Once the ensemble of experiments is created, the mean and spread of the results can be evaluated to quantify how likely it is that the experiment will give rise to a result that unluckily fluctuated upward or luckily fluctuated downward.

The knowledge of systematic uncertainties is also important since they can affect the global normalization of the event rate and also create an uncertainty in the knowledge of the mass shape. Systematic effects are included as nuisance parameters for the limit calculations. A nuisance parameter is a quantity that has no direct relation with the statistical sample itself but they are needed to account for any potential changes that might affect the results of interest. The nuisance parameters, “ α_k ”, are

CHAPTER 4. SEARCH FOR $Z' \rightarrow \tau\tau$ USING LHC COLLISION DATA OF RUN 2010 COLLECTED WITH CMS DETECTOR

generated according to the log normal probability density function for normalizations and Gaussian for mass spectrum uncertainties. If ϵ_n is an efficiency with systematic error $\delta\epsilon$, the likelihood integral becomes:

$$\int \mathcal{L}(\epsilon_1, \epsilon_2, \dots, \epsilon_n) d^n \epsilon = N^{-1} \sum_{j=1}^N \mathcal{L}(\epsilon_1 + \alpha_1^j \delta\epsilon_1, \epsilon_2 + \alpha_2^j \delta\epsilon_2, \dots, \epsilon_n + \alpha_n^j \delta\epsilon_n) \quad (4.10)$$

A “morphing” procedure is applied to introduce the effect of possible shape variations on default, unsmeared mass templates, D_i^{def} , to generate varied templates, D_i^j . After applying the morphing, the likelihood integral becomes:

$$N^{-1} \sum_{j=1}^N \mathcal{L}(\epsilon_1 + \alpha_1^j \delta\epsilon_1, \dots, \epsilon_n + \alpha_n^j \delta\epsilon_n, D_1^{def} + \alpha_1^j \delta D_1^j, \dots, D_n^{def} + \alpha_n^j \delta D_n^j) \quad (4.11)$$

where $\delta D_i^k = D_i^k - D_i^{def}$ is the difference between the smeared template for k^{th} systematic effect and default unsmeared template. It is also essential to take into account the correlations among the systematic uncertainties. To incorporate the correlations between systematic effects, the nuisance parameters can be modified as:

$$\alpha_k = f * \alpha_f + g * \alpha_g \quad (4.12)$$

where f and g represent the correlated and uncorrelated terms, respectively. The effect of nuisance parameters can be seen in Figure 4.19(a), which shows the default likelihood without any smearing or incorporation of nuisance parameters as well as several superimposed likelihood distributions which show the effect of nuisance parameters on the likelihood for $\tau_\mu \tau_h$ final state as an example. The 95% C.L. upper limit on the cross-section is obtained as:

$$0.95 = \frac{\int_0^{\sigma_{95}} \mathcal{L}(\sigma) d\sigma}{\int_0^\infty \mathcal{L}(\sigma) d\sigma} \quad (4.13)$$

Figure 4.19(b) shows an example of sensitivity study on MC basis for $\tau_\mu \tau_h$ final state, where pseudo-data was generated using background only distributions. Different scenarios are possible based on how these events are distributed. If the pseudo-data is located at the lower side of the spectrum consistent with the background expectations, the limit is expected to have a low value according to the Poisson

4.10. STATISTICAL INTERPRETATION

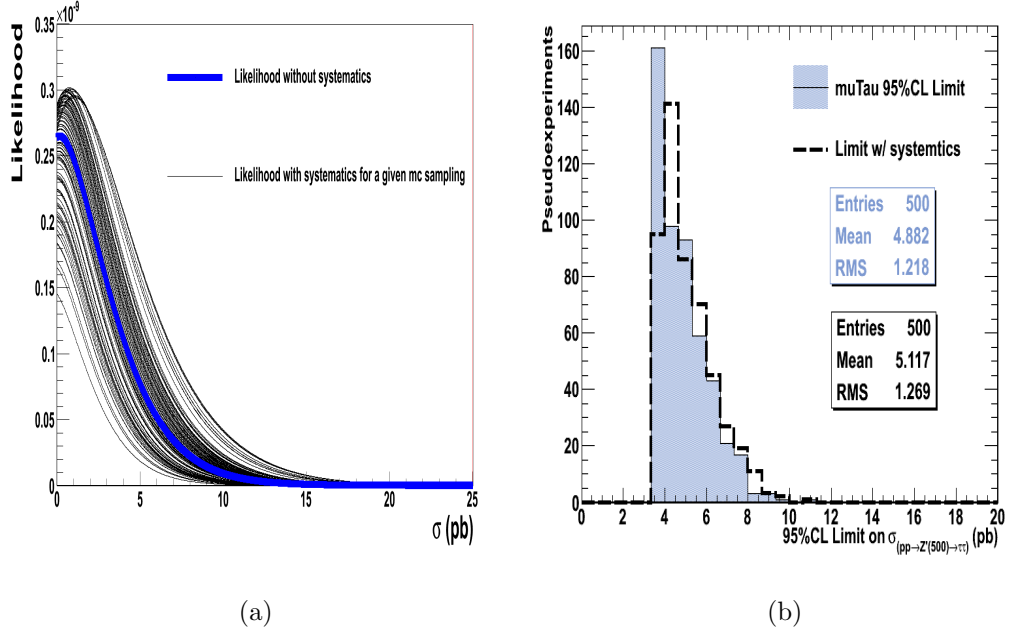


Figure 4.19: (a) Poisson likelihood, (b) 95% C.L. limits for a sample of pseudo-experiments.

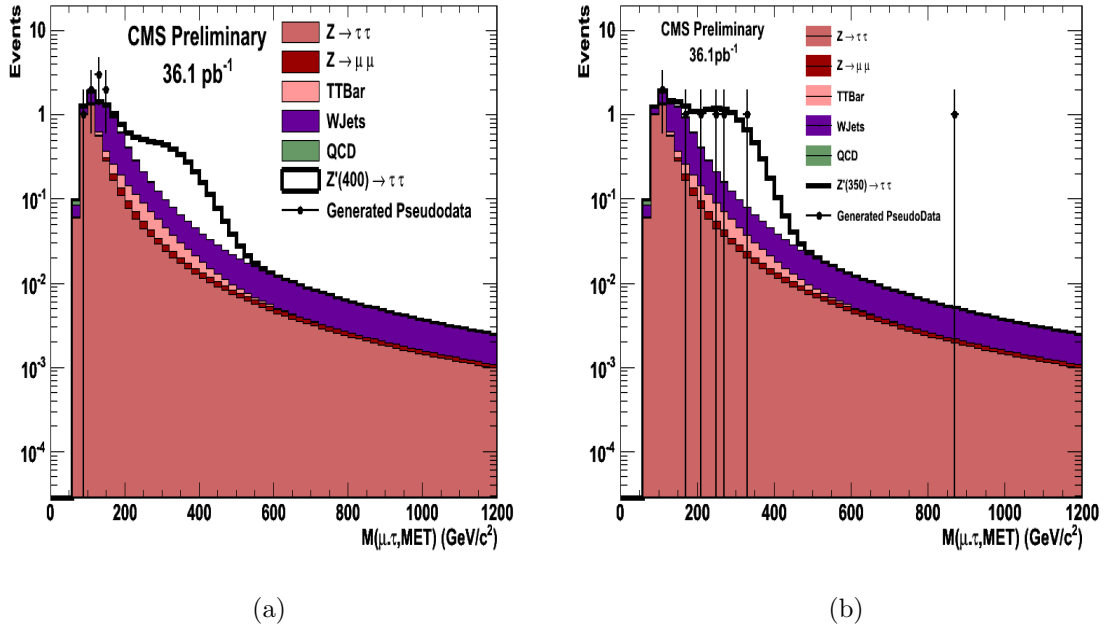


Figure 4.20: (a) Example of pseudo-experiment (with $Z'(400)$) resulting in $\sigma_{95} = 4.4$ pb (b) Example of pseudo-experiment (with $Z'(350)$) resulting in $\sigma_{95} = 12.8$ pb.

CHAPTER 4. SEARCH FOR $Z' \rightarrow \tau\tau$ USING LHC COLLISION DATA OF RUN 2010 COLLECTED WITH CMS DETECTOR

likelihood distribution. But if some events in pseudo-data fluctuate towards the high mass region, this will result in high value of the limit which may not allow us to set a stringent exclusion limit or claiming a discovery as long as the statistics are low. Figure 4.20(a) shows an example from $\tau_\mu\tau_h$ final state where the pseudo-data has fallen mostly in the low mass region, resulting in an expected cross section $\sigma_{95} = 4.4$ pb while Figure 4.20(b) shows an example where data has fluctuated unluckily into high mass region, resulting in a higher limit $\sigma_{95} = 12.8$ pb.

As mentioned in the previous Section, the combined $Z' \rightarrow \tau\tau$ search, performed by High- p_T Tau Group at CMS involves three additional final states: $\tau_e\tau_h$, $\tau_\mu\tau_h$ and $\tau_e\tau_\mu$, therefore, the joint likelihood is calculated using all the four decay modes as follows:

$$\mathcal{L}_{total} = \mathcal{L}(\tau_h\tau_h) * \mathcal{L}(\tau_\mu\tau_h) * \mathcal{L}(\tau_e\tau_h) * \mathcal{L}(\tau_e\tau_\mu) \quad (4.14)$$

4.11 Results and Conclusions

Figure 4.21 shows the invariant mass distributions for data, backgrounds, and signal (Z') of mass $350 \text{ GeV}/c^2$ and $700 \text{ GeV}/c^2$, respectively for fully hadronic final state. The number of observed events in collision data are in agreement with the expected number of events in MC and the observed mass spectrum does not reveal the $Z' \rightarrow \tau\tau$ production. Therefore, 95% C.L. upper limit on the $Z' \rightarrow \tau\tau$ production cross-section are determined as a function of Z' mass. Figure 4.22 shows the expected and experimental limits on the cross-section as well as the theoretical cross-section for varying Z' masses. The bands on the expected limits represent the 1σ and 2σ deviations obtained using a large number of pseudo-experiments where pseudo-data is obtained from background only distributions using a Poisson based random event generator. For the sake of completeness, the signal mass distributions for other three channels: $\tau_\mu\tau_h$, $\tau_e\tau_h$, and $\tau_e\tau_\mu$ are also shown in the Figure 4.23. It can be seen that from Figure 4.22, although the $\tau_e\tau_\mu$ final state is cleaner than $\tau_\mu\tau_h$ or $\tau_e\tau_h$ final state, the upper limit is larger due to the relatively smaller branching fraction of $\tau_e\tau_\mu$ final

4.11. RESULTS AND CONCLUSIONS

state. The upper limit on the Z' production cross-section times branching ratio to tau-pair can be determined from the point where experimental limit on the cross-section exceeds the theoretical value. It can be seen from Figure 4.24 that a $Z' \rightarrow \tau\tau$ with mass less than 468 GeV/c^2 can be excluded at 95% confidence level, assuming Standard Model couplings [65]. This limit exceeds the limit provided by the CDF experiment at Tevatron [1] in 2005.

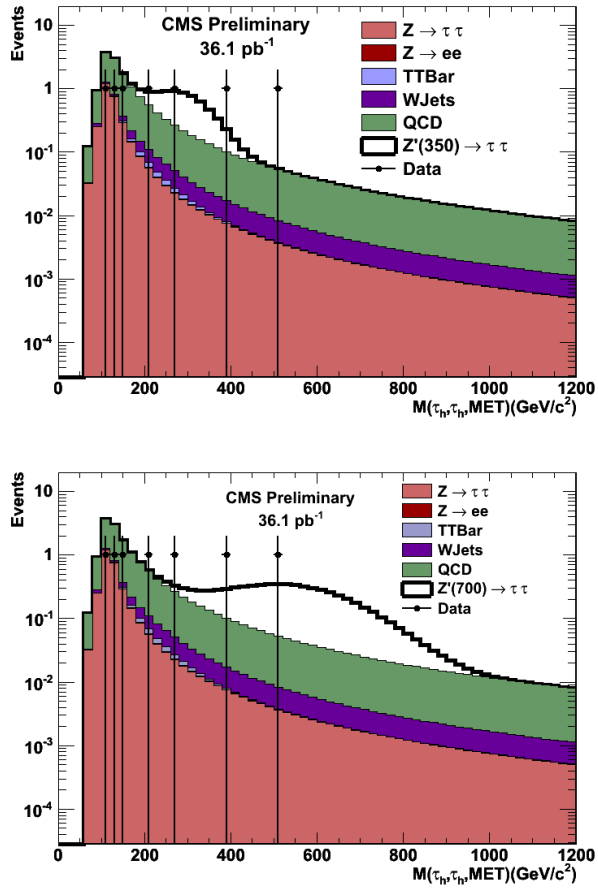
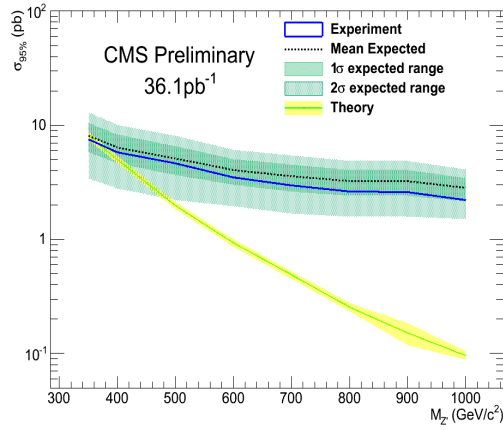
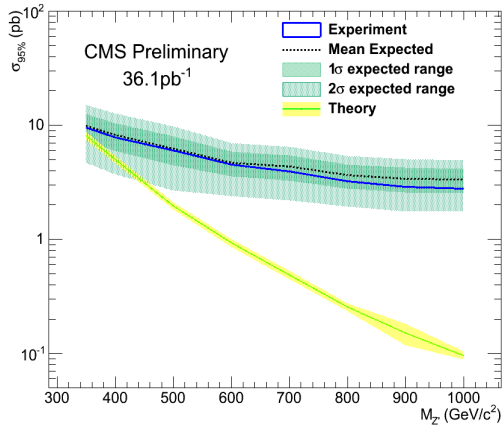


Figure 4.21: $\tau\tau$ invariant mass distributions for data, backgrounds, and signal, after all cuts for a Z' with mass of 350 GeV/c^2 (top) and 700 GeV/c^2 (bottom).

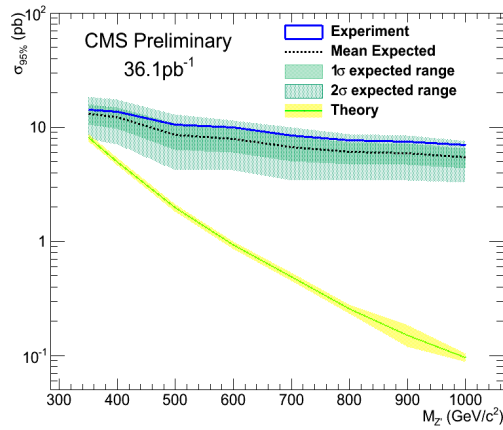
CHAPTER 4. SEARCH FOR $Z' \rightarrow \tau\tau$ USING LHC COLLISION DATA OF RUN 2010 COLLECTED WITH CMS DETECTOR



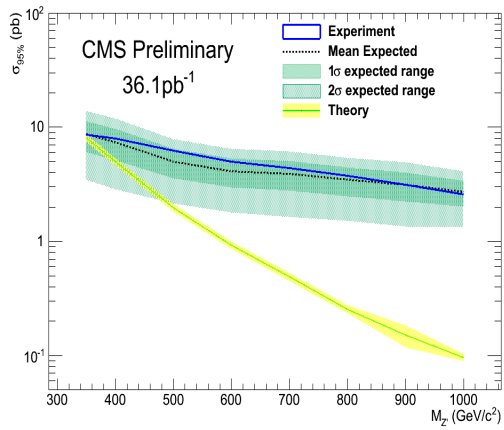
(a)



(b)



(c)



(d)

Figure 4.22: 95% C.L. upper limits on the cross-section for (a) $\tau_\mu\tau_h$, (b) $\tau_e\tau_h$, (c) $\tau_e\tau_\mu$, and (d) $\tau_h\tau_h$ channels.

4.11. RESULTS AND CONCLUSIONS

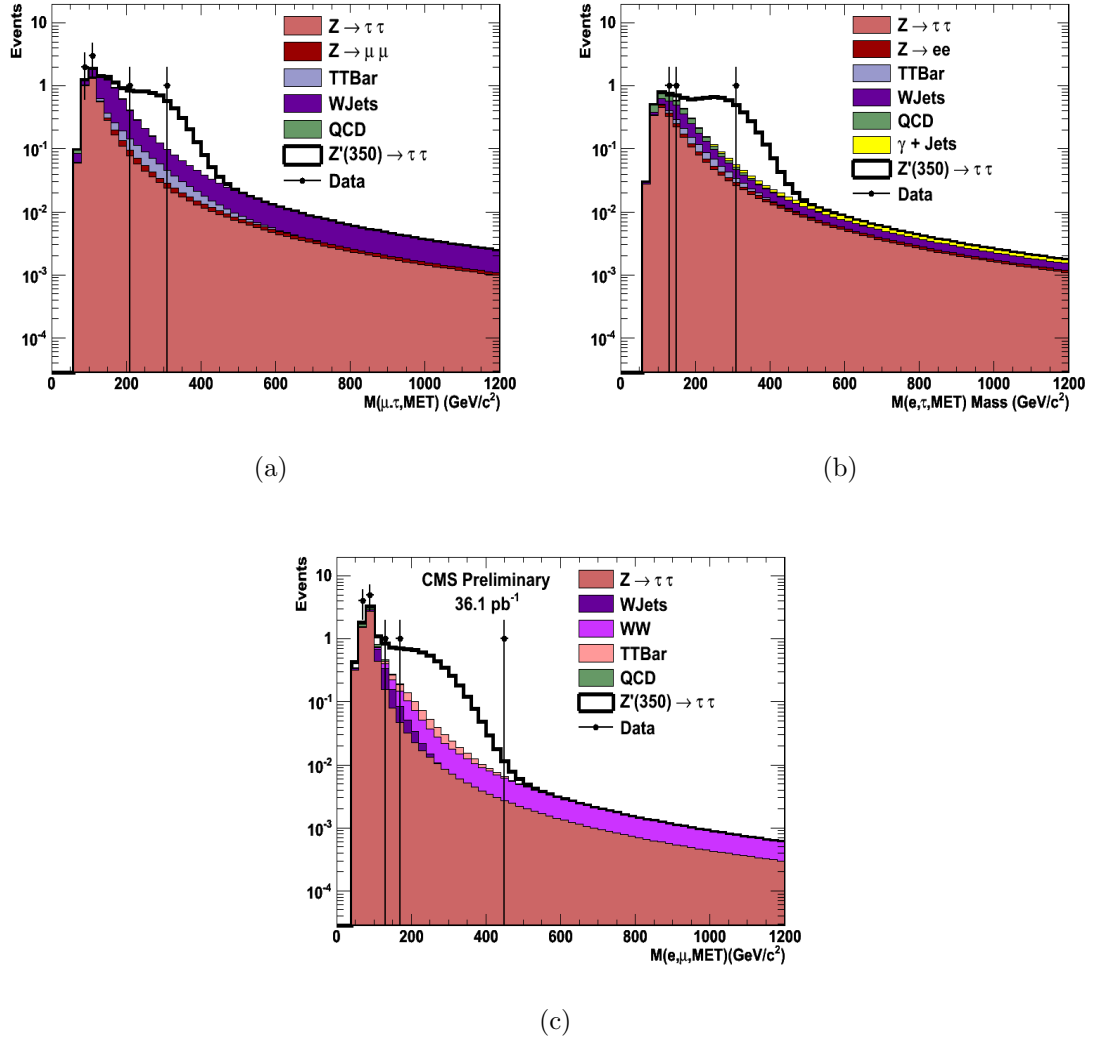


Figure 4.23: $\tau\tau$ invariant mass distributions for (a) $\tau_\mu\tau_h$, (b) $\tau_e\tau_h$, (c) $\tau_e\tau_\mu$, after all cuts for a Z' with mass of $350 \text{ GeV}/c^2$.

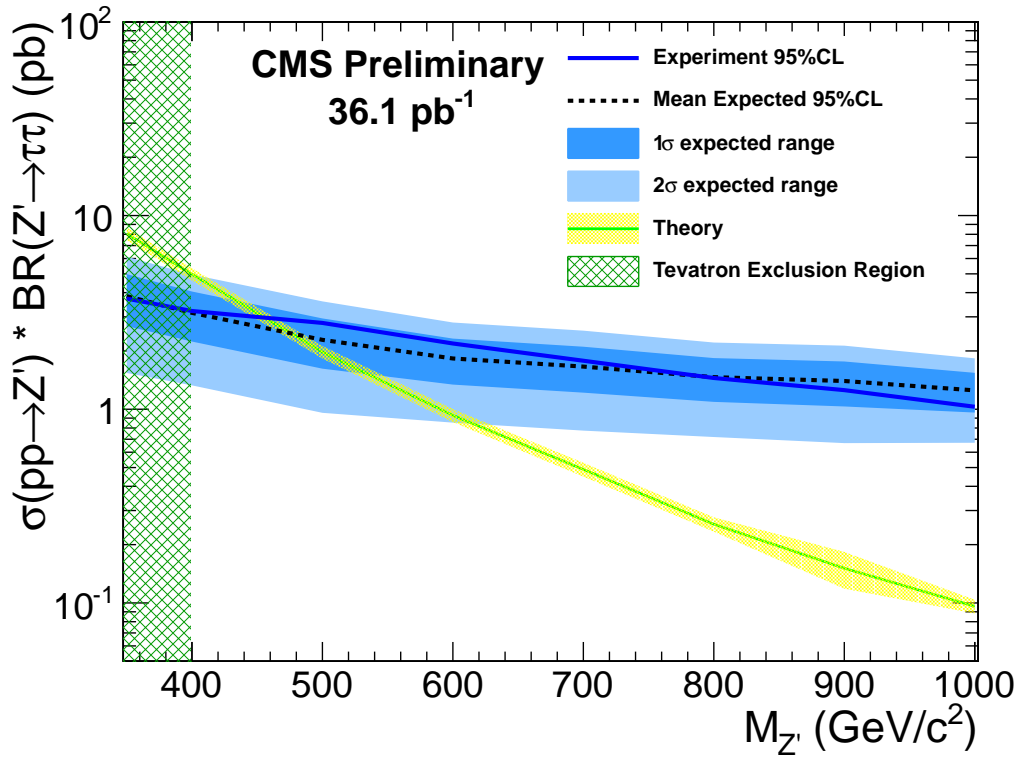


Figure 4.24: Combined $= \tau_\mu\tau_h + \tau_e\tau_h + \tau_e\tau_\mu + \tau_h\tau_h$ limit on the $Z' \rightarrow \tau\tau$ production cross-section as a function of Z' mass.

5

Search for $Z' \rightarrow \tau\tau$ using LHC collision data of Run 2011 collected with CMS detector

5.1 Introduction

The Large Hadron Collider at CERN started proton-proton collisions at $\sqrt{s} = 7$ TeV on March 14th, 2011 after a successful operation in Year 2010 and then with a short machine developement stop. In view of Year 2011 data with larger statistics, it was quite natural to search for $Z' \rightarrow \tau\tau$ with this new data. This Chapter deals with the search for $Z' \rightarrow \tau\tau$ production, using LHC collision data of Run 2011 at 7 TeV centre-of-mass energy. Most of the techniques employed in this analysis are same as the ones used with Run 2010 data. Therefore, only the techniques which have changed between the Run 2010 and Run 2011 analyses are listed in details in this Chapter. The studies presented in this Chapter focus mainly on the search for $Z' \rightarrow \tau\tau$ in the fully hadronic tau final state. The final results from the complimentary studies performed in other three decay modes of $Z' \rightarrow \tau\tau$ process: $\tau_\mu\tau_h$, $\tau_e\tau_h$, and $\tau_e\tau_\mu$ are also presented in this Chapter. In order to increase the sensitivity of this search, results from various final states are combined together taking into account the correlations

CHAPTER 5. SEARCH FOR $Z' \rightarrow \tau\tau$ USING LHC COLLISION DATA OF RUN 2011 COLLECTED WITH CMS DETECTOR

among different channels.

Since the number of proton bunches per beam increased significantly in going from LHC Run 2010 to Run 2011, the number of pile-up interactions (multiple number of interactions in a single bunch crossing) also increased with a non-negligible amount. There were ~ 2.2 average pile-up interactions per event in Run 2010, while in Run 2011 the average number of pile-up interactions increased up to ~ 6 interactions per bunch crossing (per event recorded). The number of generated pile-up interactions present in the MC samples used for this analysis did not match with the number of pile-up interactions present in the collision data, hence, some special pile-up reweighting techniques had to be applied to MC in order to match with the number of pile-up interactions present in the collision data. The details on this technique are given in the next Section.

5.2 Pile-Up Reweighting

The signal-like events were selected from the “Tau” primary datasets of the LHC collision data. The Monte Carlo samples used for this analysis were generated with PYTHIA and MADGRAPH event generators, while the decays of tau-leptons were simulated with the TAUOLA package. The full list of MC samples used in the analysis is given in the Section 3.8.2.

The Summer 11 MC (official CMS samples corresponding to LHC Run 2011) used for this study, were generated with a flat + Poissonian tail pile-up distribution which differed from the pile-up distribution observed in the collision data. Hence, all the MC samples were reweighted in order to match with the pile-up distribution present in the collision data. The pile-up spectrum for collision data was taken from the centrally produced distributions taking into account the per bunch-crossing-per-luminosity-section instantaneous luminosity from the Luminosity Database (LumiDB) together with the total pp inelastic cross-section. The pile-up weights were calculated by comparing the pile-up distribution in data with the generated pile-up interaction distribution in the MC. The resulting weights, also called pile-up weights, are denoted

as:

$$w(i) = \frac{H^{Data}(i)}{H^{MC}(i)} \quad (5.1)$$

where H denotes the histogram for pile-up distribution and i denotes the number of pile-up interactions present in the event. These weights are applied to the MC samples and the effect of this reweighting is shown in the Figure 5.1.

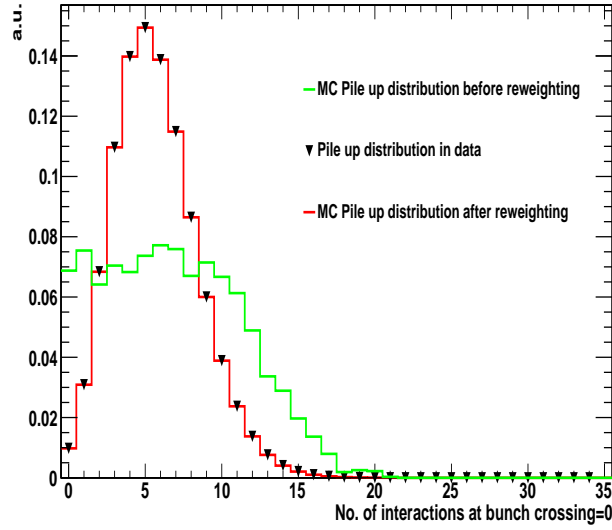


Figure 5.1: Distribution of number of pile-up interactions in a Summer 11 MC sample ($Z \rightarrow \tau\tau$) before and after reweighting. The pile-up distribution in collision data is also overlayed. The pile-up distribution in MC matches with the distribution in the collision data after pile-up reweighting is applied.

5.3 Event Selection

In order to select the signal-like events, a set of loose pre-selections is applied. The complete list of pre-selections is given below.

5.3.1 Skimming Criteria

- Event should have ≥ 2 particle flow τ 's with $p_T > 15$ GeV/c, $|\eta| < 2.1$, containing a leading pion with $p_T > 5$ GeV/c.

CHAPTER 5. SEARCH FOR $Z' \rightarrow \tau\tau$ USING LHC COLLISION DATA OF RUN 2011 COLLECTED WITH CMS DETECTOR

- Event should have ≥ 1 τ -pair with $\Delta R > 0.7$, where $\Delta R = \sqrt{\Delta\eta^2 + \Delta\phi^2}$ with $\Delta\eta$ and $\Delta\phi$ being distances in pseudorapidity and azimuthal angle between two taus. The choice of this ΔR requirement is based on the jet reconstruction algorithm from which hadronic taus are reconstructed.

As in the analysis with 2010 data, the triggers are not applied at the skim level for MC samples to avoid any differences between MC and the collision data at the skim level. Table 5.1 shows the MC skim efficiencies for various background processes. There is no pre-selection applied for the signal samples. It is believed that the MC simulated samples are not able to correctly model some rare features of QCD multijet background such as the probability for a jet to fake a tau-lepton due to the hadronization of quarks and/or gluons. For this reason, the extraction of QCD multijet background is performed with a data-driven method, hence, it is not shown in the Table of skim efficiencies.

Sample	$\sigma \times$ Filter Efficiency (pb)	Events processed	Final N events	ϵ^{Skim}
$Z \rightarrow ee$	1666	2240027	619908	0.2767
$Z \rightarrow \tau\tau$	1666	2032536	251855	0.1239
$W + jets$	31314	80945819	5492066	0.0678
$t\bar{t}$	165	1089625	45234	0.0415
QCD multijet	Data-driven	—	—	—

Table 5.1: Table showing the skim efficiencies.

5.3.2 Signal Selections

The event selection criteria for this analysis remains the same as that of the analysis with 2010 data (Chapter 4). The main difference comes from different tau-identification algorithm used in this analysis. In the 2010 analysis, the taus were identified with a simple cone algorithm, also known as shrinking cone algorithm, however for this analysis the hadronic taus are reconstructed using the Hadron-Plus-Strips (HPS) algorithm. The details of this algorithm have been discussed in the

5.3. EVENT SELECTION

Subsection 3.5.2 of Chapter 3. The event selection criteria is divided into three categories: kinematic and geometric acceptance, tau-lepton identification, and topological selections. The surviving pairs of tau candidates are kept at each intermediate stage in the selections. If an event has more than one pair of unique tau candidates passing all the selections, the tau-pair with the highest invariant mass is selected. This requirement ensures the selection of a single tau-pair candidate (passing all the selections) per event. An explicit check shows that this requirement has an efficiency of 100%. The full list of online and offline selection cuts is given below.

- **Online Event Selection**

Apart from selecting signal-like events, the purpose of online selections is to preserve a maximum fraction of the $Z \rightarrow \tau\tau$ events which are then used to validate the tau-identification selections for the $Z' \rightarrow \tau\tau$ analysis. Taking this fact into account, the un-prescaled double-tau triggers having lowest p_T thresholds have been used to select the events of interest from the collision data. With the increase in the instantaneous luminosity during data taking, various triggers had to be prescaled in order to cope with the total bandwidth permissible for the recording of events. The combination of various double-tau triggers i.e.

*HLT_DoubleIsoPFTau20_Trk5_v**, *HLT_DoubleIsoPFTau25_Trk5_eta2p1_v**,

*HLT_DoubleIsoPFTau35_Trk5_eta2p1_v**, *HLT_DoubleIsoPFTau40_Trk5_eta2p1_v**,

*HLT_DoubleIsoPFTau45_Trk5_eta2p1_v**, and *HLT_IsoPFTau40_IsoPFTau30_Trk5_eta2p1_v**

was used to select signal-like events from the collision data, depending upon the run-range summarized in Table 5.2. Note that here “*” represents different versions of the double-tau trigger depending upon the run range categories.

- **Offline Event Selection**

- **Acceptance:**

- * Event should have atleast two particle flow τ 's with $|\eta| < 2.1$, $p_T > 35$ GeV/ c having leading track $p_T > 5$ GeV/ c .

- **τ_h Identification:**

CHAPTER 5. SEARCH FOR $Z' \rightarrow \tau\tau$ USING LHC COLLISION DATA OF RUN 2011 COLLECTED WITH CMS DETECTOR

Details of the HLT Trigger Paths		
Trigger path	HLT Thresholds	Run range
HLT_DoubleIsoPFTau20_Trk5_v*	$p_T > 20 \text{ GeV}/c, \eta < 5.0$	163269-163869
HLT_DoubleIsoPFTau25_Trk5_eta2p1_v*	$p_T > 25 \text{ GeV}/c, \eta < 2.1$	165071-165633
HLT_DoubleIsoPFTau35_Trk5_eta2p1_v*	$p_T > 35 \text{ GeV}/c, \eta < 2.1$	165970-167913
HLT_DoubleIsoPFTau40_Trk5_eta2p1_v*	$p_T > 40 \text{ GeV}/c, \eta < 2.1$	166970-167913
HLT_DoubleIsoPFTau45_Trk5_eta2p1_v*	$p_T > 45 \text{ GeV}/c, \eta < 2.1$	170249-180252
HLT_IsoPFTau40_IsoPFTau30_Trk5_eta2p1_v*	$p_{T\tau_1, \tau_2} > 40, 30 \text{ GeV}/c, \eta _{\tau_1, \tau_2} < 2.1$	173692-178365

Table 5.2: Summary of the trigger paths according to the run-range applied on the collision data.

- * **Crack Veto:** The crack veto prevents the tau-leptons to fall into the crack region of the CMS detector. A crack region is a region of the CMS detector where there is no detection material present and it serves as the exit path for cables, services, and extra ancillary from tracker and calorimeter sub-detectors of the CMS detector. In terms of the pseudorapidity, the crack region is defined as the region between:
 - $|\eta| < 0.018$
 - $0.423 < |\eta| < 0.461$
 - $0.770 < |\eta| < 0.806$
 - $1.127 < |\eta| < 1.163$
 - $1.460 < |\eta| < 1.558$
- * **Rejection of muons faking tau-leptons:** Since a hadronically decaying tau-lepton can be faked by a muon, hence, a muon veto is applied to remove the muons misidentified as hadronically decaying tau-leptons. For this purpose, tau-lepton is required to have leading track that cannot be matched to a global muon track. For this analysis, loose working point of muon discriminator has been chosen.

5.3. EVENT SELECTION

- * **Rejection of electrons faking tau-leptons:** The electrons can also fake hadronically decaying tau-leptons, hence, an electron veto is imposed to remove the electrons which are misidentified as hadronically decaying tau-leptons. The electron veto requires the HPS taus to pass a discriminator which uses the information of the HCAL energy associated to the tau-lepton with respect to the measured momentum of the leading track of the tau-lepton (H/p). Additionally, the discriminator considers the amount of electromagnetic energy deposited in a narrow strip around the leading track with respect to the total electromagnetic energy of the tau-lepton. Finally, the HPS tau-leptons must not reside inside the ECAL cracks. For this analysis, medium working point of electron discriminator has been chosen.
- * **Decay Mode Finding Algorithm:** The decay mode finding (DMF) algorithm looks for the probability of decay of tau-leptons. It is imposed by requiring both tau-leptons to pass a DMF discriminator value > 0.5 .
- * **Single prong requirement:** It is required that both tau-leptons in the event should have exactly one signal track.
- * **Fake tau rejection:** Since the hadronically decaying tau-leptons produce narrow pencil like calorimetric signatures, the tau-leptons in the event are required to be isolated by demanding that there should be no track in the isolation region. Loose working point (Table 3.2) has been chosen for this analysis as a balance between the background rejection and jet-to-tau fake rate. The last two requirements are very effective against QCD multijet background.

– **Topological requirements:**

- * **Opposite sign charge requirement:** The tau-leptons forming the pair should have opposite-sign charges (determined from the sign of the leading charged hadrons) *i.e.* $Q(\tau_1) = -Q(\tau_2)$. Due to the electric charge neutrality of Z' gauge boson, the pair of tau-leptons coming from

CHAPTER 5. SEARCH FOR $Z' \rightarrow \tau\tau$ USING LHC COLLISION DATA OF RUN 2011 COLLECTED WITH CMS DETECTOR

Z' should have opposite charge. This requirement also provides a good handle to reject QCD multijet background.

* **Strong anti-parallelism:** Since Z' gauge boson is supposed to be quite heavy, the tau-leptons coming from its decay are expected to be almost back-to-back. Hence, the event is required to have tau-lepton pairs where the tau-leptons are nearly back-to-back *i.e.*:

- $-1 \leq \cos(\Delta\phi(\tau_1, \tau_2)) \leq -0.95$.

* **Missing transverse energy requirement:** Due to the presence of two neutrinos in the double hadronic tau final state, a fair amount of missing transverse energy is expected in the signal events. For this reason, an event is required to have missing transverse energy (E_T) > 20 GeV. This threshold is chosen in a way to provide the best background suppression while preserving maximum fraction of $Z \rightarrow \tau\tau$ events required to validate the tau-identification criteria.

* **ζ cut:** The event is required to satisfy the following condition:

- $P_\zeta - 0.875 \times P_\zeta^{vis} > -7$.

This requirement is specially important to suppress the contribution of $W + jets$ and $t\bar{t}$ backgrounds.

* **Anti b-tagging:** In order to suppress the contribution of $t\bar{t}$ background, a b-veto is applied. The Track Counting High Efficiency Medium Discriminator (TCHEM) has been used to remove the contamination from b-jets. The track counting algorithm identifies a b-jet if there are atleast N tracks on a secondary vertex with an impact parameter significance above a given threshold. It is required that there should be no b-jet in the event identified using TCHEM discriminator.

5.4. ESTIMATION OF SELECTION EFFICIENCIES USING MONTE-CARLO CUT-BASED METHOD

5.4 Estimation of Selection Efficiencies using Monte-Carlo Cut-based Method

The Tables 5.3, 5.4, 5.5, and 5.6 show the relative efficiencies for various selections, both for signal and relevant SM background processes. The relative efficiencies are defined with respect to the number of events passing previous selections as described below:

$$\epsilon_{rel} = \frac{\text{Number of events passing (i+1)}^{th} \text{ cut}}{\text{Number of events passing i}^{th} \text{ cut}} \quad (5.2)$$

5.5 Di-Tau Trigger Efficiency Measurement Using Fake Taus

The tau trigger at CMS involves three steps: Level-1 (L1), Level-2 (L2), and Level-3 (L3). At the first step, the tau trigger is seeded at Level-1 with either a “Tau-Jet” or a “Central-Jet”. A Level-1 Tau-jet is defined as an isolated jet satisfying “Tau veto” requirements. The isolation is imposed by requiring that the energy of the jet should be contained within the two square regions of the calorimeters, each region spanning 4x4 trigger towers (TT), i.e. 20° in ϕ and 0.348 in η . The purpose of the tau-veto is to ensure that the individual energy deposits are contained within squares of 2x2 TT, each square being 5° in ϕ and 0.087 in η . Since high energy jets have a higher probability of having spread of particles, hence, more probability of failing the isolation requirement due to “leakage”. Level-1 jets that fail the veto or isolation requirements but pass a higher transverse energy (E_T) threshold than the tau-jet threshold, *e.g.*, 28 vs 52 GeV, are classified as central jets. At Level-2, the trigger simply requires the presence of a jet above the threshold seeded by the Level-1. Finally, the Level-3 of the trigger requires a PF tau whose jet is matched to the Level-2 jet. The PF tau is required to be isolated and it should have a leading track with $p_T > 5$ GeV/c. The isolation condition on PF tau requires that there should be

CHAPTER 5. SEARCH FOR $Z' \rightarrow \tau\tau$ USING LHC COLLISION DATA OF RUN 2011 COLLECTED WITH CMS DETECTOR

Cut-wise event selection efficiency estimated from Monte-Carlo

Cut	Collision Data	$t\bar{t}$	W+jets	$Z \rightarrow ee$	$Z \rightarrow \tau\tau$
Skimming	0.5256 ± 0.0001	0.8923 ± 0.0003	0.0560 ± 0.0000	0.2690 ± 0.0003	0.1123 ± 0.0002
Preselection	0.8390 ± 0.0001	0.8568 ± 0.0004	0.5217 ± 0.0002	0.7827 ± 0.0005	0.5045 ± 0.0010
$35 \leq \text{LL } p_T$	0.7776 ± 0.0001	0.8105 ± 0.0004	0.7401 ± 0.0003	0.8391 ± 0.0005	0.5013 ± 0.0015
$35 \leq \text{SL } p_T$	0.4954 ± 0.0002	0.5419 ± 0.0006	0.3606 ± 0.0004	0.6367 ± 0.0008	0.2449 ± 0.0018
LL $ \eta \leq 2.1$	0.9913 ± 0.0001	0.9909 ± 0.0002	0.9763 ± 0.0002	0.9771 ± 0.0003	0.9772 ± 0.0013
SL $ \eta \leq 2.1$	0.9913 ± 0.0001	0.9906 ± 0.0002	0.9774 ± 0.0002	0.9810 ± 0.0003	0.9797 ± 0.0012
$0.7 \leq \Delta R(\text{LL}, \text{SL})$	0.9990 ± 0.0000	0.9887 ± 0.0002	0.9973 ± 0.0001	0.9998 ± 0.0000	0.9990 ± 0.0003
$5 \leq \text{LL Leading track } p_T$	0.9864 ± 0.0001	0.9780 ± 0.0002	0.9851 ± 0.0002	0.9870 ± 0.0002	0.9532 ± 0.0018
$5 \leq \text{SL Leading track } p_T$	0.9853 ± 0.0001	0.9718 ± 0.0003	0.9744 ± 0.0002	0.9823 ± 0.0003	0.9535 ± 0.0019
LL Crack veto	0.9055 ± 0.0002	0.9253 ± 0.0005	0.9031 ± 0.0004	0.9071 ± 0.0006	0.8968 ± 0.0027
SL Crack veto	0.9013 ± 0.0002	0.9230 ± 0.0005	0.9021 ± 0.0004	0.8994 ± 0.0006	0.9041 ± 0.0028
LL Medium electron veto	0.8914 ± 0.0002	0.8531 ± 0.0007	0.7126 ± 0.0007	0.0390 ± 0.0004	0.8672 ± 0.0034
SL Medium electron veto	0.9317 ± 0.0002	0.8914 ± 0.0006	0.8216 ± 0.0007	0.1045 ± 0.0035	0.8727 ± 0.0036

Table 5.3: Cut flow relative efficiency table, calculated from raw generator events in case of MC, i.e., before pile-up reweighting or normalization to luminosity. These efficiencies are rounded off to the last decimal shown. “LL” refers to the leading leg, and “SL” to the subleading leg. The skimming selects events with at least one pair of HPS taus, each of which must have a leading track p_T of at least 5 GeV/c, and pass the HPS discriminant by decay mode finding. The preselection is applied to both legs and involves a p_T cut of 20 GeV/c, $|\eta| < 2.2$, and HPS discriminant by decay mode finding set to true (selects 1 or 3 prong taus).

5.5. DI-TAU TRIGGER EFFICIENCY MEASUREMENT USING FAKE TAUS

Cut-wise event selection efficiency estimated from Monte-Carlo					
Cut	Collision Data	$t\bar{t}$	W+jets	$Z \rightarrow ee$	$Z \rightarrow \tau\tau$
LL Loose muon veto	0.9860 ± 0.0001	0.8598 ± 0.0007	0.5871 ± 0.0009	0.9962 ± 0.0022	0.9192 ± 0.0031
SL Loose muon veto	0.9868 ± 0.0001	0.9131 ± 0.0006	0.7292 ± 0.0011	0.9936 ± 0.0029	0.9127 ± 0.0034
LL Loose isolation	0.0616 ± 0.0002	0.0219 ± 0.0004	0.1218 ± 0.001	0.25100 ± 0.0156	0.4707 ± 0.0063
SL Loose isolation	0.0663 ± 0.0007	0.0175 ± 0.0021	0.024 ± 0.0013	0.18460 ± 0.0278	0.3409 ± 0.0087
LL HPS decay mode finding	$1 \pm 0.$	$1 \pm 0.$	$1 \pm 0.$	$1 \pm 0.$	$1 \pm 0.$
SL HPS decay mode finding	$1 \pm 0.$	$1 \pm 0.$	$1 \pm 0.$	$1 \pm 0.$	$1 \pm 0.$
LL Signal tracks = 1	0.7107 ± 0.0049	0.8333 ± 0.0459	0.7601 ± 0.0230	$1 \pm 0.$	0.7921 ± 0.0127
SL Signal tracks = 1	0.7651 ± 0.0055	0.7273 ± 0.0601	0.7909 ± 0.0251	$1 \pm 0.$	0.8383 ± 0.0130
Charge Product = -1	0.6032 ± 0.0072	0.775 ± 0.0660	0.8077 ± 0.0273	0.8889 ± 0.0524	0.9852 ± 0.0047
$-1 \leq \cos \Delta\phi(LL, SL) \leq -0.95$	0.6634 ± 0.0090	0.1613 ± 0.0661	0.3690 ± 0.0372	0.8438 ± 0.0642	0.6777 ± 0.0181
$20 \leq \cancel{E}_T$	0.2220 ± 0.0097	$1 \pm 0.$	0.5484 ± 0.0632	0.1481 ± 0.0684	0.2244 ± 0.0197
$-7 \leq \zeta$	0.6404 ± 0.0238	0.4000 ± 0.2191	0.3529 ± 0.082	$1 \pm 0.$	0.7525 ± 0.0429
Btags = 0	0.9885 ± 0.0066	$0. \pm 0.$	$1 \pm 0.$	$1 \pm 0.$	0.9737 ± 0.0184

Table 5.4: Cut flow relative efficiency table, calculated from raw generator events in case of MC, i.e., before pile-up reweighing or normalization to luminosity. These efficiencies are rounded off to the last decimal shown. “LL” refers to the leading leg, and “SL” to the subleading leg. The skimming selects events with at least one pair of HPS taus, each of which must have a leading track p_T of at least 5 GeV/c, and pass the HPS discriminant by decay mode finding. The preselection is applied to both legs and involves a p_T cut of 20 GeV/c, $|\eta| < 2.2$, and HPS discriminant by decay mode finding set to true (selects 1 or 3 prong taus).

CHAPTER 5. SEARCH FOR $Z' \rightarrow \tau\tau$ USING LHC COLLISION DATA OF RUN 2011 COLLECTED WITH CMS DETECTOR

Cut-wise event selection efficiency estimated from Monte-Carlo				
Cut	SSMZprime1000	SSMZprime350	SSMZprime500	SSMZprime750
Skimming	$1 \pm 0.$	$1 \pm 0.$	$1 \pm 0.$	$1 \pm 0.$
Preselection	0.7948 ± 0.0019	0.5700 ± 0.0021	0.6665 ± 0.0021	0.7545 ± 0.0019
$35 \leq LL$	0.9938 ± 0.0004	0.9679 ± 0.0010	0.9848 ± 0.0007	0.9926 ± 0.0004
$35 \leq SL$	0.9073 ± 0.0015	0.7512 ± 0.0025	0.8300 ± 0.0020	0.8850 ± 0.0016
LL $ \eta \leq 2.1$	0.9890 ± 0.0006	0.9776 ± 0.0010	0.9821 ± 0.0008	0.9873 ± 0.0006
SL $ \eta \leq 2.1$	0.9881 ± 0.0006	0.9777 ± 0.0010	0.9793 ± 0.0008	0.9837 ± 0.0007
$0.7 \leq \Delta R(LL, SL)$	0.9997 ± 0.0001	0.9992 ± 0.0002	0.9993 ± 0.0002	0.9994 ± 0.0001
$5 \leq LL$ Leading track p_T	0.9604 ± 0.0011	0.9527 ± 0.0015	0.9622 ± 0.0011	0.9628 ± 0.0010
$5 \leq SL$ Leading track p_T	0.9558 ± 0.0012	0.9466 ± 0.0016	0.9489 ± 0.0013	0.9526 ± 0.0012
LL Crack veto	0.9045 ± 0.0017	0.9002 ± 0.0022	0.9044 ± 0.0019	0.9046 ± 0.0016
SL Crack veto	0.8982 ± 0.0018	0.8904 ± 0.0024	0.8972 ± 0.0020	0.8968 ± 0.0018
LL Medium electron veto	0.7768 ± 0.0026	0.8066 ± 0.0032	0.7928 ± 0.0028	0.7787 ± 0.0026
SL Medium electron veto	0.7367 ± 0.0032	0.7718 ± 0.0038	0.7563 ± 0.0034	0.7438 ± 0.0031

Table 5.5: Cut flow relative efficiency table for the signal samples, calculated from raw generator events, i.e., before pile-up reweighing or normalization to luminosity. These efficiencies are rounded to the last decimal shown. “LL” refers to the leading leg, and “SL” to the subleading leg. The preselection is applied to both legs and involves a p_T cut of 20 GeV/c, $|\eta| < 2.2$, and HPS discriminant by decay mode finding set to true (selects 1 or 3 prong taus).

5.5. DI-TAU TRIGGER EFFICIENCY MEASUREMENT USING FAKE TAUS

Cut-wise event selection efficiency estimated from Monte-Carlo				
Cut	SSMZprime1000	SSMZprime350	SSMZprime500	SSMZprime750
LL Loose muon veto	0.8205 ± 0.0032	0.8534 ± 0.0036	0.8413 ± 0.0033	0.8275 ± 0.0031
SL Loose muon veto	0.7561 ± 0.004	0.80660 ± 0.0044	0.7877 ± 0.0040	0.7703 ± 0.0038
LL Loose isolation	0.5285 ± 0.0053	0.5770 ± 0.0061	0.5600 ± 0.0055	0.5342 ± 0.0051
SL Loose isolation	0.4127 ± 0.0072	0.4714 ± 0.0081	0.4551 ± 0.0074	0.4322 ± 0.0070
LL HPS decay mode finding	$1 \pm 0.$	$1 \pm 0.$	$1 \pm 0.$	$1 \pm 0.$
SL HPS decay mode finding	$1 \pm 0.$	$1 \pm 0.$	$1 \pm 0.$	$1 \pm 0.$
LL Signal tracks = 1	0.9138 ± 0.0064	0.8279 ± 0.0089	0.8423 ± 0.0080	0.8760 ± 0.0070
SL Signal tracks = 1	0.9400 ± 0.0057	0.8742 ± 0.0086	0.9056 ± 0.0070	0.9355 ± 0.0056
Charge Product = -1	0.9422 ± 0.0058	0.9792 ± 0.0040	0.9753 ± 0.0039	0.9583 ± 0.0047
$-1 \leq \cos \Delta\phi(LL, SL) \leq -0.95$	0.9626 ± 0.0048	0.9119 ± 0.0079	0.9138 ± 0.0071	0.9338 ± 0.0060
$20 \leq \cancel{E}_T$	0.9129 ± 0.0073	0.7414 ± 0.0129	0.8511 ± 0.0095	0.8731 ± 0.0083
$-7 \leq \zeta$	0.8737 ± 0.0090	0.8337 ± 0.0127	0.8450 ± 0.0104	0.8625 ± 0.0092
b-tags == 0	0.9748 ± 0.0045	0.9847 ± 0.0046	0.9763 ± 0.0048	0.9802 ± 0.0040

Table 5.6: Cut flow relative efficiency table for the signal samples, calculated from raw generator events, i.e., before pile-up reweighing or normalization to luminosity. These efficiencies are rounded to the last decimal shown. “LL” refers to the leading leg, and “SL” to the subleading leg. The preselection is applied to both legs and involves a p_T cut of 20 GeV/ c , $|\eta| < 2.2$, and HPS discriminant by decay mode finding set to true (selects 1 or 3 prong taus).

CHAPTER 5. SEARCH FOR $Z' \rightarrow \tau\tau$ USING LHC COLLISION DATA OF RUN 2011 COLLECTED WITH CMS DETECTOR

no track with $p_T > 1$ GeV/c and no photon with $E_T > 1.5$ GeV within the isolation region. The requirements at the Level-3 are quite similar to those used in the offline selections to identify the hadronic taus.

In order to measure the tau trigger efficiency, events passing the single muon triggers and having atleast one HPS tau, forming a pair with the isolated “global” muon, are selected from the collision data. The minimum ΔR between the muon and tau candidate is required to be atleast 0.7. The datasets used for this measurement are listed in Table 5.7. The denominator of the efficiency is defined as PFTau candidates at the HLT level matched to the offline tau, where the offline tau is defined as an HPS tau passing medium isolation, tight electron, and muon rejection. In addition, the offline $\mu + \tau_h$ pair is required to have an invariant mass, $M(\mu, \tau_h)$, between 30 and 75 GeV/c² in order to increase the purity of real taus.

The tau trigger efficiency is parameterized as a function of the each offline tau p_T as:

$$\epsilon = \epsilon_{Level-1} \times \epsilon_{Level-2} \times \epsilon_{Level-3}, \quad (5.3)$$

where the relative efficiencies of Level-1 and Level-2 are fitted with an error function, while the Level-3 relative efficiency is fitted with a constant (describing the plateau) minus an exponential function describing the inefficiency caused by the large background contamination present in the low p_T region. Since the thresholds applied to the trigger changed during the course of the data taking period, the measurement of trigger efficiency is carried out for each period separately. The triggers and thresholds for each run-period are listed in Table 5.8. The relative efficiencies for the four run-periods are shown in Figures 5.2, 5.3, 5.4 and 5.5.

5.6 Measurement and Validation of Signal Efficiencies

The simulation can accurately predict tau reconstruction and identification efficiencies in collision data as observed in other Z' decay final states *viz.* $\tau_\mu\tau_h$, $\tau_e\tau_h$, and $\tau_e\tau_\mu$. The origin of missing transverse energy in this case is also not particularly different from other final states, hence there is no reason to expect it to be less accurate in this

5.6. MEASUREMENT AND VALIDATION OF SIGNAL EFFICIENCIES

Dataset
/SingleMu/Run2011A-May10ReReco-v1/RAW-RECO
/SingleMu/Run2011A-PromptReco-v4/RAW-RECO
/SingleMu/Run2011A-PromptReco-v5/RAW-RECO
/SingleMu/Run2011A-PromptReco-v6/RAW-RECO
/SingleMu/Run2011B-PromptReco-v1/RAW-RECO

Table 5.7: Datasets used for the measurement of the trigger efficiency.

HLT Trigger	L1 seed	Run Period
DIsoPFTau20_Trk5	DTauJet28 OR DJet52	163269-165969
DIsoPFTau35_Trk5_eta2p1	DTauJet36 OR DJet52	165970-170248
DIsoPFTau45_Trk5_eta2p1_v{1-7}	DTauJet40_Eta2p17 OR DJet52_Central	170249-173198
DIsoPFTau45_Trk5_eta2p1_v8	DTauJet44_Eta2p17 OR DJet64_Central	173236-180252

Table 5.8: Triggers used during 2011 data taking period. The “D” in the HLT and Level-1 seed refers to “Double”.

case. The only significant difference in this final state is the use of the di-tau trigger, which brings a non-negligible inefficiency due to higher p_T threshold on taus and an imperfect efficiency plateau due to deficiency of high p_T taus.

Another difficulty in this final state is the inability to use the “standard candle” $Z \rightarrow \tau\tau$ events to validate signal efficiencies. This difficulty is due to the fact that any control region (extracted from collision data) targeting at the $Z \rightarrow \tau\tau$ process is overwhelmed by the QCD multijet backgrounds (due to the low mass of the Z boson) without significantly tightening and modifying the analysis selections. This is further hindered by the significant reduction in the $Z \rightarrow \tau\tau$ events due to the high p_T thresholds of the double hadronic tau trigger, which is required in order to maintain its rate to an acceptable level. We, therefore, rely on predictions from simulation in certain parts which have been validated in the other final states. The data-driven measurements are used to cross-check the results and to calculate correction factors

CHAPTER 5. SEARCH FOR $Z' \rightarrow \tau\tau$ USING LHC COLLISION DATA OF RUN 2011 COLLECTED WITH CMS DETECTOR

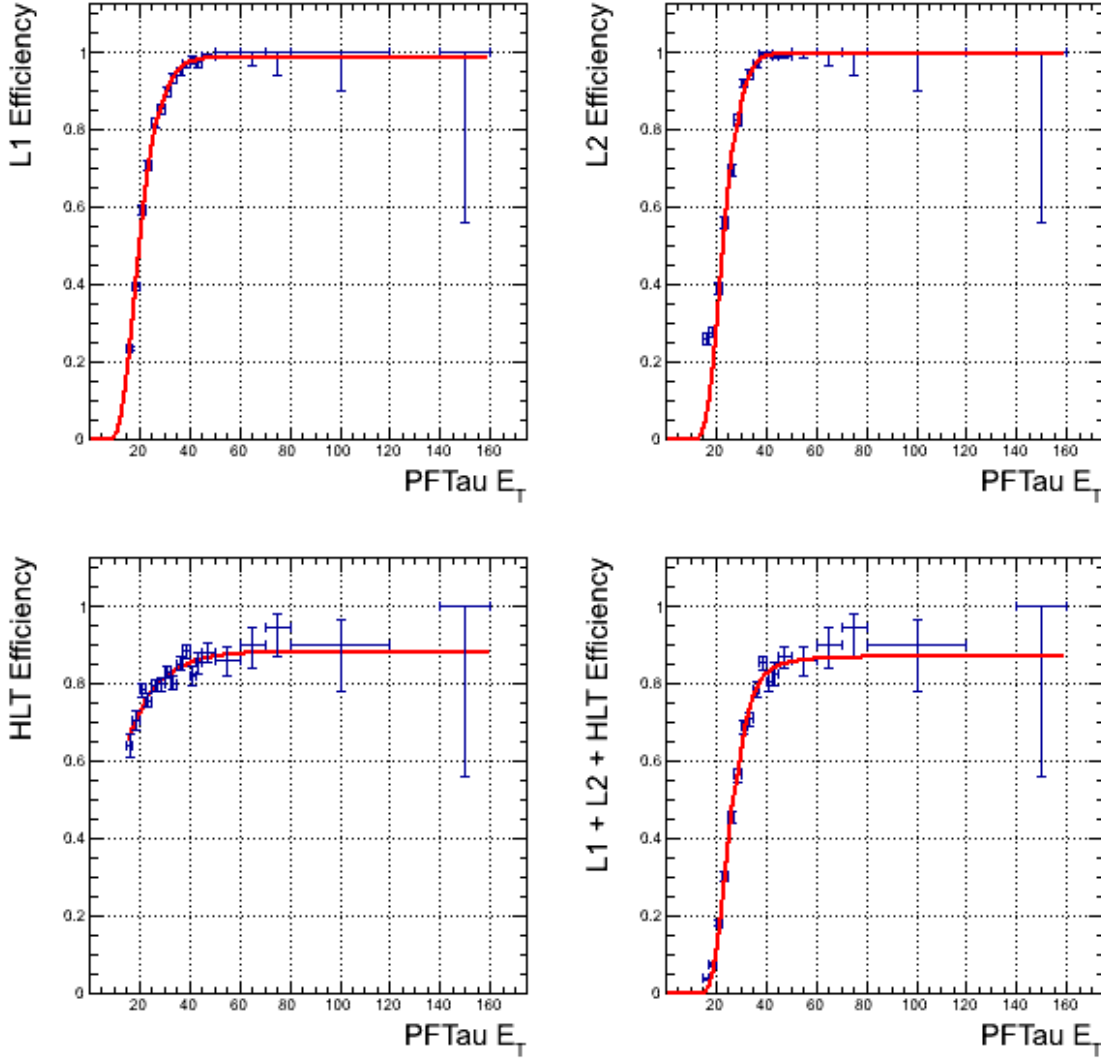


Figure 5.2: Level-1, Level-2, and Level-3 relative trigger efficiencies and overall trigger efficiency for HLT_DoubleIsoPFTau20_Trk5.

or efficiencies in areas where the simulation performance is not validated or known to be problematic *e.g.* due to low statistics. Since there are many similarities of $Z \rightarrow \tau\tau$ and signal topologies with the $Z \rightarrow ee$ events, the $Z \rightarrow ee$ events have been heavily used in order to obtain many of these additional measurements. From the reconstruction and identification point of view, the selection of true one-prong taus and electrons identified as one-prong taus are nearly identical. This allows for the validation of the isolation efficiency, which is the most important selection used

5.6. MEASUREMENT AND VALIDATION OF SIGNAL EFFICIENCIES

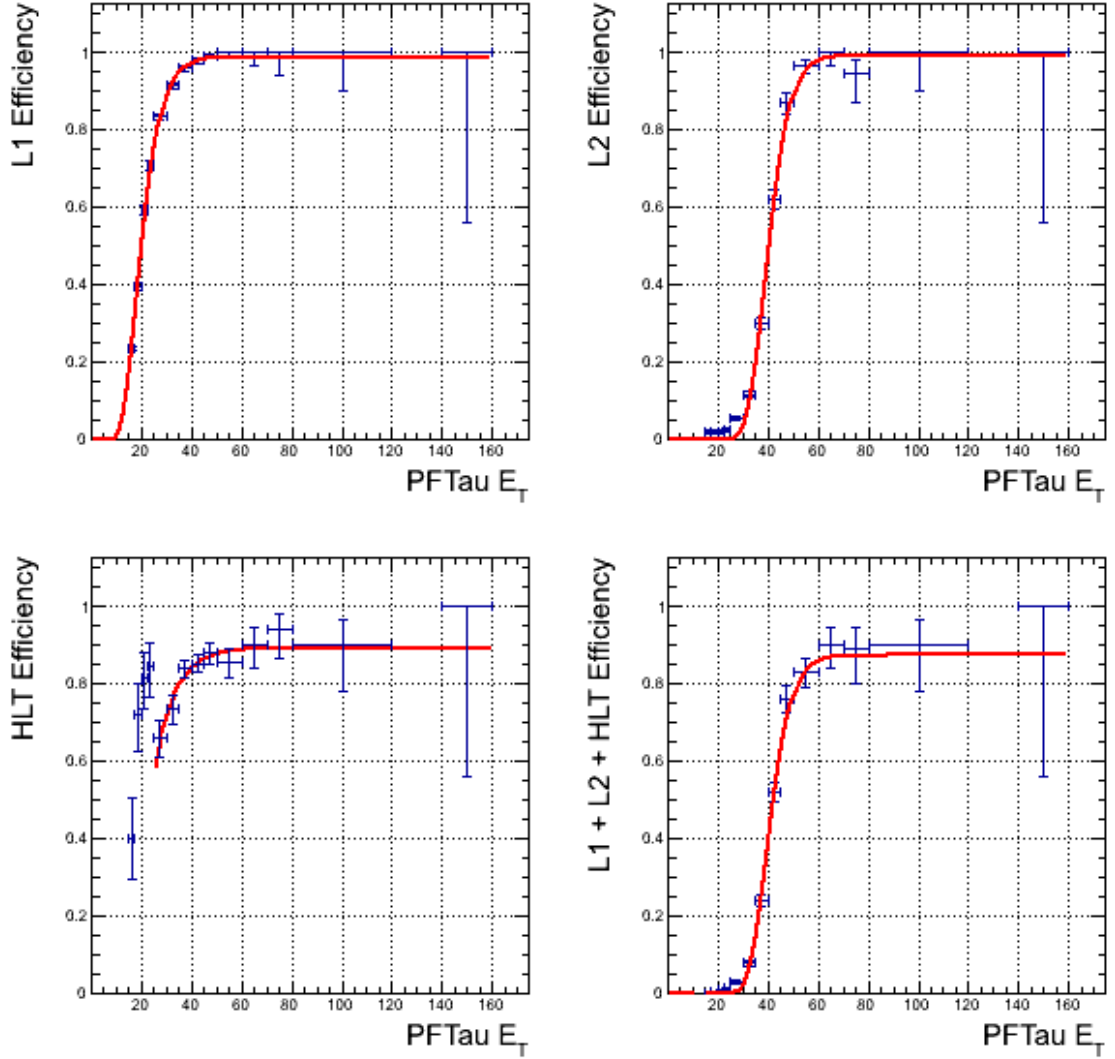


Figure 5.3: Level-1, Level-2, and Level-3 relative trigger efficiencies and overall trigger efficiency for HLT_DoubleIsoPFTau35_Trk5_eta2p1.

to suppress backgrounds, along with many other topological and fiducial-related selections.

5.6.1 Selection of a clean sample of $Z \rightarrow ee$ events and Validation of the offline code

In order to select a clean sample of $Z \rightarrow ee$ events having a topology very similar to that of signal or $Z \rightarrow \tau\tau$ events, a selection criteria resembling the signal selections,

CHAPTER 5. SEARCH FOR $Z' \rightarrow \tau\tau$ USING LHC COLLISION DATA OF RUN 2011 COLLECTED WITH CMS DETECTOR

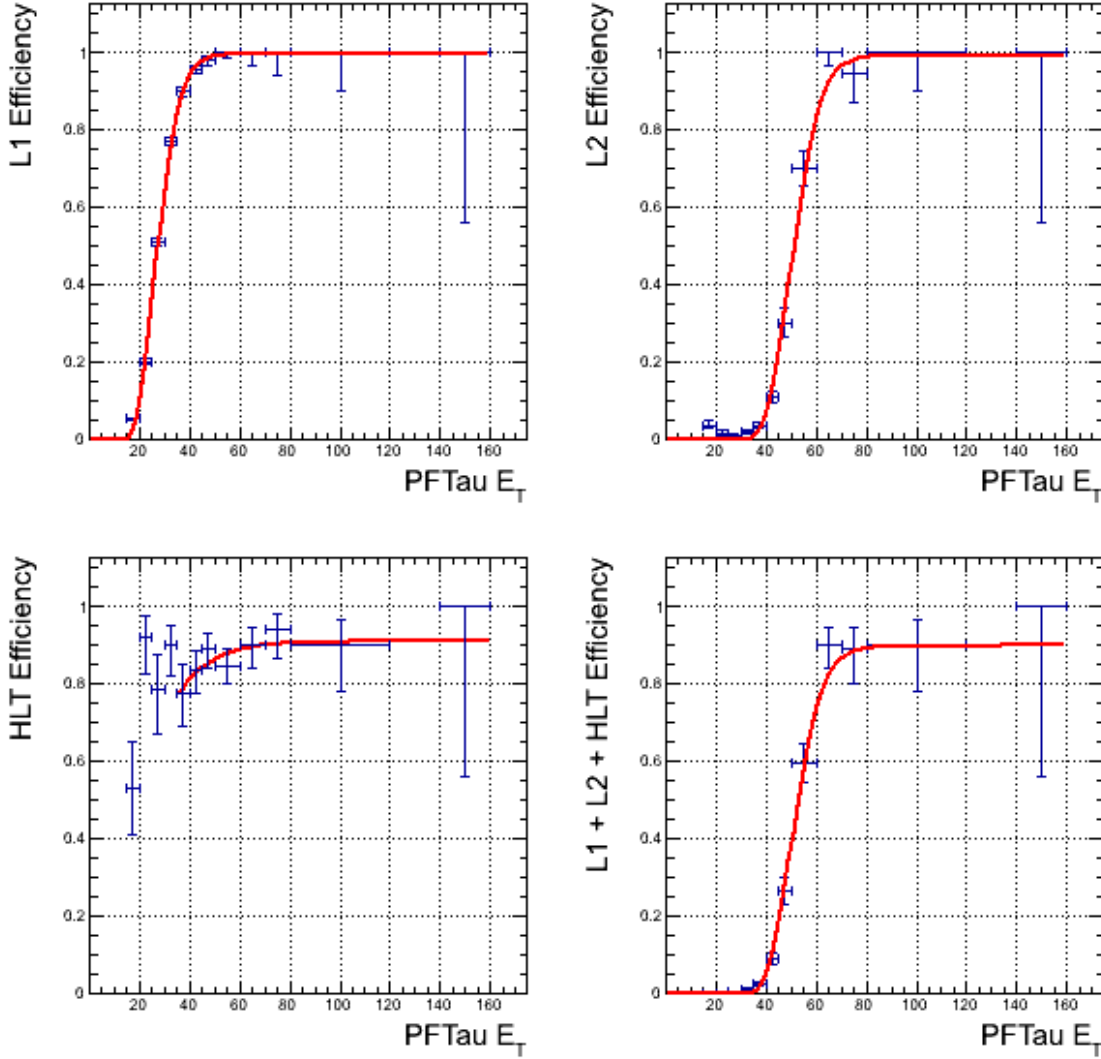


Figure 5.4: Level-1, Level-2, and Level-3 relative trigger efficiencies and overall trigger efficiency for `HLT_DoubleIsoPFTau45_Trk5_eta2p1_v{1-7}`.

is used. The only significant difference is the inversion of the electron veto, effectively disabling the electron rejection and enhancing their selection. Other changes are minor, and they are kept to maintain the same fiduciality requirements as in the main analysis (e.g. the “crack veto”). Such requirements are known to have negligible effect on the $Z \rightarrow ee$ (or signal) efficiency. An explicit list of selections is given below:

Acceptance:

- Event should have atleast one pair of HPS taus.

5.6. MEASUREMENT AND VALIDATION OF SIGNAL EFFICIENCIES

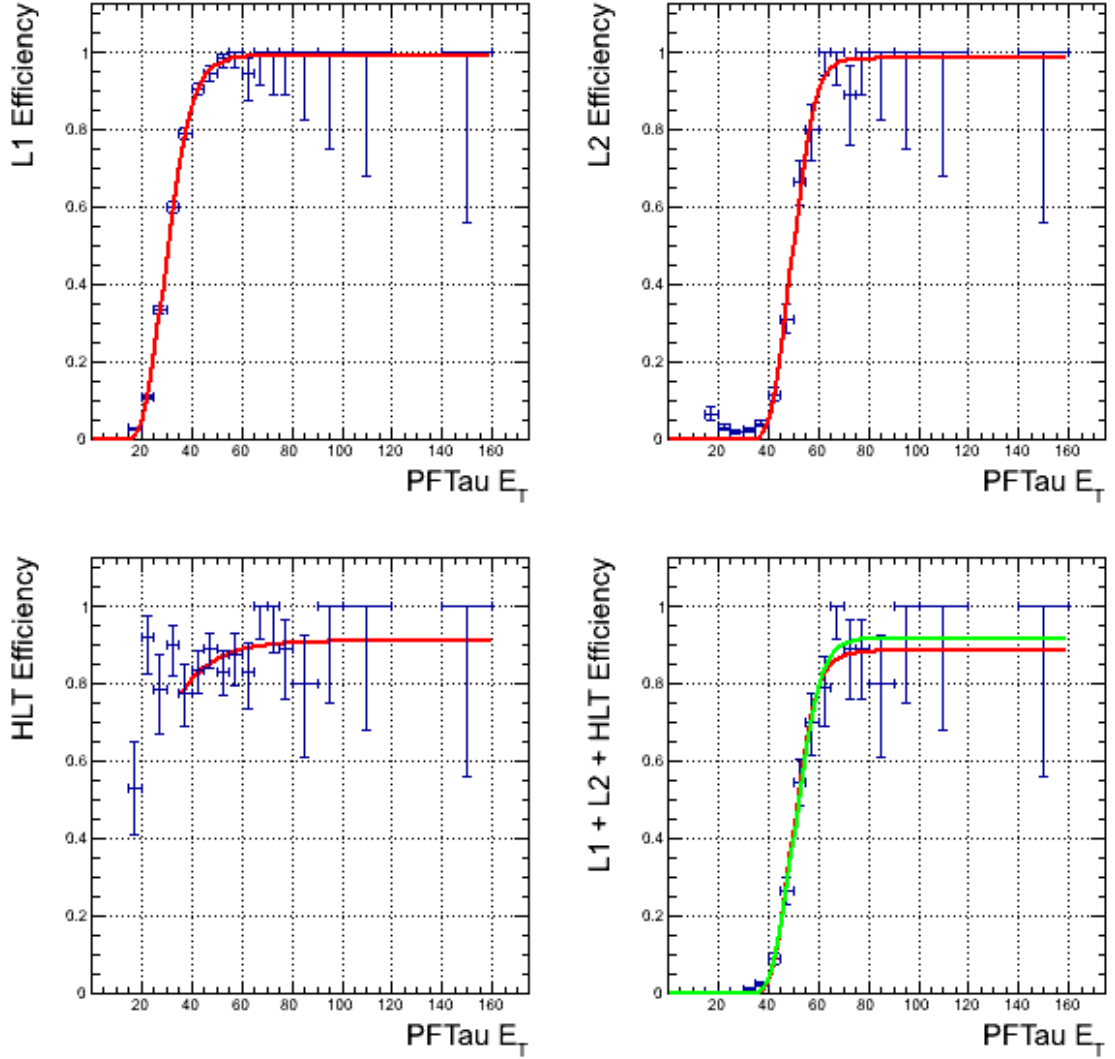


Figure 5.5: Level-1, Level-2, and Level-3 relative trigger efficiencies and overall trigger efficiency for HLT_DoubleIsoPFTau45_Trk5_eta2p1_v8 for Run2011B. In addition to the factorized efficiencies (red line), we fit the overall efficiency using only one error function shown in green.

- $p_T > 40$ GeV/ c on both tau-leptons (20 GeV/ c for studies with $e\tau_h$ samples).
- $|\eta| < 2.1$ on both tau-leptons.
- $\Delta R(\tau_1, \tau_2) > 0.7$.

τ_h identification:

CHAPTER 5. SEARCH FOR $Z' \rightarrow \tau\tau$ USING LHC COLLISION DATA OF RUN 2011 COLLECTED WITH CMS DETECTOR

- Crack veto on both tau-leptons.
- Leading track $p_T > 5 \text{ GeV}/c$ on both tau-leptons.
- Inverted tight HPS-tau electron discriminant (electron veto) on both tau-leptons.
- Loose HPS-tau muon discriminant (muon veto) on both tau-leptons.
- Loose HPS-tau isolation on both tau-leptons.

Topology:

- Charge product of both tau-leptons equal to -1.
- $-1.0 \leq \cos(\Delta\phi(\tau_1, \tau_2)) \leq -0.95$.
- $P_\zeta - 0.875 \times P_\zeta^{vis} > -7$.
- There should be no jet tagged as b-jet using TCHEM.

The validation of the offline software, τ_h discriminants and selections is performed by comparing the collision data selected in the $Z \rightarrow ee$ control region used in $Z' \rightarrow \tau\tau \rightarrow \tau_e\tau_h$ final state. In $Z' \rightarrow \tau\tau \rightarrow \tau_e\tau_h$ final state, the events were selected from the collision data using TauPlusX trigger. Since the p_T threshold on taus (mis-identified electrons) are well within the trigger plateau of the TauPlusX trigger, the trigger efficiency is essentially 100% due to the presence of two electrons per event. Using the the selections described above, an excellent agreement between the simulation and collision data was observed. Figure 5.6 shows some of the distributions obtained by extracting $Z \rightarrow ee$ control region for the $\tau_h\tau_h$ final state using $e\tau_h$ dataset. The agreement in the observed versus expected $Z \rightarrow ee$ event rates is excellent, thus confirming the reliability and validity of the τ_h -ID algorithms and selections. Remarkable agreement was also found when comparing both $Z' \rightarrow \tau\tau \rightarrow \tau_e\tau_h$ and $Z' \rightarrow \tau\tau \rightarrow \tau_h\tau_h$ analyses. The non-overlap events (from the difference in selections for the “electron leg”, like isolation *etc.*, between both analyses) were also studied, it was found that the simulation predicts both, the fraction and the properties of these events, very well (to about 1% level).

5.6. MEASUREMENT AND VALIDATION OF SIGNAL EFFICIENCIES

The double-tau trigger cannot be validated with this study since the $\tau_e\tau_h$ data samples do not select events from such trigger. This validation of the double-tau trigger is performed in the following Subsection.

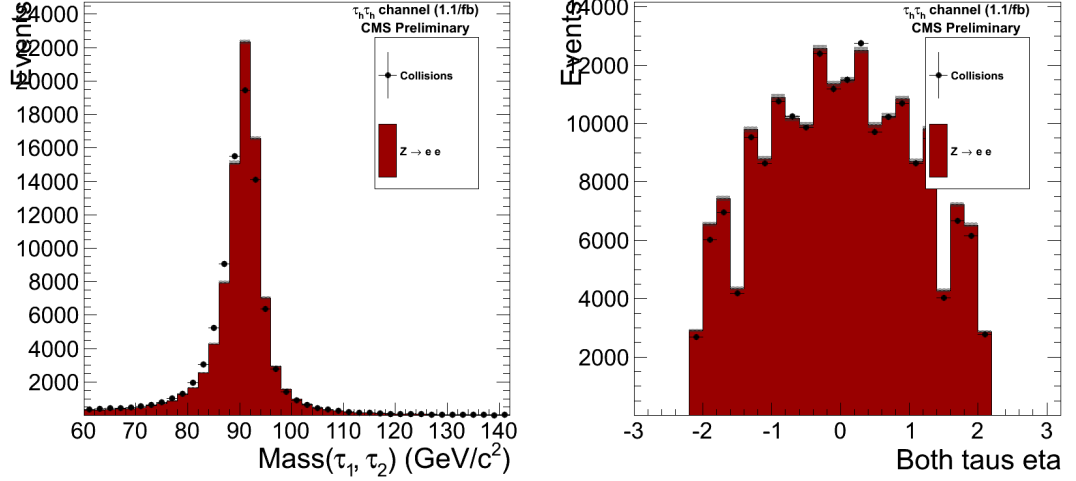


Figure 5.6: $Z \rightarrow ee$ visible mass and electrons (fake taus) η distribution of both legs in the $Z \rightarrow ee$ control region of the double hadronic tau analysis using $\tau_e\tau_h$ dataset.

5.6.2 Validation of the offline selections and the Trigger

The next measurement was to perform the similar exercise but with the data collected using double-tau trigger. In order to account for the higher trigger thresholds in the case of di-tau trigger, both the electrons are required to have $p_T > 40$ GeV/c. The rest of the selections were kept identical to those listed in the previous Section. Since the calorimetric response of electrons and pions are different, the efficiency of tau requirements in the di-tau trigger for electrons and pions was measured separately. The measurement of the efficiency of an electron to trigger a tau leg was done in the region of $|\eta| < 1$, hence, this additional requirement was applied while comparing the selected $Z \rightarrow ee$ events collected using the ditau trigger with the simulation predictions corrected for the trigger efficiency (by weighting the event with the measured efficiency for electrons as a function of the p_T of each leg). The comparison shows a good agreement as illustrated in Figure 5.7 and Table 5.9. A 2% deviation of the

CHAPTER 5. SEARCH FOR $Z' \rightarrow \tau\tau$ USING LHC COLLISION DATA OF RUN 2011 COLLECTED WITH CMS DETECTOR

scale factor from unity is treated as an additional systematic uncertainty (per event) to account for small differences in tau selections and trigger efficiency.

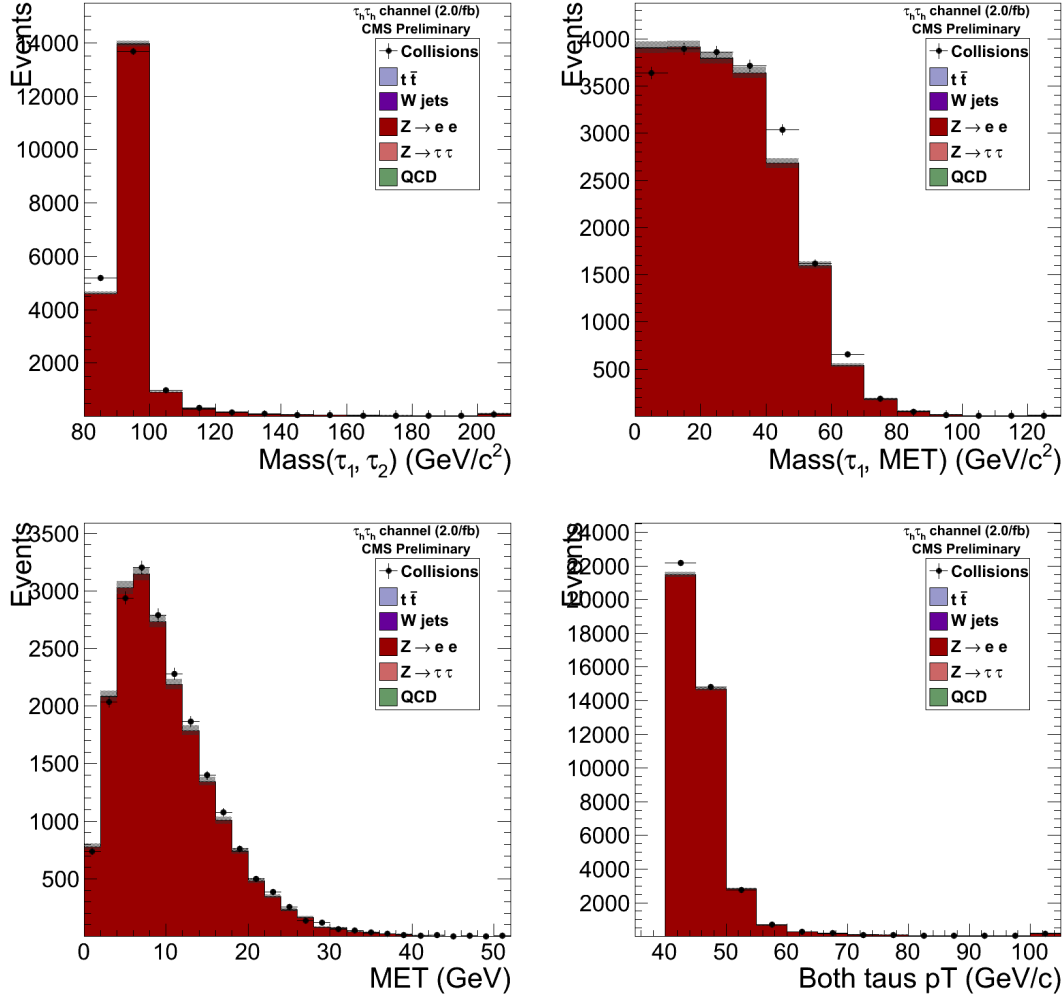


Figure 5.7: $Z \rightarrow ee$ visible mass, transverse mass of the leading leg and the \cancel{E}_T , \cancel{E}_T , and both taus p_T distribution for the $Z \rightarrow ee$ control region. Note that $|\eta| < 1.0$.

5.6.3 Validation of signal selections for the high mass events

In order to make sure that the trigger measurement does not introduce any unexpected bias for high p_T leptons (characteristic of Z' events), the inspection of $Z \rightarrow ee$ events selected using the double-tau trigger and the main analysis selections is done but with the inversion of electron veto on taus (in order to select electrons as taus).

5.6. MEASUREMENT AND VALIDATION OF SIGNAL EFFICIENCIES

Sample	Events
QCD	0 ± 5.3
$W + jets$	10.8 ± 2.8
$t\bar{t}$	0.96 ± 0.43
$Z \rightarrow \tau\tau$	8.5 ± 3.21
$Z \rightarrow ee$	20329 ± 149
Total	20349 ± 149
Observed	20708
Purity	99.90%

Table 5.9: Event rate in the $Z \rightarrow ee$ control region for the dataset considered (2.1 fb^{-1}). Note that the contributions of non-QCD backgrounds are estimated using the MC predictions.

The comparison between data and MC for the whole invariant mass and transverse momentum range are given in Figure 5.8. Note that instrumental effects that hypothetically could affect the efficiency for high momentum leptons are the same for $Z \rightarrow ee$, $Z \rightarrow \tau\tau$, and $Z' \rightarrow \tau\tau$ signal events. Therefore, no additional systematic uncertainty has been assigned specifically to events with high momentum objects.

The only missing ingredient when using $Z \rightarrow ee$ events to validate reconstruction of events with two hadronic taus is, essentially, the efficiency of the electron veto. For the case of two real electrons, the efficiency per event includes the square of the efficiency of applying the reversed electron veto. Conversely, the same quantity includes the square of efficiency of electron veto for true taus in the $Z \rightarrow \tau_h \tau_h$ case. While the latter is included in the standard systematic uncertainty for tau reconstruction and identification of this analysis, potential effects of the former are not included. One could argue that the agreement obtained in the $Z \rightarrow ee$ control region in this analysis may be accidental if the efficiency of the reversed electron veto for electrons predicted by simulation is incorrect and it is counteracted by another erroneous efficiency from the other selections. While highly unlikely, still this possibility is also incorporated

CHAPTER 5. SEARCH FOR $Z' \rightarrow \tau\tau$ USING LHC COLLISION DATA OF RUN 2011 COLLECTED WITH CMS DETECTOR

as a systematic uncertainty in the calculations. An additional uncertainty of 3% per event has been used to account for the use of $Z \rightarrow ee$ events rather than $Z \rightarrow \tau\tau$ in the validation studies [66].

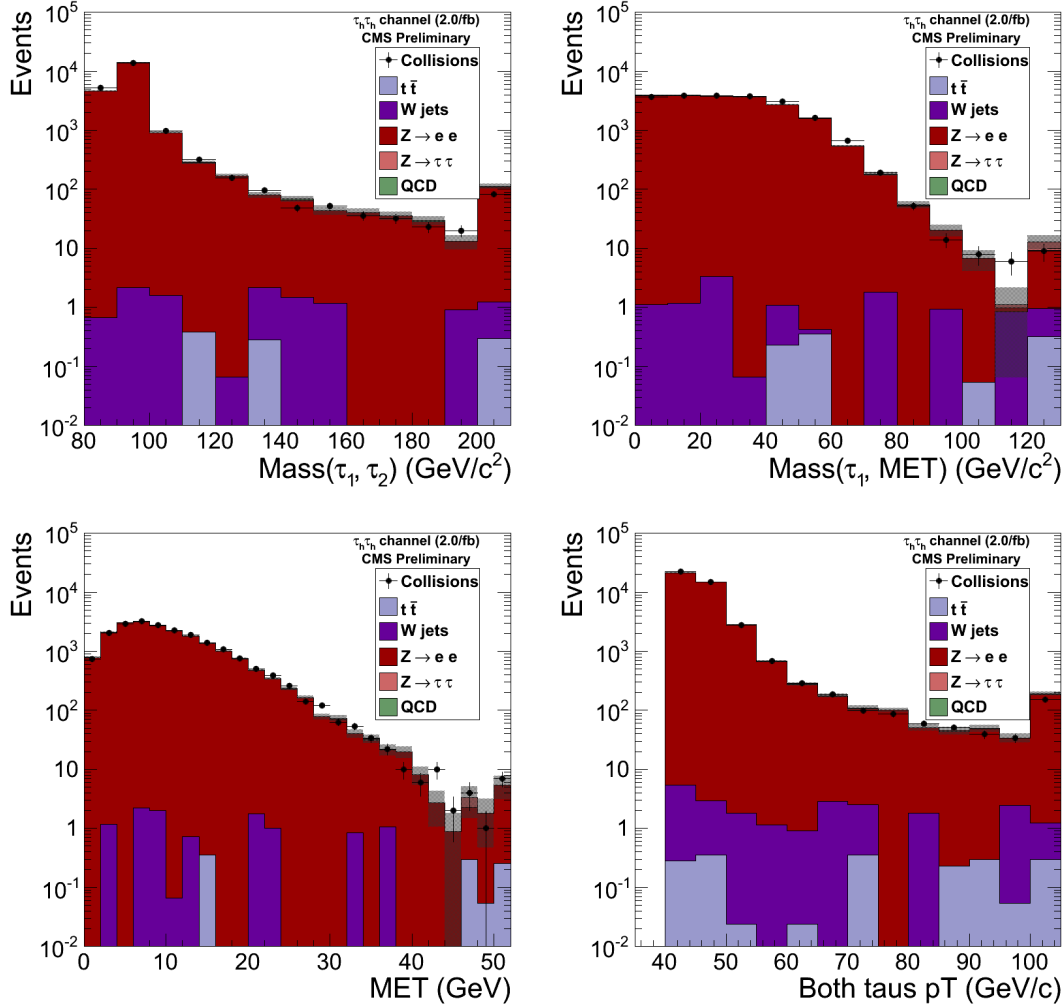


Figure 5.8: $Z \rightarrow ee$ visible mass, transverse mass of the leading leg and the \cancel{E}_T , $\cancel{E}_{T,1}$, and both taus p_T distribution for the $Z \rightarrow ee$ control region of the double hadronic tau analysis. Note that $|\eta| < 1.0$.

5.6.4 Trigger efficiency of the Di-Tau trigger

The only non-trivial factor that is not emulated by the simulation is the efficiency of the di-tau trigger. The details of the measurements are described in Section 5.5. The

5.7. VALIDATION PLOTS FOR SIGNAL SELECTIONS

trigger efficiency is measured by emulating the requirements for a single tau trigger leg (the di-tau trigger requires two instances per event) using raw trigger objects from the online trigger. With high certainty, these objects are true hadronic taus, and they are extracted from the $Z \rightarrow \tau\tau \rightarrow \tau_\mu\tau_h$ data and compared with our emulation of trigger efficiency. The measured trigger efficiency is applied separately to both taus, thus, providing the actual di-tau trigger efficiency.

5.7 Validation Plots for Signal Selections

In order to check and understand the performance of various selections cuts, the (N-1) distributions were also produced, where (N-1) distribution for a particular cut/selection means the distribution after all the signal selections, except the one for which the distribution is shown. For example, the (N-1) distribution for both taus p_T means the distribution of both taus p_T with all the signal selections applied except the p_T cut on both taus. Some of the (N-1) distributions are shown in Figure 5.9. Note that the plots refer to an integrated luminosity of 4.6 fb^{-1} . The integrated luminosity was re-measured later on with a more precise pixel based algorithm and was found to be 4.9 fb^{-1} . The agreement between the data and simulation predictions is expected to get better after renormalizing MC to 4.9 fb^{-1} since it will fill up the small gaps between the data and MC predictions in these distributions.

5.8 Background Estimation

5.8.1 Data-driven estimation of QCD multijet background

The QCD multijet background mimics the signal process if atleast two of the jets are misidentified as tau-jets. The missing transverse energy typically comes from the jet energy mismeasurements. While such mismeasurements are rare, the huge cross section of QCD multijet background makes the rate of surviving events significant in the low mass region. At higher masses (around the mass of the signal) the rate of surviving events of QCD multijet background is significantly diminished, although it

CHAPTER 5. SEARCH FOR $Z' \rightarrow \tau\tau$ USING LHC COLLISION DATA OF RUN 2011 COLLECTED WITH CMS DETECTOR

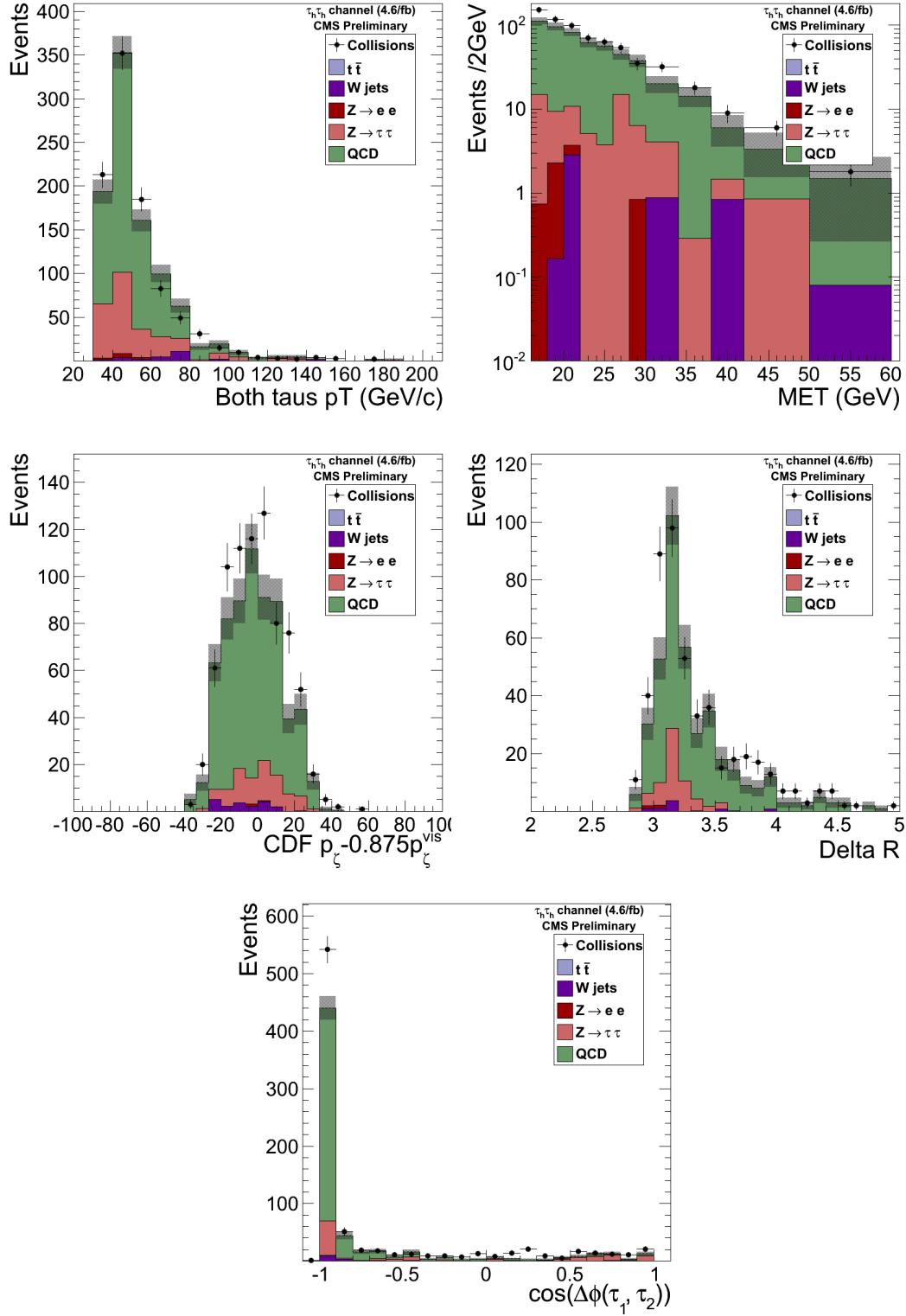


Figure 5.9: (N-1) distributions for both taus p_T , E_T , ζ , $\Delta R(\tau_1, \tau_2)$, and $\cos\Delta\phi(\tau_1, \tau_2)$.

5.8. BACKGROUND ESTIMATION

must still be evaluated.

Using simulation for modeling QCD multijet background is both impractical (one would need billions of generated events to have accurate estimates due to the low probability of them passing the selections) and unreliable, since such estimates would be dependent on the accuracy of the simulation in predicting rare fluctuations in jet fragmentation. Fortunately, it is not difficult to measure QCD multijet background directly from the collision data using like-sign events which would otherwise satisfy the exact same selections used in the actual analysis. While not perfect, this method has been used successfully for many years and was also used in the $Z' \rightarrow \tau\tau$ search with 2010 collision data. This method relies on the assumption that the number of multijet events reconstructed with opposite-sign and like-sign pairs of tau candidates are approximately the same. This equality is slightly violated due to processes where the two quarks have correlated charges in the final state, e.g. from $gg \rightarrow q\bar{q}$. While fragmentation largely smears the correlation between the visible jet charge (in the final state) and the parent quark charge, such correlation is enhanced in jets that fluctuate into a single energetic isolated track. The correlation between the track charge and the quark charge increases further with the tightness of isolation cuts applied in selecting a single track that the jet fluctuated into. Since one-prong taus have been used in the analysis, the asymmetry (arising from the correlations) is taken into account in the estimation of the QCD multijet background. The like-sign events are selected from the collision data with the exact same signal selection cuts except the opposite-sign requirement on the tau-pair is changed to like-sign *i.e.* $Q(\tau_1) = Q(\tau_2)$. The events thus selected, are heavily dominated by the QCD multijet background with only a small contamination from other backgrounds.

The rate of like-sign QCD multijet events is estimated by subtracting off the contribution of other like-sign backgrounds (non-QCD) estimated from simulation. The rate of opposite-sign QCD multijet events with the same selections is then computed as the rate of like-sign QCD multijet events corrected by the asymmetry factor, *i.e.*

CHAPTER 5. SEARCH FOR $Z' \rightarrow \tau\tau$ USING LHC COLLISION DATA OF RUN 2011 COLLECTED WITH CMS DETECTOR

the “opposite-sign-to-like-sign ratio” or $R_{OS/LS}$:

$$QCD_{LS} = (Data)_{LS} - (W + jets, t\bar{t}, DY \rightarrow \tau\tau/ee)_{LS} \quad (5.4)$$

$$R_{OS/LS} = \frac{QCD_{OS}}{QCD_{LS}} \quad (5.5)$$

$$QCD_{OS} = R_{OS/LS} \times QCD_{LS}, \quad (5.6)$$

where the notation is self explanatory. The measurement of this quantity is illustrated in Figure 5.10 and Figure 5.11, which shows the $R_{OS/LS}$ as a function of the transverse mass of the leading tau and the \cancel{E}_T . The left plot in Figure 5.10 corresponds to a minimum $p_T > 35$ GeV/ c requirement on both taus while there is no requirement on the \cancel{E}_T . In the right plot, there is no \cancel{E}_T requirement while $p_T > 50$ GeV/ c is required for both taus. Figure 5.11 corresponds to a requirement of $\cancel{E}_T > 15$ GeV/ c and $p_T > 35$ GeV/ c on each tau. Unless otherwise stated, in all the three plots the other cuts have been kept equal to those used in the selection of signal events. All three datasets are heavily dominated by QCD as shown in Figure 5.12. Since the fit results remain consistent within the uncertainty in all the three cases, the fit results from Figure 5.11 (which contains the same signal selections except a bit looser \cancel{E}_T requirement) *i.e.* $R_{OS/LS} = 1.39 \pm 0.10$ is finally used to estimate the rate of opposite-sign QCD multijet events.

5.8.2 Estimation of $Z \rightarrow \tau\tau$ background

The estimation of $Z \rightarrow \tau\tau$ background relies on the studies performed on $Z \rightarrow ee$ events as described in the previous Section. The simulation can accurately predict the tau reconstruction and identification efficiencies in the collision data as observed in other final states. Similarly, the origin of missing transverse energy is not particularly different than the other final states, so there is no reason to expect it to be any less accurate in this case. The measurements of the spectrum of $Z \rightarrow ee$ events selected using the di-tau trigger and the same signal selections, with the exception of inversion of the electron veto requirement, reassure the fact that the selections with the trigger taken as a whole does not introduce any unexpected biases.

5.8. BACKGROUND ESTIMATION

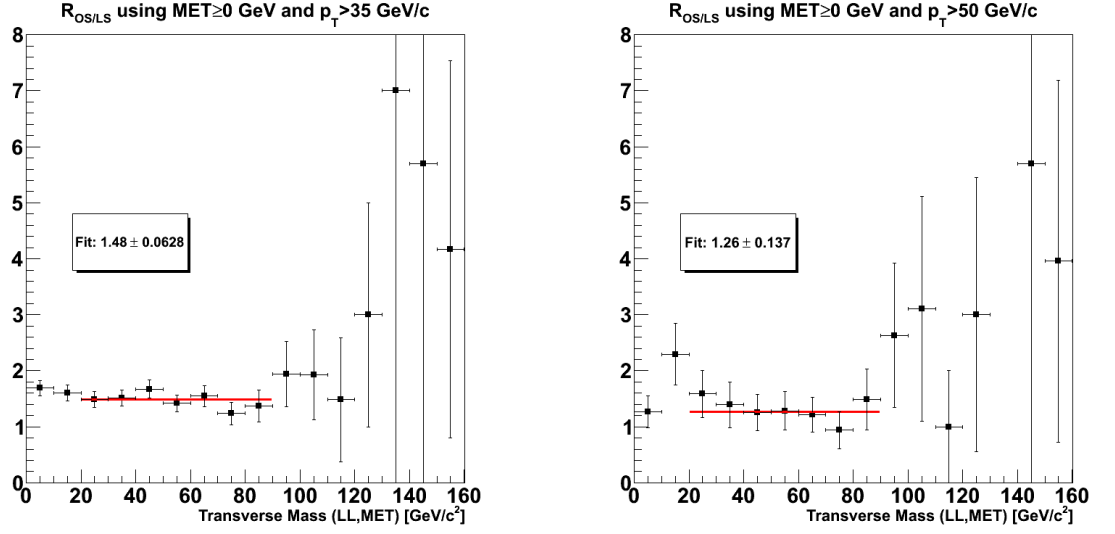


Figure 5.10: Ratio of opposite-sign to like-sign events passing all the signal selections, for different p_T and \cancel{E}_T requirements.

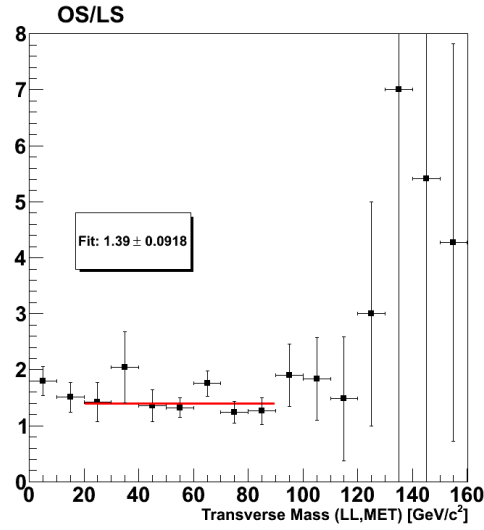


Figure 5.11: Ratio of opposite-sign to like-sign events passing all the signal selections, for $p_T > 35$ GeV/ c and $\cancel{E}_T > 15$ GeV/ c requirements.

As an additional cross-check, a region with increased $Z \rightarrow \tau\tau$ purity was created using HPS “medium” isolation working point and no minimum \cancel{E}_T requirement while keeping all other cuts at the nominal values. For this cross-check, only the first run period where the tau trigger p_T threshold was set to 20 GeV/ c (runs between 163269

CHAPTER 5. SEARCH FOR $Z' \rightarrow \tau\tau$ USING LHC COLLISION DATA OF RUN 2011 COLLECTED WITH CMS DETECTOR

Process	Event Rate
$W + jets$	2.6 ± 1.3
$t\bar{t}$	0.23 ± 0.23
$Z \rightarrow \tau\tau$	0.126 ± 0.089
$Z \rightarrow ee$	$0.0^{+3.7}_{-0.0}$
Total expected rate (excluding QCD)	$3.0^{+3.9}_{-3.0}$
Observed rate	339
Estimated like-sign QCD rate	336^{+19}_{-18}
Estimated opposite-sign QCD rate ($R_{OS/LS} = 1.39 \pm 0.10$)	467 ± 72

Table 5.10: Estimation of the event rate of like-sign events and opposite-sign QCD contributions after nominal cuts for the $\tau_h\tau_h$ analysis.

and 165970), was used, since the high trigger thresholds in later runs removed a good fraction of the $Z \rightarrow \tau\tau$ events. Figure 5.13 shows the full $M(\tau_1, \tau_2, \cancel{E}_T)$ invariant mass and the visible $M(\tau_1, \tau_2)$ mass distributions for this region, alas, with reduced statistics, but showing good agreement. Therefore, after performing all validation checks, the $Z \rightarrow \tau\tau$ rate was estimated using the simulation predictions.

5.8.3 Estimation of $Z \rightarrow ee$ background

The validation results using $Z \rightarrow ee$ data to evaluate $Z \rightarrow ee$ background expectations after all selections are directly applicable to the estimation of $Z \rightarrow ee$ background after final selections. Note, however, that the validation studies showing an excellent agreement between data and simulation account for all effects with the exception of the efficiency of the HPS tau discriminant against electrons (electron veto). Based on the studies performed in the $Z' \rightarrow \tau\tau \rightarrow \tau_e\tau_h$ final state, the rate of $Z \rightarrow ee$ background is estimated from the MC predictions with a correction factor of 1.0 ± 0.5 which is consistent with 1.

5.8. BACKGROUND ESTIMATION

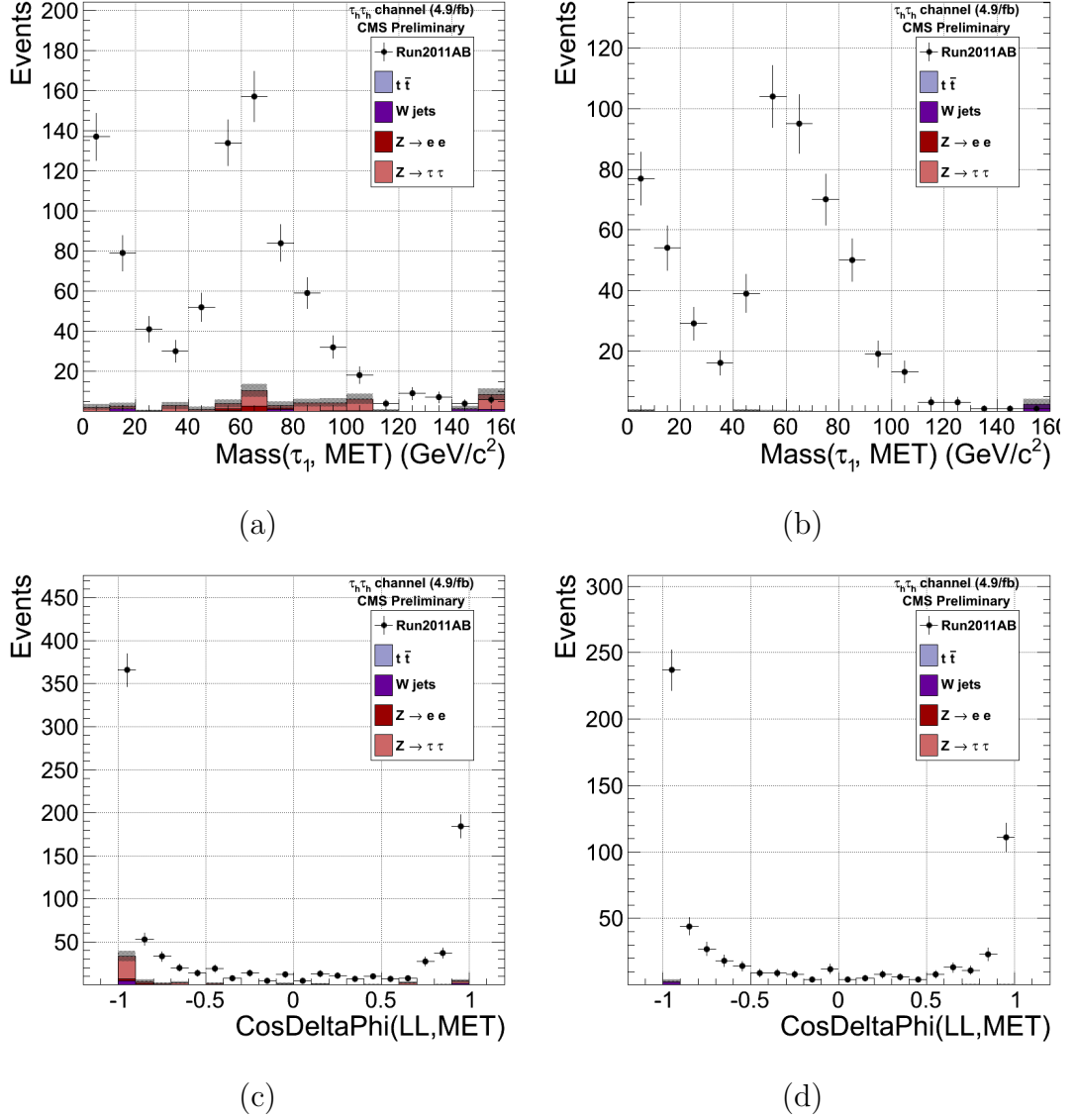


Figure 5.12: Transverse mass of the leading p_T tau and the \cancel{E}_T , (a) and (b); and the cosine of the angle between the leading p_T tau and the \cancel{E}_T , (c) (d); obtained by loosening the minimum \cancel{E}_T requirement to 15 GeV and requiring opposite-sign charges, (a) and (c); or same-sign charges, (b) and (d).

5.8.4 Estimation of $t\bar{t}$ and $W + jets$ backgrounds

Other backgrounds include $t\bar{t}$ and $W + jets$ with small contributions compared to leading backgrounds. Their contributions are estimated using simulation and corrected for the trigger efficiency. Based on the studies performed in other channels, no

CHAPTER 5. SEARCH FOR $Z' \rightarrow \tau\tau$ USING LHC COLLISION DATA OF RUN 2011 COLLECTED WITH CMS DETECTOR

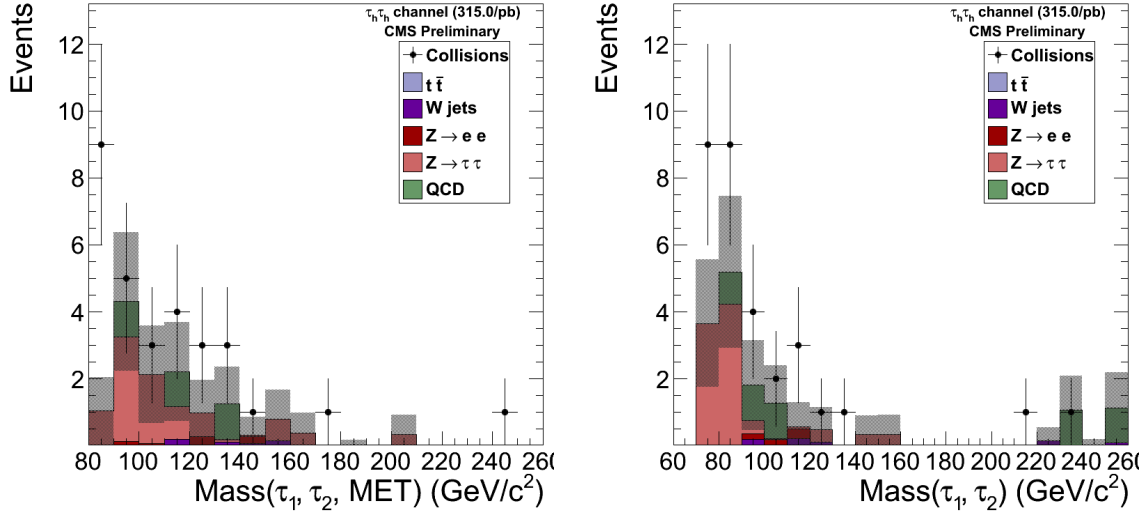


Figure 5.13: Ditaup full invariant mass, and visible mass for the $Z \rightarrow \tau\tau$ control region for the first run period explored: runs 163269 to 165970.

significant deviations of the actual contribution of these backgrounds from simulation predictions, are expected. Hence, no additional uncertainty, except the statistical uncertainty driven by the size of the simulation samples, is added.

5.8.5 Data in Low and High Mass Regions

Table 5.11 shows the expected rate of background processes after final selections in the entire di-tau mass region, as well as in the high mass region, where the sensitivity of the final fit for signal plus background dominates (the rates for $M(\tau_h, \tau_h, \cancel{E}_T) > 250$ GeV/c^2 and $M(\tau_h, \tau_h, \cancel{E}_T) > 350$ GeV/c^2 are also quoted). The number of events observed in LHC collision data of Run 2011, after unblinding the signal region, are also shown at the bottom of the Table. As expected, the QCD multijet background governs the low end of the mass spectrum, but diminishes quickly at higher values of invariant mass. The net background expectation in the high mass region, where the Z' boson would appear, is sufficiently small to obtain stringent limits for the $Z' \rightarrow \tau\tau$ production. The mass distributions are fitted to obtain smooth shapes in the high mass region as shown in Figure 5.14. The mass distributions shown in Figure 5.15 are used to calculate the limit on the $Z' \rightarrow \tau\tau \rightarrow \tau_h \tau_h$ production cross-section as a

5.9. SYSTEMATICS UNCERTAINTIES

function of Z' mass. Table 5.12 contains the expected signal rates and sensitivity for four different SSM Z' masses, for the dataset used in this analysis.

Sample	$M_{inv} > 0 \text{ GeV}/c^2$	$M_{inv} > 250 \text{ GeV}/c^2$	$M_{inv} > 350 \text{ GeV}/c^2$
QCD	$467 \pm 72 \pm 67$	$30.0 \pm 9.4 \pm 4.4$	$2.2 \pm 5.58 \pm 0.4$
$W + jets$	$5.8 \pm 1.7 \pm 0.60$	$2.3 \pm 1.4 \pm 0.2$	$0.25 \pm 0.25 \pm 0.05$
$t\bar{t}$	$0.00 \pm 0.76 \pm 0.15$	$0.00 \pm 0.76 \pm 0.15$	$0.00 \pm 0.76 \pm 0.15$
$Z \rightarrow \tau\tau$	$30.9 \pm 3.6 \pm 4.1$	$6.4 \pm 3.2 \pm 0.22$	$3.95 \pm 2.8 \pm 0.1$
$Z \rightarrow ee$	$0.66 \pm 0.33 \pm 0.22$	$0.0 \pm 3.7 \pm 0.1$	$0.00 \pm 3.7 \pm 0.1$
N_{Total}^{Bkg}	$504 \pm 72 \pm 67$	$38.7 \pm 11.0 \pm 4.4$	$6.4 \pm 7.3 \pm 0.4$
$N_{Observed}^{Data}$	488	52	7

Table 5.11: Comparison of the expected SM background contributions (rates) and events observed in data for $\int Ldt = 4.9 \text{ fb}^{-1}$, for the entire region as well as for high mass regions, where the sensitivity of this analysis dominates. The uncertainties are presented as statistical \pm systematics.

5.9 Systematics Uncertainties

The following systematic uncertainties on signal have been considered:

- **Parton Distribution Functions (PDF):** The PDF uncertainties are crucial input for LHC, both for “standard candle” processes and for exclusion and discovery. The systematic effects due to imprecise knowledge of the parton distribution functions is determined by comparing the default PDF (CTEQ6L) with CTEQ6.6L, MSTW2008nnlo, and NNPDF20 PDF and variations within the family of parametrizations [67]. The maximal deviation from the central value is used as the overall systematic due to PDFs. A 6.5% systematics uncertainty is used for this purpose.
- **Initial State Radiation (ISR) and Final State Radiation (FSR):** The ISR and FSR are important sources of systematic uncertainties for in-situ Jet

**CHAPTER 5. SEARCH FOR $Z' \rightarrow \tau\tau$ USING LHC COLLISION
DATA OF RUN 2011 COLLECTED WITH CMS DETECTOR**

Signal Sample	$M_{inv} > 0 \text{ GeV}/c^2$		$M_{inv} > 250 \text{ GeV}/c^2$		$M_{inv} > 350 \text{ GeV}/c^2$	
	Rate	$s/\sqrt{s+b}$	Rate	$s/\sqrt{s+b}$	Rate	$s/\sqrt{s+b}$
SSM $Z'(350)$	220.6 ± 8.3	8.2	164.1 ± 7.7	12	34.8 ± 3.5	5.4
SSM $Z'(500)$	84.4 ± 2.7	9.2	77.8 ± 2.7	8.8	51.2 ± 2.2	7.2
SSM $Z'(750)$	22.15 ± 0.64	1.4	21.52 ± 0.64	1.6	19.00 ± 0.60	2.6
SSM $Z'(1000)$	6.64 ± 0.19	0.70	6.61 ± 0.20	0.72	6.32 ± 0.19	0.83

Table 5.12: Comparison of the expected signal rates and the sensitivity for $\int Ldt = 4.9 \text{ fb}^{-1}$ for four different SSM Z' masses, for the entire region as well as for higher mass regions.

Energy Scale (JES) calibration. The systematic effect due to imprecise modeling of initial and final state radiation is determined by re-weighting events to account for effects such as missing a term in the soft-collinear approach [68] and missing NLO terms in the parton shower approach [69]. The uncertainties obtained are 3.1% and 2.2% for ISR and FSR respectively.

- **Luminosity:** An uncertainty of 2.2% is considered on the measured luminosity as per official measurements of CMS detector performance group (DPG) [70].
- **Tau ID Efficiency:** An uncertainty of 6.8% per hadronic tau is considered as per measurements of the tau physics objects group (POG) [57].
- **b -Tagging Efficiency:** We consider a 20% uncertainty on the mis-tag rate as measured by the b -tagging POG [71]. For the case of the signal $Z' \rightarrow \tau\tau$, the systematic uncertainty on the requirement of 0 jets mis-tagged as b -jets is determined by propagating the 20% uncertainty on the mis-tag rate through the following equation (which represents the $Z' \rightarrow \tau\tau$ efficiency for requiring 0 jets mis-tagged as b -jets):

$$\epsilon^{\text{NBtag}<1} = 1 - \sum_{n=1} P(n) \cdot \sum_{m=1}^n C(n, m) \cdot f^m \cdot (1-f)^{n-m} \quad (5.7)$$

5.9. SYSTEMATICS UNCERTAINTIES

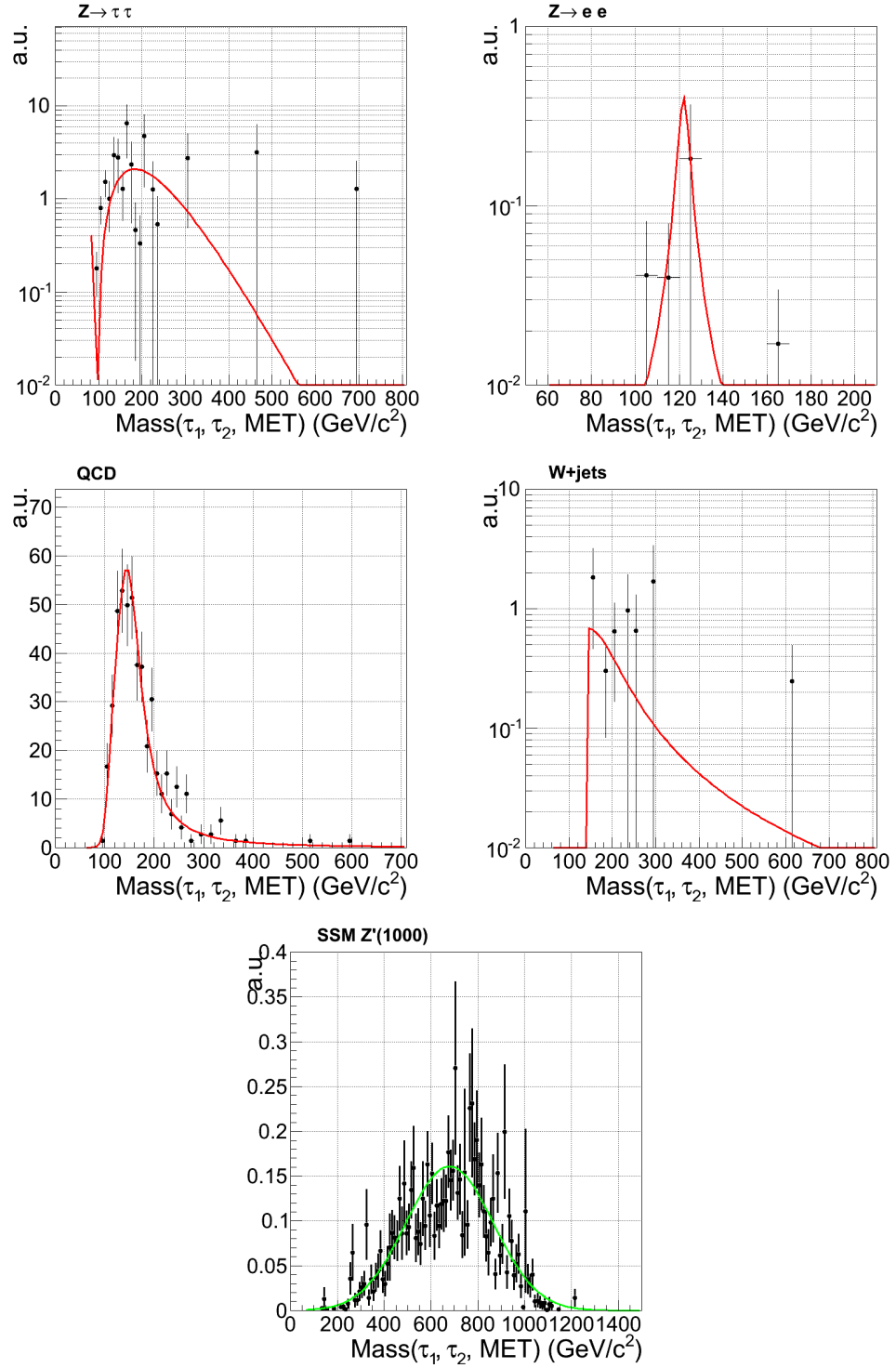


Figure 5.14: Di-tau invariant mass $M(\tau_1, \tau_2, \cancel{E}_T)$ fitted shapes after applying all selection cuts.

CHAPTER 5. SEARCH FOR $Z' \rightarrow \tau\tau$ USING LHC COLLISION DATA OF RUN 2011 COLLECTED WITH CMS DETECTOR

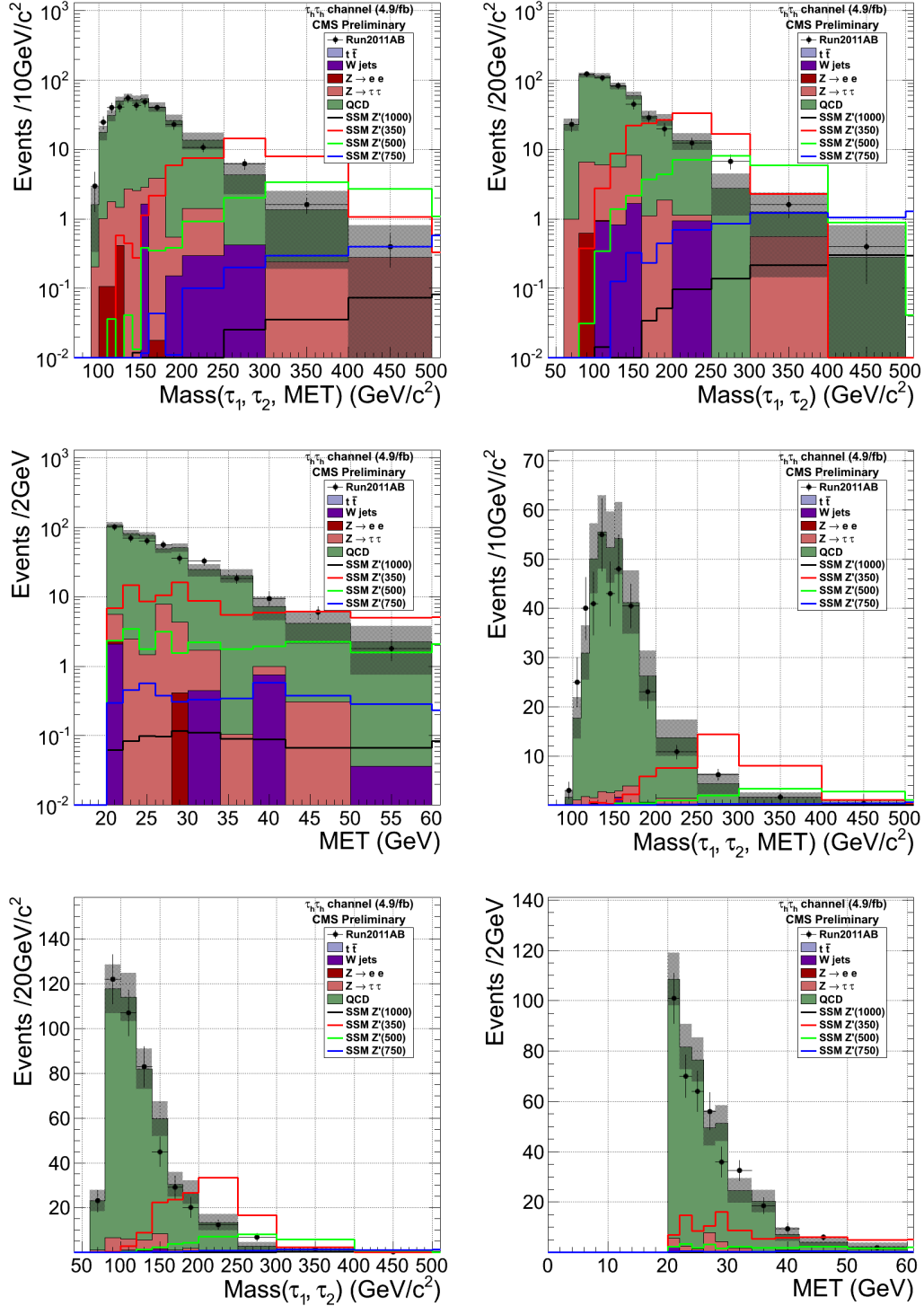


Figure 5.15: Di-tau invariant mass, visible mass, and \cancel{E}_T for the $Z' \rightarrow \tau_h\tau_h$ signal region. The right-most bin indicates the overflow.

5.9. SYSTEMATICS UNCERTAINTIES

where $P(n)$ is the probability to obtain n additional jets (non-tau and non-lepton) in the event, $C(n, m)$ the combinatorial of n choose m , and f the mis-tag rate. Based on Figure 5.16, the probability to obtain at least one additional jet in the event is approximately 1%. Therefore, based on the above equation, the mis-tag rate, uncertainty and the 1% probability to obtain at least one additional jet, we calculate a negligible systematic effect on our signal due to the mis-tag rate.

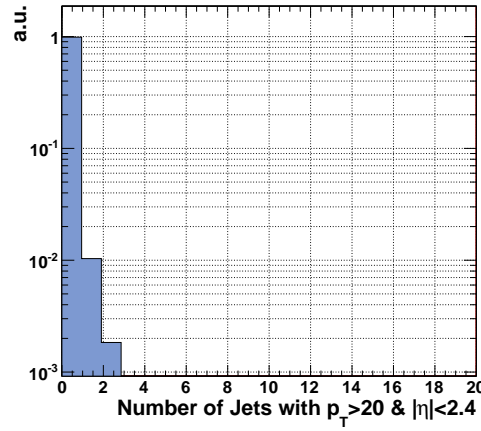


Figure 5.16: Probability, in $Z' \rightarrow \tau\tau$, to obtain n additional jets (non-tau and non-lepton) in the event.

- **Tau Energy Scale:** We consider the effect of 2% tau energy scale uncertainty measured by the tau POG on the signal acceptance. The tau 4-momentum is measured by a factor of $k = 1.02$ ($p_{smeared} = k \cdot p_{default}$) and variables are recalculated using $p_{smeared}$. By using $p_{smeared}$ calculated with a factor of $k = \pm 1.02$, the signal acceptance is found to fluctuate by 2%. Therefore, we assign a 2% systematic on the signal acceptance due to tau energy scale.
- **Jet Energy Scale:** We consider the effect of a 2-5% jet energy scale uncertainty on the signal acceptance (depending on the η and p_T of the considered jet as prescribed by the *JetMET* POG). The jet 4-momentum is measured by a factor of $k = 1.05$ ($p_{smeared} = k \cdot p_{default}$) and variables are recalculated using $p_{smeared}$. We find that by using $p_{smeared}$ calculated with a factor of $k = \pm 1.05$, the signal

CHAPTER 5. SEARCH FOR $Z' \rightarrow \tau\tau$ USING LHC COLLISION DATA OF RUN 2011 COLLECTED WITH CMS DETECTOR

acceptance fluctuates by 4%. Therefore, we assign a 4% systematic on the signal acceptance due to jet energy scale.

- Missing Transverse Energy:** The uncertainty on \cancel{E}_T for the signal process is driven by the tau energy scale (TES), jet energy scale (non-tau jets) (JES), light lepton energy/momentum scale (LES), and unclustered energy (UCE). The technical implementation of JES, TES, and LES “smearing” also involves the recalculation of the \cancel{E}_T as depicted in Figure 5.17. Therefore, the systematic effect from \cancel{E}_T due to TES, JES, and LES is included in the JES, TES, LES systematic uncertainties described above. We find that a 10% uncertainty on the unclustered energy results in atmost a 0.5% fluctuation on the signal acceptance for the mass range considered ($M_{Z'} > 350 \text{ GeV}/c^2$).

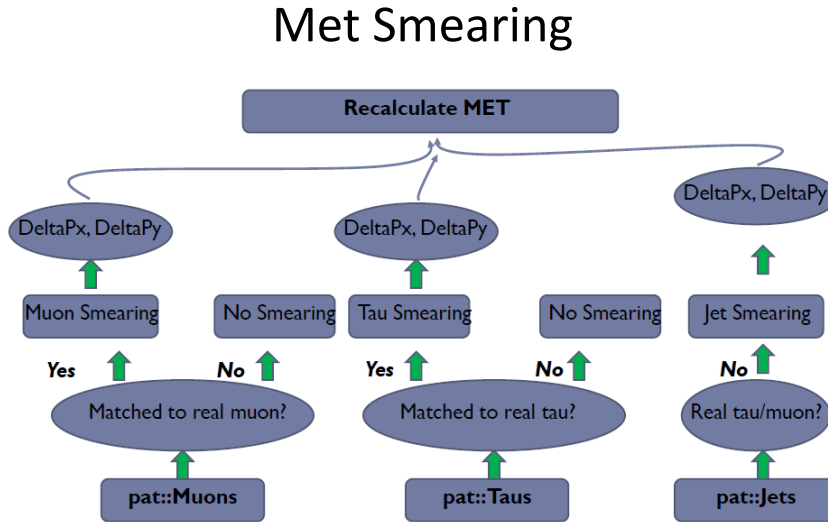


Figure 5.17: Depiction of the recalculation of MET due to JES, TES, and LES considerations.

5.10 Results and Conclusions

In this analysis, the search for a $Z' \rightarrow \tau\tau$ is performed using pp collision data of LHC collected using the CMS detector in Year 2011. The collision data corresponds to 7 TeV center-of-mass energy and an integrated luminosity of $4.94 \pm 0.11 \text{ fb}^{-1}$. The search results from the fully hadronic tau final state is presented along with the results from other three complementary Z' decay channels. The observed mass spectrum did not reveal any evidence for $Z' \rightarrow \tau\tau$ production as shown in Figure 5.18. Therefore, we determine 95% C.L. upper limits on the $Z' \rightarrow \tau\tau$ production cross-section as a function of Z' mass. Figure 5.19 shows the upper limits on the $Z' \rightarrow \tau\tau$ production cross-section as well as the theoretical $Z' \rightarrow \tau\tau$ production cross-section for various Z' masses in the context of Sequential Standard Model (SSM) and Super-string inspired E_6 models, for all the four final states considered. The bands on the expected limits represent the 1σ and 2σ deviations obtained using a large sample of pseudo-experiments where the pseudo-data is obtained from background only distributions using a Poisson based random event generator. It can be noted that although the $\tau_e\tau_\mu$ final state is cleaner than the $\tau_\mu\tau_h$ and $\tau_e\tau_h$ final states, the upper limit is larger due to the smaller branching fraction of $\tau\tau$ to $\tau_e\tau_\mu$. To determine the upper limits on the Z' production cross-section times the branching fraction to $\tau\tau$ pair, we determine a point at which the experimental limit on the $Z' \rightarrow \tau\tau$ production cross-section exceeds the theoretical value. One can see from the combined limit in Figure 5.20 that we can exclude Z'_Ψ and Z'_{SSM} resonances of masses less than 1.1 and 1.4 TeV, respectively, at 95% C.L [72]. The current exclusion limit exceeds our limit set with 2010 data, where a $Z'_{SSM} \rightarrow \tau\tau$ having mass less than $468 \text{ GeV}/c^2$ was excluded at 95% C.L using $36.1 \pm 1.4 \text{ pb}^{-1}$ of collision data collected during LHC Run 2010 [65].

CHAPTER 5. SEARCH FOR $Z' \rightarrow \tau\tau$ USING LHC COLLISION DATA OF RUN 2011 COLLECTED WITH CMS DETECTOR

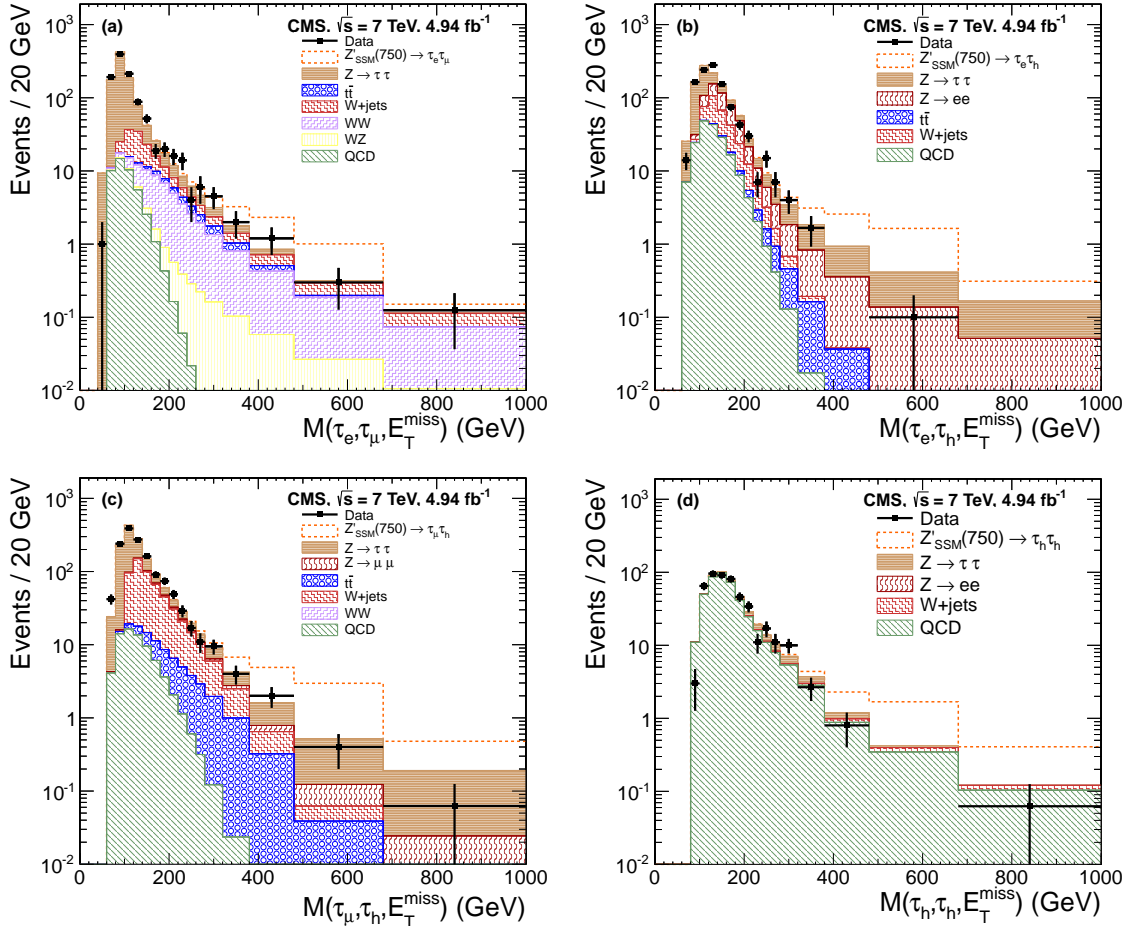


Figure 5.18: $M(\tau_1, \tau_2, E_T^{\text{miss}})$ distributions for all four final states: (a) $\tau_e \tau_\mu$, (b) $\tau_e \tau_h$, (c) $\tau_\mu \tau_h$, and (d) $\tau_h \tau_h$. The dashed line represents the mass distribution for a $Z'_{\text{SSM}} \rightarrow \tau\tau$ with a mass of 750 GeV/ c^2 .

5.10. RESULTS AND CONCLUSIONS

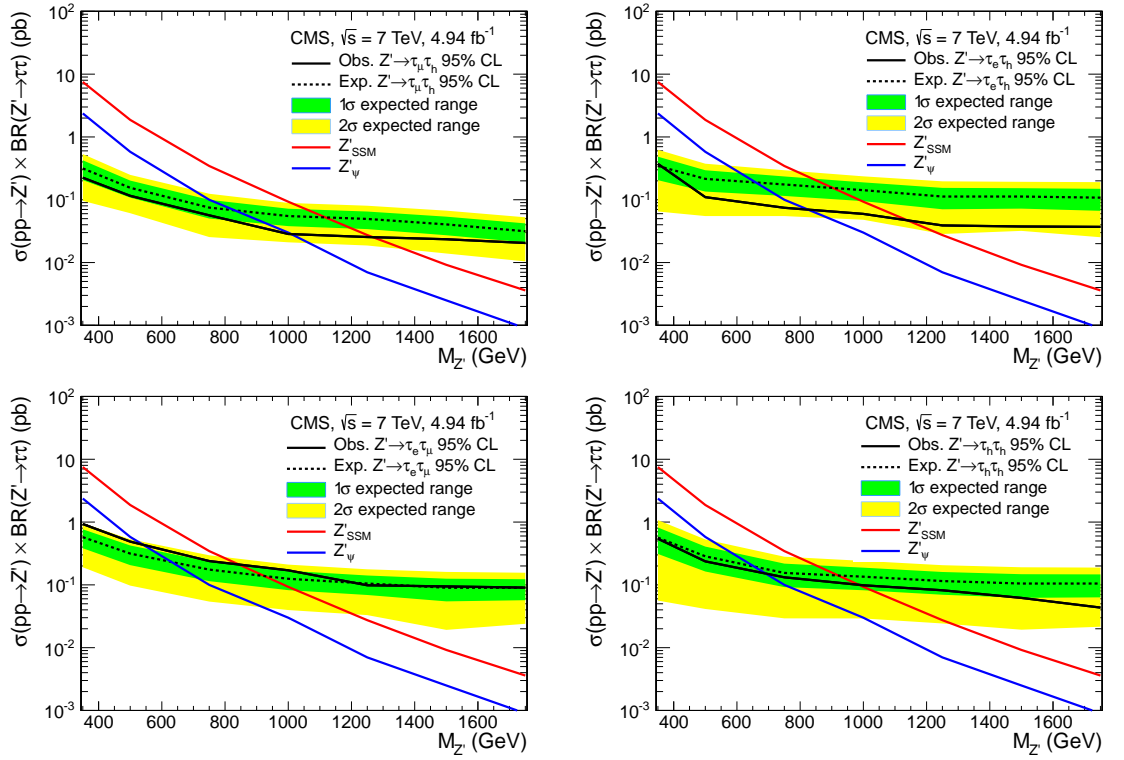


Figure 5.19: 95% C.L. upper limits on the $Z' \rightarrow \tau\tau$ production cross-section as a function of Z' mass for (a) $\tau_{\mu}\tau_h$, (b) $\tau_e\tau_h$, (c) $\tau_e\tau_{\mu}$, and (d) $\tau_h\tau_h$ final states.

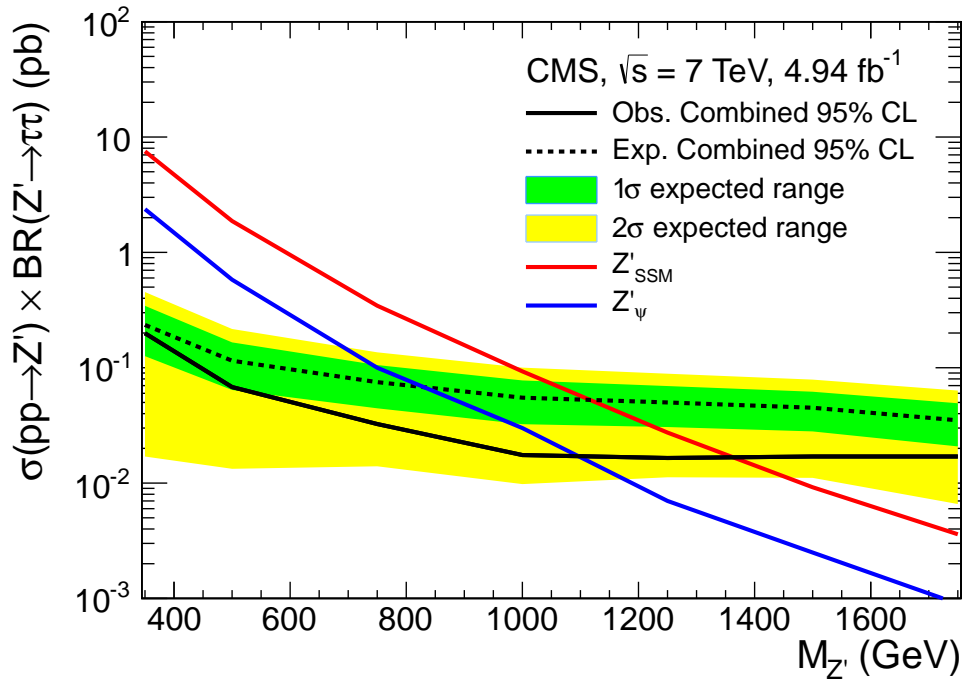


Figure 5.20: Combined 95% C.L. upper limits on the $Z' \rightarrow \tau\tau$ production cross-section as a function of Z' mass for all the four final states: $\tau_{\mu}\tau_h$, $\tau_e\tau_h$, $\tau_e\tau_{\mu}$, and $\tau_h\tau_h$.

Search for $Z' \rightarrow \tau\tau$ using LHC collision data of Run 2012 collected with CMS detector

6.1 Introduction

After an unbeatable success in Year 2011, providing very stringent and the world's best limits [73] on the Higgs boson mass, the LHC machine started its running operation on 30th March 2012 but at 8 TeV center-of-mass energy. The CMS detector recorded its first 8 TeV collision events on 5th April 2012 *i.e.* within a week after the start of the LHC machine. Till date LHC has delivered more than 16 fb^{-1} of data in its current Run 2012. This Chapter describes the studies performed for the search of a Z' gauge boson decaying to $\tau^+\tau^-$ in the $\tau_\mu\tau_h$ final state using $5.10 \pm 0.22 \text{ fb}^{-1}$ of 8 TeV collision data of LHC collected with the CMS detector.

The motivation for analyzing events where one tau-lepton decays to a muon, while the other decays to hadrons is the same for all di-tau related analyses. Because of the lowest jet-to-muon misidentification rate among the family of leptons, the mere requirement of a muon removes a substantial amount of background processes. Once this requirement is imposed, the main source of background for many di-tau related

CHAPTER 6. SEARCH FOR $Z' \rightarrow \tau\tau$ USING LHC COLLISION DATA OF RUN 2012 COLLECTED WITH CMS DETECTOR

searches is due to Drell-Yan processes giving rise to tau-leptons. Because we search for Z' gauge bosons with masses much larger than the mass of the Standard Model Z boson, this source of background can be easily discriminated against by looking at regions with larger invariant mass. This process, however, serves as a control sample to validate tau-identification and reconstruction. Other main sources of background include (1) QCD events where b-jets produce muons associated to jets, (2) $W + jets$ events where the W boson decays to a muon and the jet is misidentified as a hadronic tau, and (3) $t\bar{t}$ events where two leptons can come from the prompt decay of W bosons or one misidentified tau from a jet.

6.2 Pile-Up Reweighting

The signal-like events are selected from the “SingleMu” primary datasets of the collision data. The full list of MC samples used in this analysis is given in the Section 3.8.3.

As in the case of Run 2011 analysis, the Summer 12 MC (official CMS samples corresponding to LHC Run 2012) used for this study are reweighted in order to match with the pile-up distribution present in the collision data. The pile-up spectrum for collision data is obtained using the information from the Luminosity Database. The pile-up weights are obtained by dividing the pile-up distribution in data with the generated pile-up distribution in the MC and the weights thus obtained are applied to the MC samples.

6.3 Event Selection

In order to select signal-like events, a set of loose pre-selections is applied. The complete list of pre-selections is given below.

6.3.1 Skimming Criteria

- Event should have ≥ 1 particle flow taus with $p_T > 15$ GeV/c, $|\eta| < 2.1$.
- Event should have ≥ 1 global muons with $p_T > 8$ GeV/c, $|\eta| < 2.5$.

6.3. EVENT SELECTION

- Event should have ≥ 1 μ - τ pair with $\Delta R > 0.3$, where $\Delta R = \sqrt{\Delta\eta^2 + \Delta\phi^2}$ with $\Delta\eta$ and $\Delta\phi$ being the distances in pseudorapidity and azimuthal angle between the muon and tau.

The triggers are not applied at the skim level for MC samples to avoid any differences between MC and the collision data at the skim level. Table 6.1 shows the MC skim efficiencies for various background processes. The extraction of QCD multijet background is performed with a data-driven method, hence, it is not listed in the Table of skim efficiencies.

Sample	σ x Filter Efficiency (pb)	Events processed	Final N events	ϵ^{Skim}
$Z \rightarrow \mu\mu$	1915.083	1952620	1116313	0.5717
$Z \rightarrow \tau\tau$	1915.083	1989141	148191	0.0745
$W + jets$	36257.2	17914581	2909328	0.1624
$t\bar{t}$	225.197	1198793	444932	0.37115
QCD multijet	Data-driven	—	—	—

Table 6.1: Table shows the skim efficiencies for various MC samples.

6.3.2 Signal Selections

The event selection criteria for this analysis remains the same as that of the analysis with 2011 data (Chapter 5). The event selection criteria is divided into four categories: kinematic and geometric acceptance, muon-identification, tau-identification, and topological selections as described below.

- **Online Event Selection**

Apart from selecting signal-like events, the purpose of online selections is to preserve the maximum fraction of $Z \rightarrow \tau\tau$ events which are then used to validate the tau-identification selections used in the analysis. Taking this fact into account, the lowest un-prescaled “SingleMu” triggers having lowest p_T thresholds on muons i.e. $HLT_IsoMu24*$ have been used to select the events of interest

CHAPTER 6. SEARCH FOR $Z' \rightarrow \tau\tau$ USING LHC COLLISION DATA OF RUN 2012 COLLECTED WITH CMS DETECTOR

from the collision data. With the increase in the instantaneous luminosity during data taking, various triggers had to be prescaled in order to cope with the total bandwidth permissible for the recording of events. The “*” in the trigger names represents different versions of the “SingleMu” trigger depending upon the run-ranges.

• Offline Event Selection

– Acceptance:

- * Event should have atleast one global muon with $|\eta| < 2.1$, $p_T > 30$ GeV/ c .
- * Event should have atleast one PFtau with $|\eta| < 2.1$, $p_T > 20$ GeV/ c .
- * Event should have atleast one $\mu\tau_h$ pair with $\Delta R(\mu, \tau_h) > 0.3$.

– Muon Identification:

- * ≥ 1 μ with global track fit having $\chi^2/\text{ndof} < 10$.
- * ≥ 1 μ having atleast 1 valid muon hit in the muon chambers used in the global track fit. This is a loose (yet potentially powerful) cut to reject the muons from decays-in-flight of hadrons and punch-through at high p_T .
- * ≥ 1 μ which must use hits from segments located in atleast two muon stations. This cut, particularly effective against punch-through and accidental matches, is also consistent with the logic of the CMS muon trigger system, which also requires atleast two muon stations in order to give a meaningful estimate of the transverse momentum.
- * ≥ 1 μ with tracker track having impact parameter $d_{xy} < 2$ mm with respect to the primary vertex. This is a powerful cut to reject muons coming from cosmic rays and other backgrounds. The muons coming from the signal vertex are expected to have very small d_{xy} , however the cosmic muons as well as those from the decays-in-flight of heavy mesons would have large value of d_{xy} .

6.3. EVENT SELECTION

- * $\geq 1 \mu$ with tracker track having longitudinal distance with respect to the primary vertex (d_z) < 5 mm.
 - * $\geq 1 \mu$ having atleast 1 valid pixel hit on a silicon tracker track. This cut is quite effective against rejection of decays-in-flight.
 - * $\geq 1 \mu$ with number of tracker layers with hits > 5 .
 - * $\geq 1 \mu$ passing “Tight” working point of relative isolation (delta-beta corrected).
- τ_h Identification:
- * **Rejection of muons faking tau-leptons:** Since a hadronically decaying tau-lepton can be faked by a muon, hence, a muon veto is applied to remove the muons misidentified as hadronically decaying tau-leptons. For this purpose, the tau-lepton is required to have leading track that cannot be matched to a global muon track. For this analysis, tight working point of muon discriminator has been chosen.
 - * **Rejection of electrons faking tau-leptons:** The electrons can also fake hadronically decaying tau-leptons, hence, an electron veto is imposed to remove the electrons which are misidentified as hadronically decaying tau-leptons. The electron veto requires the HPS taus to pass a discriminator which uses the information of the HCAL energy associated to the tau-lepton with respect to the measured momentum of the leading track of the tau-lepton (H/p). Additionally, the discriminator considers the amount of electromagnetic energy deposited in a narrow strip around the leading track with respect to the total electromagnetic energy of the tau-lepton. Finally, the HPS tau-leptons must not reside inside the ECAL cracks. For this analysis, tight working point of electron discriminator has been chosen.
 - * **Decay Mode Finding Algorithm:** The decay mode finding (DMF) algorithm looks for the probability of decay of tau-leptons. It is imposed by

CHAPTER 6. SEARCH FOR $Z' \rightarrow \tau\tau$ USING LHC COLLISION DATA OF RUN 2012 COLLECTED WITH CMS DETECTOR

requiring the tau-leptons to pass a DMF discriminator value > 0.5 .

- * **Fake tau rejection:** The generic QCD jets can fake hadronically decaying tau-leptons. Tau isolation helps in removing such fake taus. In this analysis, medium working point for tau isolation has been chosen as a balance between the background rejection and jet-to-tau fake rate.

– Topological requirements:

- * **Opposite sign charge requirement:** Due to the electric charge neutrality of Z' gauge boson, the pair of muon and tau-lepton coming from the decay of Z' gauge boson should have opposite charge, therefore, it is required that the muons and tau-leptons forming the pair should have opposite sign charges *i.e.* $Q(\mu) = -Q(\tau_h)$.
- * **Strong anti-parallelism:** Since Z' gauge boson is supposed to be quite heavy, the muon and tau-lepton coming from its decay are expected to be almost back-to-back. Hence, the event is required to have muon and tau-lepton pairs where the muon and tau-lepton are nearly back-to-back *i.e.*:
 - $-1 \leq \cos(\Delta\phi(\mu, \tau_h)) \leq -0.95$.
- * **Missing transverse energy requirement:** Due to the presence of neutrinos in the final state, a fair amount of missing transverse energy is expected in the signal events. For this reason, the event is required to have missing transverse energy (\cancel{E}_T) > 30 GeV.
- * **ζ cut:** To suppress the contribution of $W + jets$ and $t\bar{t}$ backgrounds, an event is required to satisfy the following condition:
 - $P_\zeta - 0.875 \times P_\zeta^{vis} > -7$.

- * **Anti b-tagging:** In order to further suppress the contribution of $t\bar{t}$ background, a b-veto is applied. The anti-b tagging uses a combined secondary vertexing (CSV) algorithm to identify the b-jets. Medium working point has been used in the analysis requiring CSV discriminator value > 0.679 .

6.4 Background Estimation

6.4.1 Estimation of $Z \rightarrow \mu\mu$ background

The estimation of $Z \rightarrow \mu\mu$ background in the signal region is obtained by correcting the predicted rate from the simulated samples using a data-to-MC correction factor obtained from a control sample enriched with $Z \rightarrow \mu\mu$ events and having selections quite similar to the signal selections. The correction factor is used to correct the simulation prediction of $Z \rightarrow \mu\mu$ background. This approach is fairly safe approach because: (1) $Z \rightarrow \mu\mu$ has a small contribution in the signal region; (2) unlike jets, where fake rates are difficult to model, muons are much cleaner objects and are expected to be fairly well modeled by MC. A sample enriched with $Z \rightarrow \mu\mu$ events is obtained by removing the requirement on the missing transverse energy and requiring the τ_h leg to be “muon-like” by inverting the muon veto. Figure 6.1 shows various distributions obtained for events passing above selections. A good agreement for shapes and event rates between data and MC is observed which validates the robustness and performance of the selections. Table 6.2 lists the number of observed events in data as well as the expected MC contributions. The measured data-to-MC correction factor (CF) is 1.096 ± 0.003 . Taking into account the data-to-MC correction factor, the expected $Z \rightarrow \mu\mu$ contribution in the signal region is $N_{Z \rightarrow \mu\mu}^{MC} \times CF = 342.59 \pm 43.36$.

CHAPTER 6. SEARCH FOR $Z' \rightarrow \tau\tau$ USING LHC COLLISION DATA OF RUN 2012 COLLECTED WITH CMS DETECTOR

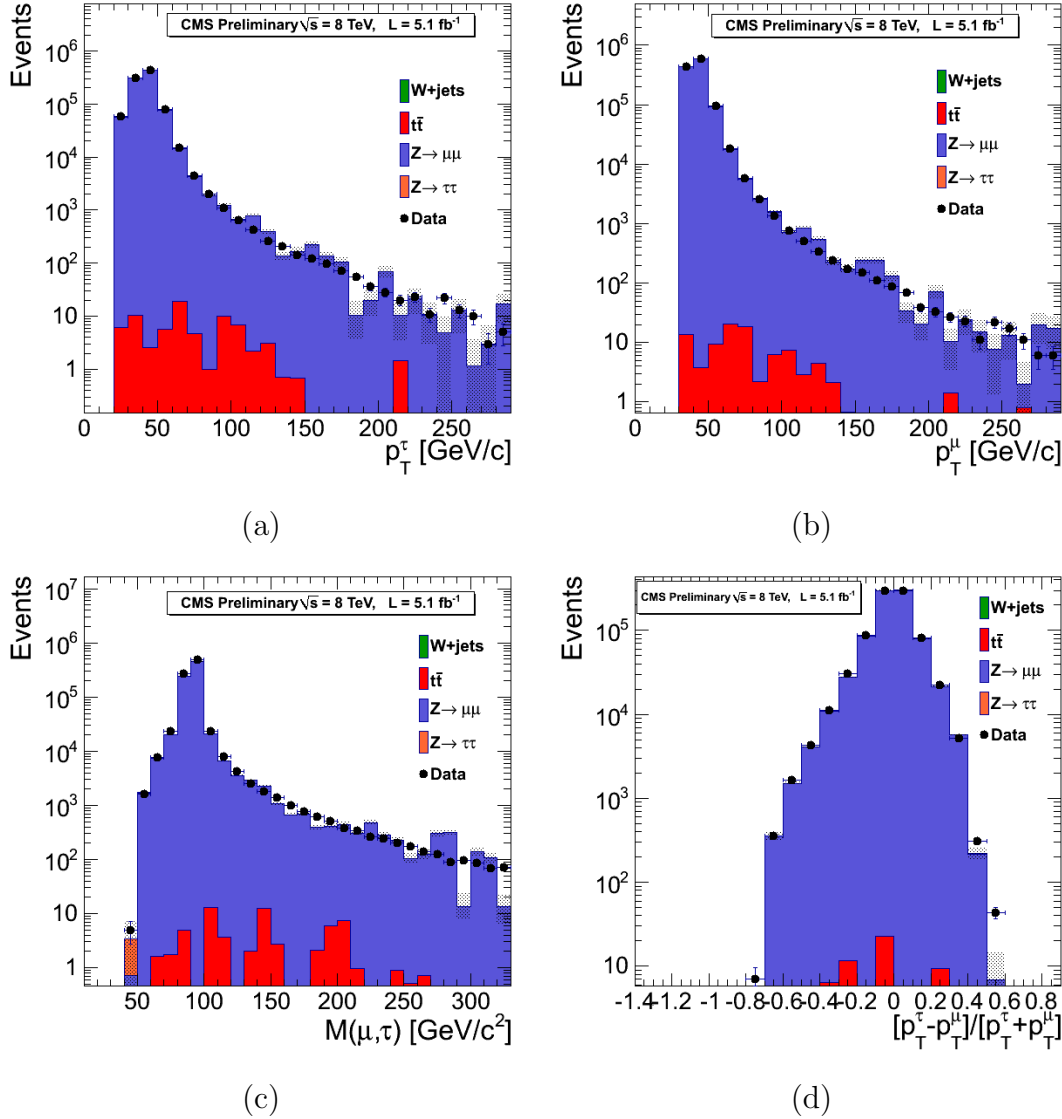


Figure 6.1: Figure shows the distribution for (a) Transverse momentum of τ -lepton, (b) Transverse momentum of μ , (c) Invariant mass of $\mu - \tau$ pair; $M(\mu, \tau)$, and (d) p_T asymmetry between μ and τ -lepton in $Z \rightarrow \mu\mu$ control region.

6.4.2 Estimation of $Z \rightarrow \tau\tau$ background

As mentioned before, an important aspect of the analysis is to use $Z \rightarrow \tau\tau$ events for the validation of tau-identification and also to ensure the robustness of the tau-lepton selections. The methodology used for the estimation of $Z \rightarrow \tau\tau$ background is quite similar to that of $Z \rightarrow \mu\mu$ background. The estimation of $Z \rightarrow \tau\tau$ background in the

6.4. BACKGROUND ESTIMATION

Sample	Events
QCD	—
$W + Jets$	35.24 ± 18.08
$t\bar{t}$	54.43 ± 7.22
$Z \rightarrow \tau\tau$	686.11 ± 55.09
$Z \rightarrow \mu\mu$	568310 ± 1635.60
N_{Total}^{Bkg}	569085.78 ± 1636.64
Data	623918

Table 6.2: Events in the $Z \rightarrow \mu\mu$ control region for data and MC.

signal region is obtained by correcting the predicted rate from the simulated samples using a data-to-MC correction factor obtained from a control sample enriched with $Z \rightarrow \tau\tau$ events and having selections quite similar to the signal selections. The sample enriched with $Z \rightarrow \tau\tau$ events is obtained by removing the requirement on the missing transverse energy, applying an upper threshold on the muon p_T *i.e.*, $p_T^\mu < 40$ GeV/c to suppress $W + jets$ events, and applying a cut on the transverse mass of $\mu - \cancel{E}_T$ *i.e.*, $M_T(\mu, \cancel{E}_T) < 40$ GeV/c² to further suppress the events with W bosons. Figure 6.2 shows various distributions obtained for events passing above selections. A reasonable agreement between the data and MC validates the tau-identification and the signal selections. Table 6.3 lists the number of observed events in data as well as the expected MC contributions. The measured data-to-MC correction factor (CF) is 0.70 ± 0.02 . Therefore, $Z \rightarrow \tau\tau$ prediction in the signal region is $N_{Z \rightarrow \tau\tau}^{MC} \times CF = 886.71 \pm 58.20$.

6.4.3 Estimation of $W + jets$ background

The estimation of $W + jets$ is performed by creating two control samples enriched with high purity of $W + jets$ events. The first control region, $W + jets$ region 1, is obtained by removing the requirements on $\cos\Delta\phi(\mu, \tau)$ and $p_\zeta - 0.875p_\zeta^{\text{vis}}$, and also requiring the transverse mass of the $\mu - \cancel{E}_T$ to be compatible with the W mass

CHAPTER 6. SEARCH FOR $Z' \rightarrow \tau\tau$ USING LHC COLLISION DATA OF RUN 2012 COLLECTED WITH CMS DETECTOR

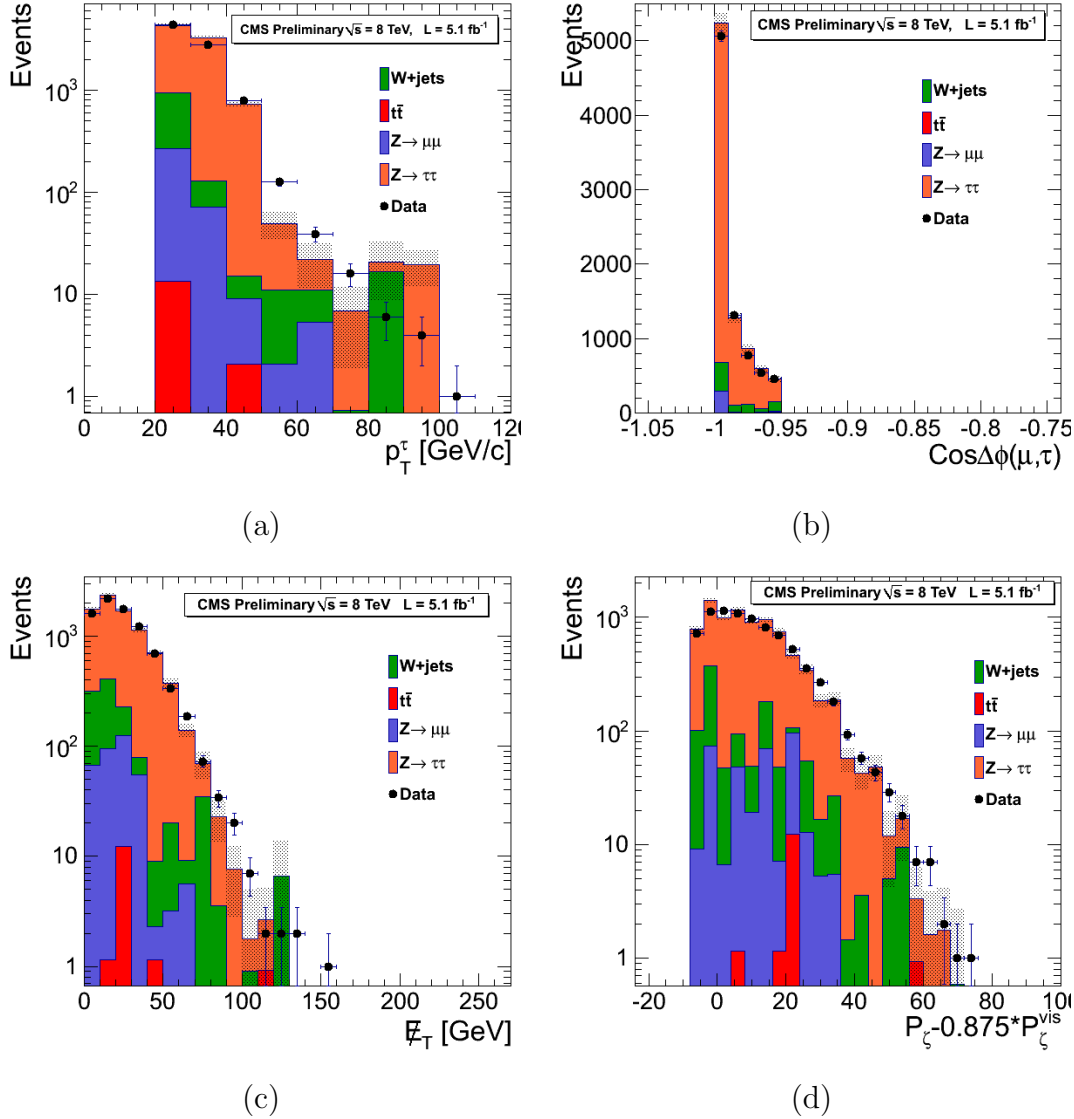


Figure 6.2: Figure shows the distribution for (a) Transverse momentum of τ -lepton, (b) $\cos\Delta\phi(\mu, \tau)$, (c) Missing Transverse Energy, and (d) One-dimensional ζ in $Z \rightarrow \tau\tau$ control region.

($50 < M_T(\mu, E_T) < 100 \text{ GeV}/c^2$). Figure 6.3 shows the $\cos\Delta\phi(\mu, \tau)$ distribution in this control region. Table 6.4 lists the number of observed events in data and expected background contribution from MC in this control region. With the above selections, a sample enriched with $W + jets$ events is obtained which is used to calculate the efficiency for requiring $\cos\Delta\phi(\mu, \tau) < -0.95$ and $p_\zeta - 0.875p_\zeta^{\text{vis}} > -7$. The second control region, $W + jets$ Control Region 2, is obtained by inverting

6.4. BACKGROUND ESTIMATION

Sample	Events
QCD	—
$W + Jets$	719.84 ± 73.15
$t\bar{t}$	15.63 ± 3.87
$Z \rightarrow \mu\mu$	337.93 ± 43.06
$Z \rightarrow \tau\tau$	10154.50 ± 211.86
N_{Total}^{Bkg}	11227.90 ± 228.26
Data	8141

Table 6.3: Events in the $Z \rightarrow \tau\tau$ control region for data and MC.

the requirements on $\cos \Delta\phi(\mu, \tau)$ and $p_\zeta - 0.875p_\zeta^{\text{vis}}$ (*i.e.* $\cos \Delta\phi(\mu, \tau) > -0.95$ and $p_\zeta - 0.875p_\zeta^{\text{vis}} < -7$) to obtain a high purity sample of W +jets events where the efficiency for $50 < M_T(\mu, \cancel{E}_T) < 100$ GeV/c² requirement can be measured. Figure 6.4 shows the $M_T(\mu, \cancel{E}_T)$ distribution in this control region. Table 6.5 lists the number of observed events in data and expected contributions in MC. The measured efficiencies are summarized in Table 6.6.

Sample	Events
QCD	—
$t\bar{t}$	293.82 ± 16.78
$Z \rightarrow \tau\tau$	874.72 ± 62.20
$Z \rightarrow \mu\mu$	1161.67 ± 76.23
$W + jets$	15298.80 ± 376.97
N_{Total}^{Bkg}	17629.01 ± 389.96
Data	17344

Table 6.4: Events in the $W + jets$ Control Region 1 for data and MC.

The $W + jets$ contribution in the signal region is estimated as follows:

$$N_{\text{Signal}}^{W+jets} = N_{\text{Region 1}}^{W+jets} \cdot \frac{\epsilon^{\cos \Delta\phi(\mu, \tau), \zeta}}{\epsilon^{M_T(\mu, \cancel{E}_T)}} \quad (6.1)$$

CHAPTER 6. SEARCH FOR $Z' \rightarrow \tau\tau$ USING LHC COLLISION DATA OF RUN 2012 COLLECTED WITH CMS DETECTOR

The estimated number of $W + jets$ events in the signal region = 2163.54 ± 53.99 .

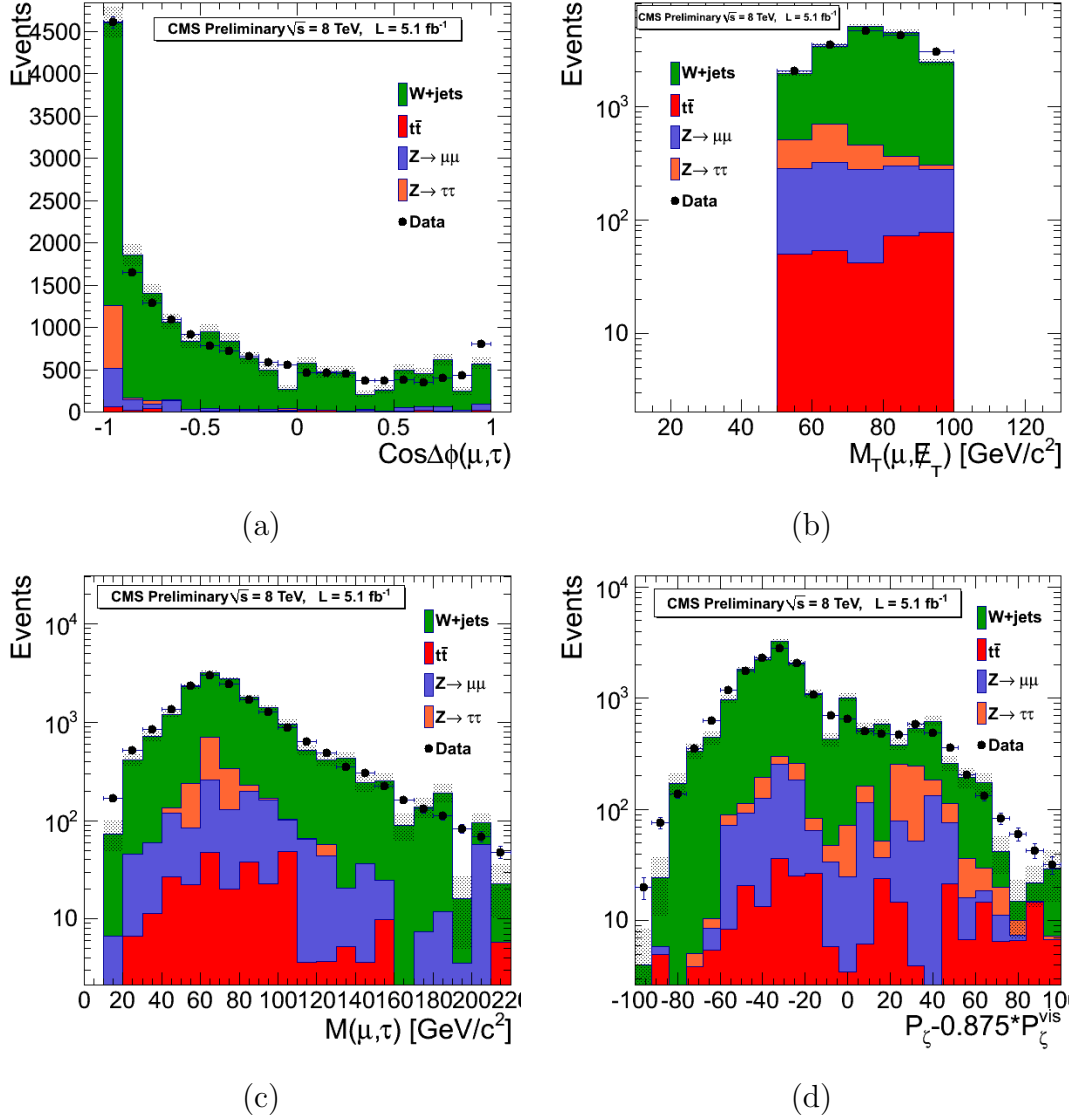


Figure 6.3: Figure shows the distribution for (a) $\cos\Delta\phi(\mu, \tau)$, (b) Transverse mass of μ - \cancel{E}_T pair, (c) Invariant mass of μ - τ pair, and (d) One-dimensional ζ in $W + jets$ Control Region 1.

6.4.4 Estimation of $t\bar{t}$ background

The estimation of $t\bar{t}$ background is performed by creating two control regions enriched with $t\bar{t}$ events. First control region is created by requiring the presence of at least one

6.4. BACKGROUND ESTIMATION

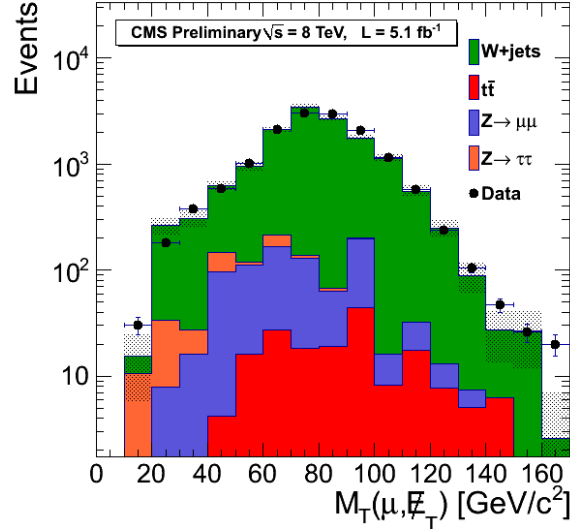


Figure 6.4: Figure shows the distribution for transverse mass of μ - \cancel{E}_T pair in $W + jets$ Control Region 2.

b-tagged jet in the event and removing the cuts $\cos\Delta\phi(\mu, \tau) < -0.95$, $p_\zeta - 0.875p_\zeta^{\text{vis}} > -7$. Figure 6.5 shows various distributions in this control region. Table 6.7 shows the number of observed events in data and expected MC background contribution in this control region. The measured data-to-MC scale factor in this control region is 1.2 ± 0.05 . The contribution of $t\bar{t}$ background in the signal region is determined as:

$$N_{\text{Signal}}^{t\bar{t}} = N_{\text{CR1}} \cdot \epsilon^{\Delta\phi(\mu, \tau), \zeta} \cdot \frac{\epsilon^{\text{NBtag} < 1}}{\epsilon^{\text{NBtag} \geq 1}}, \quad (6.2)$$

where $N_{\text{CR1}}^{t\bar{t}}$ is the number of events in the Control Region 1, $\epsilon^{\Delta\phi(\mu, \tau), \zeta}$ is the efficiency for selecting events satisfying $\cos\Delta\phi(\mu, \tau) < -0.95$ and $p_\zeta - 0.875p_\zeta^{\text{vis}} > -7$ requirements, $\epsilon^{\text{NBtag} < 1}$ is the probability to tag zero jets as b-jets, and $\epsilon^{\text{NBtag} \geq 1}$ is the probability to tag at least one jet as a b-jet. The probability to tag n jets as b-jets is measured by using a second Control Sample 2 enriched with a high purity of $t\bar{t}$ events obtained by selecting events with inverted $\cos\Delta\phi(\mu, \tau)$ and $p_\zeta - 0.875p_\zeta^{\text{vis}}$ cuts along with the requirement of high multiplicity of jets ($N_{jets} \geq 2$). Figure 6.6 shows the distribution of the number of jets tagged as b-jets in this control region. The measured efficiencies are summarized in Table 6.8. The estimated number of $t\bar{t}$ events in the signal region is 159.24 ± 11.17 .

CHAPTER 6. SEARCH FOR $Z' \rightarrow \tau\tau$ USING LHC COLLISION DATA OF RUN 2012 COLLECTED WITH CMS DETECTOR

Sample	Events
QCD	—
$t\bar{t}$	201.21 ± 13.48
$Z \rightarrow \tau\tau$	165.98 ± 27.09
$Z \rightarrow \mu\mu$	687.43 ± 58.65
$W + jets$	13591.30 ± 355.34
N_{Total}^{Bkg}	14645.92 ± 361.42
Data	14596

Table 6.5: Events in the $W + jets$ Control Region 2 for data and MC.

Cut	Eff. measured in data
$\cos\Delta\phi(\mu, \tau) \leq -0.95$ and $p_\zeta - 0.875p_\zeta^{\text{vis}} > -7$	0.096 ± 0.002
$50 < M_T(\mu, \cancel{E}_T) < 100 \text{ GeV}/c^2$	0.768 ± 0.003
Expected number of events in the signal region	2163.54 ± 53.99

Table 6.6: Cut efficiencies and expected number of $W + jets$ events in the signal region.

6.4.5 Estimation of QCD multijet background

The extraction of QCD multijet background from the collision data is performed by applying exact same selections as the signal selections but requiring events to have same-sign μ - τ pairs. The events thus selected, are dominated by the QCD multijet background with a small contamination from other non-QCD backgrounds. The rate of QCD multijet events is estimated by subtracting off the contribution of other like-sign (LS) non-QCD backgrounds. The final prediction for QCD multijet events is calculated as: $(N_{LS} - N_{cor}) \times R_{OS/LS}$, where N_{LS} refers to the number of events in the collision data with all other selections exactly same as the signal selections but requiring like-sign μ - τ pairs, N_{cor} refers to correction factor obtained from like-sign events from non-QCD backgrounds (estimated from MC), and $R_{OS/LS}$ denotes the ratio of number of events selected with opposite-sign requirement to the number of

6.4. BACKGROUND ESTIMATION

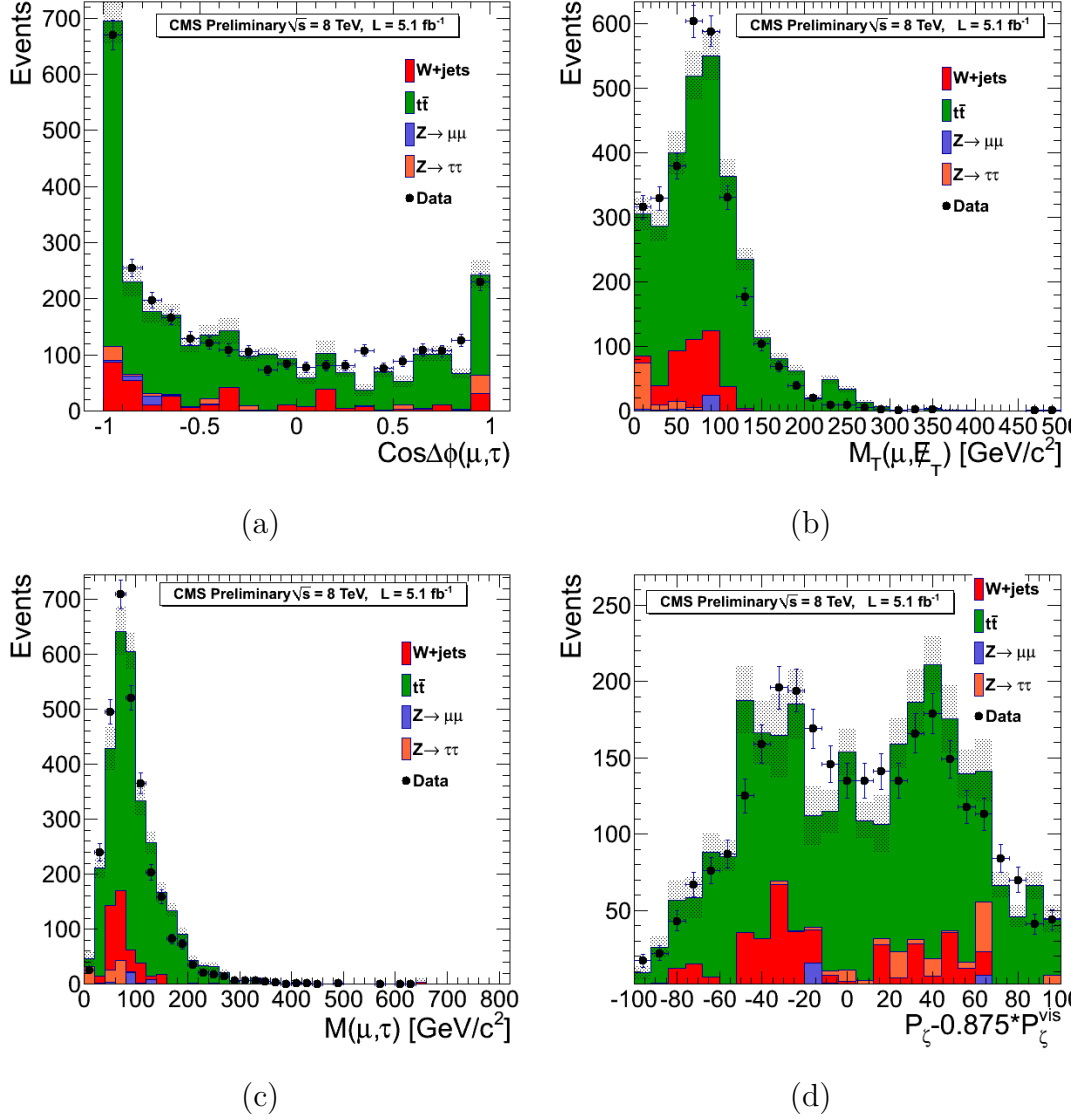


Figure 6.5: Figure shows the distribution for (a) $\cos\Delta\phi(\mu, \tau)$, (b) Transverse mass of μ - \cancel{E}_T pair, (c) Invariant mass of μ - τ pair, and (d) One-dimensional ζ in $t\bar{t}$ Control Region 1.

events selected with like-sign requirement. The ratio ($R_{OS/LS}$) is measured to be 1.1 ± 0.2 . Taking this into account the QCD multijet contribution in signal region is 326.83 ± 105.66 .

CHAPTER 6. SEARCH FOR $Z' \rightarrow \tau\tau$ USING LHC COLLISION DATA OF RUN 2012 COLLECTED WITH CMS DETECTOR

Sample	Events
QCD	—
$Z \rightarrow \tau\tau$	69.32 ± 14.64
$Z \rightarrow \mu\mu$	35.76 ± 14.0
$W + Jets$	354.74 ± 57.67
$t\bar{t}$	2053.86 ± 44.78
N_{Total}^{Bkg}	2513.68 ± 75.77
Data	2991

Table 6.7: Number of events in the $t\bar{t}$ Control Region 1 for data and MC.

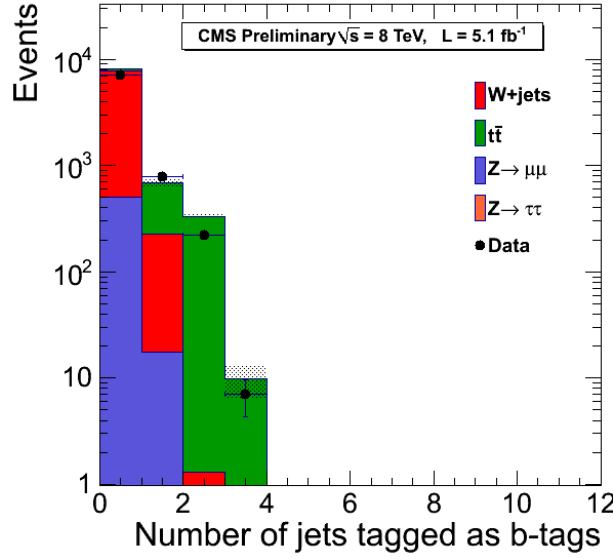


Figure 6.6: Figure shows the distribution for number of jets tagged as b-tags in $t\bar{t}$ Control Region 2.

6.5 Data in the Signal Region and Results

The number of events expected from SM backgrounds and observed events in data are shown in Table 6.9. The number of observed events in data are consistent within statistical uncertainty to the expected number of events from SM background predictions. We are now in the process of updating the results with full 2012 data available

6.5. DATA IN THE SIGNAL REGION AND RESULTS

Cut	Data
$\cos\Delta\phi \leq -0.95$ and $p_\zeta - 0.875p_\zeta^{vis} > -7$	0.0896 ± 0.005
Probability to tag 0 $b - jets$	0.4765 ± 0.0253
Expected Number of Events	159.24 ± 11.17

Table 6.8: $t\bar{t}$ extraction efficiencies and expected number of $t\bar{t}$ events in the signal region.

till date [74]. The results will then be combined with the other channels considered for this search to have a statistical interpretation of the results.

Sample	Events
$Z \rightarrow \tau\tau$	886.71 ± 58.20
$Z \rightarrow \mu\mu$	342.59 ± 43.36
$W + jets$	2163.54 ± 53.99
$t\bar{t}$	159.24 ± 11.17
QCD	326.83 ± 113.63
$N_{Tot.}^{Bkg.}$	3878.91 ± 145.67
Data	3928

Table 6.9: Number of events in the signal region for data and MC backgrounds.

CHAPTER 6. SEARCH FOR $Z' \rightarrow \tau\tau$ USING LHC COLLISION DATA OF RUN 2012 COLLECTED WITH CMS DETECTOR

In this Chapter, the search results for $Z' \rightarrow \tau\tau$ in $\tau_\mu\tau_h$ final state using pp collision data at 8 TeV, are presented. The data corresponds to an integrated luminosity of $5.10 \pm 0.22 \text{ fb}^{-1}$ collected by the CMS detector during current LHC Run 2012. No excess of events above SM background predictions is observed in the collision data.

Summary and Conclusions

The Standard Model of particle physics is an excellent theoretical framework which can explain most of the phenomena occurring in the nature. However, there are several experimental evidences which require new theoretical models to explain *e.g.* non-zero mass of neutrinos which is evident from neutrino oscillations, existence of dark matter and dark energy, *etc.* Many extensions of the Standard Model (SUSY, Extra Dimensions, *etc.*) have evolved over the time to explain such experimental observations. The Large Hadron Collider (LHC) has been designed to explore the Standard Model physics as well as the *New Physics* beyond the Standard Model. The Large Hadron Collider started its journey in Year 2009 by colliding proton-proton beams at center-of-mass energy of 0.9 TeV and then at 2.36 TeV. The story of success continued with the excellent performance of the LHC machine and its detectors. The proton-proton collisions at center-of-mass energy of 7 TeV, the highest energy reached in any particle collider till Year 2010, were also recorded in March 2010 which marked the start up of the new era of research in Experimental High Energy Physics. The Compact Muon Solenoid (CMS) detector at the LHC, collected data at 7 TeV corresponding to an integrated luminosity of $\int Ldt = 36.0 \pm 1.4 \text{ pb}^{-1}$ during Year 2010 and $\int Ldt = 4.94 \pm 0.11 \text{ fb}^{-1}$ during Year 2011 for physics analyses. During the current LHC Run 2012 at 8 TeV, the LHC has delivered more than 16 fb^{-1} of data.

In this thesis, we have performed the search for new heavy, neutral gauge bosons,

Z' , decaying into $\tau^+\tau^-$ using LHC data corresponding to Run 2010, Run 2011, and Run 2012 collected using the CMS detector. The discovery of such new gauge bosons is one among the potential discoveries expected at the LHC. A brief summary of this search is presented in the following Section.

7.1 Search for Z' gauge bosons decaying to $\tau^+\tau^-$ with the CMS detector

The present search for Z' gauge bosons decaying to $\tau^+\tau^-$ is based on the LHC data collected by the CMS detector during Years 2010, 2011 at 7 TeV, and during Year 2012 at 8 TeV. The combined search considers four dominant decay modes of $Z' \rightarrow \tau\tau$ production: (1) $\tau_h\tau_h$ (42%), (2) $\tau_e\tau_h$ (23.1%), (3) $\tau_\mu\tau_h$ (22.5%), and (4) $\tau_e\tau_\mu$ (6.2%). The $Z' \rightarrow \tau^+\tau^- \rightarrow \tau_e\tau_\mu$ final state has the smallest branching fraction, but little background contamination, while the $Z' \rightarrow \tau^+\tau^- \rightarrow \tau_h\tau_h$ mode has the largest branching fraction, but most background contamination. In this thesis, we have presented, in details, the analyses performed in fully hadronic mode ($Z' \rightarrow \tau^+\tau^- \rightarrow \tau_h\tau_h$) using LHC data of Run 2010 and Run 2011 at 7 TeV center-of-mass energy. Only final results from other three final states have been shown in order to obtain a combined statistical interpretation of the results. The present thesis also includes the analysis performed in the $Z' \rightarrow \tau\tau \rightarrow \tau_\mu\tau_h$ final state using LHC data of Run 2012 at 8 TeV center-of-mass energy.

We identify the signal-like events as the events having two oppositely charged, nearly back-to-back leptons ($e/\mu/\tau_h$). Because the decay of tau-lepton involves emission of neutrinos, a fair amount of missing transverse energy is expected in the signal-like events. Moreover, due to the presence of neutrinos in the final state, the $\tau^+\tau^-$ invariant mass distribution does not produce a narrow peak as in the case of e^+e^- and $\mu^+\mu^-$ decay modes, hence, we look for a broad enhancement in the $\tau^+\tau^-$ invariant mass distribution consistent with a resonance production. The signal selections are chosen to maintain high efficiency for signal events while providing strong background suppression, and reducing the influence of systematic effects.

7.1. SEARCH FOR Z' GAUGE BOSONS DECAYING TO $\tau^+\tau^-$ WITH THE CMS DETECTOR

In order to ensure the robustness of the analysis, the estimation of major backgrounds is performed with the help of data-driven methods. For this purpose, we define control regions with most of the selections similar to the signal selections but enriched with events from a particular background process. Once a background enriched region is created, we measure the selection efficiency in those regions and use them to extrapolate to the high mass region where the signal is expected. In cases, where a complete data-driven estimation is not possible, we calculate scale factors from the ratio of observed data events and expected MC events in the background enriched regions to estimate the background contribution in the signal region. Once the expected contribution of each background in the signal region is complete using data-driven methods, we unblind the collision data and look for excess of observed events in data over the MC background expectations. To quantify the significance of any possible excess or to set the upper limits on the $Z' \rightarrow \tau\tau$ production rate, a fit of the $\tau^+\tau^-$ invariant mass distribution is performed and results are interpreted in terms of the upper 95% confidence limit for individual search channels. Finally the combined limit is obtained by combining the posterior probability density functions while taking into account the correlation of systematic uncertainties within and across the four final decay modes.

Assuming the Sequential Standard Model (SSM) as benchmark, a search for $Z' \rightarrow \tau\tau$ performed with LHC data of Run 2010 corresponding to an integrated luminosity of $36.0 \pm 1.4 \text{ pb}^{-1}$ did not reveal any excess of observed events above the Standard Model background predictions, therefore, upper limits on $Z' \rightarrow \tau\tau$ production cross-section were obtained as a function of Z' mass. We excluded a $Z'_{SSM} \rightarrow \tau\tau$ with mass less than $468 \text{ GeV}/c^2$ [65] at 95% confidence level (as shown in Figure 7.1) exceeding the sensitivity ($M_{Z'} > 399 \text{ GeV}/c^2$) by Tevatron experiments at the Fermi National Accelerator Laboratory (FNAL) in Year 2005 [1].

We also performed this search with LHC data of Run 2011 corresponding to an integrated luminosity of $\int L dt = 4.94 \pm 0.11 \text{ fb}^{-1}$ assuming the Sequential Standard Model and Superstring-inspired E_6 models as benchmarks. Again we found no excess of events above the Standard Model background predictions, therefore, we derived

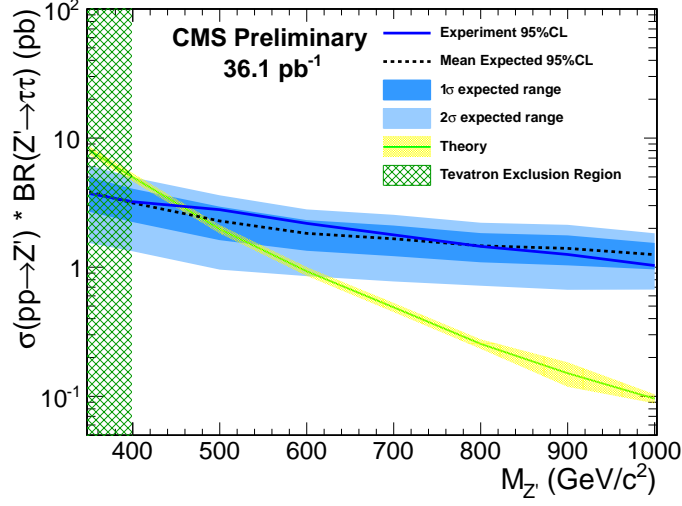


Figure 7.1: Combined $= \tau_\mu\tau_h + \tau_e\tau_h + \tau_e\tau_\mu + \tau_h\tau_h$ limit on the $Z' \rightarrow \tau\tau$ production cross-section as a function of Z' mass.

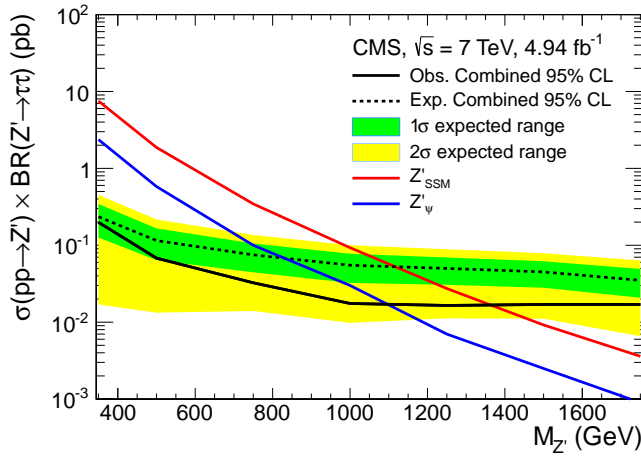


Figure 7.2: Combined 95% CL upper limit on the $Z' \rightarrow \tau\tau$ production cross-section as a function of Z' mass for all the four channels: $\tau_\mu\tau_h$, $\tau_e\tau_h$, $\tau_e\tau_\mu$, and $\tau_h\tau_h$.

7.1. SEARCH FOR Z' GAUGE BOSONS DECAYING TO $\tau^+\tau^-$ WITH THE CMS DETECTOR

upper limits on the $Z' \rightarrow \tau\tau$ production as a function of Z' mass. We excluded Sequential Standard Model resonance Z'_{SSM} and Superstring-inspired E_6 model resonance Z'_ψ below masses 1.4 TeV and 1.1 TeV, respectively, at 95% confidence level [72] as shown in the Figure 7.2. Now the search is being performed using LHC data of Run 2012 [74]. The studies performed in the $Z' \rightarrow \tau\tau \rightarrow \tau_\mu\tau_h$ final state using 5.10 ± 0.22 fb $^{-1}$ of Year 2012 data did not reveal any excess of observed events in the data above the Standard Model background expectations. Search with more data will enable us to either find potential excess of events above the Standard Model background expectations or to set more stringent limit on the Z' mass.

The most stringent limits on Sequential Standard Model resonance Z'_{SSM} at 7 TeV in the di-electron and di-muon decay channels combined are 2.21 TeV from the ATLAS experiment [27] and 2.32 TeV [28] from the CMS experiment.

Bibliography

- [1] The CDF Collaboration, “*Search for new physics using high-mass Tau pairs from 1.96 TeV ppbar collisions*”, *Phys. Rev. Lett.* *95*, 131801 (2005).
- [2] The ATLAS Collaboration, “*A search for high mass resonances decaying to $\tau^+\tau^-$ in the ATLAS detector*”, *ATLAS-CONF-067* (2012).
- [3] M. Herrero, “*The Standard Model*”, *arXiv:hep-ph/9812242v1* (1998).
- [4] M. K. Gaillard, *et al.*, “*Standard Model of Particle Physics*”, *arXiv:hep-ph/9812285v1* (1998).
- [5] F. Wilczek, “*Nobel Lecture: Asymptotic freedom: From paradox to paradigm*”, *Rev. Mod. Phys.* *77*, 857-870 (2005).
- [6] S. L. Glashow, “*Partial-symmetries of weak interactions*”, *Nucl. Phys.* *22*, 579-588 (1961); [http://dx.doi.org/10.1016/0029-5582\(61\)90469-2](http://dx.doi.org/10.1016/0029-5582(61)90469-2).
- [7] S. Weinberg, “*A Model of Leptons*”, *Phys. Rev. Lett.* *19*, 1264-1266 (1967); <http://dx.doi.org/10.1103/PhysRevLett.19.1264>.
- [8] A. Salam, “*Proc. 8th Nobel Symposium*”, *Stockholm*, ed. N. Svartholm (*Almqvist and Wiksells, Stockholm 1968*) p. 367. (1968).
- [9] UA1 Collaboration, “*Experimental observation of isolated large transverse energy electrons with associate missing energy at $\sqrt{s} = 540\text{GeV}$* ”, *Phys. Lett. B* *122*, 103-116 (1983).
- [10] UA2 Collaboration, “*Observation of single isolated electrons of high transverse momentum in events with missing transverse energy at the CERN $\bar{p}p$ Collider*”, *Phys. Lett. B* *122*, 476-485 (1983).
- [11] UA1 Collaboration, “*Experimental observation of lepton pairs of invariant mass around 95 GeV/c² at the CERN SPS Collider*”, *Phys. Lett. B* *126*, 398-410 (1983).

BIBLIOGRAPHY

- [12] *UA2 Collaboration*, “Evidence for $Z^0 \rightarrow e^+e^-$ at the CERN $\bar{p}p$ Collider”, Phys. Lett. B 129, 130-140 (1983).
- [13] *J. Ellis*, et al., “Radiative corrections to the masses of supersymmetric Higgs bosons”, Phys Lett. B, Volume 257, 83-91, doi:10.1016/0370-2693(91)90863-L (1991).
- [14] *G.A. Blair*, “Precision SUSY and the GUT Scale”, 33rd SLAC Summer Institute on Particle Physics (SSI 2005), 25 July-5 August (2005).
- [15] *Y. Ashie*, et al., “Evidence for an oscillatory signature in atmospheric neutrino oscillation”, arXiv:hep-ex/0404034v1 (2004).
- [16] *T. G. Rizzo* , “ Z' Phenomenology and the LHC”, arXiv:hep-ph/0610104v1 (2006).
- [17] *Mirjam Cveti and Stephen Godfrey*, “Discovery and Identification of Extra Gauge Bosons”, arXiv:hep-ph/9504216v1 (1995).
- [18] *Daniel Feldman, Zuowei Lui, Pran Nath*, “The Stueckelberg Z Prime at the LHC: Discovery Potential, Signature Spaces and Model Discrimination”, JHEP 0611:007 (2006).
- [19] *K Nakamura (Particle Data Group)*, “Review of Particle Physics”, Journal of Physics G: Nuclear and Particle Physics, 37(7A):075021 (2010).
- [20] *Jogesh C. Pati, Abdus Salam*, “Lepton Number as the Fourth Color”, Phys. Rev. D10, 275-289 (1974).
- [21] *Tao Han, Heather E. Logan, Bob McElrath*, et. al., “Phenomenology of the little Higgs model”, Phys. Rev. D67.095004 (2003).
- [22] *Manuel Masip, Alex Pomarol*, “Effects of SM Kaluza-Klein excitations on electroweak observables”, Phys. Rev. D60.096005 (1999).
- [23] *Thomas G. Rizzo*, “ Z' bosons and Kaluza-Klein excitations at muon colliders”, arXiv:hep-ph/0001140v1 (2000).

- [24] *Lisa Randall, Raman Sundrun*, “Large Mass Hierarchy from a Small Extra Dimension”, *Phys. Rev. Lett.* 83, 3370-3373 (1999).
- [25] *T. Rizzo*, “Zprime Phenomenology and the LHC”, Published in Boulder, Colliders and Neutrinos (TASI), arXiv:hep-ph/0610104 (2006).
- [26] *J. Hewett and T. Rizzo*, “Low Energy Phenomenology of Superstring Inspired E(6) Models”, *Phys. Rept.* 183, 193-381; doi:10.1016/0370-1573(89)90071-9 (1989).
- [27] *The ATLAS Collaboration*, “Search for high-mass dilepton resonances with 5 fb⁻¹ of pp collisions at $\sqrt{s} = 7$ TeV with the ATLAS experiment”, ATLAS-CONF-007 (2012).
- [28] *The CMS Collaboration*, “Search for narrow resonances in the dilepton mass spectra in pp collisions at $\sqrt{s} = 7$ TeV”, *Phys. Lett. B* 714, 158-179 (2012).
- [29] *The CMS Collaboration*, “The CERN Large Hadron Collider: Accelerator and Experiments”, JINST 0803 S08001 (2008).
- [30] *The CMS Collaboration*, “Observation of a new boson at a mass of 125 GeV with the CMS experiment at the LHC”, *Phys. Lett. B* 716, 30-61 (2012).
- [31] *The CMS Collaboration*, “The CMS experiment at the CERN LHC”, JINST 0803 S08004 (2008).
- [32] *The ATLAS Collaboration*, “The ATLAS Experiment at the CERN Large Hadron Collider”, JINST 0803 S08003 (2008).
- [33] *The LHCb Collaboration*, “The LHCb Detector at the LHC”, JINST 0803 S08005 (2008).
- [34] *The ALICE Collaboration*, “The ALICE experiment at the CERN LHC”, 2008 JINST 0803 S08002 (2008).
- [35] *D. Teaney, J. Lauret, and E. V. Shuryak*, “Flow at the SPS and RHIC as a Quark-Gluon plasma signature”, *Phys. Rev. Lett.* 86, 4783-4786 (2001).

BIBLIOGRAPHY

- [36] *The CMS Collaboration*, “Tracking and Primary Vertex Results in First 7TeV Collisions”, CMS Physics Analysis Summary, CMS-TRK-10-005 (2010).
- [37] *The CMS Collaboration*, “ECAL 2010 performance results”, CMS Detector Performance Summary, CMS-DP-11-008 (2011).
- [38] *A. A. Annenkov*, et al., “Lead tungstate scintillation material”, Nucl. Instrum. Meth. A 490, 30-50 (2002).
- [39] *The CMS Collaboration*, “Energy resolution of the barrel of the CMS electromagnetic calorimeter”, JINST 2 P04004 (2007).
- [40] *The CMS Collaboration*, “HCAL performance from first collisions data”, CMS Detector Performance Summary, CMS-DP-10-025 (2010).
- [41] *The CMS Collaboration*, et al., “Design, performance and calibration of the CMS hadron-outer calorimeter”, Eur. Phys. J. C 57: 653663 (2008); <http://dx.doi.org/10.1140/epjc/s10052-008-0756-6>.
- [42] *The CMS Collaboration*, et al., “The CMS muon project, technical design report”, CERN-LHCC-97-032, <http://cdsweb.cern.ch/record/343814> (1997).
- [43] *The CMS Collaboration*, et al., “Performance of the CMS drift tube chambers with cosmic rays”, JINST 5 T03015 (2010).
- [44] *The CMS Collaboration*, et al., “Performance of the CMS cathode strip chambers with cosmic rays”, JINST 5 T03018 (2010).
- [45] *The CMS Collaboration*, et al., “Performance study of the CMS barrel resistive plate chambers with cosmic rays”, JINST 5 T03017 (2010).
- [46] *R. Santonico*, et al., “Development of resistive plate counters”, Nucl. Instrum. Meth. 187, 377-380 (1981).
- [47] *R. Cardarelli*, et al., “Performance of a resistive plate chamber operating with pure CF₃Br”, Nucl. Instrum. Meth. A 333, 399-403 (1993).

- [48] *The CMS Collaboration*, “Measurement of Momentum Scale and Resolution using Low-mass Resonances and Cosmic Ray Muons”, CMS Physics Analysis Summary, CMS-TRK-10-004 (2010).
- [49] *The CMS Collaboration*, “The TriDAS project, technical design report. Volume 1: The level-1 trigger”, CERN-LHCC-2000-038, <http://cdsweb.cern.ch/record/706847> (2000).
- [50] *The CMS Collaboration*, “The TriDAS project, technical design report. Volume 2: Data acquisition and high-level trigger technical design report”, CERN-LHCC-2002-026, <http://cdsweb.cern.ch/record/578006> (2002).
- [51] *T. Sjöstrand et al.*, “PYTHIA 6.4 physics and manual”, JHEP 0605:026 (2006).
- [52] *J. Alwall et al.*, “MadGraph 5: Going beyond”, arXiv:hep-ph/1106.0522v1 (2011).
- [53] *Z. Was*, “TAUOLA the library for tau lepton decay and KKMC/KORALB/KORALZ/... status report”, arXiv:hep-ph/0011305v1 (2000).
- [54] *S. Agostinelli, et al.*, “GEANT4—a simulation toolkit”, Nucl. Instrum. and Methods in Physics Research”, A 506, 250-303 (2003).
- [55] http://lcgapp.cern.ch/project/simu/HepMC/20400/HepMC2_user_manual.pdf
- [56] *M. Pioppi, et al.*, “Tau reconstruction and identification with particle-flow techniques using the CMS detector at LHC”, Nucl. Phys. B, Proc. Suppl. 189, 311-316 (2009).
- [57] *The CMS Collaboration*, “Performance of tau reconstruction algorithms in 2010 data collected with CMS”, CMS Physics Analysis Summary, CMS-PAS-TAU-11-001 (2010).
- [58] *The CMS Collaboration*, “Missing transverse energy performance of the CMS detector”, JINST 6 P09001 (2011).

BIBLIOGRAPHY

- [59] *G. Abbiendi et al.*, “Muon Reconstruction in the CMS Detector”, CMS Analysis Note, CMS-AN-08-097 (2008).
- [60] *The CMS Collaboration*, “Performance of muon identification in pp collisions at $\sqrt{s} = 7$ TeV”, CMS Physics Analysis Summary, CMS-PAS-MUO-10-002 (2010).
- [61] *P. Langacker*, “The physics of heavy Z-prime gauge bosons”, Rev. Mod. Phys. 81 (2009) 1199-1228, doi:10.1103/RevModPhys.81.1199.
- [62] *R. Diener et al.*, “Unravelling an extra neutral gauge boson at the LHC using third generation fermions”, Phys. Rev. D 83, 115008 (2011); doi:10.1103/PhysRevD.83.115008.
- [63] *The CMS collaboration*, “Electron and muon efficiency measurements in 2010 proton-proton dataset”, CMS-AN-10-464, 2010.
- [64] *The CMS collaboration*, “Measurement of tracking efficiency”, CMS Physics Analysis Summary, CMS-TRK-10-002, 2010.
- [65] *The CMS Collaboration*, “Search for New Ditau Resonances in pp Collisions at $\sqrt{s}= 7$ TeV”, CMS Physics Analysis Summary, CMS-EXO-10-022, (2011).
- [66] *J. Cumalat, N. Dhingra, A. Florez et al.*, “Search for Heavy Resonances Decaying to Di Tau States”, CMS-AN-11-326 (2012).
- [67] *P. Nadolsky, et al.*, “Implications of CTEQ global analysis for collider observables”, Phys. Rev. D 78 013004 (2008).
- [68] *G. Nanava, et al.*, “How to use SANC to improve the PHOTOS Monte Carlo simulation of bremsstrahlung in leptonic W-Boson decays”, arXiv:hep-ph/0303260 (2003).
- [69] *G. Miu, et al.*, “W Production in an Improved Parton-Shower Approach”, arXiv:hep-ph/9812455 (1998).

- [70] *The CMS Collaboration*, “Absolute luminosity normalization”, Detector Performance Summary, CMS-DPS-11-002 (2011).
- [71] *The CMS Collaboration*, “Performance of b–Jet Identification in CMS”, CMS Physics Analysis Summary, CMS-PAS-BTV-11-001 (2011).
- [72] *The CMS Collaboration*, “Search for high-mass resonances decaying into τ -lepton pairs in pp collisions at $\sqrt{s} = 7$ TeV”, Phys. Lett. B, Volume 716, Issue 1, 82-102 (2012); doi: <http://dx.doi.org/10.1016/j.physletb.2012.07.062>.
- [73] *The CMS Collaboration*, “Combined results of searches for the standard model Higgs boson in pp collisions at $\sqrt{s} = 7$ TeV”, Phys. Lett. B 710, 26-48 (2012), doi:10.1016/j.physletb.201202.064.
- [74] *The CMS Collaboration*, “Search for Heavy Resonances Decaying to DiTau States in pp Collisions at $\sqrt{s} = 8$ TeV”, CMS Analysis Note, CMS-AN-12-309 (2012) (Under Preparation).

Publications/CMS Public Notes with Direct Contribution

1. The CMS Collaboration, “Search for high-mass resonances decaying into τ -lepton pairs in pp collisions at $\sqrt{s} = 7$ TeV”, *Phys. Lett. B*, Volume 716, Issue 1, pp. 82-102 (2012); <http://dx.doi.org/10.1016/j.physletb.2012.07.062>.
2. N. Dhingra, “Search for heavy resonances decaying to tau pairs with the CMS detector at the Large Hadron Collider”, *Pramana-Journal of Physics* (2012), [doi:10.1007/s12043-012-0392-4](https://doi.org/10.1007/s12043-012-0392-4).
3. The CMS Collaboration, “Extension of the search for the standard model Higgs boson decaying to tau pairs in pp Collisions”, *CMS Physics Analysis Summary*, CMS-HIG-12-032 (2012).
4. The CMS Collaboration, “Search for charginos and neutralinos produced in vector boson fusion processes in pp collisions at $\sqrt{s} = 8$ TeV”, *CMS Physics Analysis Summary*, CMS-SUS-12-025 (Under approval).
5. The CMS Collaboration, “Search for New DiTau Resonances in pp Collisions at $\sqrt{s} = 7$ TeV”, *CMS Physics Analysis Summary*, CMS-EXO-10-022 (2011).
6. N. Dhingra, K. Mazumdar, J.B. Singh, *et al.*, “Search for heavy resonances decaying to tau pairs with the CMS detector at the LHC”, *CMS conference Report*, CMS-CR-2011/318 (2011).

CMS Analysis Notes with Direct Contribution

1. N. Dhingra, K. Mazumdar, J.B. Singh, *et al.*, “Search for EWKinos and Sleptons Produced in Vector Boson Fusion Processes with $\sqrt{s} = 8$ TeV”, *CMS Analysis Note* CMS-AN-2012/321 (2012).

2. N. Dhingra, K. Mazumdar, J.B. Singh, *et al.*, “Search for Heavy Resonances Decaying to DiTau States in pp Collisions at $\sqrt{s} = 8$ TeV”, CMS Analysis Note CMS-AN-2012/309 (Under preparation).
3. N. Dhingra, K. Mazumdar, J.B. Singh, *et al.*, “Search for the standard model Higgs boson decaying into tautau in association with jets, W boson and Z boson at $\sqrt{s} = 7$ TeV and $\sqrt{s} = 8$ TeV, CMS Analysis Note CMS-AN-2012/206 (2012).
4. N. Dhingra, K. Mazumdar, J.B. Singh, *et al.*, “Search for Heavy Resonances Decaying to DiTau States”, CMS Analysis Note CMS-AN-2011/326 (2011).
5. N. Dhingra, K. Mazumdar, J.B. Singh, *et al.*, “Search for Heavy Resonances Decaying to Tau Pairs in CMS”, CMS Analysis Note CMS-AN-2011/007 (2011).
6. N. Dhingra *et al.*, “Trigger strategies for Higgs searches”, CMS Analysis Note CMS-AN-2011/065 (2011).

Papers/Posters presented in the Conferences

1. N. Dhingra, K. Mazumdar, J.B. Singh, *et al.*, “Search for high mass resonances decaying to tau-lepton pair in pp collisions at $\sqrt{s} = 7$ TeV”, MCnet-LPCC Summer School on Monte Carlo Event Generators for LHC, 23-27 July, 2012, CERN, Geneva, Switzerland.
2. N. Dhingra, K. Mazumdar, J.B. Singh, *et al.*, “Search for Heavy Resonances Decaying to DiTau states using CMS detector at the LHC”, VI Chandigarh Science Congress, February 26-28, 2012, Panjab University, Chandigarh, India.
3. N. Dhingra, K. Mazumdar, J.B. Singh, *et al.*, “Search for heavy resonances decaying to tau pairs with the CMS detector at the LHC”, XXV International Symposium On Lepton Photon Interactions at High Energies, August 22-27, 2011, TIFR, Mumbai, India.

4. N. Dhingra, K. Mazumdar, J.B. Singh, *et al.*, “*Perspective of searches for neutral heavy gauge boson Z' with the early LHC data in the CMS experiment*”, XIX DAE-BRNS High Energy Physics Symposium, December 13-18, 2010, LNMIIT, Jaipur, India.
5. N. Dhingra, K. Mazumdar, J.B. Singh, *et al.*, “*Search for a new heavy neutral gauge boson through its di-tau decay mode using CMS detector at the LHC*”, V Chandigarh Science Congress, February 26-28, 2010, Panjab University, Chandigarh, India.

CMS Publications

1. The CMS Collaboration, “*Observation of Z decays to four leptons with the CMS detector at the LHC*”,
<http://arxiv.org/abs/1210.3844>, Submitted to *J. High Energy Phys.* (2012).
2. The CMS Collaboration, “*Search for excited leptons in pp collisions at $\sqrt{s} = 7$ TeV*”,
<http://arxiv.org/abs/1210.2422>, Submitted to *Phys. Lett. B* (2012).
3. The CMS Collaboration, “*Search for heavy neutrinos and W bosons with right-handed couplings in a left-right symmetric model in pp collisions at 7 TeV*”,
<http://arxiv.org/abs/1210.2402>, Submitted to *Phys. Rev. Lett.* (2012).
4. The CMS Collaboration, “*Search for fractionally charged particles in pp collisions at $\sqrt{s} = 7$ TeV*”,
<http://arxiv.org/abs/1210.2311>, Submitted to *Phys. Rev. Lett.* (2012).
5. The CMS Collaboration, “*Search for supersymmetry in events with photons and low missing transverse energy in pp collisions at $\sqrt{s} = 7$ TeV*”,
<http://arxiv.org/abs/1210.2052>, Submitted to *Phys. Lett. B* (2012).
6. The CMS Collaboration, “*Search for heavy lepton partners of neutrinos in proton-proton collisions in the context of the type III seesaw mechanism*”,
<http://arxiv.org/abs/1210.1797>, Submitted to *Phys. Lett. B* (2012).

7. The CMS Collaboration, “Measurement of the relative prompt production rate of χ_{c2} and χ_{c1} in pp collisions at $\sqrt{s} = 7 \text{ TeV}$ ”,
<http://arxiv.org/abs/1210.0875>, Submitted to *Eur. Phys. J. C* (2012).
8. The CMS Collaboration, “Search for anomalous production of highly boosted Z bosons decaying to dimuons in pp collisions at $\sqrt{s} = 7 \text{ TeV}$ ”,
<http://arxiv.org/abs/1210.0867>, Submitted to *Phys. Lett. B* (2012).
9. The CMS Collaboration, “Search for electroweak production of charginos and neutralinos using leptonic final states in pp collisions at $\sqrt{s} = 7 \text{ TeV}$ ”,
<http://arxiv.org/abs/1209.6620>, Submitted to *J. High Energy Phys.* (2012).
10. The CMS Collaboration, “Measurement of the single-top-quark t -channel cross-section in pp collisions at $\sqrt{s} = 7 \text{ TeV}$ ”,
<http://arxiv.org/abs/1209.4533>, Submitted to *J. High Energy Phys.* (2012).
11. The CMS Collaboration, “Search for resonant $t\bar{t}$ production in lepton+jets events in pp collisions at $\sqrt{s} = 7 \text{ TeV}$ ”,
<http://arxiv.org/abs/1209.4397>, Submitted to *J. High Energy Phys.* (2012).
12. The CMS Collaboration, “Search for the standard model Higgs boson produced in association with W and Z bosons in pp collisions at $\sqrt{s} = 7 \text{ TeV}$ ”,
<http://arxiv.org/abs/1209.3937>, Submitted to *J. High Energy Phys.* (2012).
13. The CMS Collaboration, “Search for a narrow spin-2 resonance decaying to a pair of Z vector bosons in the semileptonic final state”,
<http://arxiv.org/abs/1209.3807>, Submitted to *Phys. Lett. B* (2012).
14. The CMS Collaboration, “Evidence for associated production of a single top quark and W boson in pp collisions at 7 TeV ”,
<http://arxiv.org/abs/1209.3489>, Submitted to *Phys. Rev. Lett.* (2012).
15. The CMS Collaboration, “Measurement of the $Y(1S)$, $Y(2S)$ and $Y(3S)$ polarizations in pp collisions at $\sqrt{s} = 7 \text{ TeV}$ ”,
<http://arxiv.org/abs/1209.2922>, Submitted to *Phys. Rev. Lett.* (2012).

16. The CMS Collaboration, “*Measurement of the top-quark mass in $t\bar{t}$ events with dilepton final states in pp collisions at $\sqrt{s} = 7$ TeV*”,
<http://arxiv.org/abs/1209.2393>, Submitted to Eur. Phys. J. C (2012).
17. The CMS Collaboration, “*Measurement of the top-quark mass in $t\bar{t}$ events with lepton+jets final states in pp collisions at $\sqrt{s} = 7$ TeV*”,
<http://arxiv.org/abs/1209.2319>, Submitted to J. High Energy Phys. (2012).
18. The CMS Collaboration, “*Observation of a diffractive contribution to dijet production in proton-proton collisions at $\sqrt{s} = 7$ TeV*”,
<http://arxiv.org/abs/1209.1805>, Submitted to Phys. Rev. D (2012).
19. The CMS Collaboration, “*Search for exclusive or semi-exclusive photon pair production and observation of exclusive and semi-exclusive electron pair production in pp collisions at $\sqrt{s} = 7$ TeV*”,
<http://arxiv.org/abs/1209.1666>, Submitted to J. High energy Phys. (2012).
20. The CMS Collaboration, “*Combined search for the quarks of a sequential fourth generation*”,
<http://arXiv.org/abs/1209.1062>, Submitted to Phys. Rev. D (2012).
21. The CMS Collaboration, “*Search for pair produced fourth-generation up-type quarks in pp collisions at $\sqrt{s} = 7$ TeV with a lepton in the final state*”,
<http://arXiv.org/abs/1209.0471>, Submitted to Phys. Lett. B (2012).
22. The CMS Collaboration, “*Search for supersymmetry in events with b -quark jets and missing transverse energy in pp collisions at 7 TeV*”,
<http://arXiv.org/abs/1208.4859>, Submitted to Phys. Rev. D (2012).
23. The CMS Collaboration , “*Study of the dijet mass spectrum in $pp \rightarrow W + \text{jets}$ events at $\sqrt{s} = 7$ TeV*”,
<http://arXiv.org/abs/1208.3477>, Phys. Rev. Lett. (2012).
24. The CMS Collaboration, “*Search for three-jet resonances in pp collisions at $\sqrt{s} =$*

7 TeV ”,

<http://arXiv.org/abs/1209.2931>, *Phys. Lett. B* (2012).

25. The CMS Collaboration, “*Observation of sequential Upsilon suppression in PbPb collisions*”,

<http://arXiv.org/abs/1208.2826>, *Submitted to Phys. Rev. Lett.* (2012).

26. The CMS Collaboration, “*Measurement of the $t\bar{t}$ production cross section in the dilepton channel in pp collisions at $\sqrt{s} = 7\text{ TeV}$* ”,

<http://arXiv.org/abs/1208.2671>, *Submitted to J. High Energy Phys.* (2012).

27. The CMS Collaboration, “*Measurement of the azimuthal anisotropy of neutral pions in PbPb collisions at $\sqrt{s_{NN}} = 2.76\text{ TeV}$* ”,

<http://arXiv.org/abs/1208.2470>, *Submitted to Phys. Rev. Lett.* (2012).

28. The CMS Collaboration, “*Search for flavor changing neutral currents in top quark decays in pp collisions at 7 TeV* ”,

<http://arxiv.org/abs/1208.0957>, *Submitted to Phys. Lett. B* (2012).

29. The CMS Collaboration, “*Search for a W' boson decaying to a bottom quark and a top quark in pp collisions at $\sqrt{s} = 7\text{ TeV}$* ”,

<http://arxiv.org/abs/1208.0956>, *Submitted to Phys. Lett. B* (2012).

30. The CMS Collaboration, “*Observation of a new boson at a mass of 125 GeV with the CMS experiment at the LHC*”,

<http://arxiv.org/abs/1207.7235>, *Phys. Lett. B* 716, pp 30-61 (2012).

31. The CMS Collaboration, “*Search for heavy Majorana neutrinos in $\mu^\pm\mu^\pm$ and $e^\pm e^\pm$ events in pp collisions at $\sqrt{s} = 7\text{ TeV}$* ”,

<http://arxiv.org/abs/1207.6079>, *Phys. Lett. B* (2012) (In Press).

32. The CMS Collaboration, “*Search for pair production of first- and second-generation scalar leptoquarks in pp collisions at $\sqrt{s} = 7\text{ TeV}$* ”,

<http://arxiv.org/abs/1207.5406>, *Submitted to Phys. Rev. D* (2012).

- 33. The CMS Collaboration, “*Study of the inclusive production of charged pions, kaons, and protons in pp collisions at $\sqrt{s} = 0.9, 2.76$, and 7 TeV*”,
<http://arxiv.org/abs/1207.4724>, Submitted to *Eur. Phys. J. C* (2012).
- 34. The CMS Collaboration, “*Forward-backward asymmetry of Drell-Yan lepton pairs in pp collisions at $\sqrt{s} = 7$ TeV*”,
<http://arxiv.org/abs/1207.3973>, Submitted to *Phys. Lett. B* (2012).
- 35. The CMS Collaboration, “*A search for a doubly-charged Higgs boson in pp collisions at $\sqrt{s} = 7$ TeV*”,
<http://arxiv.org/abs/1207.2666>, Submitted to *Eur. Phys. J. C* (2012).
- 36. The CMS Collaboration, “*Measurement of the underlying event activity in pp collisions at $\sqrt{s} = 0.9$ and 7 TeV with the novel jet-area/median approach*”,
<http://arxiv.org/abs/1207.2392>, *J. High Energy Phys.* 08 130 (2012).
- 37. The CMS Collaboration, “*Search for new physics in the multijet and missing transverse momentum final state in proton-proton collisions at $\sqrt{s} = 7$ TeV*”,
<http://arxiv.org/abs/1207.1898>, Submitted to *Phys. Rev. Lett.* (2012).
- 38. The CMS Collaboration, “*Search for supersymmetry in hadronic final states using M_{T2} in pp collisions at $\sqrt{s} = 7$ TeV*”,
<http://arxiv.org/abs/1207.1798>, Submitted to *J. High Energy Phys.* (2012).
- 39. The CMS Collaboration, “*Search for a fermiophobic Higgs boson in pp collisions at $\sqrt{s} = 7$ TeV*”,
<http://arxiv.org/abs/1207.1130>, Submitted to *J. High Energy Phys.* (2012).
- 40. The CMS Collaboration, “*Search for new physics with long-lived particles decaying to photons and missing energy in pp collisions at $\sqrt{s} = 7$ TeV*”,
<http://arxiv.org/abs/1207.0627>, Submitted to *J. High Energy Phys.* (2012).
- 41. The CMS Collaboration, “*Search for stopped long-lived particles produced in pp collisions at $\sqrt{s} = 7$ TeV*”,
<http://arxiv.org/abs/1207.0106>, *J. High Energy Phys.* 08 026 (2012).

42. The CMS Collaboration, “*Inclusive and differential measurements of the $t\bar{t}$ charge asymmetry in proton-proton collisions at $\sqrt{s} = 7$ TeV*”,
<http://arxiv.org/abs/1207.0065>, *Phys. Lett. B* (2012) (In Press).
43. The CMS Collaboration, “*Search for a light pseudoscalar Higgs boson in the dimuon decay channel in pp collisions at $\sqrt{s} = 7$ TeV*”,
<http://arxiv.org/abs/1206.6326>, Submitted to *Phys. Rev. Lett.* (2012).
44. The CMS Collaboration, “*Search for dark matter and large extra dimensions in monojet events in pp collisions at $\sqrt{s} = 7$ TeV*”,
<http://arxiv.org/abs/1206.5663>, Submitted to *J. High Energy Phys.* (2012).
45. The CMS Collaboration, “*Performance of CMS muon reconstruction in pp collision events at $\sqrt{s} = 7$ TeV*”,
<http://arxiv.org/abs/1206.4071>, Submitted to *J. Instrum.* (2012).
46. The CMS Collaboration, “*Search for new physics in events with opposite-sign leptons, jets, and missing transverse energy in pp collisions at $\sqrt{s} = 7$ TeV*”,
<http://arxiv.org/abs/1206.3949>, Submitted to *Phys. Lett. B* (2012).
47. The CMS Collaboration, “*Search for charge-asymmetric production of W' bosons in top pair + jet events from pp collisions at $\sqrt{s} = 7$ TeV*”,
<http://arxiv.org/abs/1206.3921>, Submitted to *Phys. Lett. B* (2012).
48. The CMS Collaboration, “*Measurement of the electron charge asymmetry in inclusive W production in pp collisions at $\sqrt{s} = 7$ TeV*”,
<http://arxiv.org/abs/1206.2598>, *Phys. Rev. Lett.* 109 111806 (2012).
49. The CMS Collaboration, “*Search for narrow resonances in dilepton mass spectra in pp collisions at $\sqrt{s} = 7$ TeV*”,
<http://arxiv.org/abs/1206.1849>, *Phys. Lett. B* 714 158-179 (2012).
50. The CMS Collaboration, “*Search for exotic particles decaying to WZ in pp collisions at $\sqrt{s} = 7$ TeV*”,
<http://arxiv.org/abs/1206.0433>, Submitted to *Phys. Rev. Lett.* (2012).

51. The CMS Collaboration, “*Search for new physics with same-sign isolated dilepton events with jets and missing transverse energy*”,
<http://arxiv.org/abs/1205.6615>, Phys. Rev. Lett. 109 071803 (2012).
52. The CMS Collaboration, “*Study of W boson production in PbPb and pp collisions at $\sqrt{s_{NN}} = 2.76$ TeV*”,
<http://arxiv.org/abs/1205.6334>, Phys. Lett. B 715 66-87 (2012).
53. The CMS Collaboration, “*Measurement of jet fragmentation into charged particles in pp and PbPb collisions at $\sqrt{s_{NN}} = 2.76$ TeV*”,
<http://arxiv.org/abs/1205.5872>, Submitted to J. High Energy Phys. (2012).
54. The CMS Collaboration, “*Search for a light charged Higgs boson in top quark decays in pp collisions at $\sqrt{s} = 7$ TeV*”,
<http://arxiv.org/abs/1205.5736>, J. High Energy Phys. 07 143 (2012).
55. The CMS Collaboration, “*Search for new physics in events with same-sign dileptons and b-tagged jets in pp collisions at $\sqrt{s} = 7$ TeV*”,
<http://arxiv.org/abs/1205.3933>, J. High Energy Phys. 08 110 (2012).
56. The CMS Collaboration, “*Measurement of the pseudorapidity and centrality dependence of the transverse energy density in PbPb collisions at $\sqrt{s_{NN}} = 2.76$ TeV*”,
<http://arxiv.org/abs/1205.2488>, Submitted to Phys. Rev. Lett. (2012).
57. The CMS Collaboration, “*Measurement of the Λ_b cross section and the $\overline{\Lambda}_b$ to Λ_b ratio with $J/\psi\Lambda$ decays in pp collisions at $\sqrt{s} = 7$ TeV*”,
<http://arxiv.org/abs/1205.0594>, Phys. Lett. B 714 136-157 (2012).
58. The CMS Collaboration, “*Search for heavy long-lived charged particles in pp collisions at $\sqrt{s} = 7$ TeV*”,
<http://arxiv.org/abs/1205.0272>, Phys. Lett. B 713 408-433 (2012).
59. The CMS Collaboration, “*Studies of jet quenching using isolated-photon+jet correlations in PbPb and pp collisions at $\sqrt{s_{NN}} = 2.76$ TeV*”,
<http://arxiv.org/abs/1205.0206>, Submitted to Phys. Lett. B (2012).

60. The CMS Collaboration, “*Observation of a New Ξ_b Baryon*”,
<http://arxiv.org/abs/1204.5341>, *Phys. Rev. Lett.* 108 252002 (2012).
61. The CMS Collaboration, “*Search for anomalous production of multilepton events in pp collisions at $\sqrt{s} = 7$ TeV*”,
<http://arxiv.org/abs/1204.5341>, *J. High Energy Phys.* 06 169 (2012).
62. The CMS Collaboration, “*Search for leptonic decays of W' bosons in pp collisions at $\sqrt{s} = 7$ TeV*”,
<http://arxiv.org/abs/1204.4764>, *J. High Energy Phys.* 08 023 (2012).
63. The CMS Collaboration, “*Search for physics beyond the standard model in events with a Z boson, jets, and missing transverse energy in pp collisions at $\sqrt{s} = 7$ TeV*”,
<http://arxiv.org/abs/1204.3774>, *Phys. Lett. B* 716 260-284 (2012).
64. The CMS Collaboration, “*Shape, transverse size, and charged hadron multiplicity of jets in pp collisions at $\sqrt{s} = 7$ TeV*”,
<http://arxiv.org/abs/1204.3170>, *J. High Energy Phys.* 06 160 (2012).
65. The CMS Collaboration, “*Measurement of the mass difference between top and antitop quarks*”,
<http://arxiv.org/abs/1204.2807>, *J. High Energy Phys.* 06 (2012) 109.
66. The CMS Collaboration, “*Search for anomalous $t\bar{t}$ production in the highly-boosted all-hadronic final state*”,
<http://arxiv.org/abs/1204.2488>, *Submitted to J. High Energy Phys.* (2012).
67. The CMS Collaboration, “*Azimuthal anisotropy of charged particles at high transverse momenta in PbPb collisions at $\sqrt{s_{NN}} = 2.76$ TeV*”,
<http://arxiv.org/abs/1204.1850>, *Phys. Rev. Lett.* 109 022301 (2012).
68. The CMS Collaboration, “*Measurement of the $Z/\gamma^* + b$ -jet cross section in pp collisions at $\sqrt{s} = 7$ TeV*”,
<http://arxiv.org/abs/1204.1643>, *J. High Energy Phys.* 06 126 (2012).

69. The CMS Collaboration, “*Measurement of the underlying event in the Drell-Yan process in proton-proton collisions at $\sqrt{s} = 7$ TeV*”,
<http://arxiv.org/abs/1204.1411>, Submitted to Eur. J. Phys. C (2012).
70. The CMS Collaboration, “*Measurement of the elliptic anisotropy of charged particles produced in PbPb collisions at nucleon-nucleon center-of-mass energy = 2.76 TeV*”,
<http://arxiv.org/abs/1204.1409>, Submitted to Phys. Rev. C (2012).
71. The CMS Collaboration, “*Search for heavy bottom-like quarks in 4.9 inverse femtobarns of pp collisions at $\sqrt{s} = 7$ TeV*”,
<http://arxiv.org/abs/1204.1088>, J. High Energy Phys. 05 123 (2012).
72. The CMS Collaboration, “*Search for Dark Matter and Large Extra Dimensions in pp Collisions Yielding a Photon and Missing Transverse Energy*”,
<http://arxiv.org/abs/1204.0821>, Phys. Rev. Lett. 108 261803 (2012).
73. The CMS Collaboration, “*Ratios of dijet production cross sections as a function of the absolute difference in rapidity between jets in proton-proton collisions at $\sqrt{s} = 7$ TeV*”,
<http://arxiv.org/abs/1204.0696>, Submitted to Eur. Phys. J. C (2012).
74. The CMS Collaboration, “*Measurement of the top quark pair production cross section in pp collisions at $\sqrt{s} = 7$ TeV in dilepton final states containing a τ* ”,
<http://arxiv.org/abs/1203.6810>, Phys. Rev. D 85 112007 (2012).
75. The CMS Collaboration, “*Search for heavy, top-like quark pair production in the dilepton final state in pp collisions at*”,
<http://arxiv.org/abs/1203.5410>, Phys. Lett. B 716 103-121 (2012).
76. The CMS Collaboration, “*Search for $B_s^0 \rightarrow \mu^+ \mu$ and $B^0 \rightarrow \mu^+ \mu$ decays*”,
<http://arxiv.org/abs/1203.3976>, J. High Energy Phys. 04 033 (2012).
77. The CMS Collaboration, “*Measurement of the cross section for production of $b\bar{b} X$* ”,

decaying to muons in pp collisions at $\sqrt{s} = 7 \text{ TeV}$ ”,

<http://arxiv.org/abs/1203.3458>, J. High Energy Phys. 06 110 (2012).

78. The CMS Collaboration, “*Search for microscopic black holes in pp collisions at $\sqrt{s} = 7 \text{ TeV}$ ”,*

<http://arxiv.org/abs/1202.6396>, J. High Energy Phys. 04 061 (2012).

79. The CMS Collaboration, “*Search for quark compositeness in dijet angular distributions from pp collisions at $\sqrt{s} = 7 \text{ TeV}$ ”,*

<http://arxiv.org/abs/1202.5535>, J. High Energy Phys. 05 055 (2012).

80. The CMS Collaboration, “*Jet momentum dependence of jet quenching in PbPb collisions at $\sqrt{s_{NN}} = 2.76 \text{ TeV}$ ”,*

<http://arxiv.org/abs/1202.5022>, Phys. Lett. B 712 176-197 (2012).

81. The CMS Collaboration, “*Inclusive b-jet production in pp collisions at $\sqrt{s} = 7 \text{ TeV}$ ”,*

<http://arxiv.org/abs/1202.4617>, J. High Energy Phys. 04 084 (2012).

82. The CMS Collaboration, “*Search for the standard model Higgs boson decaying to bottom quarks in pp collisions at $\sqrt{s} = 7 \text{ TeV}$ ”,*

<http://arxiv.org/abs/1202.4195>, Phys. Lett. B 710 284-306 (2012).

83. The CMS Collaboration, “*Search for neutral Higgs bosons decaying to tau pairs in pp collisions at $\sqrt{s} = 7 \text{ TeV}$ ”,*

<http://arxiv.org/abs/1202.4083>, Phys. Lett. B 713 68-90 (2012).

84. The CMS Collaboration, “*Search for large extra dimensions in dimuon and dielectron events in pp collisions at $\sqrt{s} = 7 \text{ TeV}$ ”,*

<http://arxiv.org/abs/1202.3827>, Phys. Lett. B 711 15-34 (2012).

85. The CMS Collaboration, “*Search for the standard model Higgs boson in the $H \rightarrow ZZ \rightarrow l^+l^- \tau^+ \tau^-$ decay channel in pp collisions at $\sqrt{s} = 7 \text{ TeV}$ ”,*

<http://arxiv.org/abs/1202.3617>, J. High Energy Phys. 03 081 (2012).

86. The CMS Collaboration, “*Search for the standard model Higgs boson in the $H \rightarrow ZZ \rightarrow 2l2\nu$ channel in pp collisions at $\sqrt{s} = 7$ TeV*”,
<http://arxiv.org/abs/1202.3478>, J. High Energy Phys. 03 040 (2012).
87. The CMS Collaboration, “*Study of high- p_T charged particle suppression in PbPb compared to pp collisions at $\sqrt{s_{NN}} = 2.76$ TeV*”,
<http://arxiv.org/abs/1202.2554>, Eur. Phys. J. C 72 1945 (2012).
88. The CMS Collaboration, “*Search for the standard model Higgs boson in the decay channel $H \rightarrow ZZ \rightarrow 4l$ in pp collisions at $\sqrt{s} = 7$ TeV*”,
<http://arxiv.org/abs/1202.1997>, Phys. Rev. Lett. 108 111804 (2012).
89. The CMS Collaboration, “*Search for the standard model Higgs boson decaying to W^+W^- in the fully leptonic final state in pp collisions at $\sqrt{s} = 7$ TeV*”,
<http://arxiv.org/abs/1202.1489>, Phys. Lett. B 710 91-113 (2012).
90. The CMS Collaboration, “*Combined results of searches for the standard model Higgs boson in pp collisions at $\sqrt{s} = 7$ TeV*”,
<http://arxiv.org/abs/1202.1488>, Phys. Lett. B 710 26-48 (2012).
91. The CMS Collaboration, “*Search for the standard model Higgs boson decaying into two photons in pp collisions at $\sqrt{s} = 7$ TeV*”,
<http://arxiv.org/abs/1202.1487>, Phys. Lett. B 710 403-425 (2012).
92. The CMS Collaboration, “*Search for a Higgs boson in the decay channel $H \rightarrow ZZ^* \rightarrow q\bar{q}ll^+$ in pp collisions at $\sqrt{s} = 7$ TeV*”,
<http://arxiv.org/abs/1202.1416>, J. High Energy Phys. 04 036 (2012).
93. The CMS Collaboration, “*Measurement of the inclusive production cross sections for forward jets and for dijet events with one forward and one central jet in pp collisions at $\sqrt{s} = 7$ TeV*”,
<http://arxiv.org/abs/1202.0704>, J. High Energy Phys. 06 036 (2012).
94. The CMS Collaboration, “*Suppression of non-prompt J/ψ , prompt J/ψ , and $\Upsilon(1S)$*

in PbPb collisions at $\sqrt{s_{NN}} = 2.76$ TeV,

<http://arxiv.org/abs/1201.5069>, *J. High Energy Phys.* 05 063 (2012).

95. The CMS Collaboration, “*Centrality dependence of dihadron correlations and azimuthal anisotropy harmonics in PbPb collisions at $\sqrt{s_{NN}} = 2.76$ TeV*”,

<http://arxiv.org/abs/1201.3158>, *Eur. Phys. J. C* 72 2012 (2012).

96. The CMS Collaboration, “*Measurement of isolated photon production in pp and PbPb collisions at $\sqrt{s_{NN}} = 2.76$ TeV*”,

<http://arxiv.org/abs/1201.3093>, *Phys. Lett. B* 710 256-277 (2012).

97. The CMS Collaboration, “*Measurement of the charge asymmetry in top-quark pair production in proton-proton collisions at $\sqrt{s} = 7$ TeV*”,

<http://arxiv.org/abs/1112.5100>, *Phys. Lett. B* 709 28-49 (2012).

98. The CMS Collaboration, “*Search for signatures of extra dimensions in the diphoton mass spectrum at the Large Hadron Collider*”,

<http://arxiv.org/abs/1112.0688>, *Phys. Rev. Lett.* 108 111801 (2012).

99. The CMS Collaboration, “*Exclusive $\gamma\gamma \rightarrow \mu^+\mu$ production in proton-proton collisions at $\sqrt{s} = 7$ TeV*”,

<http://arxiv.org/abs/1111.5536>, *J. High Energy Phys.* 01 052 (2012).

100. The CMS Collaboration, “ *J/ψ and $\psi(2S)$ production in pp collisions at $\sqrt{s} = 7$ TeV*”,

<http://arxiv.org/abs/1111.1557>, *J. High Energy Phys.* 02 011 (2012).

101. The CMS Collaboration, “*Measurement of the Production Cross Section of Pairs of Isolated Photons in pp collisions at $\sqrt{s} = 7$ TeV*”,

<http://arxiv.org/abs/1110.6461>, *J. High Energy Phys.* 01 133 (2012).

102. The CMS Collaboration, “*Measurement of the Rapidity and Transverse Momentum Distributions of Z Bosons in pp Collisions at $\sqrt{s} = 7$ TeV*”,

<http://arxiv.org/abs/1110.4973>, *Phys. Rev. D* 85 032002 (2012).

103. The CMS Collaboration, “*Jet Production Rates in Association with W and Z Bosons in pp Collisions at $\sqrt{s} = 7$ TeV*”,
<http://arxiv.org/abs/1110.3226>, *J. High Energy Phys.* 01 010 (2012).
104. The CMS Collaboration, “*Measurement of the weak mixing angle with the Drell-Yan process in proton-proton collisions at the LHC*”,
<http://arxiv.org/abs/1110.2682>, *Phys. Rev. D* 84 112002 (2011).
105. The CMS Collaboration, “*Measurement of energy flow at large pseudorapidities in pp collisions at $\sqrt{s} = 0.9$ and 7 TeV*”,
<http://arxiv.org/abs/1110.0211>, *J. High Energy Phys.* 02 055 (2012).
106. The CMS Collaboration, “*Forward Energy Flow, Central Charged-Particle Multiplicities, and Pseudorapidity Gaps in W and Z Boson Events from pp Collisions at $\sqrt{s} = 7$ TeV*”,
<http://arxiv.org/abs/1110.0181>, *Eur. Phys. J. C* 72 1839 (2012).
107. The CMS Collaboration, “*Performance of τ -lepton reconstruction and identification in CMS*”,
<http://arxiv.org/abs/1109.6034>, *J. Instrum.* 7 P01001 (2012).
108. The CMS Collaboration, “*Search for a Vector-like Quark with Charge $2/3$ in $t + Z$ Events from pp Collisions at $\sqrt{s} = 7$ TeV*”,
<http://arxiv.org/abs/1109.4985>, *Phys. Rev. Lett.* 107 271802 (2011).
109. The CMS Collaboration, “*Search for Supersymmetry at the LHC in Events with Jets and Missing Transverse Energy*”,
<http://arxiv.org/abs/1109.2352>, *Phys. Rev. Lett.* 107 221804 (2011).
110. The CMS Collaboration, “*Measurement of the $t\bar{t}$ Production Cross Section in pp Collisions at 7 TeV in Lepton + Jets Events Using b -quark Jet Identification*”,
<http://arxiv.org/abs/1108.3773>, *Phys. Rev. D* 84 092004 (2011).
111. The CMS Collaboration, “*Measurement of the Differential Cross Section for Isolated Prompt Photon Production in pp Collisions at 7 TeV*”,

<http://arxiv.org/abs/1108.2044>, *Phys. Rev. D*, 84 052011 (2011).

112. The CMS Collaboration, “*Measurement of the Drell-Yan Cross Section in pp Collisions at $\sqrt{s} = 7$ TeV*”, <http://arxiv.org/abs/1108.0566>, *J. High Energy Phys.* 10 007 (2011).
113. The CMS Collaboration, “*Search for $B_s^0 \rightarrow \mu^+ \mu^-$ and $B^0 \rightarrow \mu^+ \mu^-$ decays in pp collisions at $\sqrt{s} = 7$ TeV*”, <http://arxiv.org/abs/1107.5834>, *Phys. Rev. Lett.* 107 191802 (2011).
114. The CMS Collaboration, “*Dependence on pseudorapidity and on centrality of charged hadron production in PbPb collisions at $\sqrt{s_{NN}} = 2.76$ TeV*”, <http://arxiv.org/abs/1107.4800>, *J. High Energy Phys.*, 08 141 (2011).
115. The CMS Collaboration, “*Measurement of the Inclusive W and Z Production Cross Sections in pp Collisions at $\sqrt{s} = 7$ TeV*”, <http://arxiv.org/abs/1107.4789>, *J. High Energy Phys* 10 132 (2011).
116. The CMS Collaboration, “*Search for Resonances in the Dijet Mass Spectrum from 7 TeV pp Collisions at CMS*”, <http://arxiv.org/abs/1107.4771>, *Phys. Lett. B*, 704 123-142 (2011).
117. The CMS Collaboration, “*Determination of Jet Energy Calibration and Transverse Momentum Resolution in CMS*”, <http://arxiv.org/abs/1107.4277>, *JINST* 6 P11002 (2011).
118. The CMS Collaboration, “*Search for Three-Jet Resonances in pp Collisions at $\sqrt{s} = 7$ TeV*”, <http://arxiv.org/abs/1107.3084>, *Phys. Rev. Lett.*, 107 101801 (2011).
119. The CMS Collaboration, “*Search for supersymmetry in pp collisions at $\sqrt{s}=7$ TeV in events with a single lepton, jets, and missing transverse momentum*”, <http://arxiv.org/abs/1107.1870>, *J. High Energy Phys.*, 08 156 (2011).

120. The CMS Collaboration, “A search for excited leptons in pp Collisions at $\sqrt{s} = 7$ TeV”, <http://arxiv.org/abs/1107.1773>, *Phys. Lett. B*, 704 143-162 (2011).
121. The CMS Collaboration, “Inclusive search for squarks and gluinos in pp collisions at $\sqrt{s} = 7$ TeV”,
<http://arxiv.org/abs/1107.1279>, *Phys. Rev. D* 85 012004 (2012).
122. The CMS Collaboration, “Measurement of the Underlying Event Activity at the LHC with $\sqrt{s} = 7$ TeV and Comparison with $\sqrt{s} = 0.9$ TeV”,
<http://arxiv.org/abs/1107.0330>, *J. High Energy Phys.*, 09 109 (2011).
123. The CMS Collaboration, “Missing transverse energy performance of the CMS detector”,
<http://arxiv.org/abs/1106.5048>, *JINST* 6 P09001 (2011).
124. The CMS Collaboration, “Search for New Physics with a Mono-Jet and Missing Transverse Energy in pp Collisions at $\sqrt{s} = 7$ TeV”,
<http://arxiv.org/abs/1106.4775>, *Phys. Rev. Lett.* 107 201804 (2011).
125. The CMS Collaboration, “Search for New Physics with Jets and Missing Transverse Momentum in pp collisions at $\sqrt{s} = 7$ TeV”,
<http://arxiv.org/abs/1106.4503>, *J. High Energy Phys.*, 08 155 (2011).
126. The CMS Collaboration, “Measurement of the B_s^0 Production Cross Section with $B_s^0 \rightarrow J/\psi\phi$ Decays in pp Collisions at $\sqrt{s} = 7$ TeV”,
<http://arxiv.org/abs/1106.4048>, *Phys. Rev. D*, 84 052008 (2011).
127. The CMS Collaboration, “Search for Supersymmetry in Events with b Jets and Missing Transverse Momentum at the LHC”,
<http://arxiv.org/abs/1106.3272>, *J. High Energy Phys.*, 07 113 (2011).
128. The CMS Collaboration, “Measurement of the t-channel single top quark production cross section in pp collisions at $\sqrt{s} = 7$ TeV”,
<http://arxiv.org/abs/1106.3052>, *Phys. Rev. Lett.*, 107 091802 (2011).

129. The CMS Collaboration, “*Search for Light Resonances Decaying into Pairs of Muons as a Signal of New Physics*”, <http://arxiv.org/abs/1106.2375>, *J. High Energy Phys.*, 07 098 (2011).
130. The CMS Collaboration, “*Search for Same-Sign Top-Quark Pair Production at $\sqrt{s} = 7$ TeV and Limits on Flavour Changing Neutral Currents in the Top Sector*”, <http://arxiv.org/abs/1106.2142>, *J. High Energy Phys.*, 08 005 (2011).
131. The CMS Collaboration, “*Search for Physics Beyond the Standard Model Using Multilepton Signatures in pp Collisions at $\sqrt{s} = 7$ TeV*”, <http://arxiv.org/abs/1106.0933>, *Phys. Lett. B*, 704 411-433 (2011).
132. The CMS Collaboration, “*Measurement of the $t\bar{t}$ Production Cross Section in pp Collisions at $\sqrt{s} = 7$ TeV using the Kinematic Properties of Events with Leptons and Jets*”, <http://arxiv.org/abs/1106.0902>, *Eur. Phys. J. C*, 71 1721 (2011).
133. The CMS Collaboration, “*Measurement of the Ratio of the 3-jet to 2-jet Cross Sections in pp Collisions at $\sqrt{s} = 7$ TeV*”, <http://arxiv.org/abs/1106.0647>, *Phys. Lett. B*, 702 336-354 (2011).
134. The CMS Collaboration, “*Measurement of the Inclusive Jet Cross Section in pp Collisions at $\sqrt{s} = 7$ TeV*”, <http://arxiv.org/abs/1106.0208>, *Phys. Rev. Lett.*, 107 132001 (2011).
135. The CMS Collaboration, “*Measurement of the $t\bar{t}$ production cross section and the top quark mass in the dilepton channel in pp collisions at $\sqrt{s} = 7$ TeV*”, <http://arxiv.org/abs/1105.5661>, *J. High Energy Phys.*, 07 049 (2011).
136. The CMS Collaboration, “*Search for First Generation Scalar Leptoquarks in the $e\nu jj$ Channel in pp Collisions at $\sqrt{s} = 7$ TeV*”, <http://arxiv.org/abs/1105.5237>, *Phys. Lett. B*, 703 246-266 (2011).
137. The CMS Collaboration, “*Indications of Suppression of Excited Υ States in Pb-Pb*

- Collisions at $\sqrt{s_{NN}} = 2.76$ TeV*,
<http://arxiv.org/abs/1105.4894>, *Phys. Rev. Lett.*, 107 052302 (2011).
138. The CMS Collaboration, “*Measurement of $W\gamma$ and $Z\gamma$ production in pp collisions at $\sqrt{s} = 7$ TeV*”,
<http://arxiv.org/abs/1105.2758>, *Phys. Lett. B*, 701 535555 (2011).
139. The CMS Collaboration, “*Long-range and short-range dihadron angular correlations in central PbPb collisions at $\sqrt{s_{NN}} = 2.76$ TeV*”,
<http://arxiv.org/abs/1105.2438>, *J. High Energy Phys.*, 07 076 (2011).
140. The CMS Collaboration, “*Search for supersymmetry in events with a lepton, a photon, and large missing transverse energy in pp collisions at $\sqrt{s} = 7$ TeV*”,
<http://arxiv.org/abs/1105.3152>, *J. High Energy Phys.*, 06 093 (2011).
141. The CMS Collaboration, “*Measurement of the Polarization of W Bosons with Large Transverse Momenta in W+Jets Events at the LHC*”,
<http://arxiv.org/abs/1104.3829>, *Phys. Rev. Lett.*, 107 021802 (2011).
142. The CMS Collaboration, “*Charged particle transverse momentum spectra in pp collisions at $\sqrt{s} = 0.9$ and 7 TeV*”,
<http://arxiv.org/abs/1104.3547>, *J. High Energy Phys.*, 08 086 (2011).
143. The CMS Collaboration, “*Search for new physics with same-sign isolated dilepton events with jets and missing transverse energy at the LHC*”,
<http://arxiv.org/abs/1104.3168>, *J. High Energy Phys.*, 06 077 (2011).
144. The CMS Collaboration, “*Measurement of the B^0 Production Cross Section in pp Collisions at $\sqrt{s} = 7$ TeV*”,
<http://arxiv.org/abs/1104.2892>, *Phys. Rev. Lett.*, 106 252001 (2011).
145. The CMS Collaboration, “*Measurement of the differential dijet production cross section in proton-proton collisions at $\sqrt{s}=7$ TeV*”,
<http://arxiv.org/abs/1104.1693>, *Phys. Lett. B*, 700 187206 (2011).

146. The CMS Collaboration, “*Search for Neutral Minimal Supersymmetric Standard Model Higgs Bosons Decaying to Tau Pairs in pp Collisions at $\sqrt{s}=7$ TeV*”,
http://arxiv.org/abs/1104.1619, Phys. Rev. Lett., 106 231801 (2011).
147. The CMS Collaboration, “*Measurement of the Inclusive Z Cross Section via Decays to Tau Pairs in pp Collisions at $\sqrt{s} = 7$ TeV*”,
http://arxiv.org/abs/1104.1617, J. High Energy Phys., 08 117 (2011).
148. The CMS Collaboration, “*Search for Large Extra Dimensions in the Diphoton Final State at the Large Hadron Collider*”,
http://arxiv.org/abs/1103.4279, J. High Energy Phys., 05 085 (2011).
149. The CMS Collaboration, “*Measurement of the lepton charge asymmetry in inclusive W production in pp collisions at $\sqrt{s} = 7$ TeV*”,
http://arxiv.org/abs/1103.3470, J. High Energy Phys., 04 050 (2011).
150. The CMS Collaboration, “*Search for Physics Beyond the Standard Model in Opposite-sign Dilepton Events in pp Collisions at $\sqrt{s} = 7$ TeV*”,
http://arxiv.org/abs/1103.1348, J. High Energy Phys., 06 026 (2011).
151. The CMS Collaboration, “*Search for Resonances in the Dilepton Mass Distribution in pp Collisions at $\sqrt{s} = 7$ TeV*”,
http://arxiv.org/abs/1103.0981, J. High Energy Phys., 05 093 (2011).
152. The CMS Collaboration, “*Search for Supersymmetry in pp Collisions at $\sqrt{s} = 7$ TeV in Events with Two Photons and Missing Transverse Energy*”,
http://arxiv.org/abs/1103.0953, Phys. Rev. Lett., 106 211802 (2011).
153. The CMS Collaboration, “*Search for a W' boson decaying to a muon and a neutrino in pp collisions at $\sqrt{s} = 7$ TeV*”,
http://arxiv.org/abs/1103.0030, Phys. Lett. B, 701 160179 (2011).
154. The CMS Collaboration, “*Study of Z boson production in PbPb collisions at $\sqrt{s_{NN}} = 2.76$ TeV*”, *http://arxiv.org/abs/1102.5435,*
Phys. Rev. Lett., 106 212301 (2011).

155. The CMS Collaboration, “*Measurement of W^+W^- Production and Search for the Higgs Boson in pp Collisions at $\sqrt{s} = 7$ TeV*”,
http://arxiv.org/abs/1102.5429, *Phys. Lett. B*, 699 25-47 (2011).
156. The CMS Collaboration, “*Search for a Heavy Bottom-like Quark in pp Collisions at $\sqrt{s} = 7$ TeV*”, *http://arxiv.org/abs/1102.4746*,
Phys. Lett. B, 701 204223 (2011).
157. The CMS Collaboration, “*Strange Particle Production in pp collisions at $\sqrt{s} = 0.9$ and 7 TeV*”, *http://arxiv.org/abs/1102.4282*,
J. High Energy Phys., 05 064 (2011).
158. The CMS Collaboration, “*Measurement of $B\bar{B}$ angular correlations based on secondary vertex reconstruction at $\sqrt{s}=7$ TeV*”,
http://arxiv.org/abs/1102.3194, *J. High Energy Phys.*, 03 136 (2011).
159. The CMS Collaboration, “*Measurement of Dijet Angular Distributions and Search for Quark Compositeness in pp Collisions at $\sqrt{s} = 7$ TeV*”,
http://arxiv.org/abs/1102.2020, *Phys. Rev. Lett.*, 106 201804 (2011).
160. The CMS Collaboration, “*Observation and studies of jet quenching in PbPb collisions at $\sqrt{s_{NN}} = 2.76$ TeV*”,
http://arxiv.org/abs/1102.1957, *Phys. Rev. C*, 84 024906 (2011).
161. The CMS Collaboration, “*First Measurement of Hadronic Event Shapes in pp Collisions at $\sqrt{s}=7$ TeV*”, *http://arxiv.org/abs/1102.0068*,
Phys. Lett. B, 699 48-67 (2011).
162. The CMS Collaboration, “*Dijet Azimuthal Decorrelations in pp Collisions at $\sqrt{s} = 7$ TeV*”, *http://arxiv.org/abs/1101.5029*,
Phys. Rev. Lett., 106 122003 (2011).
163. The CMS Collaboration, “*Measurement of BoseEinstein Correlations in pp Collisions at $\sqrt{s} = 0.9$ and 7 TeV*”,
http://arxiv.org/abs/1101.3518, *J. High Energy Phys.*, 05 029 (2011).

164. The CMS Collaboration, “*Inclusive b -hadron production cross section with muons in pp collisions at $\sqrt{s} = 7$ TeV*”,
<http://arxiv.org/abs/1101.3512>, *J. High Energy Phys.*, 03 090 (2011).
165. The CMS Collaboration, “*Search for Heavy Stable Charged Particles in pp collisions at $\sqrt{s} = 7$ TeV*”,
<http://arxiv.org/abs/1101.1645>, *J. High Energy Phys.*, 03 024 (2011).
166. The CMS Collaboration, “*Search for Supersymmetry in pp Collisions at 7 TeV in Events with Jets and Missing Transverse Energy*”,
<http://arxiv.org/abs/1101.1628>, *Phys. Lett. B*, 698 196218 (2011).
167. The CMS Collaboration, “*Measurement of the B^+ Production Cross Section in pp Collisions at $\sqrt{s} = 7$ TeV*”,
<http://arxiv.org/abs/1101.0131>, *Phys. Rev. Lett.*, 106 112001 (2011).
168. The CMS Collaboration, “*Search for a heavy gauge boson W' in the final state with an electron and large missing transverse energy in pp collisions at $\sqrt{s} = 7$ TeV*”,
<http://arxiv.org/abs/1012.5945>, *Phys. Lett. B*, 698 21-39 (2011).
169. The CMS Collaboration, “*Upsilon production cross section in pp collisions at $\sqrt{s} = 7$ TeV*”,
<http://arxiv.org/abs/1012.5545>, *Phys. Rev. D*, 83 112004 (2011).
170. The CMS Collaboration, “*Search for Pair Production of Second-Generation Scalar Leptoquarks in pp Collisions at $\sqrt{s} = 7$ TeV*”,
<http://arxiv.org/abs/1012.4033>, *Phys. Rev. Lett.*, 106 201803 (2011).
171. The CMS Collaboration, “*Search for Pair Production of First-Generation Scalar Leptoquarks in pp Collisions at $\sqrt{s} = 7$ TeV*”,
<http://arxiv.org/abs/1012.4031>, *Phys. Rev. Lett.*, 106 201802 (2011).
172. The CMS Collaboration, “*Search for Microscopic Black Hole Signatures at the*

- Large Hadron Collider*”, <http://arxiv.org/abs/1012.3375>, *Phys. Lett. B*, 697 434-453 (2011).
173. The CMS Collaboration, “*Measurements of Inclusive W and Z Cross Sections in pp Collisions at $\sqrt{s} = 7$ TeV*”,
<http://arxiv.org/abs/1012.2466>, *J. High Energy Phys.*, 01 080 (2011).
174. The CMS Collaboration, “*Measurement of the Isolated Prompt Photon Production Cross Section in pp Collisions at $\sqrt{s} = 7$ TeV*”,
<http://arxiv.org/abs/1012.0799>, *Phys. Rev. Lett.*, 106 082001 (2011).
175. The CMS Collaboration, “*Search for Stopped Gluinos in pp collisions at $\sqrt{s} = 7$ TeV*”,
<http://arxiv.org/abs/1011.5861>, *Phys. Rev. Lett.*, 106 011801 (2011).
176. The CMS Collaboration, “*Charged particle multiplicities in pp interactions at $\sqrt{s} = 0.9, 2.36$, and 7 TeV*”,
<http://arxiv.org/abs/1011.5531>, *J. High Energy Phys.*, 01 079 (2011).
177. The CMS Collaboration, “*Prompt and non-prompt J/ψ production in pp collisions at $\sqrt{s} = 7$ TeV*”,
<http://arxiv.org/abs/1011.4193>, *Eur. Phys. J. C*, 71 1575 (2011).

Conferences/Schools/Workshops Attended

1. 23-27 July 2012, VI MCnet-LPCC Summer School on Monte Carlo Event Generators for LHC, CERN, Geneva, Switzerland.
2. 13-17 July 2012, Implications of LHC results for TeV-scale physics, CERN, Geneva, Switzerland.
3. 26-28 February 2012, VI Chandigarh Science Congress, PU, Chandigarh, India.

4. 22-27 August 2011, **XXV International Symposium On Lepton Photon Interactions at High Energies**, TIFR, Mumbai, India.
5. 8-17 June 2011, **VI CERN-Fermilab Hadron Collider Physics Summer School**, CERN, Geneva, Switzerland.
6. 26-28 February 2011, **V Chandigarh Science Congress**, PU, Chandigarh, India.
7. 13-18 December 2010, **XIX DAE-BRNS High Energy Physics Symposium**, LNMIIT, Jaipur, India.
8. 22-27 February 2010, **XIII International Workshop on Advanced Computing and Analysis Techniques in Physics Research**, Jaipur, India.
9. 21-27 October 2009, **LHC Physics WorkShop**, TIFR, Mumbai, India.